令和元年度

長岡技術科学大学 大学院工学研究科 博士後期課程

エネルギー・環境工学専攻

博士論文

論 文 題 目

Study on Preparation of Hydroxyapatite Nanoparticle Films and Their Cytocompatibility Evaluation for Biomedical Applications

(水酸アパタイトナノ粒子膜の調製と生物医学的応用のための細胞親和性の評価に関する研究)

申請者：TANIA GUADALUPE PENAFLOR GALINDO

(タニア グアダルーペ ペナフロア ガリンド)

学籍番号：17701887

Acknowledgments

I wish to express my deepest gratitude to Dr. Motohiro Tagaya of the Department of Material Science and Technology (MST), Nagaoka University of Technology (NUT), for his continuous and kindly support, supervision, guidance, patient and encouragement throughout my doctoral course in Japan side. Also, my sincere appreciation for my doctoral thesis reviewing process in NUT by Dr. Motohiro Tagaya, Dr. Takaomi Kobayashi, Dr. Nobuo Saito, Dr. Kiyoshi Ohnuma, and Dr. Kubo Shoichi.

I would like to express my thanks to the laboratory members (Mr. Kataoka, Mr. Yamada, Mr. Chai, Ms. Maruko, Mr. Kobashi, Mr. Iori, Mr. Shang, Mr. Ikeda, Mr. Hasegawa, Mr. Liu) for their advising, help and friendship. Very special thanks for Dr. Shiba Kota of NIMS for his valuable help, advice and support.

A deep appreciation for the support provided by the Analysis Center of the NUT. To Kokusaika thank you very much for your great availability for help and kindness. To my Japanese teachers, thank you very much for helping me to enter into the Japanese world.

I am very grateful to the scholarship received from National Science and Technology Council (CONACYT) of the Mexico federal government based on their generous assistance; it was possible to accomplish this stay at the NUT.

I am grateful to the University of Guanajuato for supporting me before and during my stay in Japan. My deep appreciation to Dr. Merced, Dr. Cervantes, Dr. Gerardo, Dr. Zárraga, and Dr. Baez for their advice, support, and encouragement.

To my families (my parents Susana and Gerardo, Erick, Itzel, Fernando Galindo, Maria de los Angeles, Aurelia, and all my family, Gustavos`s Family, Hasegawa Family, Ishiyama san, Yoyoko san, Mutsumikai group, Hitomi´s family, Kazu san) I send all my love and gratitude. Their continuous support and encouragement were my inspiration and motivation, especially in difficult times.

To my friends my love and thanks for your friendship and wonderful memories. I will keep with love in my heart.

Tania Guadalupe Peñaflor Galindo

TANIA GUADALUPE PENAFLOR GALINDO

December 2019

Contents

Chapter 1. General Introduction

Chapter 2. Study on Preparation of Elliptical Hydroxyapatite Nanoparticle Films and Their Protein Mediation Ability for Cell Adhesion

Chapter 1

“General Introduction”

Chapter 1

General Introduction

1.1. Introduction

The human body can regenerate itself with the aim of recovering and maintaining the structure and function of damaged organs or body parts. However, this ability can be lost in certain conditions, such as illness or severe trauma. With the purpose of maintaining the functionalities of the organs or tissues in the human body, several biomaterials have been developed to replace or implant in the human body.[1–3]

A biomaterial can be defined as one or more substances (non-drugs), which may have natural (animal tissues, proteins) or synthetic (metals, polymers or ceramics) origin, that is suitable to be incorporated in living systems for the treatment or replacement of partially or totally any tissue, organ or body functions, with the purpose of keeping or improving the quality of life of the patient.[4–6] On the other hand, the biological materials such as bone, skin, tissue, vessels produced by a living system are also used as biomaterials to implant in the body.[2]

In order to control the cytocompatibility of the implantable biomaterial, it is imperative to understand the interfacial interactions between the suitable biomaterial and the biological tissue with which it will interact.

1.2. Implantation of Biomaterials

1.2.1. Biological Response

The initial interactions of the implantable material with the biological medium and tissue with which it will interact will determine the success or failure of the implant. The simple fact of implanting a biomaterial in the human body generates an immune response since the implantation was made by surgery. The tissue injury initiates two principal immune responses, inflammation and the response for repair (wound healing reaction).[7] The success of tissue integration of the implanted biomaterial mainly depends on its ability to mimic the physiological conditions such as repair processes that occur after the injury and control of reactions like inflammation responses.[8] Immediately after being implanted,

the biomaterial covered by proteins coming from the blood causes the formation of a provisional matrix that determines the activation of the coagulation cascade, the complement system and the immune cells, which initiates the inflammatory response.[9]

The provisional matrix releases chemokines to attract phagocytic cells, which adhere to the implant by integrins. As the implant is a foreign material, the neutrophils release proteases, lysozymes, and reactive radicals to degrade the biomaterial. The biodegradable materials completely degraded during this acute state of inflammation. The inflammation ends, and the body returns to its homeostasis. This immune reaction is known as "innate response" and includes a wide variety of cells like polymorphonuclear cells (eosinophils, granulocytes, and basophils), mononuclear phagocyte cells (dendritic cells, monocytes, and macrophage cells), natural killers and innate lymphoid cells. If the implant was not degraded or residual material remains, chronic inflammation begins.[10] This inflammation was characterized by granulomatous reaction and the presence of lymphocytes and monocytes and the permanent activation of macrophages and polymorphonuclear neutrophils (PMNs), which continue releasing enzymes and radicals that damage the surrounding tissue.

The plasma cells and T and B lymphocytes are contributors to the adaptive immune response. During the innate response the macrophages are M1 phenotype with a pro-inflammatory function, but during the adaptive response the macrophages are M2 phenotype with pro-healing function. This period of chronic inflammation lasts approximately two weeks. If there are still a large number of immune cells after that period, it is often indication of an infection or a rejection of the implant. The immune response eventually finishes with the production of giant body cells.

The giant cells were the fusion of macrophages due to the inability to resolve chronic inflammation. Excess collagen and fibroblasts deposited around these cells, which results in fibrous capsule formation.[9–12] The physicochemical properties and the intrinsic properties (such as size, shape, charge, stability, molecular weight, and hydrophobicity) of the implanted biomaterial have substantial influence in the immune responses.[13] Biomaterials that exhibit bioactivity promote the desired tissue response. These biomaterials have a more specific biological response, resulting in a direct bond formation between the tissue and the biomaterial, following by the bone formation at the interface of the implanted biomaterial

and the tissue.[14–16] The immune reactions, as well as the desired reactions to an implanted biomaterial, are shown in **Figure 1.1 (a)**, and the desirable wound healing phases after biomaterial implantation in the human body are in **Figure 1.1 (b)**. Biomaterials like gold (Au), polydimethylsiloxane (PDMS), or hydroxyapatite (HAp) had used as implanted materials. Au due to the relative inertness, physicochemical and optical properties have been used in clinical and biomedical applications including drug and gene delivery, diagnosis assay, radiotherapy, cosmetic industry, implants,[17,18] and more recently in cardiac patches for treating damaged heart tissues after a heart attack, without surgery.[19] Nevertheless, it has reported contact allergy, and sometimes after a long time it can cause chronic cytotoxicity.[20–22] The properties of the PDMS including bio-inertness, low toxicity, thermal and oxidative stable, and antiadhesive properties allowed to be used in several biomedical applications such as blood containers, artificial skin, medical adhesives, drainage implants, catheters, among others.[23,24] Nonetheless, it has been observed in clinical practice collagenous encapsulation[25,26] and in the case of percutaneous devices have been noticed tunnel bacterial infection catheters.[27,28] Bioactive materials like HAp have been used in implants, demonstrated its ability to been with the human tissues. However, in some cases it has been noticed impair growth, causing inflammation to the surrounding soft tissues.[29] The difficulty of controlling the cytocompatibility of the biomaterials is shown in **Figure 1.2**. Some New strategies are being developed to design materials to use the immune system to improve the integration of the implant, avoid foreign body reaction, and prevent the formation of the fibrous capsule, to obtain successful implantation of the biomaterial.

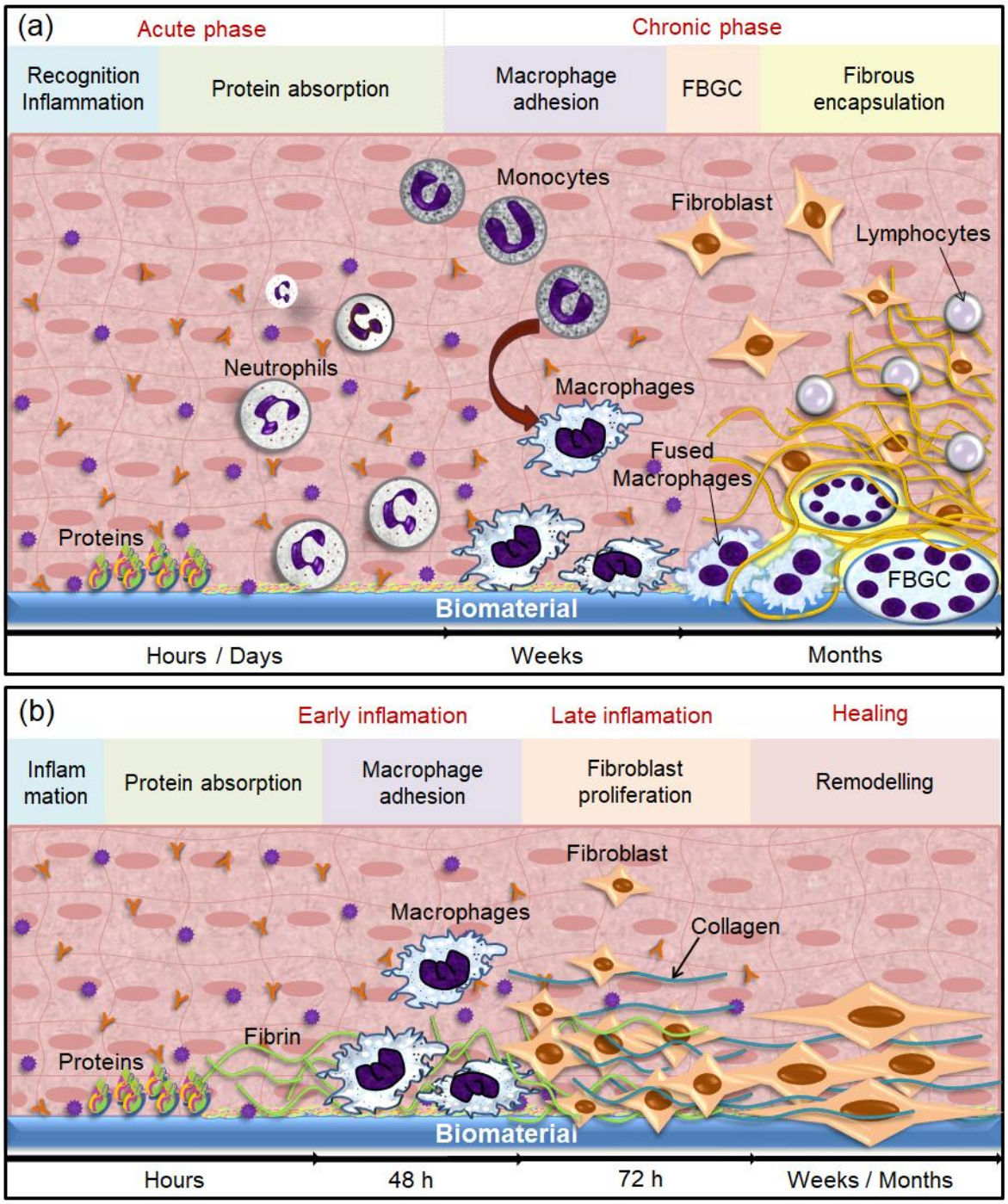

Figure 1.1. (a) Schematic representation of the sequence of events that occur when a biomaterial implanted in the human body. The picture shows the main cells involved in the immune response, from the initiation to the foreign body giant cells (FBGC) and fibrous encapsulation, and (b) illustration of the desirable wound healing phases after biomaterial implantation in the human body.

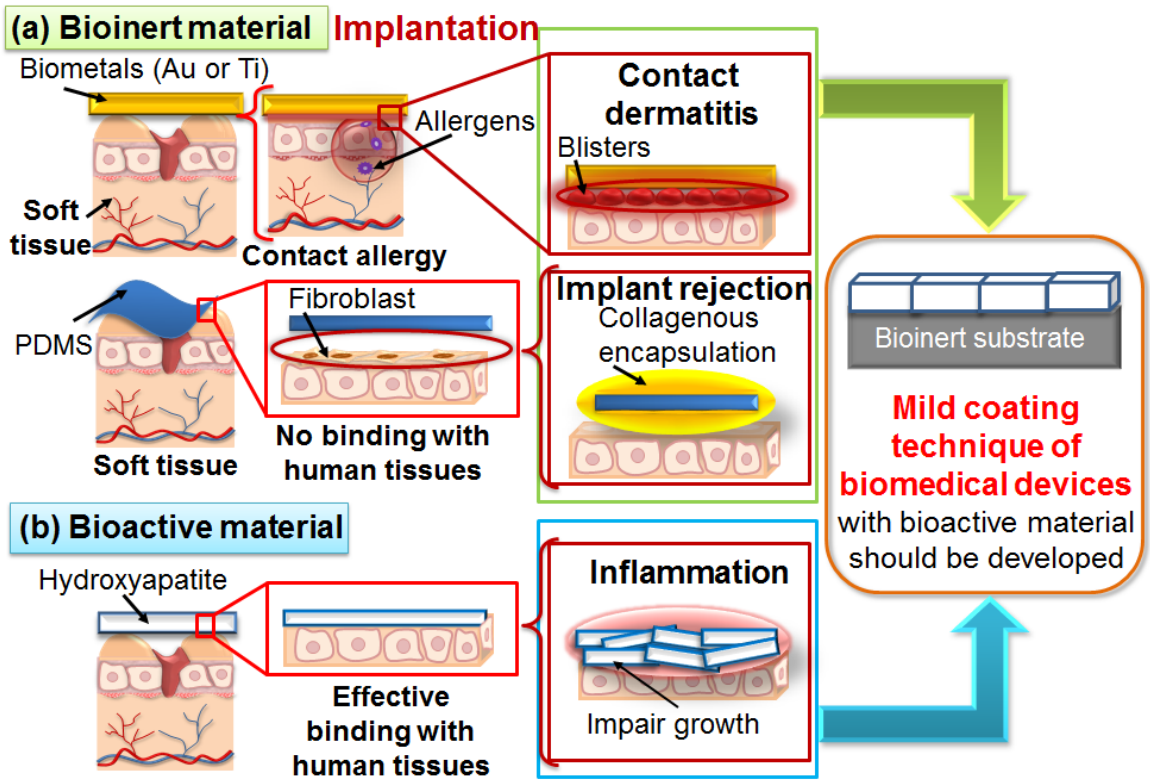

Figure 1.2. The difficulty of controlling cytocompatibility of the (a) bioinert and (b) bioactive materials and their problems after implantation, suggesting the mild coating technique of biomedical devices with bioactive material is recurred to improve the cytocompatibility of the medical devices.

1.2.2. Percutaneous Devices and Their Bacterial Infection

A percutaneous device is an instrument made with a foreign material (non-biological) which penetrates into and through the skin, providing a connection to the exterior of the body and the interior of the body (organ or cavity). This device has a wide variety of clinical and biomedical research purposes.[30] Some of the applications the percutaneous devices are micro-surgery, continuous infusions, blood sampling, external circulation, monitoring tissue parameters including pH, bio-potentials, CO_2, H_2O, dialysis, among others.[31]

Nevertheless, due to the low cytocompatibility of the percutaneous device material with human tissue, percutaneous long-term or permanent devices tend to fail.[32] The interfacial failure modes identified are marsupialization, migration, avulsion, and infection, all of these alone or in combination. Single or multiple etiological factors may be responsible for these failure modes.

The identified interfacial failure causes are marsupialization, migration, avulsion, infection, alone, or in combination. Single or multiple etiological factors can be responsible for the failed implantation. Skin defects can be surgically created around the implant during the penetration process, epidermal healing characteristics that prevent the formation of a suitable seal at the implant-skin interface and mechanical forces that may disrupt dermal attempts to seal the interface.[30] Because there is no proper connection between the percutaneous device and the skin, eventually, the interface becomes infected, which makes it necessary to remove the implant.

One of the most commonly used percutaneous devices is the catheter. In medicine, a catheter (from the Greek *katheter* which means instrument that is sent below) is a shaped and elongated narrow tube that can be introduced into a tissue or vein with the aim of exploring cavities. Catheters allow the injection of nutrients, drugs, fluid drainage or access other medical instruments.[33] The catheters are usually inserted into a body cavity, a pipe, or a blood vessel. These devices can be thin tubes, called soft flexible catheters or catheters thicker and non-flexible called hard catheters. A catheter can be left in the body, whether temporarily or permanently. The catheters are generally inserted percutaneously, and frequently some complications arise after the catheter is placed; these complications can be caused by several factors including exit/tunnel infection, external cuff extrusion, pericatheter leak, inflammation, catheter obstruction, infusion or pressure pain.[34] However, the most relevant complication of the catheter is the catheter-related infection.[35] In catheterized patients, bacteria can adhere rapidly to the surface on indwelling devices in a process known as bacteria docking after the interlocking, creating an extracellular stronger polymeric matrix, which adheres to the catheter surface, where bacteria colonize in a process known as biofilm.[36–38] This biofilm acts as pathogen reservoir[39] and is more resistant to the antibacterial treatment, resulting in catheter-related infections and many cases, in death.[40]

The catheter-related infection is the significant microbial growth (more than 15 colony forming units (CFU)) cultivated in a segment of the catheter.[41,42] Usually, these infections start at the end of the catheter, then penetrates the skin and then extraluminal extend along the catheter surface, or appear in the catheter lumen and extending intraluminal into the bloodstream. Only in sporadic cases these infections are initiated by hematogenous seeding

in the intravascular portion of the catheter; and even in more rare circumstances, infection may appear by the solution infused through the catheter.

The microorganisms that commonly cause these infections include *Staphylococcus aureus* (*S. aureus*), *Pseudomonas aerugonosa*, *Enterobacteriaceae*, *Enterococci*, *Escherichia coli* (*E. coli*), *Candida spp*, *Coagulase-negative staphylococci*, *Acinetobacter spp*.[43]

Due to the poor compatibility of silicone rubber catheter, it cannot bind with the body tissues, creating a space (passway) between the skin and the percutaneous device. Using this passway, the bacteria can easily permeate inside the body (Skin Downgrowth), and it can cause bacterial infection (see **Figure 1.3**). To prevent bacterial infection, the surface coating technique by cytocompatible materials on a silicone rubber is required.

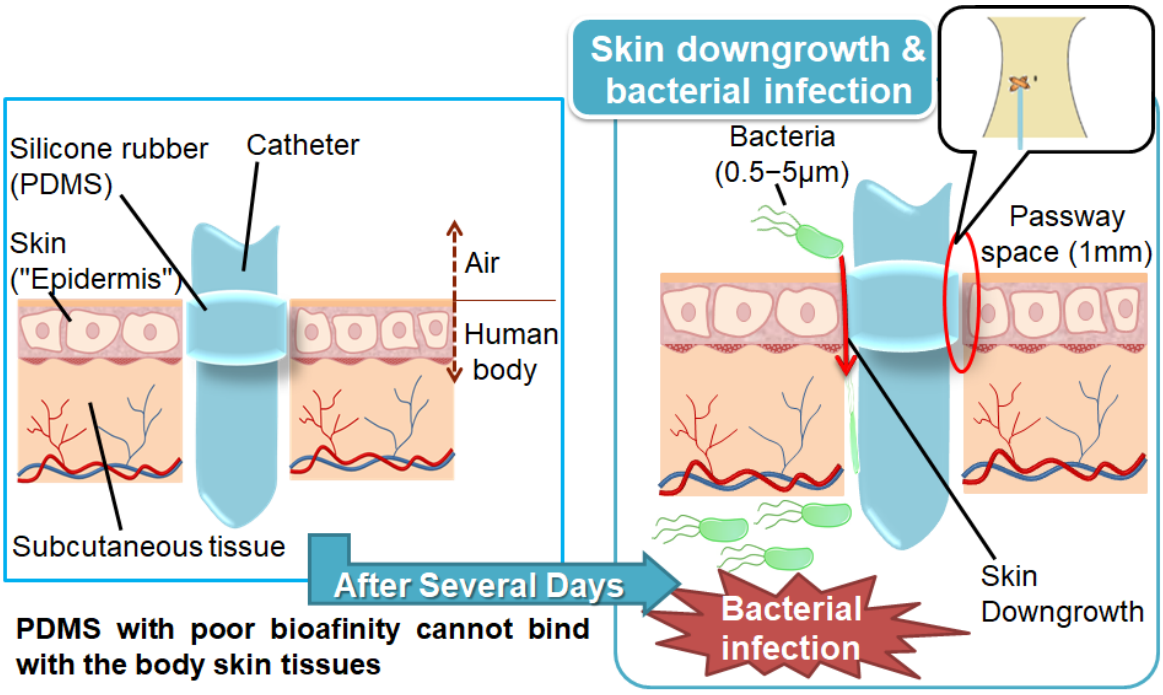

Figure 1.3. Scheme of the silicone catheter as a percutaneous device that is a tissue access device for monitoring tissue parameters including O_2, CO_2, pH, temperatures, biopotentials, and enzymes at the human body. Due to the poor bio-affinity of the silicone rubber with the skin tissues, after several days the down growth mechanism appears and generates a bacterial infection.

1.2.3. Assignments for Achieving both Biocompatibility and Antibacterial Activity

The ability of a substance to kill or inhibit bacterial growth is known as antibacterial activity.[39] The international norm ISO 22196 defines the antibacterial activity as the difference in the logarithm of the viable cell count found on an antibacterial-treated product and an untreated product after inoculation with and incubation of bacteria.[44]

Owing to the increasing concern about microbial infections, in particular, hospital-acquired diseases (many of them are catheter-related infections), there is a growing interest in creating an effective and safe antimicrobial agents. Additionally, if the material also has cytocompatibility, the medical devices will be highly favored.[45] Materials with cytocompatibility and antibacterial activity have been used in several biomedical products, including wound or burn dressings, catheters, and bone cement.[46,47]

In order to achieve a material with both cytocompatibility and antibacterial activity, it has been incorporated metal ions such as silver (Ag), copper (Cu), zinc (Zn) and Au, in cytocompatible materials including titania (TiO_2), silicates, bioactive glass (BG), and HAp.[48] Ag-doped BG showed antibacterial activity against *E. coli*) and *S. aureus* without altering the cytocompatibility or bioactivity of BG with the human osteoblast-like MG-63 cells.[49] The immobilization of Ag nanoparticles (NPs) on nano silicate platelets resulted in a mild inflammatory response and an excellent antibacterial activity.[50]

The incorporation of Ag into TiO_2 nanotubes enhanced the cytocompatibility and the antibacterial activity against *S. aureus*[51]. Similar results were obtained when doping HAp with Ag,[52–54] Cu,[55] Au,[56] and Zn ions.[57,58] Ag NPs have been widely investigated because of their well know effective antimicrobial activity towards a broad range of microorganisms, such as bacteria and fungus. At low concentrations, Ag ions are non-toxic for eukaryotic cells, but at higher concentrations, the Ag started been cytotoxic.[59]

The antibacterial effect of Ag NPs, Cu, and other metallic ions is proposed to arise from the release of metallic ions or oxidation. It is known that the metallic ions that cause damages to bacterial DNA, proteins, and enzymes, for that reason can directly inhibit bacteria growth. Notably, the productions of the reactive oxygen species (ROS) are responsible for the antibacterial effect of the metal ions and their mediated cytotoxicity in different cells.[60–62] Cu and Zn ions are trace element in the human body and are essential

for various metabolic processes in most of the living organisms, while in higher amounts, they are potentially toxic.[63] However, Zn also has a stimulatory effect on bone formation *in vitro* and *in vivo*.[64]

Zn plays essential roles in growth and development, the immune response, neurological functions, and reproduction. On the cellular level, the purpose of Zn has catalytic, structural, and regulatory features.[65] U.S. Food and Nutrition Board set the tolerable upper intake level (UL) for adults is 40 mg/day, including dietary and supplemental Zn.[66,67] HAp is the most promising material because of its cytocompatibility, bioactivity, osseointegration, reasonable action exchange rate with metals, high strength, and low fracture toughness.

1.3. Hydroxyapatite Nanoparticles

Human bone is an organic-inorganic composite having the components of collagen fibrils containing embedded and well-disposed, nanocrystalline HAp with 25–50 nm in length and rod-like shape.[68] Bone can repair and regenerate itself for damage. Nevertheless, the old age, diseases, and trauma can negatively affect bone functions, and these functions only can be restored with surgical reconstruction by the implantation of bioceramics, which aims to generate an environment to stimulate specific cellular responses to promote osteogenesis.[69]

The nanotechnology has allowed the preparation of nanostructured biomaterials, giving way to the third generation of bioceramics, focused on the enhanced bioactivity and the initial physiological trace inducing an enhanced cell to respond at the molecular level in order to regenerate the tissues due to their similarity to the inorganic component of human bone and dental enamel.[70] Nanobioceramic is defined as ceramic less than 100 nm in at least one direction.[71]

The nanobioceramics, including HAp, have been demonstrate to have highly cytocompatibility, good bioactivity, flexible structure, are stable at physiological environment, corrosion resistant as well as remarkable higher specific surface area, volume ratio and contain more quantity of grain boundaries than the conventional counterparts offering better surface properties such as topography, energy, roughness, and wettability that potentially favor the cell response.[72,73] The properties of the

nanobioceramics have potential applications in biomedicine field. Besides, NPs become more active with regard to dissolution and recrystallization processes that are important characteristics in the bone biomineralization process.[69] The nanobioceramics play a crucial role, enables the design of bioceramic that can provide better suited to biological tissues to empower their regeneration through the natural signaling pathways and using the natural components such as cells, growth factors and proteins adjusting the interactions between the biological tissue and the bioceramics.

1.3.1. Structures and Their Properties

HAp is a crystalline isomorphic biomaterial, classified as a ceramic. This material has a molecular weight of 1004.64 g/mol, a theoretical density of 3.156 g/cm^3 and a molar ratio of Ca/P of 1.67 related to its stoichiometry.[74] The bioactivity of calcium phosphates is related to the crystal structure, the porosity and its rate of dissolution in the body, the latter in turn is affected by the molar Ca/P ratio. Calcium phosphates with highest Ca/P are precipitated in alkaline solution, and those with lower Ca/P ratios are precipitated in acid solution. Generally HAp is produced in neutral or alkaline solution.[75,76] The crystalline structure of HAp is characterized by a hexagonal system with space group $P6_3/m$, although it may have a slight variation in cell sizes associated with the presence of impurities such as magnesium (replacing part of calcium), carbonates (replacing some phosphate) and fluorine (replacing some hydroxyl).[77] In this condition a very low solubility is presented, and as biomaterial structure, solubility ensures high chemical exchange activity in the extracellular medium. The lattice constants of hexagonal HAp are a=9.423Å and c=6.875Å. The hexagonal HAp has mirror planes at z=1/4 and 3/4 and the hydroxyl arrangement shows two fold disorder.[78,79]

There are two crystallographically independent Calcium atoms in the unit cell (see **Figure 1.4**). The **Figure 1.4 (a)** shows the crystal structure of the HAp projected along with the c-axis, centered on hexagonal c-axis channel. **Figure 1.4 (b)** exhibits the overview of the HAp unit cell structure, indicating the negatively-charged c-plane due to the rich content of phosphate ions and the positively-charged a-plane due to the content of calcium ions.[80] The Ca(2) atom is surrounded by six oxygen atoms belonging to phosphate (PO_4) groups and the hydroxyl (OH) group, whereas the Ca(1) atom is nearly octahedrally

surrounded by six oxygen atoms. The Ca(2) triangles stack along the *c*-axis, rotating mutually 60° from each other. In the HAp structure, the OH group is not located at the center, but shifted above or below the center of the triangle.[81] The phosphorus atom is surrounded by four oxygen atoms and forms a tetrahedron. The PO_4 tetrahedron is almost regular with only slight distortion. Ca(2) is exposed on the crystal surface, thus playing a large role in the physical properties of HA, such as surface charge, and in interactions with organic compounds.[74,81]

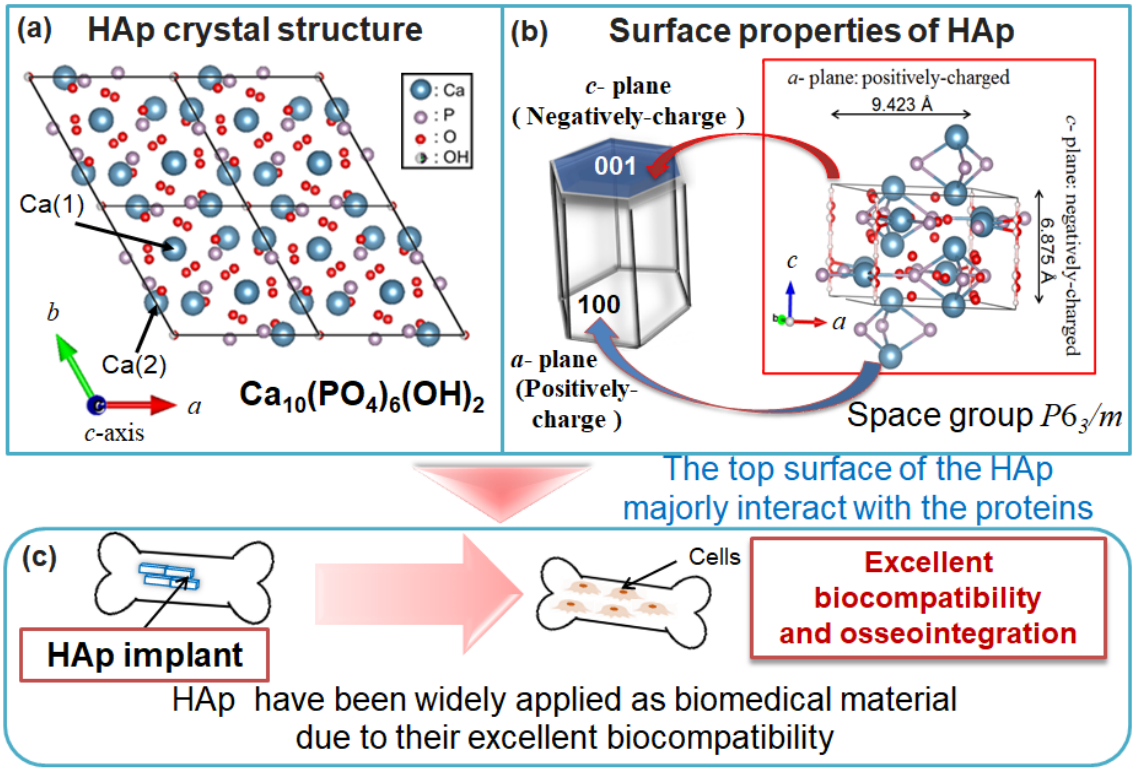

Figure 1.4. (a) Crystal structure of HAp in the top view along with *c*-axis, which were centered on hexagonal c-axis channel, (b) the overview structure to exhibit the rich phosphate and hydroxyl ions at *c*-plane and the calcium ions at *a*-plane (Drawing using VESTA (10) from the CIF obtained from American Mineralogist Crystal Structure Database), and (c) HAp applications.

The HAp is highly cytocompatible and presents bioactive properties. The crystal structure, morphology, thermal stability and mechanical properties play an important role in the biological responses of bonce cells. HAp physicochemical bonds to the bone and promotes bone formation necessary for implant osseointegration (see **Fig. 1.4 (c)**).[82] This property is needed to minimize damage in the surrounding tissues and to increase the

implant efficiency. However, even that HAp can form a direct bod with neighboring bones, for its application as biomaterial, it should also consider other important factors such as strength, hardness, porosity, dissolution, adhesion, etc., besides physical and chemical aspects; and it should not ignore the intent to use, as the environment where they will place has specific characteristics, considering it is not the same use as filler, as a support or as a substitute.[83]

HAp has several attractive useful properties in the medical field; the main characteristics are: it has a very slow resorption and it allows a better new bone, it is osteoconductive, cytocompatible, resorbable (10−30%), osteophilic, undergoes a process of osseointegration and it has a highly porous structure; this porous structure allows a better neovascularization of the formed bone.[84] The problem with this material in monolithic form is its unsatisfactory mechanical properties, so that it is undesirable use in weight bearing parts. This problem could be solved by the reinforcement using a material with good mechanical properties.

The properties of the HAp can significantly affect the particle composition, assembly, size and the morphology. The nano-sized HAp (20–80 nm) had been showed more efficient osteoblast adhesion and proliferation and improved mineralization.[85] Since the sizes of the microparticles are not much smaller than the cells, the microparticles are not able to penetrate in the cell wall and will be promptly degraded by phagocytosis.[15] Among the nano-scale levels, it has been reported that the HAp NPs with the size of around 20 nm are better for the cell proliferation and inducing apoptosis in some cancer cells.[86–88] It was found that the spherical and rod-like shapes of the HAp NPs showed remarkable less cytotoxicity as compared with the needle and plate-like shapes of those.[89]

The obtained sizes and shapes of the HAp depend strongly on the synthetic route as well as the synthetic parameters.[90] The HAp nanostructures of the spherical shapes with the sizes of 5–200 μm, rod-like shapes with those of 5 nm–150 μm, needle-like shape with those of 40 nm–150 μm can be synthesized by diverse methods such as mechanochemical method,[91,92] hydrolysis method,[93,94] sol-gel method,[95–97] hydrothermal method,[98] chemical precipitation method,[99] emulsion method[100] and solid state reactions.[101] Nevertheless, the mechanochemical, chemical precipitation and sol-gel methods frequently result in the irregular shapes with agglomerations. Within the precipitation method, chemical agents

have been used as the modifiers to control the sizes and morphologies.[102] The most-reported agents are i) complex ligands such as citric acid,[103,104] ethylenediaminetetraacetic acid (EDTA),[105,106] tartaric acid or acetic acid,[107,108] ii) organic molecules as amino acids,[109] polymers[110,111] and surfactants like cetyltrimethylammonium bromide (CTAB).[112] For example, CTAB has been used as rod-like micelle template. After the addition of the CTAB into the solution, the bromine ions on the surfaces of the formatted micelle of CTAB are replaced quickly with the phosphate ions. The precursors reacted with the phosphate ions on the surfaces of the CTAB micelles formed the HAp nanostructure.[113]

1.3.2. Heteroelement-Substitution

HAp is a member of the "apatite" that is a general term for crystalline mineral with a general composition of $M_{10}(ZO_4)_6X_2$.[114–116] The name was taken from the Greek word "apatite" that means deceit. Many elements could occupy the M, Z and X sites like:

M=Ca, Mg, Sr, Ba, Mn, Fe, Zn, Cd, Pb, Na, K, Al, etc.

Z=P, V, As, S, Si, Ge, CO_3, etc.

X=F, Cl, OH, O, Br, CO_3, etc.

The flexibility of the structure of the stoichiometric HAp with the formula $Ca_{10}(PO_4)_6(OH)_2$ allows the substitution of the calcium (Ca^{2+}), phosphate (PO_4^{3-}) and hydroxyl (OH^-) ions by isomorphic anionic and cationic ions.[117] The amount and size of the substituted ions will affect the lattice parameters of the unit cell.[118] The OH can be substituted by Cl, F, CO_3, etc, while PO_4^{3-} side can be supersede by CO_3, SiO_4, Ti, etc. The Ca site can be replaced by several cations, e.g. Mg, Na, K, Sr, Mn, La, Cu, Zn.[119] The ionic substitutions will generate a change in the lattice parameters, crystallinity, surface charge, and morphology. The Zn ion substitution can occur at the Ca(1) and Ca(2) sites. However, it have been reported that the substitution at Ca(2) site is more energetically favored for Zn with tetrahedral coordination which produce structural distortion.[120–123]

Biological apatite is a non-stoichiometric form of HAp, characterized by Ca^{2+} deficiency but containing trace elements such as cations (Mg^{2+}, Mn^{2+}, Zn^{2+}, Na^{2+}, Sr^{2+}) or anions (HPO_4^{2-} or CO_3^{2-}). Reports confirm that this substitution by cations can lead advantageous effects on biomaterial properties, such as the degree of structural order (i.e. crystallinity, lattice parameters, surface charge, morphology), which have a direct impact in the

solubility, bioactivity, mechanical properties and thermal stability of the resulted HAp.[124,125] The most common advantageous effect is obtained with the incorporation of CO_3^{2-} ion, which constitute 5–8% of apatite in bone, by weight.[126] The CO_3^{2-} ion can replace both OH^- and PO_4^{3-} within the HAp structure, termed A-type and B-type replacement, respectively. B-type replacement is common in bones, and it is an essential factor in altering the melting point of the biological apatite.[127,128] Increases in positive charge with the replacement of PO_4^{3-} by CO_3^{2-} are balanced out either by the loss of Ca^{2+} sites or by the introduction of Na^+ ions; the name for this type of apatite is calcium-deficient HAp (CDHA) is greater for biological interest than stoichiometric because the mineral portion of bone is primarily CDHA partially substituted with carbonate.[129] This has shown that CDHA plays an important role during the formation and bone turnover.

1.3.3. Biomedical Applications

Nano-sized HAp with enhanced bioactivity, cytocompatibility, mechanical properties and higher resorbability as compared with the micro-sized HAp,[130–132] has been widely applied for the several biomedical applications as shown in **Figure 1.5**. Among the most important biomedical applications, bone filling and medical implants,[133–135] bone tissue engineering scaffolds,[136] bioactive coatings, and composites with antibacterial properties,[137] drug delivery systems,[138,139] bioimaging and diagnosis material,[140,141] and biosensor.[142] The shapes, sizes, crystalline phases and the functional groups are responsible for the surface reactivity of the HAp (i.e., biorelevant parameters). The cells can incorporate the particles inside when the particles have the appropriate sizes and charge were up to about 200 nm and are positively charged.[143] The HAp NPs with crystalline sizes less than 100 nm have the ability to cross the natural barrier and interfaces of the cells and also can deliver drugs in sites with difficult access sites of delivery, in addition, have the possibility to associate and can bind with the DNA and proteins owing to the cell structure. The dynamic and energetic length scales of the HAp NPs match which those exhibited by many biological processes.[144] The interfacial properties of the non-stoichiometric HAp due to calcium and hydroxide ions deficiency confer a higher solubility and interfacial reactivity, favoring both the biomolecular adsorption as well as the ion exchange.[145] For bone regeneration, it is attempted to synthesize the chemical and crystallographically HAp NPs, which were more

effective for promoting cell proliferation and cellular activity,[146,147] to obtain excellent cytocompatibility and optimal mechanical properties in terms of hardness, rigidity, bioresorbability, and biodegradability.[148,149]

The cell cultured with the spherical HAp NPs suspension showed better osteoblast proliferation, cell adhesion, migration and cell-matrix interactions, suggesting that spherical HAp NPs are more hazardous than needle-like shape particles.[150,151] *In vitro* studies showed that HAp NPs with a particle size of 20 nm have enhanced cell viability and proliferation of bone marrow mesenchymal stem cells and inhibited the growth of osteosarcoma cells.[152] The HAp NPs with a diameter of about 50 nm showed the apoptotic action of hepatoma cell line.[153] For bioimaging properties such as photostability, the cytocompatibility, and spherical shapes are necessary properties.[154]

The HAp NPs doped with lanthanide or europium ions are prepared by integrating into the HAp structure by ion exchange during synthesis for bioimaging applications. These NPs have the crystalline sizes around 10–50 nm are included in the lattice to endow the NPs with luminescence moiety and are detected due to the fluorescence caused by an external stimulus.[154–156] This strategy is better than the use of fluorophores since it avoids inconveniences as poor stability and photobleaching.[157] For the antibacterial activity applications, studies have been done by doping the HAp with metals such as Ag, Cu or Zn, obtaining a decrease in bacterial growth in all cases.[158] However, of these metals, Zn is the less toxic metal. In the case of HAp doped with Zn, when the Zn was incorporated into the structure, the NPs decreased in size, which favored the cytocompatibility with the fibroblasts cells *in vitro* and increased the antibacterial activity due to the bioresorbability and biodegradability properties.[159] The doping with Zn promoted the proliferation and differentiation of fibroblast cells as compared with pure HAp.[160,161] The Sr–substituted HAp showed better cell adhesion and proliferation than HAp, without toxic effects on extracellular matrix formation and mineralization.[162]

The Rod-like-HAp NPs showed better biomimetic features in bone fillers, promoted the osseointegration, followed by bone tissue regenerations since the physiological HAp in the had tissues are rod-like-HAp NPs. Thus, filling the bone with the similar HAp NPs increases the concentration of bioactive molecules generating the successful osseointegration *in vivo* and *in vitro*.[163,164]

The micropores (around 1–10 μm) and macropores (> 100 nm) have an important effect in the bone formation. The microporosity is related with the osteoinduction process and promoted cartilage formation before the osteogenesis,[165] while the micropores induced direct osteogenesis.[166] It has been reported than pores sizes of 100 μm enhanced cell spreading and migration, whereas pores of > 300 μm promoted the formation of bone and capillaries.[167] The applications of the HAp NPs are remarkably influenced by their shapes, sizes, and crystallinity. The spherical HAp NPs can imitate the hierarchical features of the human bones, which enhanced the cell adhesion, proliferation, differentiation and osseointegration *in vivo*.[164] The control of these parameters is the fundamental factor to determine the physicochemical properties and biological activity of the HAp.

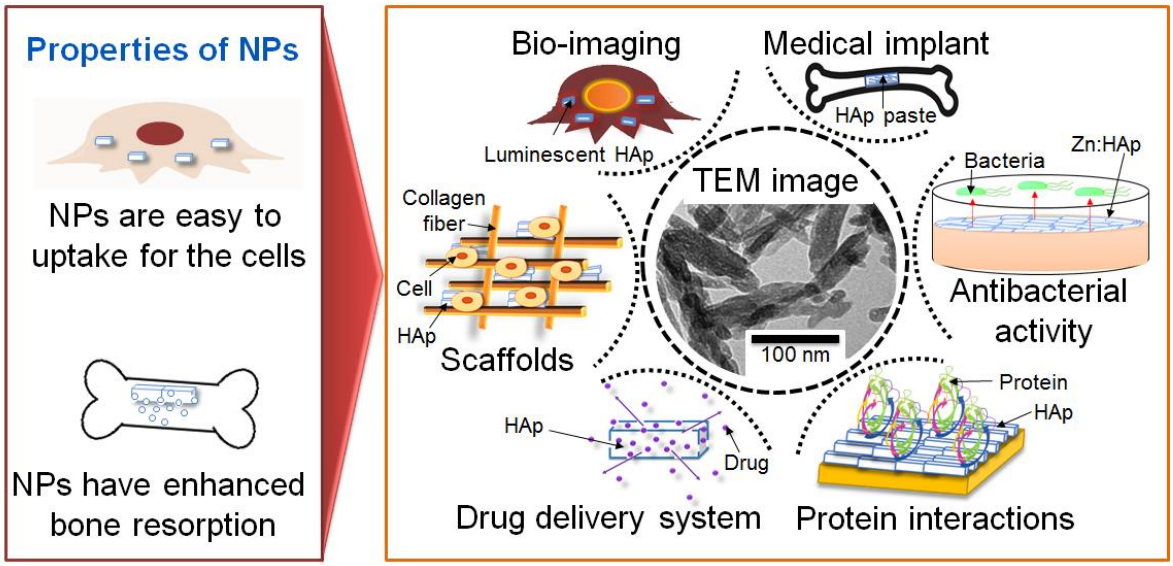

Figure 1.5. Illustration of the diverse biomedical applications of the HAp NPs. The NPs are important for biomedical applications; however, the interactive mechanism is not clear.

1.4. Design of Biomedical Substrates

1.4.1. Surface Modification

Studies on polymers applied to the medical field began in the 20th century nonetheless, at the end of 1950´s, the use of polymers in medicine and medical applications was intensified, since their good cytocompatibility, low toxicity, bio-inert nature, good mechanical properties as strength, abrasion resistance and flexibility.[168–171] The nature of the chemical bonds of the main chain of the polymer determines the polymer properties.[172] In the non-degradable polymers, the carbon-carbon bond is chemically and biologically stable and inert. Nevertheless, the physiochemical properties can be modified by the oxidation of the carbon backbone, changing the mechanical properties, crystallinity, hydrophobicity, weight, solubility, chemical composition, melt and glass transition temperatures of the polymer.[173–175]

The biodegradable polymers have hydrolytically unstable linkages. In the backbone of the polymers, the end group contains ester, amide or ether bonds.[176] The functional groups frequently found in these biodegradable polymers are esters, anhydrides, orthocenters and amides.[177] Biodegradable polymers, as well as non-degradable polymers have been widely used in the biomedical applications such as medical devices,[178] sutures,[177] drug delivery systems,[179–182] scaffolds for tissue engineering,[183,184] implants,[185,186] and organ regeneration.[187,188] The chemical compositions and structures of the polymer surfaces will determine the interfacial interactions that take place between the biological media (such as proteins, cells and tissues) and the polymer substrates.[189] In order to improve the bio-interactions, specificity, bio-functionality, bio-recognisability, and cytocompatibility of the polymers, several techniques have been used for modifying the biomedical polymer surfaces such as modification of the roughness, the domains or ionic charge, to introduce functional sites, adsorption of molecules, or making more hydrophilic.[190]

The surface modification methods can be divided in two categories; (1) physicochemical methods alter the atoms and molecules of the polymer surface. Among the most used physicochemical methods are ion beam etching, plasma etching, corona discharge, ion beam implantation, ion exchange, UV irradiation, chemical reactions like nonspecific oxidation, functional group modification, addition and derivatization reactions, surfactant or hydrophilic polymer immobilization.[191] In contrast, it can be raised that (2) coating of the

polymer surface with an external hydrophilic layer.[192] These methods include photografting, chemical grafting, radiation grafting, electron beam induced grafting, plasma, gas phase deposition, silanization, gas phase deposition, laser ablation, biological methods,[193] and patterning.[190] These treatments have been used to obtain the functional groups at the surface, leading to the increase the energy, lubricity, electrical conductivity and dyeability at the surface, improve hydrophilicity, introduce surface cross-linking, remove contaminants or weak boundaries layers.[194] Thin surface modifications which only modify the outermost molecular layer would be ideal in order to do not change the mechanical and functional properties of the polymer, although the minimum thickness required depends on the length of the molecule to be incorporated.[190] The intermolecular interactions at the overlayer of the modified region will produce the surface rearrangement through the diffusion or translation of the atoms or molecules at the surface as a response of the stresses transmitted from the matrix across the interfaces.[195] If the interactions between the overlayer and the substrate are not strong, or the surface modification layer is very thin, surface reversals will occur.[196] Among the surface modification methods, oxygen plasma treatments have widely been used to form the reactive silanol groups on the surface of the siloxane component, which increase the hydrophilicity, wettability, characteristic and cytocompatibility at the surfaces of biomedical polymers including devices or implants.[197–199]

One of the most used polymers in biomedical applications is PDMS, due to the low toxicity, high flexibility, good thermal and oxidative stability, low modulus, anti-adhesive nature, soft and rubbery behavior, bio-inert, transparency in visible region, and can control the free volume for the aim of accommodation of metal NPs.[200] Anteriorly, our group has reported the incorporation amount and state of Au NPs into the PDMS by controlling the cross-linking degree during the hydrosilylation reaction. The general reaction between the siloxane oligomer (liquid PDMS) and the siloxane cross-linker for generate the linked PDMS shows the UV-visible adsorption spectra and photographs of Au-PDMS composite films containing 2 to 10 wt% of cross-linker to PDMS. In Au-PDMS composite films containing low cross-linker concentration (less than 4 wt%), the aggregation of Au NPs was found. The Au-PDMS composite films containing 6 wt% of cross-linker, the Au NPs was dispersed in the film.[201]

1.4.2. Surface Functionalization

The surface structure of the cytocompatible polymer is able to enhance the protein adsorption, and then the cells interact with the proteins, leading to the cells to form tissues on the biomedical polymer. In this manner, it is desirable to tailor the surface of the biomedical polymer in order to provide a cytocompatible physicochemical environment to guide the cells to form tissues.[202–205] These specific requirements will depend on the medical applications. For tissue engineering, it is necessary to give good cytocompatibility, cell adhesion and biodegradable properties.[206] On the other hand, for drug delivery systems, it is desirable multi-response properties for intelligent control of drug release.[207] A great variety of superficial physicochemical properties can be obtained through the surface modification; however, to obtain specific requirements, it is necessary to functionalize the polymer surfaces.[208] The surface modification can serve as the bench for the surface functionalization to improve the properties.[209]

Two commonly-used strategies to functionalize polymers can be raised: (1) Functional groups are introduced into the polymer monomers. Although hydrophilic co-monomers can be inserted into the pre-polymerization system by chemical functionalization, these monomers can alter the bulk properties, which is not desirable for the biomedical applications.[192] (2) Functional groups are introduced into the polymer chain by the further modification of the prepared polymer.[210] Strategies for functionalization of biomedical polymers including: topographical (surface graft polymerization or thin film deposition by chemical vapor deposition (CVD)) and immobilization (such as proteins, nucleic acids, and carbohydrates).[211] It has been reported that plasma treatment allows to precise the control of chemical functionalization and the morphology of the surface of biodegradable and non-biodegradable polymers, which results in coating with good stability and better compatibility with the biomolecules and host cells in liquid media (see **Figure 1.6**).[212,213] Some cytocompatible polymers exhibit hydrophobic surface, which impairs the desired cellular response. The functionalization through graft polymerization has been extensively studied.[214–217] The surface graft polymerization method tailors the properties of the polymer through the direct introduction of other types of monomers on the polymeric surface without alteration of the bulk properties.[210]

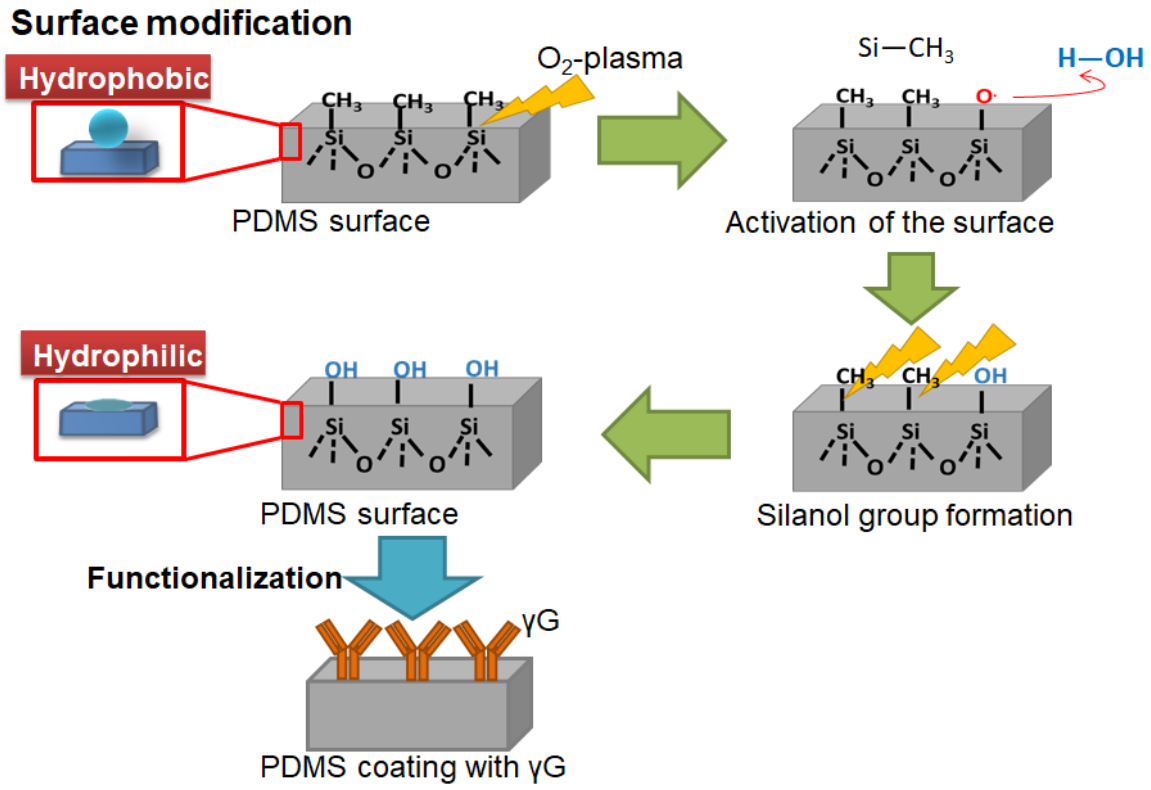

Figure 1.6. Schematic representation of the surface modification of the PDMS by plasma treatment from hydrophobic to hydrophilic PDMS surface, the corroboration by static contact angle with 2 mL water droplets and the subsequent functionalization by coverage with gamma globulin (γG)**.**

1.4.3. Applications

Hydrophobic polyurethane (PU) scaffolds were modified by grafting hydrophilic methacrylic acid (AA) monomers (under UV light), resulted in hydrophilic polyurethane methacrylic acid (PMAA) with better cell compatibility than pure polyurethane (PU).[218,219]

By plasma enhanced CVD (PECVD), the different kinds of polymeric surfaces can form different types of thin films depending on inorganic coatings such as carbon nanotubes,[220] diamond-like carbon,[221] ZnO,[222] TiO_2,[223] and SnO_2.[224] Diamond-like carbon (DLC) has been used as a cytocompatible hard coating on biomedical polymers, showing higher flexible properties.[225] The amorphous nature of DLC allows incorporating elements like Si, F, P, Ag and N, which improve the properties of the polymer.[226–228]

1.5. Mild Coating of Hydroxyapatite Nanoparticles on Substrates without Chemical Reagents

1.5.1. Electrophoretic Deposition

Artificial bone is one of the most transplanted tissues. For this reason, the interest to develop new and more cytocompatible inorganic-organic composites is increasing,[229] not only because the physicochemical properties of the composites provide the necessary properties for the bone replacement, but also because the human bone tissues are the nanocomposites formed by the inorganic HAp (70 mass %) embedded in an organic matrix composed of collagen (30 mass%) and non-collagenous proteins.[230,231]

The objective of the incorporation of HAp into cytocompatible polymer matrix enhances the mechanical strength and provides the topographic features to improve the integrity of implants and the surrounding bone and to stimulate bone tissue ingrowth.[232] The coating methodology has the advantages to cover porous and irregularly shaped surfaces and to have control over the thickness.[233] The electrophoretic deposition (EPD) is a functional coating technique associated with the movement of charged particles in a liquid, which takes place by applying an electric field. The charged particles of the suspension can be deposited on the conductive or semiconducting substrate, creating the uniform particulate film. The film thickness depends on the several factors such as viscosity, conductivity, zeta potential,[234] and particle concentration in the suspension, deposition time, and applied voltage.[235–237] The coverage of some polymers with HAp has been investigated by EPD using A.C. (alternating current) or D.C. (direct current) in different alcoholic solvents for the biomedical applications.[238] The advantages of EPD are the possibility of uniform covering of the substrates with complex shapes, control of the microstructures, rapid deposition, simple and low-cost techniques, room temperature and suitability of co-deposition.[238–240] A schematic representation of the EPD process is shown in **Figure 1.7**. In the suspension, the alcoholic solvent is adsorbed on the *c*-plane of HAp to generate the ionic dissociation.[241] Thus, the negatively-charged ethoxide ion and positively-charged HAp particles were formed. Thus, the positively-charged HAp NPs, dispersed in the alcoholic solvent, move towards the negatively charged substrates under the influence of the applied electric

field and the HAp NPs are deposited on the polymer forming the dense particulate layer.[242] The EPD of the HAp-alginate and HAp-Chitosan (CS) composites have been reported with the uniform coatings at the thicknesses up to 60 μm.[243,244] However, it has sought to improve the physicochemical properties of the composites through the co-deposition with the other materials such as bioactive glass, obtaining the bioactive glass-HAp-alginate and bioactive glass-HAp-CS composite coatings for the biomedical applications. The film thickness in the range was up to the several micrometers, although the deposit states were non-uniform because of the use of relatively larger bioglass particles.[245]

The co-deposition of carbon nanotubes (CNTs) and HAp NPs with the crystal sizes of 20–40 nm has been investigated to obtain the microstructured HAp-CS-CNTs composite coatings, indicating the enhanced, mechanical properties (hardness, elastic modulus and adhesion strength), bioactivity and corrosion resistant properties.[239] The co-deposition of polyether ether ketone (PEEK) and HAp to obtain the PEEK-HAp composite coatings with approximately 70 μm of thickness has been successfully obtained for the improved bioactivity.[238] The cathodic EPD of graphene (Gr), CS and HAp on Ti substrate in ethanol suspension resulted in HAp/CS/Gr coatings with the crystalline domain size of 42.6, 25.1 and 22.0 nm, respectively. The HAp/CS/Gr coatings showed the improved morphology, thermal stability, and bioactivity by the incorporation of Gr.[246] Our group has reported the EPD of the HAp NPs doped with Zn (Zn:HAp) on the conductive silicone (Ti-silicone) to improve the cytocompatibility and to provide the antibacterial activity. The thickness of the Zn:HAp NP layer was 20–50 nm. It was observed that there was the better adhesion and spreading of the fibroblasts on the Zn:HAp film doped with 5 mol% of Zn ion (0.5-Zn: HAp).[247]

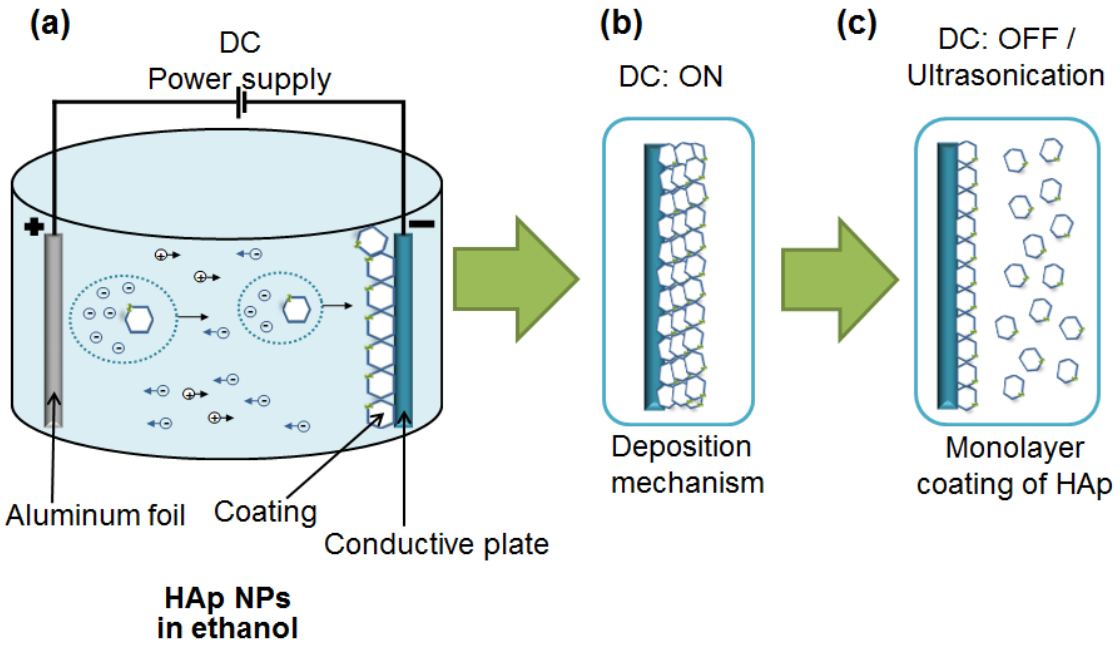

Figure 1.7. (a) Scheme of the EPD procedure of the HAp NPs in ethanol with a direct current (DC) of 100V, b) deposition mechanism in ethanol. The positively charged HAp NPs bind with the negatively charged conductive film by Van der Waals forces. (c) Resultant EPD system. After ultrasonification only the first layer remains.

1.5.2. Biomimetic Process

The biomineralization (or biological mineralization) is a well-regulated process, which is responsible for the controlled formation of inorganic materials from aqueous solution in living organisms.[248] The formation of the inorganic biomaterials is demonstrated by the result of the combination of three physicochemical stages of supersaturation, nucleation and crystal growth. At the first stage, the inorganic ions in the supersaturated body fluid start forming the nuclei.[249] The surface reactions between the nuclei develop the aggregation-based crystal growth.[250] The interactions between the aggregates and the ions in the solution generate the formation of stable clusters, followed by the anisotropic crystals growth and phase transformation from the amorphous calcium phosphate (ACP) to octacalcium phosphate (OCP). The next step is the transition from OCP to the well-ordered biological HAp crystals (BAp).[251–253] The schematic representation of the biomineralization process is shown in **Figure 1.8**. In the living body, the osteoblasts secrete a collagen-proteoglycan matrix. This matrix is important to control the mineralization.[254] The collagen can stabilize the amorphous

clusters until them becomes HAp and orientates the formation of the HAp along the *c* axis, which allows to the preferential binding with acidic extracellular matrix (ECM) proteins on its surface.[248]

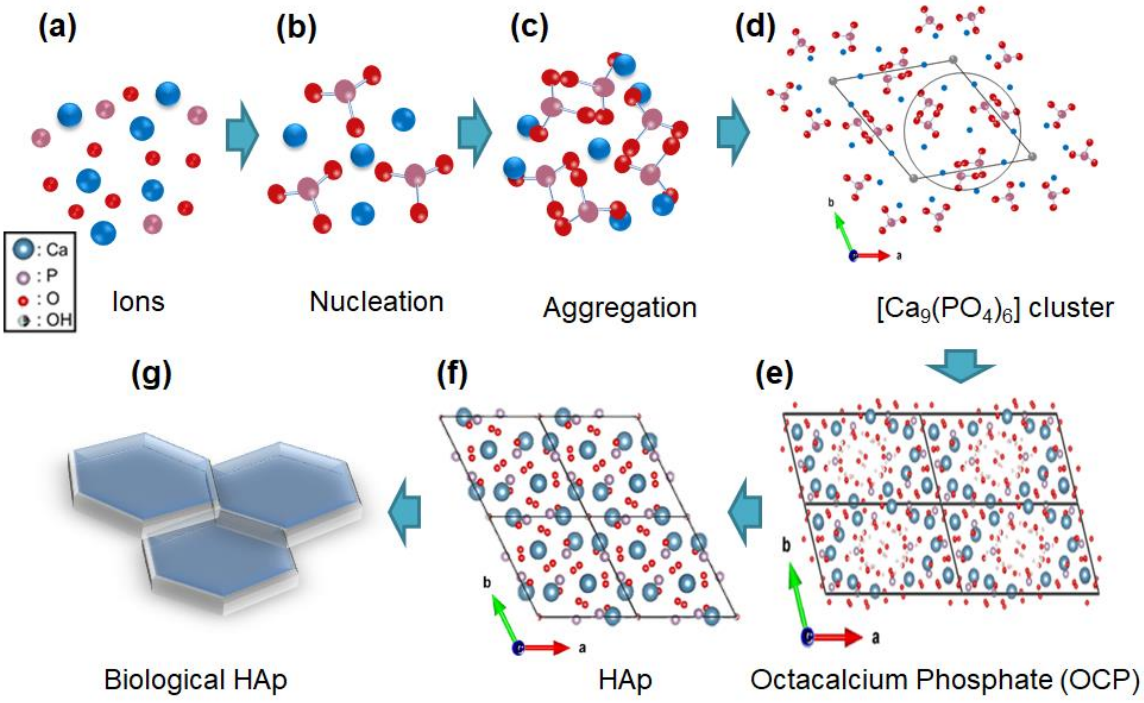

Figure 1.8. Scheme of the biomineralization process. (a) ions in solution, b) nucleation, c) aggregation, d) amorphous calcium phosphate, the circle shows the Postner cluster unit $[Ca_9(PO_4)_6]$ projected on the *ab* plane, (e) octacalcium phosphate, projected on the *ab* plane, (f) HAp, projected on the *ab* plane and (g) biological HAp. (Drawing using VESTA (10) from the CIF obtained from American Mineralogist Crystal Structure Database).

The new technology called "bio-inspired growth" has been sought to emulate the natural biomineralization process in order to obtain bioactivity and mechanical properties, which can improve the bio-interactions with the human bone.[255] The organic-inorganic fusion interfaces can be constructed by placing the polymer in simulated body fluid (SBF), which is a metastable solution containing the supersaturated calcium (Ca^{2+}) and phosphate (PO_4^{3-}) ions. This process is a simple and inexpensive technique that can coat complex shapes.[256] It has been reported the synthesis of the nanocomposite with cytocompatibility and similar structures to the natural bone by the mineralization of nano-HAp on the assembled collagen.[257] It has been observed that the formation of HAp begins by the union between the Ca^{2+} ions and

the negative ions on the polymer surface. The number and arrangement of the functional groups in the surface are important factors for HAp formation.[258] The higher functional groups on the polymer produce the higher HAp nucleation rate.[259] The nucleation occurs at the specific sites and the polymer directs the nucleation.[260,261] As described above, some functional groups on the surface of the polymers such as silanol groups (Si–OH),[262,263] carboxyl groups (–COOH),[264] and sulfonic groups ($–SO_3H$) can effectively induce the formation of HAp through the interactions with the Ca^{2+} ions.[265] The Ca^{2+} ions are the key factor for the HAp coating on polymers.

The control of the deposition and growth conditions of the deposited HAp can be carried out by changing the composition of the SBF solution. The thickness of the coated HAp can be controlled by the immersion time.[266] Our group has studied the biomineralization process to promote the BAp growth from SBF by three different processes in **Figure 1.9**. Process 1: the bare (Au, Ti, and HAp) substrates induced the BAp growth by the immersion. Process 2: the fetal bovine serum (FBS) proteins preadsorbed on the substrates showed the slight BAp growth, indicating the significant inhibition of the BAp growth.[267] Process 3: BAp coating technique on tissue culture poly(styrene) through the film formation by the L-α-phosphatidyl-choline phospholipid vesicle (PV) was achieved, obtaining the transparent HAp-PV film with the stabilility against the sterilization treatments, suggesting the cell culture dishes application.[268]

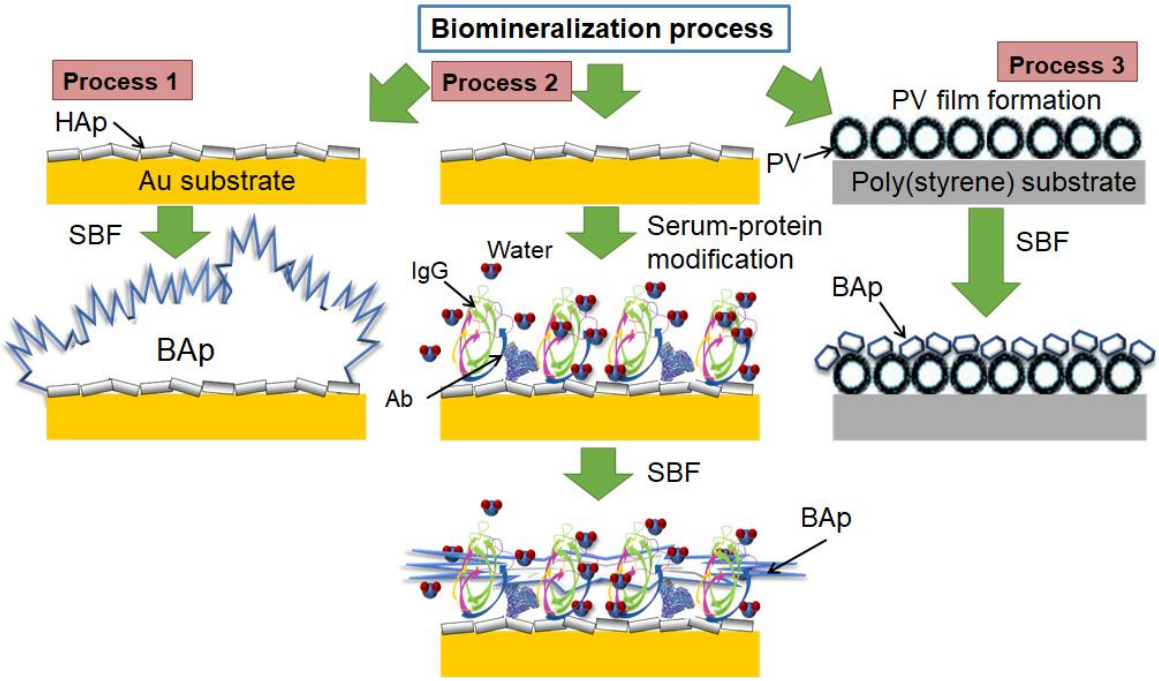

Figure 1.9. Scheme of the biomineralization process for inducing the biological apatite (BAp) growth from a simulated body fluid (SBF) by three different processes. Process 1: The bare substrates induced BAp growth by immersion in SBF while process 2: the fetal bovine serum (FBS) proteins pre-adsorbed on the substrates showed slight BAp growth, indicating a significantly inhibition of the BAp growth. Process 3: BAp coating technique on tissue culture poly(styrene) through the film formation by the hybridization of BAp with L-α-phosphatidyl-choline phospholipid vesicle (PV).

1.5.3. Other Techniques

It has been observed that the incorporation of HAp into the polymer matrix can enhance the mechanical properties, increase the roughness and produce topography that allows to mimics the nanostructure of the bone.[269] The most used techniques for the manufacture of HAp/cytocompatible polymer composites are solvent-solution casting method,[270] plasma spraying process,[271] electrospinning,[272] electrochemical deposition,[273] thermally induced phase separation (TIPS) also known as freeze-drying method,[274] and pulsed laser deposition.[275] The advantage and disadvantages of the HAp coating techniques on solid substrates are shown in **Table 1.1**. The calcium deficient HAp NPs (d-HAp NPs) dispersed in N, N-dimethylformamide (DMF) were successfully deposited on PLA by the solvent-casting technique. The d-HAp NPs were homogeneously distributed on the films and had similar morphology, composition, and crystalline structure to BAp. The thickness of the PLA/d-HAp nanocomposite film was

about 0.1 mm. The tensile modulus of PLA/d-HAp nanocomposite film was 2.77 GPa, which was higher as compared with that of pure PLA (1.66 GPa).[276]

The potential toxicity of the solvents is the major drawback of the solvent-casting technique. The fabrication of nanofibrous (NF) gelatin/HAp composite scaffold by TIPS technique mimicked the physical architecture and chemical composition of ECM in natural bone. The NF-gelatin/apatite scaffolds showed significantly higher mechanical strength and better osteogenic differentiation, suggesting the use in bone tissue engineering.[277] This technique could present the toxicity due to the used solvents. The HAp/cellulose nanocomposite films were developed by the incorporation of HAp NPs with the particle sizes of 20–40 nm into the cellulose matrix in NaOH/urea aqueous solution and subsequent coagulation with a Na_2SO_4 aqueous solution. The thermal stability and tensile strength of the HAp/cellulose nanocomposite films were improved as compared with those of the pure cellulose. The HAp/cellulose nanocomposite films showed excellent cytocompatibility with non-toxicity.[278] These techniques to form the inorganic-organic composites are more innovative, although they have the disadvantage of being more complicated and with a higher cost.

Table 1.1. Advantages and disadvantages of the HAp coating techniques on solid substrates.

Technique	Thickness	Advantages	Disadvantages
Electron Beam and Sputtering	0.5−3 mm	Coatings with uniform thickness Dense coatings	Long time Amorphous Coatings
Laser Ablation	0.05−5 mm	Dense and Porous coatings	Developing Technique
Dynamic Mixed Method	0.05−1.3 mm	High adhesion between the coating and the substrate	Developing Technique Expensive Amorphous Coatings
Dip Coating	0.05−0.5 mm	Cheap and Fast Coating different geometries	High temperature sintering HAp decomposition
Sol-Gel Method	< 1 μm	Coating different geometries Low temperatures Relatively inexpensive because the coatings are thin	High temperature sintering HAp decomposition
Hot Isostatic Pressing	0.2−20 mm	Dense coatings	No coating complex geometries Elevated temperatures Differences in elastic properties Expensive
Thermal Spray and Plasma Spray	30−200 μm	High deposition rate Relatively inexpensive	High temperatures HAp decomposition

1.6. Bioceramic Cell- Interactive Substrates

1.6.1. Cell-Interactive Bioceramic/Polymer Interfaces

The process of bone tissue formation is called as osteogenesis and is carried out by two ossification mechanisms: intramembranous (IM) and endochondrial (EC).[279] In the IM ossification, the mesenchymal stem cells (MSCs) derived from neural-crest are attached at the bone formation site, and then the MSCs proliferate and condense into compact nodules and subsequently differentiate into osteoblasts.

The osteoblasts capture the calcium, carbonate and phosphate ions for the formation of HAp NPs from the blood and deposit them in the osteoid matrix, and also secrete the matrix components to promote calcification tissue. In this process, the transcription factor and morphogenic proteins are expressed.[280] EC ossification is responsible for the formation of long bones. After the condensation, the MSCs differentiate into chondrocytes to form cartilage templates that will later be replaced by endochondral bone. In the growth plate, the extracellular matrix (ECM) is composed of type II, IX, X and XI collagen, proteoglycans containing glycosaminoglycans (chondroitin sulfate), hyaluronic acid, molecular components like matrilines, cartilage oligomeric matrix protein, among others.[281] In the HAp/polymer fusion interfaces, as mentioned in section 4, the HAp provides good osteoconductivity, bioactivity and a cytocompatible interface, while the polymer contributes with a continuous and flexible structure to obtain the high surface area and high porosity composites, which allows the anchoring, growth, and differentiation of cells for bone formation such as fibroblasts.[282] However, the polymer/bioceramic interfacial functions for providing the preferential biomolecular interactions at the nanoscales were not understood so far.

For the porous composite structures, the study of the interactions between the HAp/bio-inert polymer and the cells is carried out using *in vitro* cell culture models. One of the most important states for the cells/HAp/polymer interactions, which can be called “bio-fusion materials”, is the characteristics of cellular adhesion.[283] It has been reported that the chemical compositions, crystallinity, topographical structures, particle sizes and surface properties can directly affect the cell adhesion, proliferation, and differentiation.[284] The topography of the composites promotes the adsorption of specific proteins, which affects the cellular characteristics. The surface roughness can induce the cell adhesion, and proliferation.[285] It has been demonstrated that the pore interconnectivity, pore size, and total porosity are important factors for cellular attachment, proliferation and nutrient. If the pores are very small, cell migration is difficult, which generates the cellular encapsulation around the implanted composite. The limited diffusion of nutrients and the reuse of waste cause necrotic regions. If the pores are very large, the surface area decreases, which hinders cell adhesion. The pore size determines the number of struts and ligands available for cell adhesion.[286] In the

composites, the pores diameters of 186–200 μm can transport nutrients and metabolites and ingrowth blood vessels, while the pore diameters of 10–100 μm to take nutrients and throw waste and ingrowth capillaries.[287] It has been reported that the osteoblastic cell could be attached easily to the HAp coated surface, allowing osteoids formation with chemical and biological interactions between the implanted composites and the bones,[288] indicating the importance of the HAp surface properties.

It has been studied the initial attachment of human osteoblasts (HOBs) on poly(ε-caprolactone) (PCL) and PLA as the matrix for compositing two HAp particles of (a) 50-μm-sized and sintered (HAp_{50}) and (b) submicron-sized (HAP_S). After the cell culture for 4 h, the cells on the PLA/HAp composites showed a higher degree of cellular spreading than the case on PCL/HAp. The cells on PLA/HAp_{50} and PCL/HAp_{50} with the rough macro-textures exhibited more elongated morphology than those on the composites with HAP_S. After the 24 hours, the cell activity on PCL/HAp and PLA/HAp composites was remarkably higher than the case on the pure polymers films. The "point exposure" of the HAp provides suitable composites for controlling the cell density on implant surfaces.[289] It was reported a synthetic HAp/collagen composite with the similar composition and structure of natural bone. In the *in vivo* and *in vitro* studies of the biological reactions, the composites were resorbed by the osteoclasts through phagocytosis and also promoted the adhesion of osteoblasts to form a new bone in the surrounding.[290] Our group achieved the microstructures of HAp NPs composited with SU-8 polymer micropatterns by a nano/microfabrication technique and studied the interfacial phenomena of hepatocytes. The hepatocytes interacted and promoted the cellular aggregation and then preferential adhesion on the HAp NPs sites. The preferential adhesion was observed by a quartz crystal microbalance with dissipation (QCM-D) technique and optical microscope.[291]

1.6.2. Control of Cell-Protein-Hydroxyapatite Interfacial Interactions

The cell adhesion, proliferation, migration, differentiation and survival can be modulated by the ECM proteins. The ECM can influence diverse types of cells such as osteoblast, osteoclasts, osteocyte, and bone linings cells.[229] The ECM can be constituted by several constituents like arginine-glycine-asparagine (RGD), peptides such as

collagen (Col), laminin, fibronectin (Fn), vitronectin (Vtn).[292] The numerous *in vivo* studies showed that the implanted materials are immediately covered by the interstitial fluids and blood proteins, indicating the importance of the adsorbed proteins for the initial interaction.[293] In particular, the fibrillar proteins such as Fgn and Vtn favor the adhesion and migration of cells.[294] The attachments of the cells can occur via the integrin-mediated receptor, followed by the clustering of transmembrane receptors to start the signaling cascade and finally regulate the attachment and the characteristics of the cells, leading to the improvement of the environment for cellular interactions (cell-cell and cell-material).[295,296] The way in which the proteins are adsorbed causes the specific cellular reactions to the underlying physicochemical properties of the material.[294]

To control the cell function, it is necessary to clarify the ECM protein absorption because the structural organization of the proteins can result in the different initial interactions with the cells.[297] The adsorption of proteins depends on the surficial properties like free energy, wettability, roughness and charge. The porous HAp improved protein adsorption and provided the better viability as compared with the case by the dense HAp.[287]

The water molecules from the solvents can be absorbed on the HAp surface to form the hydration layers, which has a great influence on the three-dimensional arrangement of the proteins. The interactions between the HAp NPs and the proteins are strongly influenced by the water at the interface (i.e., hydration layer), suggesting that the hydration layer plays an important role in the determination of the structure, dynamics and bioactivity of the proteins.[298–301] Here, the strength of surface hydration is mainly determined by the physicochemical properties of the HAp NPs. The hydration layer causes a steric repulsion when the proteins approach to the surface for the unfavorable decrease in entropy. In the polymer research field, the interfacial water can be classified into three categories: (a) non-freezing water which plays an important role in the cytocompatibility, (b) intermediate water which prevents that the proteins have a direct contact with the surface, and (c) free water that behave as the bulk. The non-freezing and intermediated water can be defined as bonding water, because these are the ones that affect the ability of protein binding with the HAp. (see **Figure 1.10**).[302–304] The

negative- and positive-charged ions of the HAp NPs can bind with the water molecules, and the hydration layer could increase the nonspecific protein adsorption.[305] Although the water–protein interactions are crucial for the protein structural stability, functional dynamics and biological responses.[306] The phenomena at the interface are not fully understood in the bioceramic research field. In the previous reports about the hydration,[307] the possible schematic representation of protein adsorption on HAp is shown in **Figure 1.11**. In the beginning, the hydrated Fgn interacts with the hydration layer with possible dehydration. Then, the Fgn absorbs on HAp occurs, when the αC domain of the positively-charged Fgn interacts with the negatively-charged phosphate ions and hydroxyl groups of HAp. Because of the Fgn saturation and the Fgn-Fgn hydrophobic interactions, the adsorbed Fgn change the conformation from "side-on" to "end-on" in **Figure 1.11(a)**. The adsorption model of albumin (Ab) could be "side-on" at the initial adsorption region at the monolayer. The positively-charged calcium ions on the HAp effectively bond with the imidazole and carboxyl groups of the Ab. The nonfreezing water could suppress the denaturalization of the adsorbed proteins, suggesting the concept of "bio-fusion interfaces" as shown in **Figure 1.11(b)**.[308]

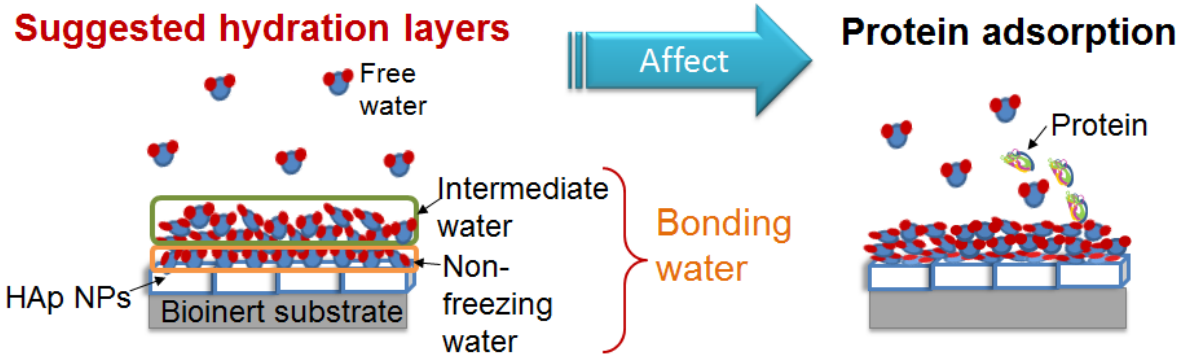

Figure 1.10. Scheme of the possible HAp NP interfacial interactions related with the suggested hydration layer and the consecutive protein adsorption.

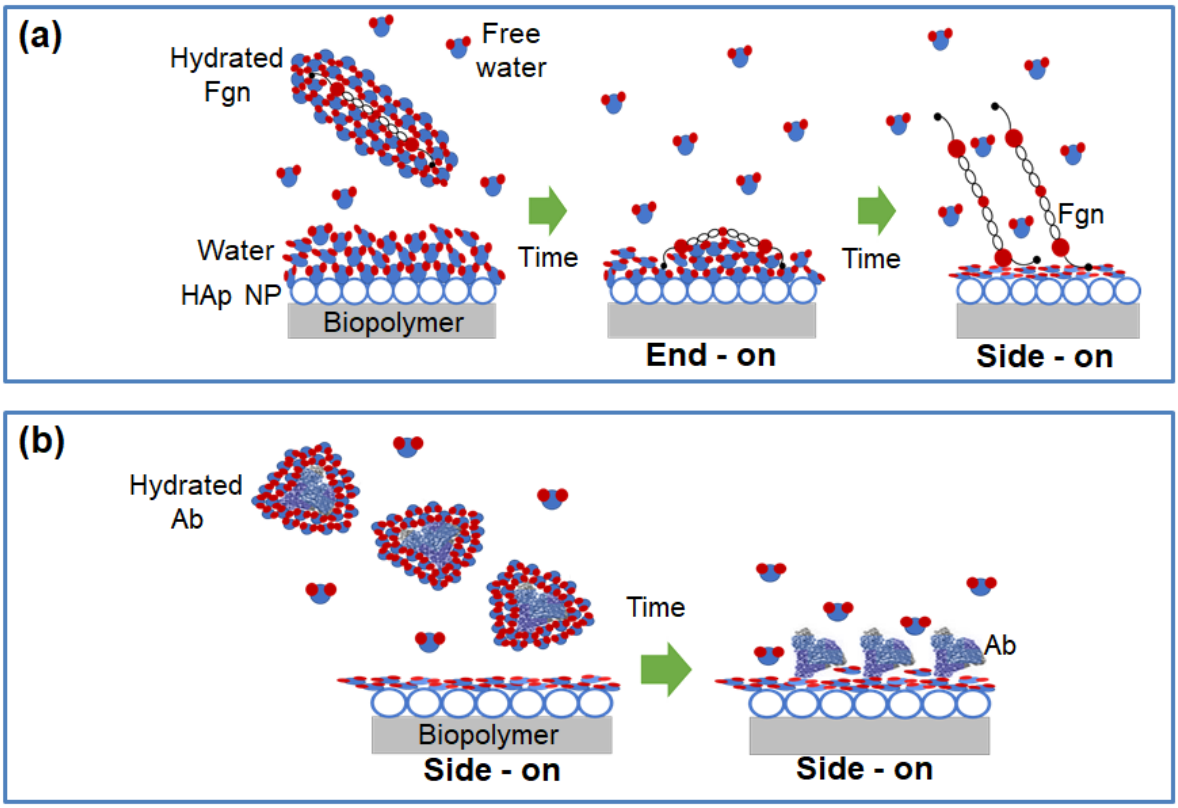

Figure 1.11. Possible schemes of the protein interactions with the hydration layer on the HAp surface during the protein adsorption. (a) In the beginning the hydrated Fgn interacts with the hydration layer with possible dehydration. Then the Fgn absorbs on HAp. Finally, conformational change from "side-on", at initial adsorption region to "end-on" at saturated adsorption region. (b) The adsorption model of Ab could be "side-on" at initial adsorption region and also at the monolayer. The nonfreezing water could suppress the denaturalization of the adsorbed proteins suggesting fusion interfaces.

Several HAp/polymer/cell interactions have been studied to improve the bone tissue regeneration and to control cell adhesion. HAp bonded with insulin was incorporated in PLGA to obtain insulin-HAp/PLGA composites. The *in vitro* studies showed the better cell adhesion and differentiation with an accelerated osteogenesis on the insulin-HAp/PLGA composites as compared with the case on HAp/PLGA and pure PLGA, suggesting its possible application as an artificial bone for implantation and as scaffolds for bone tissue regeneration.[309] *In vitro*, the cellular response of HOBs to the HAp roughness was studied. With the increase in the roughness increased the adhesion, proliferation and detachment strength of the cells. The detachment strength could be due to the specific adsorption of serum proteins such as Fn. The substrates pre-adsorbed

with Fn have resulted in a high detachment strength.[310] Previously, our group investigated the interfacial phenomenon between the pre-adsorbed protein layer and cells on HAp and oxidized polystyrene (PSox) by Voight-based viscoelastic model. With the increase in the cell adhesion, the interfacial layer was changed from elastic to viscose.

The cells on the pre-treated HAp showed the rough fibrous pseudopods, whereas the pseudopods on the pre-treated PSox were particulate, suggesting the change in the cytoskeleton and ECM.[311,312] Our group observed the change in the arrangement of the ECM and the cytoskeleton at the interfaces due to the interactions between the cells and the proteins. The first interfacial phenomenon was carried out by the pre-adsorption of Ab, Fn and Col, followed by the adsorption in FBS and finally the cellular adhesion of osteoblasts. The Col adsorption had the higher elasticity and viscosity than the cases in the Fn and Ab adsorption. The Fn and Col formed the viscous interfacial layer and cell adhesion to exhibit the elongated cellular shapes with fibrous pseudopods, contrary to the modification of Ab that had the round shapes **Figure 1.12 (a)** showed the scheme of the evaluation for the effect of different pre-adsorbed proteins on the interfacial phenomenon during the initial adhesion of the osteoblasts by the analyses with QCM-D and confocal laser scanning microscope (CLSM). The results of the cellular morphologies adhered on the pre-adsorbed proteins on HAp were shown in **Figure 1.12 (b)** on the adsorbed FBS, **(c)** on the adsorbed FBS-Fgn, **(d)** on the adsorbed FBS-Ab, and **(e)** on the adsorbed FBS-Col,[313] suggesting the experimental proof of the protein/bioceramic fusion interfaces for the cell activation. The use of HAp/polymer composites depends on the mechanical requirements of the application. The rigid polymer substrates can be used for the bone replacement or implanted to provide the structural support or as tempered for bone regeneration, while the soft polymer substrates can be used to replace cartilage, tendon, or to build blood vessels or catheters.

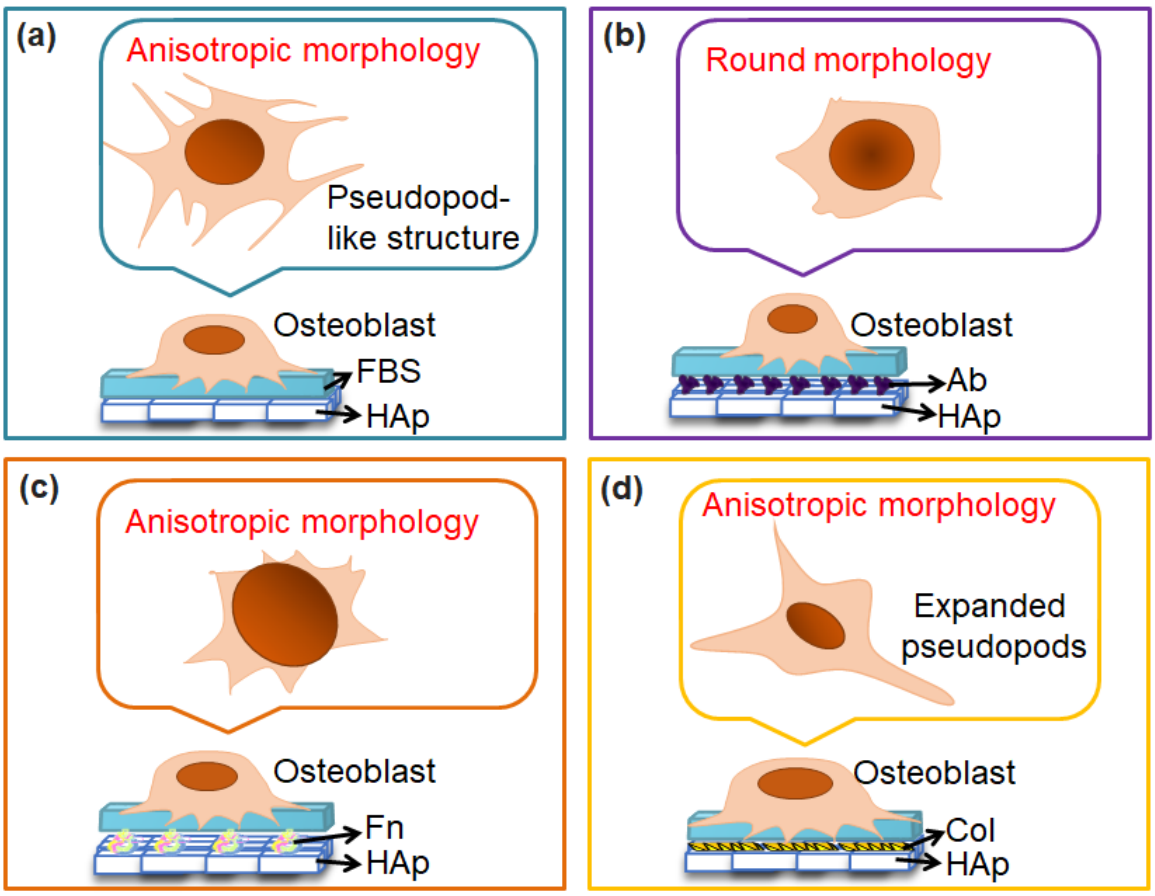

Figure 1.12. Scheme of the evaluation of effect of interfacial phenomena between the proteins and the osteoblast-like cells at initial adhesion of the cells adhered on (a) fetal bovine serum (FBS), (b) FBS-Ab, (c) FBS-Fn, and (d) FBS-Collagen adsorbed on the HAp.

1.7. Purpose of This Study

In this study, the control of the shape and size of the HAp to obtain rounder HAp with nanoparticle size in order to control the cytocompatibility and the subsequent thin film formation without using toxic reagents was achievement trough two strategies. The first strategy was by the use of nonionic surfactant assistant synthesis to obtain HAp NPs with elliptical shape (E−HAp NPs) for enhance the cytocompatibility of the particles. In order to understand the HAp films-protein interfacial interactions and the relationship of the HAp films−Protein−Cell interfacial interactions were investigated in order to control the cytocompatibility with the cells. The second strategy was achieved by the incorporation of ions (Zn and carbonate ions) in the HAp structure to obtain NPs with rounder shape. The Ca ion is substituted by the Zn ion to obtain (Zn:HAp NPs) with rounder shape and higher cytocompatibility and with antibacterial activity. The Phosphate ion substitution by

carbonate ions to achieve a carbonate containing HAp NPs (CHAp NPs) which is a material with excellent good cytocompatibility and biodegradability, due to the similarity with the HAp contained in the human bones and teeth. Nano-sized particles to fill the interspace between the silicone rubber and the cells and the bacteria can no longer permeate through the interspace and cannot cause bacterial infection. Development of a fixation technique without chemical reagents (e.g., Use of electric field, plasma treatment, thermos-compression). No silane coupling agents because are cytotoxic. The HAp Films−Protein−Cell interfacial interactions were investigated with the purpose of understands these interactions. The schematic representation of the scope of this study is shown in **Figure 1.13**.

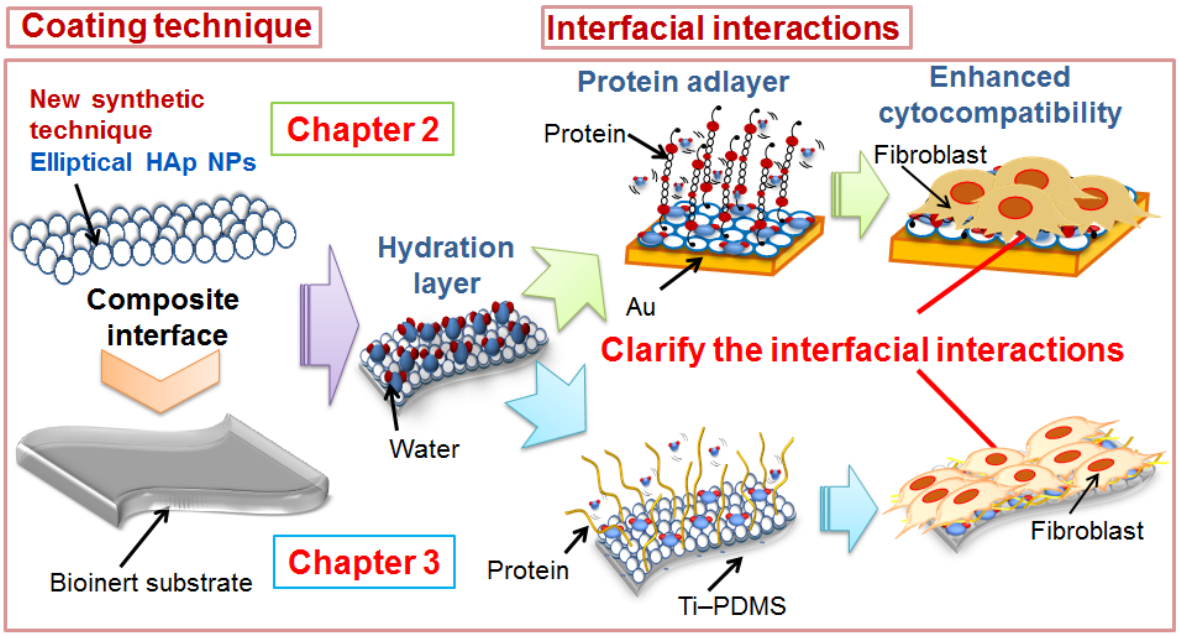

Figure 1.13. Scheme of the purpose of this study. New synthetic technique of elliptical HAp NPs to obtain self-assembled bioinert-bioactive composite films by coating technique and study their interfacial interactions for biomedical devices applications.

1.8. Contents of This Thesis

In this thesis was investigated the relationship between the cells the HAp NPs and how this relationship is modified by the modification of the shape and size of HAp NPs as shown in **Figure 1.14**.

The thesis contains four chapters. In Chapter 1: "*General introduction*" it was suggested that the surface modification of bioinert materials like Au and PDMS with HAp, is necessary in order to improve and control the cytocompatibility, due to the crystallographically and chemically similarity of the HAp with the components of human's hard tissues (bones and teeth). Importantly, naturally-formed HAp is not absolutely pure and has some impurities of ions (Zn^{2+}, Mg^{2+}, K^{+}, etc.). The incorporation of these ions improves the cytocompatibility and in the case of the Zn ion will provide also an antibacterial property. The shape and size are important factors that affect the absorption of the proteins and as a consequence the cell adhesion, it was reported than nano-sized and rounder shape had better cytocompatibility. However, the mechanism is still unknown. The investigations of the interfacial interactions between the HAp NPs−Protein−Cell are required to design medical devices which enhance cytocompatible properties.

In Chapter 2: "*Study on Preparation of Elliptical Hydroxyapatite Nanoparticle Films and their Protein Mediated Ability for Cell Adhesion*" the use of nonionic surfactant ($ChEO_{15}$) allows controlling the shape of the HAp NPs, leading the formation of the E−HAp NPs. EPD method was used to deposit the E−HAp NPs substrate to obtain the E−HAp film. The shape and size of E−HAp NPs of the film play an important role in the hydration layer structures due to the different Ca/P ratio exposure. The hydration layer structure ratios had a direct impact on the Fgn adsorption and conformation. A comparative study of the adsorption mechanism, interfacial interactions, and conformation of adsorbed Fgn were studied. Fgn−surface interactions showed a higher affinity for E−HAp than for the traditional synthetic process of HAp with Neddle-like shape (N−HAp) and Au substrate. Therefore, the biomaterial physicochemical properties affected the protein conformation and orientation upon the adsorption states through the specific surface protein interactions, and subsequent cell adhesion and spreading. The E−HAp film leads the formation of effectively bioactive surfaces, which promote the cellular adhesion with higher production of collagen type I.

In Chapter 3: "*Preparation and Biological Evaluation of Nanoparticle Zinc-substituted Hydroxyapatite Films*" the Zinc-substituted HAp NPs were synthesized by a wet chemical method. In the method, the initial (Ca+Zn)/P ratio of 1.67 (Zn:HAp) and 2.00 (Zn:CHAp) were adjusted from the reagents ($CaCl_2$, $ZnCl_2$, and K_2HPO_4) to resultantly form the

stoichiometric and carbonate HAp NPs, respectively. The initial $ZnCl_2$ was changed as the dopant concentration of Zn/(Ca+Zn) = 0.0, 2.5, 5.0 and 10 mol%. An EPD at the optimized voltage of 100 V was used for the surface modification of biomedical polymers. All the particle films electrically plated on a Ti-PDMS substrate demonstrated no cytotoxicity. The hydration layer structures was studies on the Zn:HAp and Zn:CHAp films. Comparative studies of the interfacial interactions of adsorbed fetal bovine serum (FBS) were studied. Moreover, the nanocrystalline Zn:HAp and Zn:CHAp films were summarized to provide good cytocompatibility as well as antibacterial properties on biomedical polymer surfaces, suggesting useful catheter surface modification technique. Nevertheless, Zn:CHAp films significatively provided the bioactive properties for fibroblast ingrowth, suggesting the Zn and carbonate ions effect on the cytocompatibility.

In Chapter 4: "*Summary*", in this chapter it is summarized the HAp films-hydration layer structures-protein-cell interfacial interactions. It is expected that the new synthetic technique of HAp film can be applicable for medical devices with enhanced cytocompatibility.

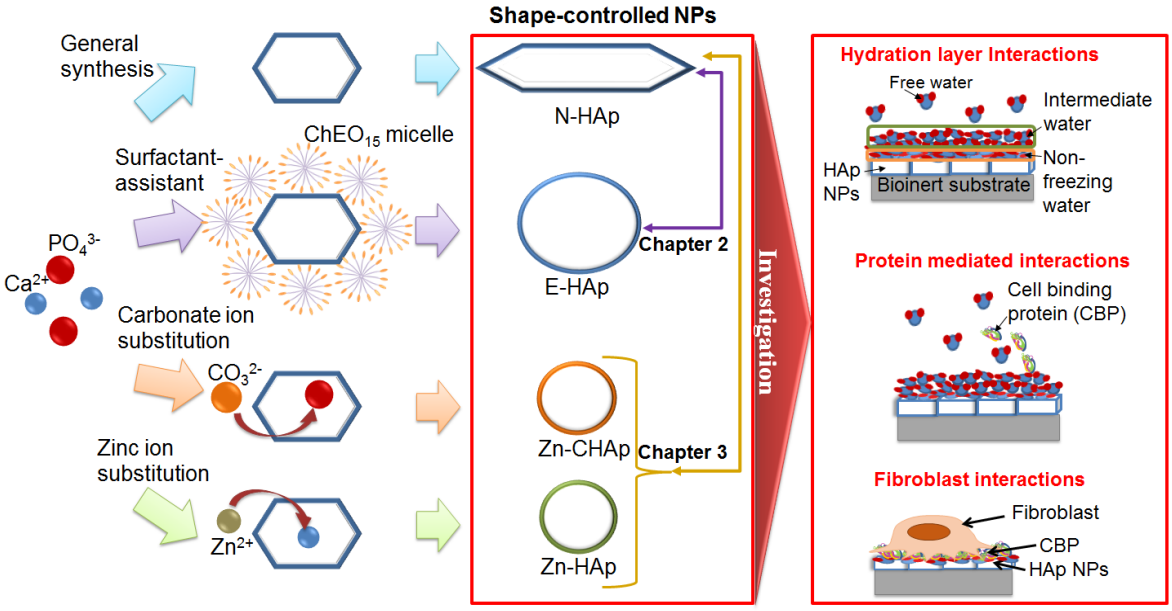

Figure 1.14. Scheme of the contents of this thesis, showing the synthesis of the HAp by general method to obtain N−HAp NPs. Control of the shape by surfactant-assistant method using $ChEO_{15}$ to obtain E−HAp NPs, and carbonated-substituted HAp methodology to obtain Zn:CHAp, and zinc-substituted HAp in order to obtain Zn:HAp NPs and the study of the relationship between HAp−Hydration layers−protein−fibroblast interfacial interactions.

References

(1) Bergmann, C.; Stumpf, A. *Dental Ceramics*; Topics in Mining, Metallurgy and Materials Engineering; Springer Berlin Heidelberg: Berlin, Heidelberg, **2013**.

(2) Park, J. B.; Lakes, R. S. *Biomaterials : An Introduction*; Springer, **2007**.

(3) Ratner, B. D.; Buddy D. *Biomaterials Science : An Introduction to Materials in Medicine*; Elsevier Academic Press, **2004**.

(4) Shi, D. *Introduction to Biomaterials*; Co-Published With Tsinghua University Press, **2005**.

(5) Teoh, S. H. Introduction To Biomaterials Engineering And Processing — An Overview; **2004**; pp 1–16.

(6) Article, R.; Kheirallah, M.; Almeshaly, H.; Kheirallah, M. Bone Graft Substitutes for Bone Defect Regeneration. A Collective Review. *Int. J. Dent. Oral Sci. Int J Dent. Oral Sci* **2016**, *03* (5), 247–257.

(7) Kelly, S. H.; Shores, L. S.; Votaw, N. L.; Collier, J. H. Biomaterial Strategies for Generating Therapeutic Immune Responses. *Adv. Drug Deliv. Rev.* **2017**, *114*, 3–18.

(8) Kirkpatrick, C.; Krump-Konvalinkova, V.; Unger, R.; Bittinger, F.; Otto, M.; Peters, K. Tissue Response and Biomaterial Integration: The Efficacy of in Vitro Methods. *Biomol. Eng.* **2002**, *19* (2–6), 211–217.

(9) Franz, S.; Rammelt, S.; Scharnweber, D.; Simon, J. C. Immune Responses to Implants – A Review of the Implications for the Design of Immunomodulatory Biomaterials. *Biomaterials* **2011**, *32* (28), 6692–6709.

(10) Chung, L.; Maestas, D. R.; Housseau, F.; Elisseeff, J. H. Key Players in the Immune Response to Biomaterial Scaffolds for Regenerative Medicine. *Adv. Drug Deliv. Rev.* **2017**, *114*, 184–192.

(11) Gardner, A. B.; Lee, S. K. C.; Woods, E. C.; Acharya, A. P. Biomaterials-Based Modulation of the Immune System. *Biomed Res. Int.* **2013**, *2013*, 732182.

(12) Boehler, R. M.; Graham, J. G.; Shea, L. D. Tissue Engineering Tools for Modulation of the Immune Response. *BioTechniques*. **2011**, pp 239–254.

(13) Andorko, J. I.; Christopher, I.; Jewell, M.; Jewell, C. M. Designing Biomaterials with Immunomodulatory Properties for Tissue Engineering and Regenerative Medicine. *Bioeng. Transl. Med.* **2017**, *2*, 139–155.

(14) Zhou, H.; Lee, J. Nanoscale Hydroxyapatite Particles for Bone Tissue Engineering. **2011**.

(15) Stevens, M. M. Biomaterials for Bone Tissue Engineering. *Mater. Today* **2008**, *11* (5), 18–25.

(16) Thamaraiselvi, T. V.; Rajeswari, S. *Biological Evaluation of Bioceramic Materials-A Review*; **2004**, *24* (31), 172.

(17) Huang, X.; Neretina, S.; El-Sayed, M. A. Gold Nanorods: From Synthesis and Properties to Biological and Biomedical Applications. *Adv. Mater.* **2009**, *21* (48), 4880–4910.

(18) Zhang, X. Gold Nanoparticles: Recent Advances in the Biomedical Applications. *Cell Biochem. Biophys.* **2015**, *72* (3), 771–775.

(19) Dvir, T.; Timko, B. P.; Brigham, M. D.; Naik, S. R.; Sandeep, S.; Levy, O.; Jin, H.; Parker, K. K.; Langer, R.; Daniel, S. Nanowired Three Dimensional Cardiac Patches. **2012**, *6* (11), 720–725.

(20) Abdelhalim, M. A. K. Exposure to Gold Nanoparticles Produces Cardiac Tissue Damage That Depends on the Size and Duration of Exposure. *Lipids Health Dis.* **2011**, *10* (1), 205.
(21) Abdelhalim, M. A. K. Gold Nanoparticles Administration Induces Disarray of Heart Muscle, Hemorrhagic, Chronic Inflammatory Cells Infiltrated by Small Lymphocytes, Cytoplasmic Vacuolization and Congested and Dilated Blood Vessels. *Lipids Health Dis.* **2011**, *10* (1), 233.
(22) Abdelhalim, M. A. K. Exposure to Gold Nanoparticles Produces Pneumonia, Fibrosis, Chronic Inflammatory Cell Infiltrates, Congested and Dilated Blood Vessels, and Hemosiderin Granule and Emphysema Foci. *J. Cancer Sci. Ther.* **2012**, *4* (3), 46–50.
(23) Abbasi, F.; Mirzadeh, H.; Katbab, A. A. Modification of Polysiloxane Polymers for Biomedical Applications: A Review. *Polym. Int.* **2001**, *50* (12), 1279–1287.
(24) Abbasi, F.; Mirzadeh, H.; Katbab, A. A. Bulk and Surface Modification of Silicone Rubber for Biomedical Applications. *Polym. Int.* **2002**, *51* (10), 882–888.
(25) Bélanger, M. C.; Marois, Y. Hemocompatibility, Biocompatibility, Inflammatory and *in Vivo* Studies of Primary Reference Materials Low-Density Polyethylene and Polydimethylsiloxane: A Review. *J. Biomed. Mater. Res.* **2001**, *58* (5), 467–477.
(26) Caballero, M.; Bernal-Sprekelsen, M.; Calvo, C.; Farrè, X.; Quintó, L.; Alòs, L. Polydimethylsiloxane versus Polytetrafluoroethylene for Vocal Fold Medialization: Histologic Evaluation in a Rabbit Model. *J. Biomed. Mater. Res. Part B Appl. Biomater.* **2003**, *67B* (1), 666–674.
(27) Maki, D. G.; Stolz, S. M.; Wheeler, S.; Mermel, L. A. Prevention of Central Venous Catheter-Related Bloodstream Infection by Use of an Antiseptic-Impregnated Catheter. *Ann. Intern. Med.* **1997**, *127* (4), 257.
(28) Maki, D. G.; Weise, C. E.; Sarafin, H. W. A Semiquantitative Culture Method for Identifying Intravenous-Catheter-Related Infection. *N. Engl. J. Med.* **1977**, *296* (23), 1305–1309.
(29) Francis, M. D.; Russell, R. G.; Fleisch, H.; Fleisch, H. Diphosphonates Inhibit Formation of Calcium Phosphate Crystals in Vitro and Pathological Calcification in Vivo. *Science* **1969**, *165* (3899), 1264–1266.
(30) Affeld, K.; Grosshauser, J.; Goubergrits, L.; Kertzscher, U. Percutaneous Devices: A Review of Applications, Problems and Possible Solutions. *Expert Rev. Med. Devices* **2012**, *9* (4), 389–399.
(31) Bode, A. S.; Tordoir, J. H. M. Vascular Access For Hemodialysis Therapy; Springer, Berlin, Heidelberg, **2013**; pp 235–303.
(32) Mooney, V.; Schwartz, S. A.; Roth, A. M.; Gorniowsky, M. J. Percutaneous Implant Devices. *Ann. Biomed. Eng.* **1977**, *5* (1), 34–46.
(33) Banode, S. R.; Attar, M. S.; Picche, G. *Brief Review of Different Types of Parentral Devices*. **2015**, *6* (8), 1133–1139.
(34) Smith, J. R.; Lamprou, D. A. Polymer Coatings for Biomedical Applications: A Review. *Trans. IMF* **2014**, *92* (1), 9–19.
(35) Álvarez, C. A.; Cortés, J. A.; Gómez, C. H.; Fernández, J. A.; Sossa, M. P.; Beltrán, F.; Izquierdo, G. M.; Andrade, F. M.; Ortiz, G.; Padilla, A. Guías de Práctica Clínica Para La Prevención de Infecciones Intrahospitalarias Asociadas Al Uso de Dispositivos Médicos. *Infectio* **2010**, *14* (4), 292–308.

(36) Speranza, G.; Gottardi, G.; Pederzolli, C.; Lunelli, L.; Canteri, R.; Pasquardini, L.; Carli, E.; Lui, A.; Maniglio, D.; Brugnara, M. Role of Chemical Interactions in Bacterial Adhesion to Polymer Surfaces. *Biomaterials* **2004**, *25* (11), 2029–2037.

(37) Monteiro, D. R.; Gorup, L. F.; Takamiya, A. S.; Ruvollo-Filho, A. C.; Camargo, E. R. de; Barbosa, D. B. The Growing Importance of Materials That Prevent Microbial Adhesion: Antimicrobial Effect of Medical Devices Containing Silver. *Int. J. Antimicrob. Agents* **2009**, *34* (2), 103–110.

(38) Fajuri M, P.; Pino A, P.; Castillo M, A. Uso de Catéter Venoso Central de Inserción Periférica En Pediatría. *Rev. Chil. pediatría* **2012**, *83* (4), 352–357.

(39) Cloutier, M.; Mantovani, D.; Rosei, F. Antibacterial Coatings: Challenges, Perspectives, and Opportunities. *Trends Biotechnol.* **2015**, *33* (11), 637–652.

(40) Rasamiravaka, T.; Labtani, Q.; Duez, P.; El Jaziri, M. The Formation of Biofilms by *Pseudomonas Aeruginosa* : A Review of the Natural and Synthetic Compounds Interfering with Control Mechanisms. *Biomed Res. Int.* **2015**, *2015*, 1–17.

(41) Jefferson, K. K. What Drives Bacteria to Produce a Biofilm? *FEMS Microbiol. Lett.* **2004**, *236* (2), 163–173.

(42) Bridier, A.; Sanchez-Vizuete, P.; Guilbaud, M.; Piard, J.-C.; Naïtali, M.; Briandet, R. Biofilm-Associated Persistence of Food-Borne Pathogens. *Food Microbiol.* **2015**, *45*, 167–178.

(43) Arciola, C. R. New Concepts and New Weapons in Implant Infections. *Int. J. Artif. Organs* **2009**, *32* (9), 533–536.

(44) Hodges, E. A. *Anti-Microbial Self-Assembling "Click" Monolayers Utilizing Silver Nanoparticles for Indwelling Medical Devices Anti-Microbial Self-Assembling-Click‖ Monolayers Utilizing Silver Nanoparticles For Indwelling Medical Devices*; Mater thesis, **2008**.

(45) Zhang, L.; Keogh, S.; Rickard, C. M. Reducing the Risk of Infection Associated with Vascular Access Devices through Nanotechnology: A Perspective. *Int. J. Nanomedicine* **2013**, *8*, 4453–4466.

(46) Atiyeh, B. S.; Costagliola, M.; Hayek, S. N.; Dibo, S. A. Effect of Silver on Burn Wound Infection Control and Healing: Review of the Literature. *Burns* **2007**, *33* (2), 139–148.

(47) Mofazzal Jahromi, M. A.; Sahandi Zangabad, P.; Moosavi Basri, S. M.; Sahandi Zangabad, K.; Ghamarypour, A.; Aref, A. R.; Karimi, M.; Hamblin, M. R. Nanomedicine and Advanced Technologies for Burns: Preventing Infection and Facilitating Wound Healing. *Adv. Drug Deliv. Rev.* **2018**, *123*, 33–64.

(48) Wang, X.; Chang, J.; Wu, C. Bioactive Inorganic/Organic Nanocomposites for Wound Healing. *Appl. Mater. Today* **2018**, *11*, 308–319.

(49) El-Rashidy, A. A.; Waly, G.; Gad, A.; Roether, J. A.; Hum, J.; Yang, Y.; Detsch, R.; Hashem, A. A.; Sami, I.; Goldmann, W. H. Antibacterial Activity and Biocompatibility of Zein Scaffolds Containing Silver-Doped Bioactive Glass. *Biomed. Mater.* **2018**, *13* (6), 065006.

(50) Lin, J. J.; Lin, W. C.; Li, S. D.; Lin, C. Y.; Hsu, S. Evaluation of the Antibacterial Activity and Biocompatibility for Silver Nanoparticles Immobilized on Nano Silicate Platelets. *ACS Appl. Mater. Interfaces* **2013**, *5* (2), 433–443.

(51) Lan, M. Y.; Liu, C. P.; Huang, H. H.; Lee, S. W. Both Enhanced Biocompatibility and Antibacterial Activity in Ag-Decorated TiO_2 Nanotubes. *PLoS One* **2013**, *8* (10),

e75364.
(52) Wang, J.; Gong, X.; Hai, J.; Li, T. Synthesis of Silver–Hydroxyapatite Composite with Improved Antibacterial Properties. *Vacuum* **2018**, *152*, 132–137.
(53) Kumar-Saini, R.; Prasad-Bagri, L.; Bajpai, A. K. Nano-Silver Hydroxyapatite Based Antibacterial 3D Scaffolds of Gelatin/Alginate/Poly (Vinyl Alcohol) for Bone Tissue Engineering Applications. *Colloids Surfaces B Biointerfaces* **2019**, *177*, 211–218.
(54) Mocanu, A.; Furtos, G.; Rapuntean, S.; Horovitz, O.; Flore, C.; Garbo, C.; Danisteanu, A.; Rapuntean, G.; Prejmerean, C.; Tomoaia-Cotisel, M. Synthesis; Characterization and Antimicrobial Effects of Composites Based on Multi-Substituted Hydroxyapatite and Silver Nanoparticles. *Appl. Surf. Sci.* **2014**, *298*, 225–235.
(55) Hadidi, M.; Bigham, A.; Saebnoori, E.; Hassanzadeh-Tabrizi, S. A.; Rahmati, S.; Alizadeh, Z. M.; Nasirian, V.; Rafienia, M. Electrophoretic-Deposited Hydroxyapatite-Copper Nanocomposite as an Antibacterial Coating for Biomedical Applications. *Surf. Coatings Technol.* **2017**, *321*, 171–179.
(56) Huang, Y.-T.; Yamauchi, Y.; Lai, C.-W.; Chen, W.-J. Evaluating the Antibacterial Property of Gold-Coated Hydroxyapatite: A Molecular Biological Approach. *J. Hazard. Mater.* **2014**, *277*, 20–26.
(57) Wang, Q.; Tang, P.; Ge, X.; Li, P.; Lv, C.; Wang, M.; Wang, K.; Fang, L.; Lu, X. Experimental and Simulation Studies of Strontium/Zinc-Codoped Hydroxyapatite Porous Scaffolds with Excellent Osteoinductivity and Antibacterial Activity. *Appl. Surf. Sci.* **2018**, *462*, 118–126.
(58) Sergi, R.; Bellucci, D.; Candidato, R. T.; Lusvarghi, L.; Bolelli, G.; Pawlowski, L.; Candiani, G.; Altomare, L.; De Nardo, L.; Cannillo, V. Bioactive Zn-Doped Hydroxyapatite Coatings and Their Antibacterial Efficacy against Escherichia Coli and Staphylococcus Aureus. *Surf. Coatings Technol.* **2018**, *352*, 84–91.
(59) Zhang, H.; Hatoko, M.; Yin, D.; Yang, Y.; Zeng, Y.; Komasa, S.; Kusumoto, T.; Nishizaki, H.; Shimizu, H.; Zhao, W. Antibacterial Activity and Biocompatibility of Nanoporous Titanium Doped with Silver Nanoparticles and Coated with N-Acetyl Cysteine. *J. Hard Tissue Biol.* **2018**, *27* (4), 351–358.
(60) Damm, C.; Münstedt, H.; Rösch, A. The Antimicrobial Efficacy of Polyamide 6/Silver-Nano- and Microcomposites. *Mater. Chem. Phys.* **2008**, *108* (1), 61–66.
(61) Abdal Dayem, A.; Hossain, M.; Lee, S.; Kim, K.; Saha, S.; Yang, G. M.; Choi, H.; Cho, S. G.; Abdal Dayem, A.; Hossain, M. K. The Role of Reactive Oxygen Species (ROS) in the Biological Activities of Metallic Nanoparticles. *Int. J. Mol. Sci.* **2017**, *18* (1), 120.
(62) Ciobanu, C. S.; Iconaru, S. L.; Chifiriuc, M. C.; Costescu, A.; Le Coustumer, P.; Predoi, D. Synthesis and Antimicrobial Activity of Silver-Doped Hydroxyapatite Nanoparticles. *Biomed Res. Int.* **2013**, *2013*, 916218.
(63) Stanić, V.; Dimitrijević, S.; Antić-Stanković, J.; Mitrić, M.; Jokić, B.; Plećaš, I. B.; Raičević, S. Synthesis, Characterization and Antimicrobial Activity of Copper and Zinc-Doped Hydroxyapatite Nanopowders. *Appl. Surf. Sci.* **2010**, *256* (20), 6083–6089.
(64) Yang, Y. C.; Chen, C. C.; Wang, J. B.; Wang, Y. C.; Lin, F. H. Flame Sprayed Zinc Doped Hydroxyapatite Coating with Antibacterial and Biocompatible Properties. *Ceram. Int.* **2017**, *43*, S829–S835.

(65) Chasapis, C. T.; Loutsidou, A. C.; Spiliopoulou, C. A.; Stefanidou, M. E. Zinc and Human Health: An Update. *Arch. Toxicol.* **2012**, *86* (4), 521–534.
(66) Goldhaber, S. B. Trace Element Risk Assessment: Essentiality vs. Toxicity. *Regul. Toxicol. Pharmacol.* **2003**, *38* (2), 232–242.
(67) Devaney, B.; Ziegler, P.; Pac, S.; Karwe, V.; Barr, S. I. Nutrient Intakes of Infants and Toddlers. *J. Am. Diet. Assoc.* **2004**, *104*, 14–21.
(68) Zhou, H.; Lee, J. Nanoscale Hydroxyapatite Particles for Bone Tissue Engineering. *Acta Biomater.* **2011**, *7* (7), 2769–2781.
(69) Stevens, M. M. Biomaterials for Bone Tissue Engineering. *Mater. Today* **2008**, *11* (5), 18–25.
(70) Variola, F.; Vetrone, F.; Richert, L.; Jedrzejowski, P.; Yi, J. H.; Zalzal, S.; Clair, S.; Sarkissian, A.; Perepichka, D. F.; Wuest, J. D. Improving Biocompatibility of Implantable Metals by Nanoscale Modification of Surfaces: An Overview of Strategies, Fabrication Methods, and Challenges. *Small* **2009**, *5* (9), 996–1006.
(71) Karageorgiou, V.; Kaplan, D. Porosity of 3D Biomaterial Scaffolds and Osteogenesis. *Biomaterials* **2005**, *26* (27), 5474–5491.
(72) Pepla, E.; Besharat, L. K.; Palaia, G.; Tenore, G.; Migliau, G. Nano-Hydroxyapatite and Its Applications in Preventive, Restorative and Regenerative Dentistry: A Review of Literature. *Ann. Stomatol. (Roma).* **2014**, *5* (3), 108–114.
(73) Ferraz, M. P.; Monteiro, F. J.; Manuel, C. M. Hydroxyapatite Nanoparticles: A Review of Preparation Methodologies, *J. Appl. Biomater. Biom.* **2018**, *2 (*2), 74–80.
(74) Aoki, H. Science and Medical Applications of Hydroxyapatite. *JAAS 1991*, 123–134.
(75) Jevtić, M.; Mitrić, M.; Škapin, S.; Jančar, B.; Ignjatović, N.; Uskoković, D. Crystal Structure of Hydroxyapatite Nanorods Synthesized by Sonochemical Homogeneous Precipitation. *Cryst. Growth Des.* **2008**, *8* (7), 2217–2222.
(76) Orlovskii, V. P.; Komlev, V. S.; Barinov, S. M. Hydroxyapatite and Hydroxyapatite-Based Ceramics. *Inorg. Mater.* **2002**, *38* (10), 973–984.
(77) Basu, S.; Basu, B. Doped Biphasic Calcium Phosphate: Synthesis and Structure. *J. Asian Ceram. Soc.* **2019**, 1–19.
(78) Bierbaum, S.; Hintze, V.; Scharnweber, D. Functionalization of Biomaterial Surfaces Using Artificial Extracellular Matrices. *Biomatter* **2012**, *2* (3), 132–141.
(79) Al-Jawad, M.; Steuwer, A.; Kilcoyne, S. H.; Shore, R. C.; Cywinski, R.; Wood, D. J. 2D Mapping of Texture and Lattice Parameters of Dental Enamel. *Biomaterials* **2007**, *28* (18), 2908–2914.
(80) Olszta, M. J.; Cheng, X.; Jee, S. S.; Kumar, R.; Kim, Y.-Y.; Kaufman, M. J.; Douglas, E. P.; Gower, L. B. Bone Structure and Formation: A New Perspective. *Mater. Sci. Eng. R Reports* **2007**, *58* (3–5), 77–116.
(81) Elliott, J. C.; James C. *Structure and Chemistry of the Apatites and Other Calcium Orthophosphates*; **1994**, *18*, 111–189.
(82) Puleo, D. .; Nanci, A. Understanding and Controlling the Bone–Implant Interface. *Biomaterials* **1999**, *20* (23–24), 2311–2321.
(83) Burg, K. J.; Porter, S.; Kellam, J. F. Biomaterial Developments for Bone Tissue Engineering. *Biomaterials* **2000**, *21* (23), 2347–2359.
(84) Legeros, R. Z.; Craig, R. G. Strategies to Affect Bone Remodeling: Osteointegration. *J. Bone Miner. Res.* **2009**, *8* (S2), S583–S596..
(85) Lu, J.; Yu, H.; Chen, C. Biological Properties of Calcium Phosphate Biomaterials for

Bone Repair: A Review. *RSC Adv.* **2018**, *8* (4), 2015–2033.
(86) Shi, Z.; Huang, X.; Cai, Y.; Tang, R.; Yang, D. Size Effect of Hydroxyapatite Nanoparticles on Proliferation and Apoptosis of Osteoblast-like Cells. *Acta Biomater.* **2009**, *5* (1), 338–345.
(87) Yuan, Y.; Liu, C.; Qian, J.; Wang, J.; Zhang, Y. Size-Mediated Cytotoxicity and Apoptosis of Hydroxyapatite Nanoparticles in Human Hepatoma HepG2 Cells. *Biomaterials* **2010**, *31* (4), 730–740.
(88) Zhao, X.; Ng, S.; Heng, B. C.; Guo, J.; Ma, L.; Tan, T. T. Y.; Ng, K. W.; Loo, S. C. J. Cytotoxicity of Hydroxyapatite Nanoparticles Is Shape and Cell Dependent. *Arch. Toxicol.* **2013**, *87* (6), 1037–1052.
(89) Zhao, Y.; Zhang, Y.; Ning, F.; Guo, D.; Xu, Z. Synthesis and Cellular Biocompatibility of Two Kinds of HAP with Different Nanocrystal Morphology. *J. Biomed. Mater. Res. Part B Appl. Biomater.* **2007**, *83B* (1), 121–126.
(90) Lin, K.; Wu, C.; Chang, J. Advances in Synthesis of Calcium Phosphate Crystals with Controlled Size and Shape. *Acta Biomater.* **2014**, *10* (10), 4071–4102.
(91) Sadat-Shojai, M.; Khorasani, M. T.; Dinpanah-Khoshdargi, E.; Jamshidi, A. Synthesis Methods for Nanosized Hydroxyapatite with Diverse Structures. *Acta Biomater.* **2013**, *9* (8), 7591–7621.
(92) Nasiri-Tabrizi, B.; Honarmandi, P.; Ebrahimi-Kahrizsangi, R.; Honarmandi, P. Synthesis of Nanosize Single-Crystal Hydroxyapatite via Mechanochemical Method. *Mater. Lett.* **2009**, *63* (5), 543–546.
(93) Shih, W. J.; Chen, Y. F.; Wang, M. C.; Hon, M. H. Crystal Growth and Morphology of the Nano-Sized Hydroxyapatite Powders Synthesized from CaHPO4·2H2O and CaCO3 by Hydrolysis Method. *J. Cryst. Growth* **2004**, *270* (1–2), 211–218.
(94) Nakahira, A.; Sakamoto, K.; Yamaguchi, S.; Kaneno, M.; Takeda, S.; Okazaki, M. Novel Synthesis Method of Hydroxyapatite Whiskers by Hydrolysis of Alpha-Tricalcium Phosphate in Mixtures of Water and Organic Solvent. *J. Am. Ceram. Soc.* **2004**, *82* (8), 2029–2032.
(95) Feng, W.; Mu-sen, L.; Yu-peng, L.; Yong-xin, Q. A Simple Sol–Gel Technique for Preparing Hydroxyapatite Nanopowders. *Mater. Lett.* **2005**, *59* (8–9), 916–919.
(96) Beganskienė, A.; Beganskienė, A.; Dudko, O.; Sirutkaitis, R.; Giraitis, R. *Sol-Gel Coatings for Optical and Bioapplications View Project Layered Double Hydroxides View Project Water Based Sol-Gel Synthesis of Hydroxyapatite*; **2003**; Vol. 9.
(97) Kuriakose, T. A.; Kalkura, S. N.; Palanichamy, M.; Arivuoli, D.; Dierks, K.; Bocelli, G.; Betzel, C. Synthesis of Stoichiometric Nano Crystalline Hydroxyapatite by Ethanol-Based Sol–Gel Technique at Low Temperature. *J. Cryst. Growth* **2004**, *263* (1–4), 517–523.
(98) Liu, J.; Ye, X.; Wang, H.; Zhu, M.; Wang, B.; Yan, H. The Influence of PH and Temperature on the Morphology of Hydroxyapatite Synthesized by Hydrothermal Method. *Ceram. Int.* **2003**, *29* (6), 629–633.
(99) Wang, P.; Li, C.; Gong, H.; Jiang, X.; Wang, H.; Li, K. Effects of Synthesis Conditions on the Morphology of Hydroxyapatite Nanoparticles Produced by Wet Chemical Process. *Powder Technol.* **2010**, *203* (2), 315–321.
(100) Bose, S.; Saha, S. K. Synthesis and Characterization of Hydroxyapatite Nanopowders by Emulsion Technique. *Chem. Mater.* **2003**, *15* (23), 4464–4469.
(101) Güler, H.; Gündoğmaz, G.; Kurtuluş, F.; Çelik, G.; Gacanoğlu, Ş. S. Solid State

Synthesis of Calcium Borohydroxyapatite. *Solid State Sci.* **2011**, *13* (11), 1916–1920.

(102) Mohandes, F.; Salavati-Niasari, M. Simple Morphology-Controlled Fabrication of Hydroxyapatite Nanostructures with the Aid of New Organic Modifiers. *Chem. Eng. J.* **2014**, *252*, 173–184.

(103) Han, Y.; Li, S.; Wang, X.; Chen, X. Synthesis and Sintering of Nanocrystalline Hydroxyapatite Powders by Citric Acid Sol–Gel Combustion Method. *Mater. Res. Bull.* **2004**, *39* (1), 25–32.

(104) Wang, A.; Liu, D.; Yin, H.; Wu, H.; Wada, Y.; Ren, M.; Jiang, T.; Cheng, X.; Xu, Y. Size-Controlled Synthesis of Hydroxyapatite Nanorods by Chemical Precipitation in the Presence of Organic Modifiers. *Mater. Sci. Eng. C* **2007**, *27* (4), 865–869.

(105) Xin, R.; Ren, F.; Leng, Y. Synthesis and Characterization of Nano-Crystalline Calcium Phosphates with EDTA-Assisted Hydrothermal Method. *Mater. Des.* **2010**, *31* (4), 1691–1694.

(106) Seo, D. S.; Lee, J. K. Synthesis of Hydroxyapatite Whiskers through Dissolution–Reprecipitation Process Using EDTA. *J. Cryst. Growth* **2008**, *310* (7–9), 2162–2167.

(107) Wei, W.; Zhang, X.; Cui, J.; Wei, Z. Interaction between Low Molecular Weight Organic Acids and Hydroxyapatite with Different Degrees of Crystallinity. *Physicochem. Eng. Asp.* **2011**, *392*, 67–75.

(108) Wang, Y. J.; Chen, J. H.; Cui, Y. X.; Wang, S. Q.; Zhou, D. M. Effects of Low-Molecular-Weight Organic Acids on Cu(II) Adsorption onto Hydroxyapatite Nanoparticles. *J. Hazard. Mater.* **2009**, *162* (2–3), 1135–1140.

(109) Zhang, G.; Shen, Z.; Liu, M.; Guo, C.; Sun, P.; Yuan, Z.; Li, B.; Ding, D.; Chen, T. Synthesis and Characterization of Mesoporous Ceria with Hierarchical Nanoarchitecture Controlled by Amino Acids. *J. Phys. Chem. B.* **2006**, *110* (51), 25782-25790.

(110) Wang, A.; Yin, H.; Liu, D.; Wu, H.; Wada, Y.; Ren, M.; Xu, Y.; Jiang, T.; Cheng, X. Effects of Organic Modifiers on the Size-Controlled Synthesis of Hydroxyapatite Nanorods. *Appl. Surf. Sci.* **2007**, *253* (6), 3311–3316.

(111) Huang, Y. T.; Imura, M.; Nemoto, Y.; Cheng, C. H.; Yamauchi, Y. Block-Copolymer-Assisted Synthesis of Hydroxyapatite Nanoparticles with High Surface Area and Uniform Size. *Sci. Technol. Adv. Mater.* **2011**, *12* (4), 045005.

(112) Yan, L.; Li, Y.; Deng, Z.-X.; Zhuang, J.; Sun, X. Surfactant-Assisted Hydrothermal Synthesis of Hydroxyapatite Nanorods. *Int. J. Inorg. Mater.* **2001**, *3* (7), 633–637.

(113) Shiba, K.; Motozuka, S.; Yamaguchi, T.; Ogawa, N.; Otsuka, Y.; Ohnuma, K.; Kataoka, T.; Tagaya, M. Effect of Cationic Surfactant Micelles on Hydroxyapatite Nanocrystal Formation: An Investigation into the Inorganic−Organic Interfacial Interactions. *Cryst. Growth Des.* **2016**, *16* (3), 1463–1471.

(114) Xie, Y.; Li, K.; Zheng, X. Biological Coatings for Implant Surface Modification; **2017**; pp 183–228.

(115) Heimann, R. B. Structure, Properties, and Biomedical Performance of Osteoconductive Bioceramic Coatings. *Surf. Coatings Technol.* **2013**, *233*, 27–38.

(116) Sha, L.-K.; Chappell, B. W. Apatite Chemical Composition, Determined by Electron Microprobe and Laser-Ablation Inductively Coupled Plasma Mass Spectrometry, as a Probe into Granite Petrogenesis. *Geochim. Cosmochim. Acta.* **1999**, *63* (22), 3861–3881.

(117) Calasans-Maia, M. D.; Melo, B. R. De; Alves, A. T. N.; Resende, R. F. De B.; Louro, R. S.; Sartoretto, S. C.; Granjeiro, J. M.; Alves, G. G.; Calasans-Maia, M. D.; Melo, B. R. de. Cytocompatibility and Biocompatibility of Nanostructured Carbonated Hydroxyapatite Spheres for Bone Repair. *J. Appl. Oral Sci.* **2015**, *23* (6), 599–608.

(118) Miyaji, F.; Kono, Y.; Suyama, Y. Formation and Structure of Zinc-Substituted Calcium Hydroxyapatite. *Mater. Res. Bull.* **2005**, 40 (2), 209–220.

(119) Kumar, G. S.; Thamizhavel, A.; Yokogawa, Y.; Kalkura, S. N.; Girija, E. K. Synthesis, Characterization and in Vitro Studies of Zinc and Carbonate Co-Substituted Nano-Hydroxyapatite for Biomedical Applications. *Mater. Chem. Phys.* **2012**, *134* (2–3), 1127–1135.

(120) Hu, W.; Ma, J.; Wang, J.; Zhang, S. Fine Structure Study on Low Concentration Zinc Substituted Hydroxyapatite Nanoparticles. *Mater. Sci. Eng. C.* **2012**, *32* (8), 2404–2410.

(121) Friederichs, R. J.; Chappell, H. F.; Shepherd, D. V.; Best, S. M. Synthesis, Characterization and Modelling of Zinc and Silicate Co-Substituted Hydroxyapatite. *J. R. Soc. Interface.* **2015**, *12* (108), 20150190.

(122) Matsunaga, K.; Murata, H.; Mizoguchi, T.; Nakahira, A. Mechanism of Incorporation of Zinc into Hydroxyapatite. *Acta Biomater.* **2010**, *6* (6), 2289–2293.

(123) Tang, Y.; Chappell, H. F.; Dove, M. T.; Reeder, R. J.; Lee, Y. J. Zinc Incorporation into Hydroxylapatite. *Biomaterials* **2009**, *30* (15), 2864–2872.

(124) Matsunaga, K. First-Principles Study of Substitutional Magnesium and Zinc in Hydroxyapatite and Octacalcium Phosphate. *J. Chem. Phys.* **2008**, *128* (24), 245101.

(125) Bianco, A.; Cacciotti, I.; Lombardi, M.; Montanaro, L.; Bemporad, E.; Sebastiani, M. F-Substituted Hydroxyapatite Nanopowders: Thermal Stability, Sintering Behaviour and Mechanical Properties. *Ceram. Int.* **2010**, *36* (1), 313–322.

(126) Dorozhkin, S. V. Calcium Orthophosphates. *J. Mater. Sci.* **2007**, *42* (4), 1061–1095.

(127) Barralet, J.; Best, S.; Bonfield, W. Carbonate Substitution in Precipitated Hydroxyapatite: An Investigation into the Effects of Reaction Temperature and Bicarbonate Ion Concentration. *J. Biomed. Mater. Res.* **1998**, *41* (1), 79–86.

(128) LeGeros, R. Z.; Trautz, O. R.; Klein, E.; LeGeros, J. P. Two Types of Carbonate Substitution in the Apatite Structure. *Experientia* **1969**, *25* (1), 5–7.

(129) Boanini, E.; Gazzano, M.; Bigi, A. Ionic Substitutions in Calcium Phosphates Synthesized at Low Temperature. *Acta Biomater.* **2010**, *6* (6), 1882–1894.

(130) Chevalier, J.; Gremillard, L. Ceramics for Medical Applications: A Picture for the next 20 Years. *J. Eur. Ceram. Soc.* **2009**, *29* (7), 1245–1255.

(131) Rusu, V. M.; Ng, C.-H.; Wilke, M.; Tiersch, B.; Fratzl, P.; Peter, M. G. Size-Controlled Hydroxyapatite Nanoparticles as Self-Organized Organic–Inorganic Composite Materials. *Biomaterials* **2005**, *26* (26), 5414–5426.

(132) Ghomi, H.; Fathi, M. H.; Edris, H. Preparation of Nanostructure Hydroxyapatite Scaffold for Tissue Engineering Applications. *J. Sol-Gel Sci. Technol.* **2011**, *58* (3), 642–650.

(133) Carter, C. B.; Norton, M. G. Ceramics in Biology and Medicine. In *Ceramic Materials*; Springer New York: New York, NY, **2013**; pp 659–676.

(134) Dorozhkin, S. V. Bioceramics of Calcium Orthophosphates. *Biomaterials* **2010**, *31* (7), 1465–1485.

(135) Giannoudis, P. V.; Dinopoulos, H.; Tsiridis, E. Bone Substitutes: An Update. *Injury* **2005**, *36* (3), S20–S27.
(136) Dorozhkin, S. Calcium Orthophosphate-Based Bioceramics. *Materials (Basel).* **2013**, *6* (9), 3840–3942.
(137) Kolmas, J.; Groszyk, E.; Kwiatkowska-Róhycka, D. Substituted Hydroxyapatites with Antibacterial Properties. *Particul. Sci. Technol.* **2014**, *35* (1), 29–37
(138) Dorozhkin, S. V. Calcium Orthophosphate Deposits: Preparation, Properties and Biomedical Applications. *Mater. Sci. Eng. C* **2015**, *55*, 272–326.
(139) Parent, M.; Baradari, H.; Champion, E.; Damia, C.; Viana-Trecant, M. Design of Calcium Phosphate Ceramics for Drug Delivery Applications in Bone Diseases: A Review of the Parameters Affecting the Loading and Release of the Therapeutic Substance. *J. Control. Release* **2017**, *252*, 1–17.
(140) Vallet-Regí, M.; Navarrete, D. A. A. *Nanoceramics in Clinical Use : From Materials to Applications*. Royal Society of Chemistry (Great Britain) **2015**.
(141) Okada, M.; Matsumoto, T. Synthesis and Modification of Apatite Nanoparticles for Use in Dental and Medical Applications. *Jpn. Dent. Sci. Rev.* **2015**, *51* (4), 85–95.
(142) Tagaya, M.; Ikoma, T.; Hanagata, N.; Chakarov, D.; Kasemo, B.; Tanaka, J. Reusable Hydroxyapatite Nanocrystal Sensors for Protein Adsorption. *Sci. Technol. Adv. Mater.* **2010**, *11* (4), 045002.
(143) Dorozhkin, S. V. Nanosized and Nanocrystalline Calcium Orthophosphates. *Acta Biomater.* **2010**, *6* (3), 715–734.
(144) Ridi, F.; Meazzini, I.; Castroflorio, B.; Bonini, M.; Berti, D.; Baglioni, P. Functional Calcium Phosphate Composites in Nanomedicine. *Adv. Colloid Interface Sci.* **2017**, *244*, 281–295.
(145) Shepherd, J. H.; Friederichs, R. J.; Best, S. M. Synthetic Hydroxyapatite for Tissue Engineering Applications. *Hydroxyapatite Biomed. Appl.* **2015**, 235–267.
(146) Karageorgiou, V.; Kaplan, D. Porosity of 3D Biomaterial Scaffolds and Osteogenesis. *Biomaterials* **2005**, *26* (27), 5474–5491.
(147) Wang, W.; Yeung, K. W. K. Bone Grafts and Biomaterials Substitutes for Bone Defect Repair: A Review. *Bioact. Mater.* **2017**, *2* (4), 224–247.
(148) Champion, E. Sintering of Calcium Phosphate Bioceramics. *Acta Biomater.* **2013**, *9* (4), 5855–5875.
(149) Dorozhkin, S. V. Multiphasic Calcium Orthophosphate (CaPO4) Bioceramics and Their Biomedical Applications. *Ceram. Int.* **2016**, *42* (6), 6529–6554.
(150) Tran, N.; Webster, T. J. Nanotechnology for Bone Materials. *Wiley Interdiscip. Rev. Nanomedicine Nanobiotechnology* **2009**, *1* (3), 336–351.
(151) Engel, E.; Michiardi, A.; Navarro, M.; Lacroix, D.; Planell, J. A. Nanotechnology in Regenerative Medicine: The Materials Side. *Trends Biotechnol.* **2008**, *26* (1), 39–47.
(152) Bettinger, C. J.; Langer, R.; Borenstein, J. T. Engineering Substrate Topography at the Micro- and Nanoscale to Control Cell Function. *Angew. Chemie Int. Ed.* **2009**, *48* (30), 5406–5415.
(153) Meena, R.; Kesari, K. K.; Rani, M.; Paulraj, R. Effects of Hydroxyapatite Nanoparticles on Proliferation and Apoptosis of Human Breast Cancer Cells (MCF-7). *J. Nanoparticle Res.* **2012**, *14* (2), 712.
(154) Deshmukh, K.; Shaik, M. M.; Ramanan, S. R.; Kowshik, M. Self-Activated Fluorescent Hydroxyapatite Nanoparticles: A Promising Agent for Bioimaging and

Biolabeling. *ACS Biomater. Sci. Eng.* **2016**, *2* (8), 1257–1264.
(155) Perez, R. A.; Seo, S. J.; Won, J. E.; Lee, E. J.; Jang, J. H.; Knowles, J. C.; Kim, H. W. Therapeutically Relevant Aspects in Bone Repair and Regeneration. *Mater. Today* **2015**, *18* (10), 573–589.
(156) Neacsu, I. A.; Stoica, A. E.; Vasile, B. S.; Andronescu, E. Luminescent Hydroxyapatite Doped with Rare Earth Elements for Biomedical Applications. *Nanomaterials.* **2019**. *9* (2), 239.
(157) Rosticher, C.; Viana, B.; Maldiney, T.; Richard, C.; Chanéac, C. Persistent Luminescence of Eu, Mn, Dy Doped Calcium Phosphates for in-Vivo Optical Imaging. *J. Lumin.* **2016**, *170*, 460–466.
(158) Takeuchi, A.; Ohtsuki, C.; Miyazaki, T.; Kamitakahara, M.; Ogata, S. I.; Yamazaki, M.; Furutani, Y.; Kinoshita, H.; Tanihara, M. Heterogeneous Nucleation of Hydroxyapatite on Protein: Structural Effect of Silk Sericin. *J. Royal Soc. Interface*. **2005** *2* (4), 373–378.
(159) Zhang, C.; Yang, J.; Quan, Z.; Yang, P.; Li, C.; Hou, Z.; Lin, J. Hydroxyapatite Nano-and Microcrystals with Multiform Morphologies: Controllable Synthesis and Luminescence Properties. *Cryst. Growth Des*. **2009**, *9* (6), 2725–2733.
(160) Begam, H.; Kundu, B.; Chanda, A.; Nandi, S. K. MG63 Osteoblast Cell Response on Zn Doped Hydroxyapatite (HAp) with Various Surface Features. *Ceram. Int.* **2017**, *43* (4), 3752–3760.
(161) Ghorbani, F. M.; Kaffashi, B.; Shokrollahi, P.; Seyedjafari, E.; Ardeshirylajimi, A. PCL/Chitosan/Zn-Doped NHA Electrospun Nanocomposite Scaffold Promotes Adipose Derived Stem Cells Adhesion and Proliferation. *Carbohydr. Polym.* **2015**, *118*, 133–142.
(162) Xue, W.; Hosick, H. L.; Bandyopadhyay, A.; Bose, S.; Ding, C.; Luk, K. D. K.; Cheung, K. M. C.; Lu, W. W. Preparation and Cell-Materials Interactions of Plasma Sprayed Strontium-Containing Hydroxyapatite Coating. *Surf. Coat. Tech.* **2007,** *201* (8), 4685–4693.
(163) Rosa, A. L.; Beloti, M. M.; Oliveira, P. T.; Van Noort, R. Osseointegration and Osseoconductivity of Hydroxyapatite of Different Microporosities. *J. Mater. Sci. Mater. Med.* **2002**, *13* (11), 1071–1075.
(164) Joos, U.; Wiesmann, H. P.; Szuwart, T.; Meyer, U. Mineralization at the Interface of Implants. *Int. J. Oral Maxillofac. Surg.* **2006**, *35* (9), 783–790.
(165) Habibovic, P.; Sees, T. M.; van den Doel, M. A.; van Blitterswijk, C. A.; de Groot, K. Osteoinduction by Biomaterials—Physicochemical and Structural Influences. *J. Biomed. Mater. Res. Part A* **2006**, *77A* (4), 747–762.
(166) Zhang, K.; Fan, Y.; Dunne, N.; Li, X. Effect of Microporosity on Scaffolds for Bone Tissue Engineering. *Regenerative biomaterials* **2018**, *5* (2), 115–124.
(167) Zhou, H.; Lee, J. Nanoscale Hydroxyapatite Particles for Bone Tissue Engineering. *Acta Biomater.* **2011**, *7* (7), 2769–2781.
(168) Dorozhkin, S. V. Calcium Orthophosphates as Bioceramics: State of the Art. *J. Funct. Biomater.* **2010**, *1* (1), 22–107.
(169) Leng, Y.; Chen, J.; Qu, S. TEM Study of Calcium Phosphate Precipitation on HA/TCP Ceramics. *Biomaterials* **2003**, *24* (13), 2125–2131.
(170) Bose, S.; Saha, S. K. Synthesis and Characterization of Hydroxyapatite Nanopowders by Emulsion Technique. *Chem. Mater.* **2003**, *15* (23), 4464–4469.

(171) Bose, S.; Tarafder, S. Calcium Phosphate Ceramic Systems in Growth Factor and Drug Delivery for Bone Tissue Engineering: A Review. *Acta Biomater.* **2012**, *8* (4), 1401–1421.
(172) Nair, L. S.; Laurencin, C. T. Biodegradable Polymers as Biomaterials. *Prog. Polym. Sci.* **2007**, *32* (8–9), 762–798.
(173) Griffith, L. G. Polymeric Biomaterials. *Acta Mater.* **2000**, *48* (1), 263–277.
(174) Hoffman, A. S. Surface Modification of Polymers: Physical, Chemical, Mechanical and Biological Methods. *Macromol. Symp.* **1996**, *101* (1), 443–454.
(175) Goddard, J. M.; Hotchkiss, J. H. Polymer Surface Modification for the Attachment of Bioactive Compounds. *Prog. Polym. Sci.* **2007**, *32* (7), 698–725.
(176) Ulery, B. D.; Nair, L. S.; Laurencin, C. T. Biomedical Applications of Biodegradable Polymers. *J. Polym. Sci. Part B Polym. Phys.* **2011**, *49* (12), 832–864.
(177) Middleton, J. C.; Tipton, A. J. Synthetic Biodegradable Polymers as Orthopedic Devices. *Biomaterials* **2000**, *21* (23), 2335–2346.
(178) Lasprilla, A. J. R.; Martinez, G. A. R.; Lunelli, B. H.; Jardini, A. L.; Filho, R. M. Poly-Lactic Acid Synthesis for Application in Biomedical Devices — A Review. *Biotechnol. Adv.* **2012**, *30* (1), 321–328.
(179) Lu, Y.; Chen, S. C. Micro and Nano-Fabrication of Biodegradable Polymers for Drug Delivery. *Adv. Drug Deliv. Rev.* **2004**, *56* (11), 1621–1633.
(180) Soppimath, K. S.; Aminabhavi, T. M.; Kulkarni, A. R.; Rudzinski, W. E. Biodegradable Polymeric Nanoparticles as Drug Delivery Devices. *J. Control. Release* **2001**, *70* (1–2), 1–20.
(181) Uhrich, K. E.; Cannizzaro, S. M.; Langer, R. S.; Shakesheff, K. M. Polymeric Systems for Controlled Drug Release. *Chem. Rev.* **1999**, *99* (11), 3181–3198.
(182) Bajpai, A. K.; Shukla, S. K.; Bhanu, S.; Kankane, S. Responsive Polymers in Controlled Drug Delivery. *Prog. Polym. Sci.* **2008**, *33* (11), 1088–1118.
(183) Dhandayuthapani, B.; Yoshida, Y.; Maekawa, T.; Sakthi Kumar, D. Polymeric Scaffolds in Tissue Engineering Application: A Review. *Int. J. Polym. Sci.* **2011**, *2011*.
(184) O'Brien, F. J. Biomaterials & Scaffolds for Tissue Engineering. *Mater. Today* **2011**, *14* (3), 88–95.
(185) Daniels, A. U.; Chang, M. K. O.; Andriano, K. P.; Heller, J. Mechanical Properties of Biodegradable Polymers and Composites Proposed for Internal Fixation of Bone. *J. Appl. Biomater.* **1990**, *1* (1), 57–78.
(186) Hofmann, G. O. Biodegradable Implants in Traumatology: A Review on the State-of-the-Art. *Arch. Orthop. Trauma Surg.* **1995**, *114* (3), 123–132.
(187) Seal, B.; Otero, T.; Panitch, A. Polymeric Biomaterials for Tissue and Organ Regeneration. *Mater. Sci. Eng. R Reports.* **2001**, *34* (4–5), 147–230.
(188) Zhang, L.; Webster, T. J. Nanotechnology and Nanomaterials: Promises for Improved Tissue Regeneration. *Nano Today* **2009**, *4* (1), 66–80.
(189) Kingshott, P.; Andersson, G.; McArthur, S. L.; Griesser, H. J. Surface Modification and Chemical Surface Analysis of Biomaterials. *Curr. Opin. Chem. Biol.* **2011**, *15* (5), 667–676.
(190) Ratner, B. D. Surface Modification of Polymers: Chemical, Biological and Surface Analytical Challenges. *Biosens. Bioelectron.* **1995**, *10* (9–10), 797–804.
(191) Neděla, O.; Slepička, P.; Švorčík, V. Surface Modification of Polymer Substrates for

Biomedical Applications. *Materials (Basel).* **2017**, *10* (10), 1115.
(192) Song, R.; Hu, X.; Guan, P.; Li, J.; Du, C.; Qian, L.; Wang, C. Surface Modification of Imprinted Polymer Microspheres with Ultrathin Hydrophilic Shells to Improve Selective Recognition of Glutathione in Aqueous Media. *Mater. Sci. Eng. C* **2016**, *60*, 1–6.
(193) Falconnet, D.; Csucs, G.; Michelle Grandin, H.; Textor, M. Surface Engineering Approaches to Micropattern Surfaces for Cell-Based Assays. *Biomaterials* **2006**, *27* (16), 3044–3063.
(194) Ogaki, R.; Alexander, M.; Kingshott, P. Chemical Patterning in Biointerface Science. *Mater. Today* **2010**, *13* (4), 22–35.
(195) Chan, C. M.; Ko, T. M.; Hiraoka, H. Polymer Surface Modification by Plasmas and Photons. *Surf. Sci. Rep.* **1996**, *24* (1–2), 1–54.
(196) Chu, P. .; Chen, J. .; Wang, L. .; Huang, N. Plasma-Surface Modification of Biomaterials. *Mater. Sci. Eng. R Reports* **2002**, *36* (5–6), 143–206.
(197) Oehr, C. Plasma Surface Modification of Polymers for Biomedical Use. *Nucl. Instruments Methods Phys. Res. Sect. B Beam Interact. with Mater. Atoms* **2003**, *208*, 40–47.
(198) Liston, E. M.; Martinu, L.; Wertheimer, M. R. Plasma Surface Modification of Polymers for Improved Adhesion: A Critical Review. *J Adhes Sci Technol.* **1993**, *7* (10), 1091–1127.
(199) Wei, Q. F.; Gao, W. D.; Hou, D. Y.; Wang, X. Q. Surface Modification of Polymer Nanofibres by Plasma Treatment. *Appl. Surf. Sci.* **2005**, *245* (1–4), 16–20.
(200) Dong, H.; Bell, T. State-of-the-Art Overview: Ion Beam Surface Modification of Polymers towards Improving Tribological Properties. *Surf. Coatings Technol.* **1999**, *111* (1), 29–40.
(201) Tagaya, M.; Nakagawa, M. Incorporation of Decanethiol-Passivated Gold Nanoparticles into Cross-Linked Poly(Dimethylsiloxane) Films. *Smart Mater. Res.* **2011**, *2011*.
(202) Armentano, I.; Dottori, M.; Fortunati, E.; Mattioli, S.; Kenny, J. M. Biodegradable Polymer Matrix Nanocomposites for Tissue Engineering: A Review. *Polym. Degrad. Stab.* **2010**, *95* (11), 2126–2146.
(203) Minati, L.; Migliaresi, C.; Lunelli, L.; Viero, G.; Dalla Serra, M.; Speranza, G. Plasma Assisted Surface Treatments of Biomaterials. *Biophys. Chem.* **2017**, *229*, 151–164.
(204) Gupta, B.; Plummer, C.; Bisson, I.; Frey, P.; Hilborn, J. Plasma-Induced Graft Polymerization of Acrylic Acid onto Poly(Ethylene Terephthalate) Films: Characterization and Human Smooth Muscle Cell Growth on Grafted Films. *Biomaterials* **2002**, *23* (3), 863–871.
(205) Lee, S. D.; Hsiue, G. H.; Chang, P. C.-T.; Kao, C. Y. Plasma-Induced Grafted Polymerization of Acrylic Acid and Subsequent Grafting of Collagen onto Polymer Film as Biomaterials. *Biomaterials* **1996**, *17* (16), 1599–1608.
(206) Tian, H.; Tang, Z.; Zhuang, X.; Chen, X.; Jing, X. Biodegradable Synthetic Polymers: Preparation, Functionalization and Biomedical Application. *Prog. Polym. Sci.* **2012**, *37* (2), 237–280.
(207) Cen, L.; Neoh, K. G.; Kang, E. T. Surface Functionalization Technique for Conferring Antibacterial Properties to Polymeric and Cellulosic Surfaces. *Langmuir*,

2003, *19* (24), 10295–10303.
(208) Meyer-Plath, A.; Schröder, K.; Finke, B.; Ohl, A. Current Trends in Biomaterial Surface Functionalization—Nitrogen-Containing Plasma Assisted Processes with Enhanced Selectivity. *Vacuum* **2003**, *71* (3), 391–406.
(209) Bazaka, K.; Jacob, M. V.; Crawford, R. J.; Ivanova, E. P. Plasma-Assisted Surface Modification of Organic Biopolymers to Prevent Bacterial Attachment. *Acta Biomater.* **2011**, *7* (5), 2015–2028.
(210) Yoshida, S.; Hagiwara, K.; Hasebe, T.; Hotta, A. Surface Modification of Polymers by Plasma Treatments for the Enhancement of Biocompatibility and Controlled Drug Release. *Surf. Coatings Technol.* **2013**, *233*, 99–107.
(211) Pham, Q. P.; Sharma, U.; Mikos, A. G. Electrospinning of Polymeric Nanofibers for Tissue Engineering Applications: A Review. *Tissue Eng.* **2006**, *12* (5), 1197–1211.
(212) Cheruthazhekatt, S.; Černák, M.; Slavíček, P.; Havel, J. Gas Plasmas and Plasma Modified Materials in Medicine. *J. Appl. Biomed.* **2010**, *8* (2), 55–66.
(213) Petlin, D. G.; Tverdokhlebov, S. I.; Anissimov, Y. G. Plasma Treatment as an Efficient Tool for Controlled Drug Release from Polymeric Materials: A Review. *J. Control. Release* **2017**, *266*, 57–74.
(214) Bitar, R.; Cools, P.; De Geyter, N.; Morent, R. Acrylic Acid Plasma Polymerization for Biomedical Use. *Appl. Surf. Sci.* **2018**, *448*, 168–185.
(215) Bacakova, L.; Filova, E.; Parizek, M.; Ruml, T.; Svorcik, V. Modulation of Cell Adhesion, Proliferation and Differentiation on Materials Designed for Body Implants. *Biotechnol. Adv.* **2011**, *29* (6), 739–767.
(216) Morita, S.; Takasu, A. Adhesion Control of Human Umbilical Vein Endothelial Cells Using Clickable Poly(2-Oxazoline)-Grafted Biosynthesized Extracellular Matrix Protein. *Polymer (Guildf).* **2018**, *136*, 194–204..
(217) Le, P. N.; Huynh, C. K.; Tran, N. Q. Advances in Thermosensitive Polymer-Grafted Platforms for Biomedical Applications. *Mater. Sci. Eng. C* **2018**, *92*, 1016–1030.
(218) Choi, H. S.; Kim, Y. S.; Zhang, Y.; Tang, S.; Myung, S. W.; Shin, B.-C. Plasma-Induced Graft Co-Polymerization of Acrylic Acid onto the Polyurethane Surface. *Surf. Coatings Technol.* **2004**, *182* (1), 55–64.
(219) Hsu, S. H. S.; Chen, W. C. Improved Cell Adhesion by Plasma-Induced Grafting of l-Lactide onto Polyurethane Surface. *Biomaterials* **2000**, *21* (4), 359–367.
(220) Xie, X. L.; Mai, Y.-W.; Zhou, X.-P. Dispersion and Alignment of Carbon Nanotubes in Polymer Matrix: A Review. *Mater. Sci. Eng. R Reports* **2005**, *49* (4), 89–112.
(221) Ahmed, M. H.; Byrne, J. A.; McLaughlin, J. Evaluation of Glycine Adsorption on Diamond like Carbon (DLC) and Fluorinated DLC Deposited by Plasma-Enhanced Chemical Vapour Deposition (PECVD). *Surf. Coatings Technol.* **2012**, *209*, 8–14.
(222) Xiao, Z. Y.; Liu, Y. C.; Zhao, D. X.; Zhang, J. Y.; Lu, Y. M.; Shen, D. Z.; Fan, X. W. Optical Property of Hexagonal Nanocrystalline Zno Film on Si Substrate Prepared by Plasma-Enhanced CVD. *J. Lumin.* **2007**, *122*, 822–824.
(223) Shearer, J. C.; Fisher, M. J.; Hoogeland, D.; Fisher, E. R. Composite SiO_2/TiO_2 and Amine Polymer/TiO2 Nanoparticles Produced Using Plasma-Enhanced Chemical Vapor Deposition. *Appl. Surf. Sci.* **2010**, *256* (7), 2081–2091.
(224) Grüniger, A.; Bieder, A.; Sonnenfeld, A.; von Rohr, P. R.; Müller, U.; Hauert, R. Influence of Film Structure and Composition on Diffusion Barrier Performance of SiOx Thin Films Deposited by PECVD. *Surf. Coatings Technol.* **2006**, *200* (14–15),

4564–4571.
(225) Nagashima, S.; Hasebe, T.; Tsuya, D.; Horikoshi, T.; Ochiai, M.; Tanigawa, S.; Koide, Y.; Hotta, A.; Suzuki, T. Controlled Formation of Wrinkled Diamond-like Carbon (DLC) Film on Grooved Poly(Dimethylsiloxane) Substrate. *Diam. Relat. Mater.* **2012**, *22*, 48–51.
(226) Vasudev, M. C.; Anderson, K. D.; Bunning, T. J.; Tsukruk, V. V.; Naik, R. R. Exploration of Plasma-Enhanced Chemical Vapor Deposition as a Method for Thin-Film Fabrication with Biological Applications. *ACS Appl. Mater. Interfaces*. **2013**, *5* (10), 3983–3994.
(227) Martinu, L.; Zabeida, O.; Klemberg-Sapieha, J. E. Plasma-Enhanced Chemical Vapor Deposition of Functional Coatings. *Handb. Depos. Technol. Film. Coatings* **2010**, 392–465.
(228) Allen, M.; Myer, B.; Rushton, N. In Vitro Andin Vivo Investigations into the Biocompatibility of Diamond-like Carbon (DLC) Coatings for Orthopedic Applications. *J. Biomed. Mater. Res.* **2001**, *58* (3), 319–328.
(229) Roseti, L.; Parisi, V.; Petretta, M.; Cavallo, C.; Desando, G.; Bartolotti, I.; Grigolo, B. Scaffolds for Bone Tissue Engineering: State of the Art and New Perspectives. *Mater. Sci. Eng. C.* **2017**, *78*, 1246–1262.
(230) Chiara, G.; Letizia, F.; Lorenzo, F.; Edoardo, S.; Diego, S.; Stefano, S.; Eriberto, B.; Barbara, Z. Nanostructured Biomaterials for Tissue Engineered Bone Tissue Reconstruction. *Int. J. Mol. Sci.* **2012**, *13* (1), 737–757.
(231) Venkatesan, J.; Bhatnagar, I.; Manivasagan, P.; Kang, K.-H.; Kim, S.-K. Alginate Composites for Bone Tissue Engineering: A Review. *Int. J. Biol. Macromol.* **2015**, *72*, 269–281.
(232) Swetha, M.; Sahithi, K.; Moorthi, A.; Srinivasan, N.; Ramasamy, K.; Selvamurugan, N. Biocomposites Containing Natural Polymers and Hydroxyapatite for Bone Tissue Engineering. *Int. J. Biol. Macromol.* **2010**, *47* (1), 1–4.
(233) Jones, M. A.; Oh, S.; Oh, N.; Appleford, M.; Ong, J. L. Bioceramics for Tissue Engineering Applications-A Review. *Am. J. Biochem. Biotechnol.* **2006**, *2* (2), 49–56.
(234) Cordero-Arias, L.; Boccaccini, A. R. Electrophoretic Deposition of Chondroitin Sulfate-Chitosan/Bioactive Glass Composite Coatings with Multilayer Design. *Surf. Coatings Technol.* **2017**, *315*, 417–425.
(235) Zangari, G. Electrodeposition of Alloys and Compounds in the Era of Microelectronics and Energy Conversion Technology. *Coatings* **2015**, *5* (2), 195–218.
(236) Corni, I.; Ryan, M. P.; Boccaccini, A. R. Electrophoretic Deposition: From Traditional Ceramics to Nanotechnology. *J. Eur. Ceram. Soc.* **2008**, *28* (7), 1353–1367.
(237) Besra, L.; Liu, M. A Review on Fundamentals and Applications of Electrophoretic Deposition (EPD). *Prog. Mater. Sci.* **2007**, *52* (1), 1–61.
(238) Baştan, F. E.; Atiq Ur Rehman, M.; Avcu, Y. Y.; Avcu, E.; Üstel, F.; Boccaccini, A. R. Electrophoretic Co-Deposition of PEEK-Hydroxyapatite Composite Coatings for Biomedical Applications. *Colloids Surfaces B Biointerfaces* **2018**, *169*, 176–182.
(239) Farrokhi-Rad, M.; Shahrabi, T.; Mahmoodi, S.; Khanmohammadi, S. Electrophoretic Deposition of Hydroxyapatite-Chitosan-CNTs Nanocomposite Coatings. *Ceram. Int.*

2017, *43* (5), 4663–4669.
(240) Farrokhi-Rad, M. Electrophoretic Deposition of Fiber Hydroxyapatite/Titania Nanocomposite Coatings. *Ceram. Int.* **2018**, *44* (1), 622–630.
(241) Ikoma, T.; Tagaya, M.; Hanagata, N.; Yoshioka, T.; Chakarov, D.; Kasemo, B.; Tanaka, J. Protein Adsorption on Hydroxyapatite Nanosensors with Different Crystal Sizes Studied *In Situ* by a Quartz Crystal Microbalance with the Dissipation Method. *J. Am. Ceram. Soc.* **2009**, *92* (5), 1125–1128.
(242) Farrokhi-Rad, M. Electrophoretic Deposition of Hydroxyapatite Fiber Reinforced Hydroxyapatite Matrix Nanocomposite Coatings. *Surf. Coatings Technol.* **2017**, *329*, 155–162.
(243) Pang, X.; Zhitomirsky, I. Electrodeposition of Nanocomposite Organic–Inorganic Coatings For Biomedical Applications. *Int. J. Nanosci.* **2005**, *04* (03), 409–418.
(244) Pang, X.; Zhitomirsky, I. Electrophoretic Deposition of Composite Hydroxyapatite-Chitosan Coatings. *Mater. Charact.* **2007**, *58* (4), 339–348.
(245) Zhitomirsky, D.; Roether, J. A.; Boccaccini, A. R.; Zhitomirsky, I. Electrophoretic Deposition of Bioactive Glass/Polymer Composite Coatings with and without HA Nanoparticle Inclusions for Biomedical Applications. *J. Mater. Process. Technol.* **2009**, *209* (4), 1853–1860.
(246) Đošić, M.; Eraković, S.; Janković, A.; Vukašinović-Sekulić, M.; Matić, I. Z.; Stojanović, J.; Rhee, K. Y.; Mišković-Stanković, V.; Park, S.-J. In Vitro Investigation of Electrophoretically Deposited Bioactive Hydroxyapatite/Chitosan Coatings Reinforced by Graphene. *J. Ind. Eng. Chem.* **2017**, *47*, 336–347.
(247) Peñaflor-Galindo, T. G.; Kataoka, T.; Fujii, S.; Okuda, M.; Tagaya, M. Preparation of Nanocrystalline Zinc-Substituted Hydroxyapatite Films and Their Biological Properties. *Colloid Interface Sci. Commun.* **2016**, *10* (11), 15–19.
(248) Banfield, J. F.; Welch, S. A.; Zhang, H.; Ebert, T. T.; Penn, R. L. Aggregation-Based Crystal Growth and Microstructure Development in Natural Iron Oxyhydroxide Biomineralization Products. *Science (80).* **2000**, *289* (5480), 751–754.
(249) Morin, C.; Hellmich, C. Mineralization-driven Bone Tissue Evolution Follows from Fluid-to-Solid Phase Transformations in Closed Thermodynamic Systems. *J. Theor. Biol.* **2013**, *335*, 185–197.
(250) Anderson, H. C. Mechanism of Mineral Formation in Bone. *Lab. Invest.* **1989**, *60* (3), 320–330.
(251) Onuma, K.; Ito, A. Cluster Growth Model for Hydroxyapatite. *Chem. Mater.* **1998**. *10* (11), 3346–3351
(252) Treboux, G.; Layrolle, P.; Kanzaki, N.; Onuma, K.; Ito, A. Symmetry of Posner's Cluster. *J. Am. Chem. Soc.* **2000**, *122* (34), 8323–8324.
(253) Gabin Treboux,; Pierre Layrolle; Noriko Kanzaki; Kazuo Onuma, and; Ito, A. Existence of Posner's Cluster in Vacuum. *J. Phys. Chem. A.* **2000**, *104* (21), 5111–5114.
(254) Shih, Y. V.; Varghese, S. Tissue Engineered Bone Mimetics to Study Bone Disorders Ex Vivo: Role of Bioinspired Materials. *Biomaterials* **2019**, *198*, 107–121.
(255) Ozawa, H.; Hoshi, K.; Amizuka, N. Current Concepts of Bone Biomineralization. *J. Oral Biosci.* **2008**, *50* (1), 1–14.
(256) Saddiqi, N. H.; Patra, D.; Seeger, S. Hydroxyapatite Biomineralization on Functionalized Silicone Nanofilaments. *Colloid Interface Sci. Commun.* **2017**, *16*, 1–

5.
(257) Song, J.; Malathong, V.; Bertozzi, C. R. Mineralization of Synthetic Polymer Scaffolds: A Bottom-Up Approach for the Development of Artificial Bone. *J. Am. Chem. Soc.* **2005***, 127* (10), 3366–3372.
(258) Ohtsuki, C.; Kamitakahara, M.; Miyazaki, T. Coating Bone-like Apatite onto Organic Substrates Using Solutions Mimicking Body Fluid. *J Tissue Eng Regen Med*. **2007**, *1*(1), 33–38.
(259) Huh, H. W.; Zhao, L.; Kim, S. Y. Biomineralized Biomimetic Organic/Inorganic Hybrid Hydrogels Based on Hyaluronic Acid and Poloxamer. *Carbohydr. Polym.* **2015**, *126*, 130–140.
(260) Mann, S. Molecular Recognition in Biomineralization. *Nature* **1988**, *332* (6160), 119–124.
(261) Mann, S. Molecular Tectonics in Biomineralization and Biomimetic Materials Chemistry. *Nature* **1993**, *365* (6446), 499–505.
(262) Hosoya, K.; Ohtsuki, C.; Kawai, T.; Kamitakahara, M.; Ogata, S.; Miyazaki, T.; Tanihara, M. A Novel Covalently Crosslinked Gel of Alginate and Silane with the Ability to Form Bone-like Apatite. *J. Biomed. Mater. Res.* **2004**, *71A* (4), 596–601.
(263) Miyazaki, T.; Ohtsuki, C.; Tanihara, M. Synthesis of Bioactive Organic–Inorganic Nanohybrid for Bone Repair through Sol–Gel Processing. *J. Nanosci. Nanotechnol.* **2003**, *3* (6), 511–515.
(264) Miyazaki, T.; Ohtsuki, C.; Akioka, Y.; Tanihara, M.; Nakao, J.; Sakaguchi, Y.; Konagaya, S. Apatite Deposition on Polyamide Films Containing Carboxyl Group in a Biomimetic Solution. *J. Mater. Sci. Mater. Med.* **2003**, *14* (7), 569–574.
(265) Kawai, T.; Ohtsuki, C.; Kamitakahara, M.; Tanihara, M.; Miyazaki, T.; Sakaguchi, Y.; Konagaya, S. A Comparative Study of Apatite Deposition on Polyamide Films Containing Different Functional Groups under a Biomimetic Condition. *J. Ceram. Soc. Japan* **2005**, *113* (1321), 588–592.
(266) Stoch, A.; Jastrzębski, W.; Brożek, A.; Stoch, J.; Szaraniec, J.; Trybalska, B.; Kmita, G. FTIR Absorption–Reflection Study of Biomimetic Growth of Phosphates on Titanium Implants. *J. Mol. Struct.* **2000**, *555* (1–3), 375–382.
(267) Chai, Y.; Yamaguchi, T.; Tagaya, M. Fabrication of Phospholipid Vesicle-Interacted Calcium Phosphate Films with Sterilization Stability. **2017**, *17*, 4983.
(268) Tagaya, M.; Ikoma, T.; Takeguchi, M.; Hanagata, N.; Tanaka, J. Interfacial Serum Protein Effect on Biological Apatite Growth. *J. Phys. Chem. C* **2011**, *115* (45), 22523–22533.
(269) Liu, X.; Smith, L. A.; Hu, J.; Ma, P. X. Biomimetic Nanofibrous Gelatin/Apatite Composite Scaffolds for Bone Tissue Engineering. *Biomaterials* **2009**, *30* (12), 2252–2258.
(270) Kim, S.-H.; Lim, B.-K.; Sun, F.; Koh, K.; Ryu, S.-C.; Kim, H.-S.; Lee, J. Preparation of High Flexible Composite Film of Hydroxyapatite and Chitosan. *Polym. Bull.* **2009**, *62* (1), 111–118.
(271) Wu, G. M.; Hsiao, W. D.; Kung, S. F. Investigation of Hydroxyapatite Coated Polyether Ether Ketone Composites by Gas Plasma Sprays. *Surf. Coatings Technol.* **2009**, *203* (17–18), 2755–2758.
(272) Sun, F.; Zhou, H.; Lee, J. Various Preparation Methods of Highly Porous Hydroxyapatite/Polymer Nanoscale Biocomposites for Bone Regeneration. *Acta*

Biomater. **2011**, *7* (11), 3813–3828.
(273) Redepenning, J.; Venkataraman, G.; Chen, J.; Stafford, N. Electrochemical Preparation of Chitosan/Hydroxyapatite Composite Coatings on Titanium Substrates. *J. Biomed. Mater. Res.* **2003**, *66A* (2), 411–416.
(274) Liuyun, J.; Yubao, L.; Chengdong, X. Preparation and Biological Properties of a Novel Composite Scaffold of Nano-Hydroxyapatite/Chitosan/Carboxymethyl Cellulose for Bone Tissue Engineering. *J. Biomed. Sci.* **2009**, *16* (1), 65.
(275) Zhou, W. Y.; Lee, S. H.; Wang, M.; Cheung, W. L.; Ip, W. Y. Selective Laser Sintering of Porous Tissue Engineering Scaffolds from Poly(l-Lactide)/Carbonated Hydroxyapatite Nanocomposite Microspheres. *J. Mater. Sci. Mater. Med.* **2008**, *19* (7), 2535–2540.
(276) Deng, X.; Hao, J.; Wang, C. Preparation and Mechanical Properties of Nanocomposites of Poly(d,l-Lactide) with Ca-Deficient Hydroxyapatite Nanocrystals. *Biomaterials* **2001**, *22* (21), 2867–2873.
(277) Tajbakhsh, S.; Hajiali, F. A Comprehensive Study on the Fabrication and Properties of Biocomposites of Poly(Lactic Acid)/Ceramics for Bone Tissue Engineering. *Mater. Sci. Eng. C.* **2017**, *70*, 897–912.
(278) He, M.; Chang, C.; Peng, N.; Zhang, L. Structure and Properties of Hydroxyapatite/Cellulose Nanocomposite Films. *Carbohydr. Polym.* **2012**, *87* (4), 2512–2518.
(279) Gusić, N.; Ivković, A.; VaFaye, J.; Vukasović, A.; Ivković, J.; Hudetz, D.; Janković, S. Nanobiotechnology and Bone Regeneration: A Mini-Review. *Int. Orthop.* **2014**, *38* (9), 1877–1884.
(280) Salgado, A. J.; Coutinho, O. P.; Reis, R. L. Bone Tissue Engineering: State of the Art and Future Trends. *Macromol. Biosci.* **2004**, *4* (8), 743–765.
(281) Berendsen, A. D.; Olsen, B. R. Bone Development. *Bone* **2015**, *80*, 14–18.
(282) Ma, P. X. Biomimetic Materials for Tissue Engineering. *Adv. Drug Deliv. Rev.* **2008**, *60* (2), 184–198.
(283) Mattioli-Belmonte, M.; Giavaresi, G.; Biagini, G.; Virgili, L.; Giacomini, M.; Fini, M.; Giantomassi, F.; Natali, D.; Torricelli, P.; Giardino, R. Tailoring Biomaterial Compatibility: In Vivo Tissue Response versus in Vitro Cell Behavior. *Int. J. Artif. Organs* **2003**, *26* (12), 1077–1085.
(284) Gao, C.; Peng, S.; Feng, P.; Shuai, C. Bone Biomaterials and Interactions with Stem Cells. *Bone Res.* **2017**, *5* (1), 17059.
(285) Costa-Rodrigues, J.; Fernandes, A.; Lopes, M. A.; Fernandes, M. H. Hydroxyapatite Surface Roughness: Complex Modulation of the Osteoclastogenesis of Human Precursor Cells. *Acta Biomater.* **2012**, *8* (3), 1137–1145.
(286) Murphy, C. M.; O'Brien, F. J.; Little, D. G.; Schindeler, A. Cell-Scaffold Interactions in the Bone Tissue Engineering Triad. *Eur. Cell. Mater.* **2013**, *26*, 120–132.
(287) Cerroni, L.; Filocamo, R.; Fabbri, M.; Piconi, C.; Caropreso, S.; Condò, S. . Growth of Osteoblast-like Cells on Porous Hydroxyapatite Ceramics: An in Vitro Study. *Biomol. Eng.* **2002**, *19* (2–6), 119–124.
(288) Haider, A.; Haider, S.; Han, S. S.; Kang, I.-K. Recent Advances in the Synthesis, Functionalization and Biomedical Applications of Hydroxyapatite: A Review. *RSC Adv.* **2017**, *7* (13), 7442–7458.

(289) Rizzi, S. C.; Heath, D. J.; Coombes, A. G. A.; Bock, N.; Textor, M.; Downes, S. Biodegradable Polymer/Hydroxyapatite Composites: Surface Analysis and Initial Attachment of Human Osteoblasts. *J. Biomed. Mater. Res.* **2001**, *55* (4), 475–486.
(290) Kikuchi, M.; Itoh, S.; Ichinose, S.; Shinomiya, K.; Tanaka, J. Self-Organization Mechanism in a Bone-like Hydroxyapatite/Collagen Nanocomposite Synthesized in Vitro and Its Biological Reaction in Vivo. *Biomaterials* **2001**, *22* (13), 1705–1711.
(291) Tagaya, M.; Yamazaki, T.; Tsuya, D.; Sugimoto, Y.; Hanagata, N.; Ikoma, T. Nano/Microstructural Effect of Hydroxyapatite Nanocrystals on Hepatocyte Cell Aggregation and Adhesion. *Macromol. Biosci.* **2011**, *11* (11), 1586–1593.
(292) Tagaya, M.; Yamazaki, T.; Migita, S.; Hanagata, N.; Ikoma, T. Hepatocyte Adhesion Behavior on Modified Hydroxyapatite Nanocrystals with Quartz Crystal Microbalance. *Bioceram. Dev. Appl.* **2011**, *1*, 1–4.
(293) Guarino, V.; Benfenati, V.; Cruz-Maya, I.; Borrachero-Conejo, A. I.; Zamboni, R.; Ambrosio, L. Bioinspired Scaffolds for Bone and Neural Tissue and Interface Engineering. *Funct. 3D Tissue Eng. Scaffolds* **2018**, 51–74.
(294) Wilson, C. J.; Clegg, R. E.; Leavesley, D. I.; Pearcy, M. J. Mediation of Biomaterial–Cell Interactions by Adsorbed Proteins: A Review. *Tissue Eng.* **2005**, *11* (1–2), 1–18.
(295) Sawyer, A. A.; Hennessy, K. M.; Bellis, S. L. Regulation of Mesenchymal Stem Cell Attachment and Spreading on Hydroxyapatite by RGD Peptides and Adsorbed Serum Proteins. *Biomaterials* **2005**, *26* (13), 1467–1475.
(296) Ngiam, M.; Liao, S.; Patil, A. J.; Cheng, Z.; Chan, C. K.; Ramakrishna, S. The Fabrication of Nano-Hydroxyapatite on PLGA and PLGA/Collagen Nanofibrous Composite Scaffolds and Their Effects in Osteoblastic Behavior for Bone Tissue Engineering. *Bone* **2009**, *45* (1), 4–16.
(297) Zhu, X. D.; Fan, H. S.; Xiao, Y. M.; Li, D. X.; Zhang, H. J.; Luxbacher, T.; Zhang, X. D. Effect of Surface Structure on Protein Adsorption to Biphasic Calcium-Phosphate Ceramics in Vitro and in Vivo. *Acta Biomater.* **2009**, *5* (4), 1311–1318.
(298) Chong, S. H.; Ham, S. Dynamics of Hydration Water Plays a Key Role in Determining the Binding Thermodynamics of Protein Complexes. *Sci. Rep.* **2017**, *7* (1), 1–10.
(299) Papoian, G. A.; Ulander, J.; Wolynes, P. G. Role of Water Mediated Interactions in Protein-Protein Recognition Landscapes. *J. Am. Chem. Soc.* **2003**, *125* (30), 9170–9178.
(300) Huggins, D. J.; Marsh, M.; Payne, M. C. Thermodynamic Properties of Water Molecules at a Protein-Protein Interaction Surface. *J. Chem. Theory Comput.* **2011**, *7* (11), 3514–3522.
(301) Chen, S.; Li, L.; Zhao, C.; Zheng, J. Surface Hydration: Principles and Applications toward Low-Fouling/Nonfouling Biomaterials. *Polymer (Guildf).* **2010**, *51* (23), 5283–5293.
(302) Tanaka, M.; Mochizuki, A. Effect of Water Structure on Blood Compatibility? Thermal Analysis of Water in Poly(Meth)Acrylate. *J. Biomed. Mater. Res.* **2004**, *68A* (4), 684–695.
(303) Tanaka, M.; Hayashi, T.; Morita, S. The Roles of Water Molecules at the Biointerface of Medical Polymers. *Polym. J.* **2013**, *45* (7), 701–710.
(304) Tanaka, M.; Motomura, T.; Ishii, N.; Shimura, K.; Onishi, M.; Mochizuki, A.;

Hatakeyama, T. Cold Crystallization of Water in Hydrated Poly(2-Methoxyethyl Acrylate) (PMEA). *Polym. Int.* **2000**, *49* (12), 1709–1713.

(305) Li, L.; Chen, S.; Zheng, J.; Ratner, B. D.; Jiang, S. Protein Adsorption on Oligo(Ethylene Glycol)-Terminated Alkanethiolate Self-Assembled Monolayers: The Molecular Basis for Nonfouling Behavior. *J. Phys. Chem. B* **2005**, *109* (7), 2934–2941.

(306) Qin, Y.; Wang, L.; Zhong, D. Dynamics and Mechanism of Ultrafast Water–Protein Interactions. *Proc. Natl. Acad. Sci.* **2016**, *113* (30), 8424–8429.

(307) Yamada, S.; Tagaya, M. Analytical Investigation of Hydration and Protein Adsorption Structures on Hydroxyapatite-Based Mesoporous Silica Particles. *Mater. Lett.* **2017**, *209*, 441–445.

(308) Tagaya, M.; Ikoma, T.; Hanagata, N.; Tanaka, J. Analytical Investigation of Protein Mediation Between Biomaterials and Cells. *Mater. Express* **2012**, *2* (1), 1–22.

(309) Haider, A.; Gupta, K.; Kang, I.-K. PLGA/NHA Hybrid Nanofiber Scaffold as a Nanocargo Carrier of Insulin for Accelerating Bone Tissue Regeneration. *Nanoscale Res. Lett.* **2014**, *9* (1), 314.

(310) Deligianni, D. D.; Katsala, N. D.; Koutsoukos, P. G.; Missirlis, Y. F. Effect of Surface Roughness of Hydroxyapatite on Human Bone Marrow Cell Adhesion, Proliferation, Differentiation and Detachment Strength. *Biomaterials* **2000**, *22* (1), 87–96.

(311) Tagaya, M.; Ikoma, T.; Takemura, T.; Hanagata, N.; Okuda, M.; Yoshioka, T.; Tanaka, J. Detection of Interfacial Phenomena with Osteoblast-like Cell Adhesion on Hydroxyapatite and Oxidized Polystyrene by the Quartz Crystal Microbalance with Dissipation. *Langmuir* **2011**, *27* (12), 7635–7644.

(312) Tagaya, M.; Ikoma, T.; Takemura, T.; Migita, S.; Okuda, M.; Yoshioka, T.; Hanagata, N.; Tanaka, J. Initial Adhesion Behavior of Fibroblasts onto Hydroxyapatite Nanocrystals. *Bioceram. Dev. Appl.* **2011**, *1*, 1–4.

(313) Tagaya, M.; Ikoma, T.; Takemura, T.; Hanagata, N.; Yoshioka, T.; Tanaka, J. Effect of Interfacial Proteins on Osteoblast-like Cell Adhesion to Hydroxyapatite Nanocrystals. *Langmuir* **2011**, *27* (12), 7645–7653.

Chapter 2

“Study on Preparation of Elliptical Hydroxyapatite Nanoparticle Films and Their Protein Mediation Ability for Cell Adhesion”

Chapter 2

Study on Preparation of Elliptical Hydroxyapatite Nanoparticle Films and Their Protein Mediation Ability for Cell Adhesion

2.1. Introduction

Hydroxyapatite [($Ca_{10}(PO_4)_6(OH)_2$), HAp] is a non-toxic, bioactive and osteoconductive material, highly valuable for biomedical applications due to its compatibility with the human body as a result of its similarity to the composition of human hard tissues.[1–7] It is well known that the physicochemical properties in biomedical fields mainly depend on the appropriate stoichiometry, shape, morphology and size of the HAp particles. Previous studies have reported that the HAp nanoparticles (NPs) exhibited enhanced resorbability and higher bioactivity as compared with the case of microparticles.[8–10] Therefore, the behavior of the HAp NPs in the body depends on their microstructure and shape. It has been reported that HAp NPs with irregular shape causes inflammatory reactions in soft tissues and the bone formation was slower as compared with the case of the spherical HAp NPs, suggesting that the use of rounded and smooth particles is preferable for filling tissue defects.[11–13] The spherical HAp NPs can contribute to the cell migration and extracellular matrix (ECM) growth through the vacancies that were formed between the particles.[14,15] Another advantage of the spherical particles is that they bear no risk for irritation or damage of mucosal layers of the cells.[16,17] The spherical microsized-HAp particles have been synthetized by a micro-emulsion method with the use of surfactants.[18,19] Among the surfactants, polyethylene glycol, triethanolamine (TEA), ethylenediamine tetra-acetic acid (EDTA), sodium dodecyl sulfate (SDS), sodium dodecylbenzene sulfonate (SDBS), cetyltrimethylammonium bromide (CTAB) and (2-ethylhexyl) sulfosuccinate (AOT) have been the most commonly used.[20] The disadvantage is that this method uses a large amount of oil and surfactant, and these phases cannot be recycled. The spherical microsized-HAp particles were synthesized in water-in-oil micro-emulsions consisting of cyclohexane as the oil phase, and a mixed

poly(oxyethylene) nonyl phenol ether as the surfactant.[21,22] In contrast to the mentioned above method, the aqueous phase is the major phase in the emulsion, which can be formed by a small amount of oil and surfactant phases.[23,24]

When a biomaterial is implanted in the human body, the proteins in the biological solution are adsorbed immediately on the biomaterial surface.[25,26] During the interaction of the biomaterial with the biological environment, the proteins adsorbed on the surfaces determine the cytocompatibility of the biomaterial. The adsorbed proteins play an important role in the cell adhesion, grow and proliferation.[27,28] A quite numbers of studies have clarified the factors involved in the adsorption layer (adlayer) of the proteins on the surface. Several factors such as surface chemistry, charge, domain size, curvature, topography and wettability of the biomaterials affect the protein adsorption. The changes in the underlying chemistry could cause an alteration in the protein adlayer and affect directly the conformation and orientation of the protein, and therefore, the cell adhesion.[29–31]

The cell adhesion is dominantly influenced by the fibrous glycoproteins of ECM, which are fibrinogen (Fgn), collagen, elastin, fibronectin (Fn), laminin, vitronectin (Vtn), thrombospondins, and tenascins.[32,33] Fgn is a major plasma glycoprotein coagulation factor. This structural glycoprotein facilitates adhesion, spreading and aggregation of the cells, which are important properties in the hemostasis process.[34,35] The adsorption amount and state of Fgn on the cytocompatible materials such as HAp NPs and Au NPs are an important parameter for improving the cell adhesion on the biomaterial surfaces.[36,37] Diverse techniques have been used to obtain information on the rate and amount of adsorbed Fgn to determine the surface-bonding interactions and structures. Some useful techniques are the circular dichroism (CD), grazing angle Fourier transform infrared spectroscopy (GA-FT–IR), fluorescence and electron spin resonance with spin labeling, quartz crystal microbalance with dissipation (QCM-D), atomic force microscopy (AFM) and surface plasmon resonance (SPR).[38–42] Although the Fgn adsorption has been studied extensively focusing on the adsorption amount of Fgn, the protein–biomaterial interactions have not been completely understood yet. Thus, the investigation of the interactions between the HAp NPs and the proteins can provide the basis for the biological reactivity.

The interactions between the HAp NPs and the proteins are strongly influenced by the water at the interface (i.e., hydration layer), suggesting that the hydration layer plays an

important role in the determination of the structure, dynamics and bioactivity of the proteins.[43–46] Here, the strength of surface hydration is mainly determined by the physicochemical properties of the HAp NPs. The hydration layer causes a steric repulsion when the proteins approach to the surface for the unfavorable decrease in entropy. In the polymer research field, the interfacial water can be classified into three categories: (a) non–freezing water which plays an important role in the cytocompatibility, (b) intermediate water which prevents that the proteins have a direct contact with the surface, and (c) free water that behave as the bulk.[47,48] The negative- and positive-charged ions of the HAp NPs can bind with the water molecules, and the hydration layer could increase the nonspecific protein adsorption.[49] Although the water–protein interactions are crucial for the protein structural stability, functional dynamics and biological responses,[50] the phenomena at the interface are not fully understood in the bioceramic research field.

In this study, the synthesis of the well-controlled elliptical HAp NPs (E–HAp NPs) in the presence of non-ionic surfactants [poly(oxyethylene) cholesteryl ethers, $ChEO_{15}$] were investigated. The deposition of the synthesized needle–like HAp (N–HAp) and elliptical HAp (E–HAp) NPs on Au substrate surfaces were performed in order to clarify the hydration structures and water–protein–cellular interfacial interactions of the film surfaces. SPR comparative studies for the Fgn adsorption on E–HAp, N–HAp and Au NP films were performed to clarify the bonding affinity and conformational changes of the Fgn adsorbed on both surfaces. The changes of the secondary structures of the protein (Fgn) adsorbed on E–HAp, N–HAp and Au NP films were also determined based on the deconvolution technique of the amide I band in the infrared light absorption spectra.

2.2. Experimental

2.2.1. Materials

Dipotassium hydrogen phosphate (K_2HPO_4, 99.0 wt%), calcium chloride dihydrate ($CaCl_2 \cdot 2H_2O$, 99.0 wt%), 20 vol% of tetramethylammonium hydroxide aqueous solution (TMAOH: $(CH_3)_4NOH$) and ethanol (C_2H_5OH, 99.5 wt%), formaldehyde (37 vol %) as special grade chemicals were purchased from Wako Chemical Co., Ltd. The poly(oxyethylene)cholesteryl ether ($ChEO_{15}$: $C_{27}H_{45}(OCH_2CH_2)_{15}$) as special grade chemical was purchased from Nihon emulsion Co., Ltd. The molecular structure of the $ChEO_{15}$ is shown in **Figure 2.1**. The fibrinogen (Fgn: Calbiochem Co., Ltd, Mw.: 340 kDa) were dispersed in phosphate buffer saline (PBS: DS Pharma Biomedical Co., Ltd) with the ions (K^+: 4.15 mM, Na^+: 153.09 mM, HPO_4^{2+}: 9.57 mM, Cl^-: 139.57 mM). The molecular structure of Fgn is shown in **Figure 2.2**. Fetal bovine serum (FBS: JRH biosciences Co. Ltd., model number: 12603C), Dulbecco's minimum essential medium (DMEM: Aldrich-Sigma Co. Ltd.) and 0.05 w/v% trypsin-0.053M-EDTA (Wako Co. Ltd., No. 204-16935) were used. Fibroblast NIH3T3 cells (RCB1862) were provided by Riken Bio Resource Center. A plastic cell culture flask with an area of 75 cm^2 was purchased from BD Bioscience. A polyclonal rabbit antimouse collagen type I R2 chain (sc-28654) and fluorescein isothiocyanate-labeled goat antirabbit immunoglobulin G antibody (FITC-labeled IgG, F2765) were purchased from Santa Cruz Biotechnology and Invitrogen (VSA), respectively. All chemicals were used without further purification.

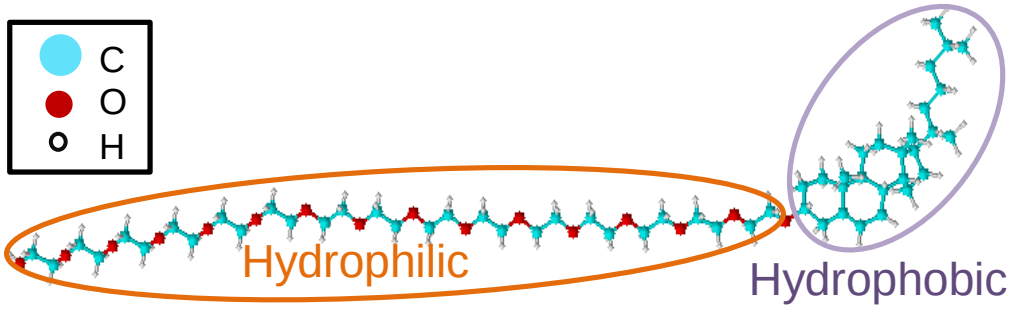

Figure 2.1. Molecular structure of $ChEO_{15}$. The Phase diagram of the binary water/$ChEO_{15}$ shows that at the synthesis temperature the $ChEO_{15}$ is in the micellar phase, forming spherical micelles with an approximate length of 13 nm.

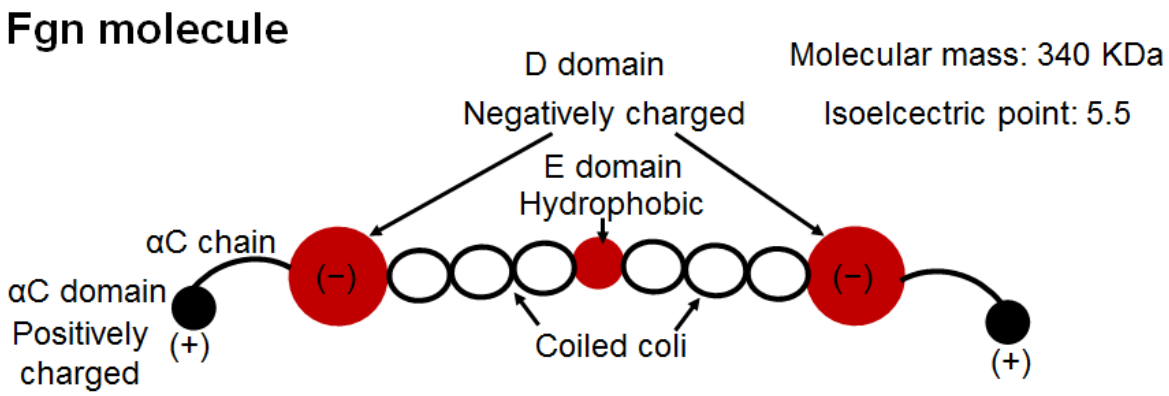

Figure 2.2. Molecular structure of Fgn. The αC domains are positively charged, the D and E domains are considered as hydrophobic domains. However at neutral pH, the D domain can be also negatively charged. The Fgn has a molecular mass of 340 kDa and an isoelectric point of 5.5. The size of the Fgn is 9 x 45 x 6 nm.

2.2.2. Synthesis of Elliptical HAp (E–HAp) NPs

In this study, the elliptical HAp NPs (E–HAp NPs) were synthesized as follows. $ChEO_{15}$ (3.0 mmol) was dissolved in ultrapure water and then K_2HPO_4 (3.0 mmol) was added into the dissolution. The aqueous solution containing $CaCl_2•2H_2O$ (5.0 mmol) was dropped into the $ChEO_{15}/K_2HPO_4$ solution at the flow rate of 1 mL/min, 40 °C. The solution was refluxed with continuous stirring at 60 °C. After 24 hours, the pH value was adjusted to be 13 using TMAOH, and the temperatures was increased to 80 °C. The solution continued at refluxed with continuous stirring for 3 h. The solution was centrifuged (10000 g, 5 min, 4 °C) to obtain the sediment solid product, which was washed with ethanol and ultrapure water 2 times. The product was dried at 90 °C for 24 h, obtaining the E–HAp–bef NPs. As the reference, the sample without $ChEO_{15}$ was synthesized and defined as needle–like HAp NPs (N–HAp–bef NPs). These samples were calcined at 250 °C for 3 h and subsequent at 550 °C for 6 h to obtain the E–HAp and N–HAp NPs.

2.2.3. Formation of E–HAp NP Films

For the formation of HAp NP film, the deposition of the HAp NPs samples, "E–HAp and N–HAp NPs without calcination", on the Au substrate (GE Healthcare Life Sciences Co., Ltd.) was performed by an electrophoretic deposition (EFD) based on our previous report.[51] Before the deposition, the sensor was cleaned by UV/O_3 treatment (ASUMI

GIKEN, Limited, ASM401N, λ_{irr}=185 nm and 254 nm) for 5 min. The ethanolic suspension containing 1 wt% of the HAp NPs was ultrasonically agitated for 15 min to remove the hybridized surfactant and be stably dispersed in the solution. The deposition was conducted by the applied DC voltages of 100 V/cm for 1 min, followed by the ultrasonication in 20 mL of ethanol for 1 min and were subsequently washed by 20 mL of ethanol. As the reference, the Au substrate without coating was used in this study. For the FT–IR measurement, 35 μL (cm^2 of substrate area)$^{-1}$ of the ethanolic suspension containing 0.1 wt% of the HAp NPs ("E–HAp and N–HAp NPs without calcination") was spin-coated (6000 rpm, 10 s) on the Si (100) substrate (Mitsubishi Materials Trading Co., Ltd.). As the reference, the Si (100) substrate without coating was used. These thin films formed on the metallic substrates were dried at 100 ^{o}C for 12 h and calcined at 250 °C for 3 h.

2.2.4. Preparation of Fibroblast Suspension and Their Culture

Mouse embryonic fibroblast NIH3T3 cells (RCB1862), provided by Riken Bio Resource Center, were cultured in a plastic cell culture flask with an area of 75 cm^2 (BD Bioscience, USA) containing 15 mL of Dulbecco's modified Eagle's medium (DMEM: Invitrogen Co.,Ltd.) supplemented with 10 vol% fetal bovine serum (FBS: No. 12603C, SAFC Bioscience Co.,Ltd.) and 1vol% penicillin/streptomycin. The fibroblast cells were cultured at 37°C, in a humidified atmosphere of 5% CO_2 environment, and were subcultured after 7 days using 1 mL of 0.05 w/v% trypsin-0.053 M-ethylenediaminetetraacetic acid (trypsin-EDTA: No. 204-16935,Wako Co., Ltd.) for 10 min at 37 °C. After being washed with 15 mL of PBS, the cells were homogeneously dispersed in 15 mL of PBS, and were separated by centrifugation (2000 rpm, 2 min), and dispersed in 15 mL of 10 % FBS/DMEM. The centrifugation and dispersion were carried out twice. The number of cells in the suspension was counted and adjusted at the desired seeding density in subsequent procedures.

2.2.5. Characterization of E–HAp NPs

2.2.5.1. Basic Evaluation of E–HAp NPs

The elemental composition was determined by an X-ray fluorescence analysis (XRF: ZSX Primus II, Rigaku, Co., Ltd. Japan). The XRF analysis was performed using a sample pellet which was made by pressurizing sample powder without dilution. The fundamental parameters of the software (EZ scanning program, Rigaku, Japan) were obtained using the semi-quantitative analysis method. All the measurements and data analysis were conducted using the software. The infrared spectra were recorded on a Fourier transform infrared spectrometer (FT–IR: JASCO Co., Ltd., FT/IR-4600ST). The FT–IR spectra were measured with pellets containing KBr. The weight ratio between sample powder and KBr was 1:10. All the spectra were recorded after subtracting the background spectrum of pristine KBr. The spectra were obtained wavelength range of 4000–400 cm^{-1} with an accumulation time of 128 and a resolution of 2 cm^{-1}.

X-ray diffraction (XRD) patterns were recorded with a powder X-ray diffractometer (Smart Lab, Rigaku Co., Ltd., Japan) with an X-ray source of CuKα line (λ = 0.15418 nm), a voltage/current of 40 kV/30 mA, scan speed of 5.0º min^{-1} and sampling width of 0.01º. The primary optics is equipped with soller slits (0.04 rad), a divergence slit (1°) and a scattering slit (1°), and the secondary optics is equipped with a receiving slit (0.1 mm), soller slits (0.04 rad), a graphite monochrometer and a detector. The present phases were determined by comparing the X-ray patterns with hydroxyapatite (JCPDS 9-432) standard. The lattice parameters were determined by Rietveld refinement of the diffraction profiles with a PDXL program. The crystallographic characteristics of the crystals can be determined from the X-ray diffraction´s data. For the hexagonal cell parameters "*a*" and "*c*" of the crystallographic system of HAp, the relationship between the distance, "*d*", of two adjacent net planes and the (*hkl*) Miller indices of the reflection planes, is given by the Bragg's law, **Eq. (2-1)**.

$$d = \frac{1}{\sqrt{\frac{3}{4} * \frac{h^2 + hk + k^2}{a^2} + \frac{l^2}{c^2}}} \tag{2-1}$$

The crystalline sizes were estimated using the Scherer equation as shown in **Eq. (2-2)**, where D_{hkl} indicates the crystalline size, λ is the x-ray wavelength (0.15418 nm), β is the full-width at half-maximum (in radians) of 200, 002 and 300 diffraction, θ is the diffraction angle (Bragg´s angle, degree), and K=0.89.[52]

$$D_{hkl} = \frac{K\lambda}{\beta cos\theta} \tag{2-2}$$

According to Scherer's equation, crystalline sizes (D_{002} *and* D_{300}) were calculated from the half width of the 002 and 300 diffractions.

For the determination of the surface properties, the glass sample holder tubes were filled with the 100 mg of E–HAp and N–HAp NPs. Prior to the measurement, the NPs were dry and degassed under vacuum at 120ºC for 4 h using a pretreatment device (BELPREP-vacII, Microtrac/BEL Co., Ltd., Japan). For each NPs sample, the measurements were performed 3 times after conducting a 3-min leak check to ensure data reproducibility, sufficient sealing and complete drying of the specimens. The specific surface area (S_{BET}) and pore size distributions were determined through nitrogen (N_2) adsorption and desorption instrument (BELSORP-miniII, Microtrac/BEL Co., Ltd., Japan). The films was analyzed under N_2 conditions, 77 K, the adsorption relative pressure upper limit of 0.99, and desorption relative pressure lower limit of 0.05. The Brunauer-Emmett-Teller (BET)[53] surface areas and Barrett-Joyner-Halenda (BJH)[54] pore sizes distribution were applied to the analysis. These calculations were performed with the calculation software BELMASTER (TM) manufactured by Microtrac/Bel Co., Ltd.

The BET theory is for explain the multi-layer adsorption of gas molecules on a solid surface and is considered as an expansion of Langmuir equation, which is for the single layer gas adsorption. The BET equation can be described as:

$$\frac{P}{V(P_0-P)} = \frac{1}{V_m C} + \frac{C-1}{V_m C} * \frac{P}{P_0} \tag{2-3}$$

By plotting the $P/v(P_0 - P)$ against the P/P_0, a straight line is obtained, where the slope is $(C-1)/V_m C$ and the intercept is $1/V_m C$. In the equation (2-3) P is the pressure

of the gas, P_0 is the saturation pressure of the gas, V_m is the volume of the gas necessary to form a unimolecular adsorbed layer, and $C = e^{(q_1 - q_2)/RT}$, where q_1 is the heat of the first adsorption layer, and q_2 is the heat of the liquefaction, R is the gas constant and T is the temperature. This graph is used to obtain the specific surface area, substituting V_m in **equation 2-4**:

$$S_{BET} = \frac{V_m}{22414} * K_A * s \tag{2-4}$$

Where K_A is the Avogadro´s number. Since the cross-sectional occupied area occupied by the adsorbed of nitrogen at the liquid nitrogen temperature is 0.162 m^2, s can be calculated as:

$$s = 4.35 * V_m \tag{2-5}$$

The BJH method was used for calculate the pore size distributions from experimental isotherms using the Kelvin model of pore filling (**eq. 2-6**).

$$r_k = r_p - t = \frac{-2\sigma V cos\theta}{RTln(P/P_0)} \tag{2-6}$$

Here, r_p is the pore diameter, r_k is the pore diameter where the capillary condensation occurs, t is the he thickness of the multilayer adsorption, σ is the surface tension of liquid nitrogen, and θ is the contact angle, V is the liquid molar volume of nitrogen. This technique was developed for porous adsorbents with a wide range of pore sizes. The theory can be summarized as (**eq. 2-7**):

$$V - V_x = \int_{rp_n}^{\infty} \pi (r - t)^2 L(r) dr \tag{2-7}$$

Where V is the total volume Vx is the volume of gas adsorbed at saturation pressure, $L(r)dr$ is the total length of pores whose radii is between r and $r + dr$. rp_n is the radius of the largest pore still completely filled with liquid adsorbate at any pressure.

The determination of the particle size and the volume distribution of the nanoparticles, was measured by the nanoparticle qNano multi-analyzer (Meiwafosis Co., Ltd., qNano), which is based on the electric resistance nanopulse method.[55,56] The E–HAp and N–HAp NPs were ultrasonically dispersed in PBS (pH = 7, phosphate ion concentration of 100 mM) at the particle concentration of 0.1 mg/mL for the volume evaluation. Then, the dispersion solution was diluted $1 / (2\times10^{-4})$ times for counting at least 100 particles for the measurement. The average particle volume (*Ave.*) and the coefficient of variation (*cv*) were calculated. Here, the current values were set to be 80 to 130 nA with the applied voltage of 0.6 V. The calibration sample used was carbonylated polystyrene standard particles (Izon Science, Ltd.) with an average diameter of 100 nm were placed in the PBS buffer solution at the concentration of 2×10^9 particles/mL.

The morphologies were observed on the carbon-coated Cu grid using a transmission electron microscope (TEM; JEOL Co., Ltd., JEM-1400) with magnifications typically up to ×1,000,000, at an accelerating voltage of 120 kV, and the short length (*S*) and long length (*L*) distributions of the ECP hybrids were calculated by counting 300 particles.

2.2.5.2. Measurement of Au Substrate Wettability with UV/Ozone Treatment

The change in the wettability of the Au substrate with the UV/O_3 treatment was measured on a contact-angle meter (Excimer Inc., Smart Contact 100, probe: ultrapure water) at the droplet volume of 3.1 μL under static condition.

2.2.5.3. Characterization of E–HAp NP Films

The surface structures of the E–HAp and N–HAp NPs on the Au substrate were analyzed by an atomic force microscope (AFM: Nanocute, SII Investments, Inc.) in an area of 1.0×1.0 μm^2. A silicon probe mounted on a cantilever (SII Micro Cantilever SI-AF01, SII Investments, Inc.) was employed. The surface roughness (R_{rms}) was calculated by the root mean squares in the Z-range images. The software used for the calculations of coverage percent and roughness was SPIWin SPI3800N software. From

scanning, the AFM equipment developed a front image and a three-dimensional image of the morphology. Once the morphological image was made, obtained, the roughness of the area and of the line was obtained, in the parameter of mean square roughness (**equation (2-8)**), respectively, as follows:[57]

$$R_{rms} = \sqrt{\frac{\sum_{n=1}^{N}(|z_n - \bar{z}|)^2}{N-1}} \quad (2\text{-}8)$$

Where z_n is a segment height, $\bar{z}$ is average height of all segments, and *N* is the number of segments. Roughness provides the information about area roughness trend across the swept area; whereas the roughness of the line yields the roughness value in a selected trajectory.

For the determination of the surface properties, the E–HAp and N–HAp NP films were broken into small pieces and that small pieces of the films were used to fill the glass sample holder tubes (100 mg). Prior to the measurement, the films were dry and degassed under vacuum at 120ºC for 4 h using a pretreatment device (BELPREP-vacII, Microtrac/BEL Co., Ltd., Japan). For each film, the measurements were performed 3 times after conducting a 3-min leak check to ensure data reproducibility, sufficient sealing and complete drying of the specimens. The specific surface area (S_{BET}) and pore size distributions were determined through nitrogen (N_2) adsorption and desorption instrument (BELSORP-miniII, Microtrac/BEL Co., Ltd., Japan). The films was analyzed under N_2 conditions, 77 K, the adsorption relative pressure upper limit of 0.99, and desorption relative pressure lower limit of 0.05. The Brunauer-Emmett-Teller (BET)[53] surface areas and Barrett-Joyner-Halenda (BJH)[54] pore sizes distribution were applied to the analysis. These calculations were performed with the calculation software BELMASTER (TM) manufactured by Microtrac/Bel Co., Ltd.

2.2.5.4. FT–IR Spectral Measurement for Analyzing Hydration Layers

The infrared spectra were obtained by a Fourier transform infrared spectrometer (FT–IR; JASCO Co., Ltd., FT/IR-4600ST) and were measured in the range between 400–4000 cm^{-1} with an accumulation of 128 times with a spectral resolution of 1 cm^{-1}. The Si (100)

substrate pre-treated with UV/ozone for 5 minutes was Au-sputtered at 5 mA for 1 min (SC-701 Quick coater, Sanyu denshi Co. Ltd., Japan) in order to cover the surface of Si(100) with a thin Au layer (~10nm). The Si(100) substrate without Au-coating was used as the background. Peak separation is achieved by curve fitting, in which the experimental spectrum is fitted by a function which is the sum of the individual peaks with Gaussian or Lorentzian shape. The deconvolution of the hydroxyl –OH stretching bands was fitted with the product of Gaussian and Lorentzian peaks (**Eq. (2-9)**):[58]

$$I = \sum_1^n B_n e^{\left[\frac{-(v-v_{0,n})^2}{s_n^2}\right]}\left[1 + \frac{(v-v_{0,n})^2}{S\cdot^2{}_n}\right]^{-1} \quad (2\text{-}9)$$

Where ν_0 is the peak maximum, s is the peak width and s' is the bandwidth term of the Lorentzian part, and B is the peak position.

For evaluating the hydration layers, the O–H stretching band was deconvoluted into the three components free water (3200 ± 20 cm^{-1}), intermediate water (3400 ± 20 cm^{-1}), and non–freezing water molecules (3600 ± 20 cm^{-1}).[59] The components of the deconvoluted O–H stretching bands of the Au substrates were calculated as the integrated area ratio of the band of bounding (i.e., intermediate and non–freezing water molecules) to that of free water molecules.

2.2.6. Surface Plasmon Resonance (SPR) Measurement for Fibrinogen (Fgn) Adsorption Ability

The SPR technique was used to measure the Fgn interactions with the HAp NP films was performed on a SPR instrument (Biacore X, GE Healthcare Life Sciences Co., Ltd.) under the excitation wavelength at 760 nm. The change in the resonance angles was calibrated as $\Delta\theta$ = 0.1 deg. (1000 RU), which can be proportional to the weight mass of the bonded Fgn at 1 ng/mm^2. The refractive index changes on the Au substrate (sensing area: 1.4 mm^2) provide the Fgn binding amount and kinetics. The $\Delta\theta$ can be obtained through the change in the refractive index by the Fgn adsorption within the decay length of the evanescent field (l_{decay}) at the interface between the Au substrate and PBS. The l_{decay} can be given by the following **Eq. 2-10**:[60]

$$l_{decay} \cong \frac{\lambda}{2\pi}\sqrt{-\frac{\epsilon_{r,Au}+\epsilon_{r,w}}{\epsilon_{r,w}^2}} \quad (2\text{-}10)$$

Where λ is the excitation wavelength at 760 nm, $\varepsilon_{r,Au}$ is the dielectric constant of Au (21.8 at 760 nm), and $\varepsilon_{r,w}$ is the dielectric constant of water (1.33). As a result, the l_{decay} in this study was 328 nm, which is longer than the Fgn adsorption layer thickness. The schematic representation of the SPR measurement is shown in **Figure 2.5**.

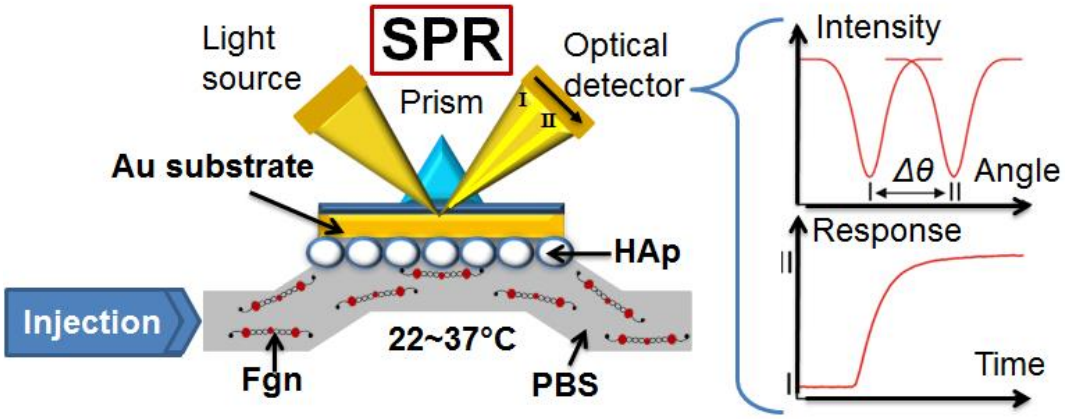

Figure 2.5. Schematic representation of SPR analysis during Fgn adsorption. The surface refractive index is monitored over time as Fgn binding events occur.

It was studied the protein adsorption on the E–HAp and N–HAp NP films. Fibrinogen bovine plasma (Fgn, 99.0 wt%) with the molecular weight of 340 kDa was used and (K^+: 4.15 mM, Na^+: 153 mM, HPO_4^{2+}: 9.57 mM, Cl^-: 139.57 mM) to prepare the solution with the different Fgn concentrations of 2.9, 15, 29, 44 and 59 nM for analyzing the kinetic constants at the initial adsorption stage. 50 μL was injected on the HAp NP films at the flow rate of 5 μL/min. After the injection, the adsorption behavior at the dynamic states was monitored for the 10 mins. On the basis of 1:1 Langmuir binding model, the resonance curve was fitted with the **Eq. (2-11)** for the linear analysis.[61]

$$k_{obs} = k_d - k_a \bullet C_f \quad (2\text{-}11)$$

Where k_{obs} is appearance kinetic constant, k_d is dissociation constant, k_a is binding constant, and C_f is feed protein concentration in PBS.

In the following, the adsorption amounts were measured. 5 μL of the Fgn solution was injected on the HAp NP films at the flow rate of 5 μL/min. After the injection, the adsorption behavior at the static states was monitored. Then, 10 μL of PBS was injected at the flow rate of 10 μL/min to remove the non-binding Fgn from the film surfaces.

Fgn was dispersed in PBS to prepare the solution with the different Fgn concentrations of 0.29, 2.9, 29, 294, 735 and 1470 and 2941 nM for analyzing the adsorption isotherms at the equilibrium stage for 60 min. The adsorption amount on the E–HAp, N–HAp and Au NP films was determined by the response changes after washing with PBS. The adsorption amount at the equilibrium state (W) was calculated by the **Eq. (2-12)** based on the adsorption isotherms. On the basis of the Langmuir adsorption isotherm formula, the equation of state for the one-component adsorption can be represented as follows:[62]

$$C / W = 1 / (K_{eq} \cdot W_{max}) + (1 / W_{max}) C \qquad (2\text{-}12)$$

C, K_{eq} and W_{max} are the Fgn concentration in the equilibrium state, the adsorption equilibrium constant and the maximum adsorption amount, respectively. The K_{eq} and W_{max} were determined from the slope of a C/W versus C plot. The Fgn adsorption based on the correlation coefficient (0.9939 for Au substrate and 0.99465 for HAp NP films) was found to be Langmuir-type monolayer adsorption.

In the higher Fgn concentration of 2941 nM for the adsorption time of 1 h, the adsorption amount at 27 ^{o}C was measured at the different phosphate ion concentrations (10, 25, 50, 75 and 100 mM) in PBS. The adsorption at the phosphate ion concentration of 10 mM in PBS was measured at the different temperature of 22, 24.5, 27, 30, 32 and 37 ^{o}C. The adsorption amount was determined by the response changes after washing with PBS.

2.2.7. Real-Time Monitoring of Fgn Adsorption by Quartz Crystal Microbalance with the Dissipation (QCM-D) Method

Bovine plasma Fgn (pI: 5.5 and MW 340 K) was used in the protein adsorption analyses. The protein solution at 1.0 mg/mL was adjusted with 10 mM phosphate buffer solution (NaH_2PO_4 and Na_2HPO_4, pH 7.0).

QCM-D (D300, Q-Sense AB) measurements were performed by monitoring the frequency shift (Δf, Hz) and dissipation shift (ΔD) at 15 MHz. The temperature was kept at 37.00 ± 0.05 ^{o}C. The Δf value was converted to $\Delta f_{n=3}/3$ at a frequency of 5 MHz. A PBS amount of 0.5 ml was introduced into the sensor chamber. The Δf and ΔD readings were stabilized for 30–60 min. Then, 0.5 ml of the Fgn solution was introduced and the Δf and ΔD curves were measured for 60 min. The weight change due to adsorption was calculated with the Sauerbrey equation:[63]

$$\Delta m = -c * \Delta f_{n=3}/3 \quad (2\text{-}13)$$

where c is a constant equal to 17.7 ngHz^{-1}cm^{-2}. The adsorption amount at the equilibrium state (W) was calculated on the basis of the one-component adsorption Langmuir adsorption isotherm formula presented in equation (2-12).

The viscoelastic properties of the adsorbed Fgn were evaluated using the time-saturated ΔD /Δf value ($\Delta D_{sat}/\Delta f_{sat}$) in the ΔD–Δf plot. The $\Delta D_{sat}/\Delta f_{sat}$ values from the measured Δf and ΔD curves have been used to evaluate the conformational adsorption state.[64–66] These values correspond to the energy dissipation per unit adsorption mass, characterizing the viscoelasticity of the adlayer. The Δf and ΔD curves were fitted with the Voigt-based viscoelastic model to characterize the adlayers as a Newtonian fluid.[65]

The QCM-D data were simulated using the QSoft 401 and the analysis of the Δf and ΔD curves was carried out using the Q-sense Dfind software.

2.2.8. FT–IR Spectral Analysis for Fgn Adsorption Secondary Structures

For the FT–IR measurement, the adsorption at the phosphate ion concentration of 10 mM in PBS and the Fgn concentration of 2941 nM for the adsorption time of 1 h was conducted at the different temperature of 22 and 37 ^{o}C, and was washed by ultrapure water and freeze-dried. Based on our previous report,[67] the adsorbed protein secondary structures

on the HAp NP films at the different temperature of 22 and 37 ^{o}C were measured by a Fourier transform infrared spectroscopy (FT–IR: JASCO Co., Ltd., FT/IR-4600ST) at the cumulated number of 128 times and the spectral resolution of 1 cm^{-1}. The spectra were recorded after subtracting a background spectrum of pristine Si(100). The spectra of the freeze-dried films adsorbed Fgn at the equilibrium stage were measured and deconvoluted into six components at the wavenumber regions between the ranges of 1600–1735 cm^{-1}. In the concrete, the C=O stretching band was deconvoluted into six components (1630±2, 1645 ± 2, 1655±2, 1665±2, 1680±2 and 1690±2 cm^{-1}) belonging to β–sheet, random, α–helix, turn, β–-turn (1) and β–turn (2), respectively. All the deconvolutions were performed by fitting with the Gaussian functions (**Eq. 2-14**) using the SOLVER option in the software (Microsoft Co. Ltd., Excel 2013).

$$y = A\exp\left\{-(x-B)^2 / C^2\right\} \tag{2-14}$$

Where A is the peak height, B is the peak position and C is the deviation

By the generalized reduced gradient method, the SOLVER calculation was done until the satisfied states of all the constraints and optimization conditions. The residual values decreased down to be less than 7.0 %. The ratio of the mono-component area was calculated from the separated spectrum. As the references, the spectra of Fgn alone without further purifications were measured and deconvoluted as described above.

2.2.9. Localized FT–IR Spectroscopic Measurement of Fibroblasts and Their Immunostaining by Type I Collagen

The localized FT–IR spectroscopic measurement was recorded on a FT–IR spectroscopy (Spectrum GX, Perkin-Elmer, Inc.) with an accumulation of 256 times and spectral range of 4000–750 cm^{-1} at a spectral and resolution of 2.0 cm^{-1}. The IR beam entered the chamber through a polarizer and a KBr window, and the once-reflected beam was detected by a mercury cadmium telluride (MCT) detector. After culturing for 2 h from the cell seeding at the concentration of 10^6 cells/mL. The adhered cells were washed with PBS and the cell surfaces were measured with an

aperture size of 50 × 50 μm^2. The spectroscopic images were collected using Spotlight 150i/200i infrared microscopy system.[68]

The immunostaining of the type I collagen in the fibroblasts was carried out according to the previous report.[69] The cells were cultured for 120 min. and then fixed with 3.7 vol % formaldehyde in PBS for 10 min and were stained with 100 μL of the polyclonal rabbit antimouse collagen type I R2 chain as a primary antibody, and the fluorescein isothiocyanate (FITC)-labeled IgG was used as a secondary antibody, which was diluted 15-fold in PBS including BSA (1 wt %) for 4 h and washed three times with 1 mL of PBS. The cells in PBS were sealed with a cover glass to prevent evaporation during the observation with a confocal laser scanning fluorescence microscope (Olympus CKX41, UIS2 (Universal Infinity-corrected) optical system).

2.3. Results and Discussion

2.3.1. Evaluation Results of E–HAp NPs

Figure 2.6 shows the FT–IR spectrum of the E–HAp and N–HAp NPs before and after calcination; all the samples had the characteristic FT–IR spectra of the HAp. The band observed around 3530cm^{-1} is due to the presence of structural hydroxyl group in the HAp NPs structure.[70] The broad band from 3600 to 2600 cm^{-1} was attributed to the surface OH groups of the adsorbed hydration layer (free, intermediate and non−freezing water).[71] The band around 1645 cm^{-1} corresponds to the OH vibration of the free water.[72,73] The P−O vibrations of the phosphate ions bands were at around 1000–1100, which belong to stretching vibration, the band 962 cm^{-1} is assigned to a no degenerated symmetric stretching mode of the P−O bond of the phosphate group, and the bands at 600 and 560 cm^{-1} and 470 cm^{-1}, corresponds to the triply degenerated bending mode of the O−P−O.[74–76] The bands at around 1530, 1460 and 876 cm^{-1}, are characteristic of the carbonate ions (e.g, HCO_3^-, CO_3^{2-}) in the structures. The double bands around 1530 and 1460 cm^{-1} are attributed to the symmetric mode with its transition moment parallel to the C–O bond (ν_s) and the asymmetric mode with its transition moment perpendicular to the same C–O bond (ν_{as}).[77–79] The incorporation of carbonate ions in the structure of the HAp NPs can be due to the interactions of the HAp NPs and the atmospheric CO_2 which can dissolved into the solution during the synthesis. According to the phase diagram of the $ChEO_{15}$−water, at the

synthesis temperature of E–HAp NPs, the $ChEO_{15}$ had micellar phase (W_m) forming a spherical micelle.[22,80] It has been reported that the ethylene oxide units of the $ChEO_{15}$ micelles interacted with the calcium ion in the solution allowing the formation of "caged Ca-complexation" structures.[81] However, in the FT–IR spectra results before calcination, there was no bands of organic compounds observed (methylene oxide units) for that reason it was concluded there is no complexation interaction between the $ChEO_{15}$ micelles and Ca ions of the E–HAp NPs during nucleation. The decrease in size of the E–HAp NPs could be due to the size of the $ChEO_{15}$ micelles. The $ChEO_{15}$ micelles occupy a large space which prevents the growth of E–HAp NPs.

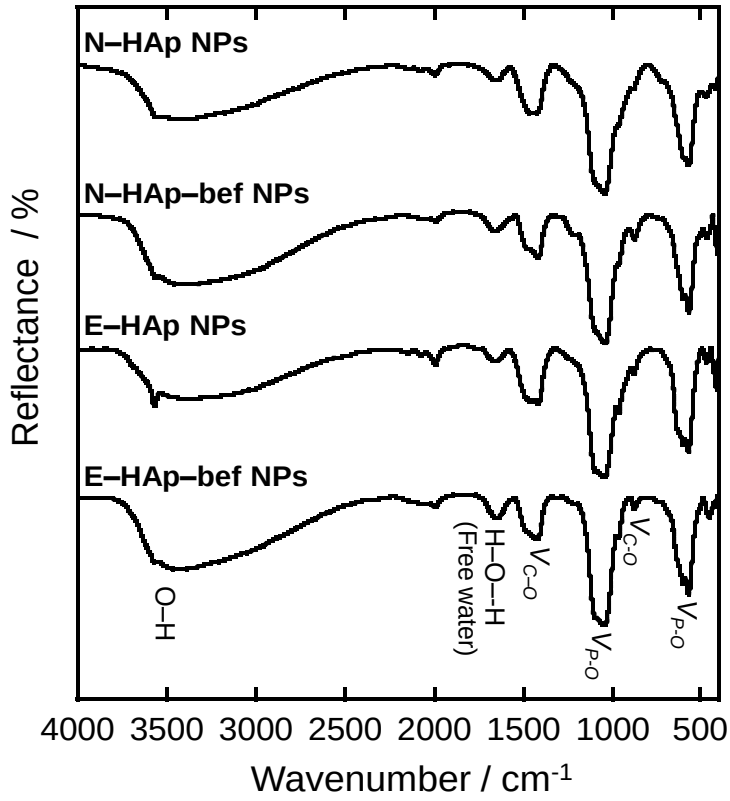

Figure 2.6. FT–IR spectra of the N–HAp and E–HAp NPs synthesized in the presence of $ChEO_{15}$ before and after the calcination, demonstrating that there are no residues of surfactant after calcination. The band around 3500 cm^{-1} correspond to the adsorbed water (free, intermediate, and non–freezing water) and the hydroxyl group (O–H) of the N–HAp and E–HAp NPs**.**

The chemical composition of the E–HAp and N–HAp NPs before and after calcination was summarized in **Table 2.1.** The chemical composition of the E–HAp and N–HAp NPs was similar and the Ca/P ratio was the same for both HAp NPs after and before calcination. The carbon content before calcination was higher for E–HAp NPs than N–HAp NPs, which could be due to small residues of surfactant in the E–HAp NPs. Nevertheless, after calcination the carbon content is almost the same, suggesting that the complete elimination of the $ChEO_{15}$ in the E–HAp NPs.

Table 2.1. Chemical composition of the N–HAp and E–HAp NPs synthesized in the presence of $ChEO_{15}$ before and after the calcination.

Atomic element	N–HAp–bef NPs	N–HAp NPs	E–HAp–bef NPs	E–HAp NPs
C (mol%)	6.9	5.2	7.8	5.6
O (mol%)	62.1	61.6	60.3	60.5
P (mol%)	10.3	10.6	10.4	10.8
Cl (mol%)	0.2	0.2	0.1	0.1
K (mol%)	0.2	0.2	0.2	0.2
Ca (mol%)	20.3	22.2	21.2	22.8
Ca/P	2.0	2.1	2.0	2.1

The X-ray diffraction patterns of the E–HAp NPs and the N–HAp NPs before and after the calcination are shown in **Figure 2.7** In all the samples, the plane indices can be assigned to a HAp single phase (ICDD: 00-009-0432). The resultant crystalline sizes (D_{002} and D_{300}) and the D_{002}/D_{300} ratios of the HAp NPs synthesized in the presence of $ChEO_{15}$ before and after calcination are shown in **Table 2.2**. Before the calcination, the D_{300} crystalline sizes of the E–HAp NPs synthesized in the presence of $ChEO_{15}$ were larger as compared with the reference (N–HAp NPs) to successfully provide the smaller D_{002}/D_{300} ratios. The molecular states of the $ChEO_{15}$ in the solution were micelles, according to the phase diagram of the $ChEO_{15}$/water system as the function of temperature and $ChEO_{15}$ weight fraction.[22,80] Moreover, it has been reported that the oxyethylene groups of the nonionic surfactants are

capable to complex with the calcium ions in an aqueous solutions, resultantly forming the micelle polar sphere with calcium rich domains that interact with the phosphate ions and leading a fast formation of E–HAp NPs.[81–83] After the calcination, the crystalline sizes of the E–HAp NPs were preserved and were similar to those of the N–HAp NPs which grew along with the *a*-axis. The D_{002}/D_{300} ratios of the E–HAp NPs were smaller as compared with those of the N–HAp NPs. The E–HAp NPs generally exhibited the anisotropic elliptical-like shapes (i.e., D_{002}/D_{300} ratio > 2.0).[84]

The D_{002}/D_{300} ratio of calcinated E–HAp NPs was 1.9. This ratio was smaller as compare with N–HAp NPs. It is inferred that the use of the nonionic surfactants suppresses the growing along with the *c*-axis and change the preferential growth direction thought the *a*-axis, as it has happened with the use of other non-ionic surfactants.[85] Therefore, the poly(oxyethylene) cholesteryl ether enhanced the mineralization forming HAp at the lower D_{002}/D_{300} ratios, which are similar to the biosynthesis of HAp in humans and animals with cholesterol.[86]

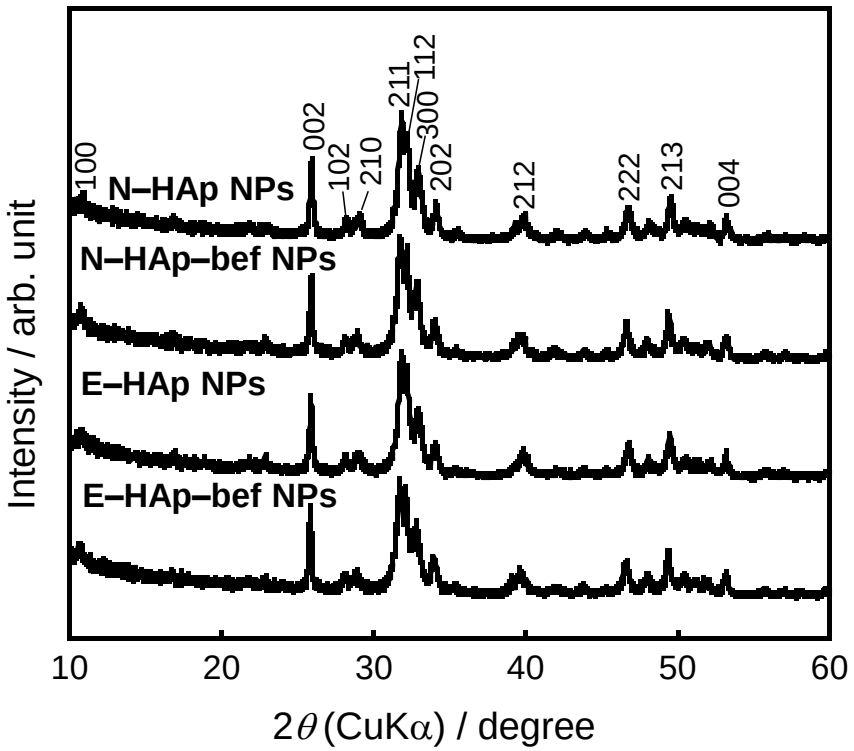

Figure 2.7. XRD patterns of the N–HAp and the E–HAp NPs synthesized in the presence of $ChEO_{15}$ before and after the calcination, indicating that all the plane indexes can be attributed to HAp (ICDD: 00-009-0432).

The S_{BET} and *BJH* pore sizes of the calcined HAp NPs were summarized in **Table 2.2**. The S_{BET} values of all the calcined E–HAp NPs were lower as compared with that of the N–HAp NPs. The E–HAp NPs had the highest S_{BET} values, respectively, which is higher than that reported for the HAp NPs synthesized with the other nonionic surfactants.[81,87]

The N_2 adsorption and desorption isotherms and the D_{BJH} pore size distributions of the calcined E–HAp and N–HAp NPs were shown in **Figure 2.8** In the isotherms of all the HAp NPs corresponded to type IIa with nonporous or macroporous adsorbents based on IUPAC classification,[88] which are based on the result of unrestricted monolayer-multilayer adsorption. The D_{BJH} pore size distributions of the calcined E–HAp NPs were different from that of N–HAp NPs. and the porosity states would be attributed to the template $ChEO_{15}$ molecular structures.

Table 2.2. Crystalline sizes, D_{002}/D_{300} ratios, S_{BET} and D_{BJH} of the HAp NPs synthesized in the presence of $ChEO_{15}$ before and after the calcination.

Sample	*Before calcination*				*After calcination*				
	Crystalline sizes		D_{002} / D_{300}	S_{BET} (m^2/g)	Crystalline sizes		D_{002} / D_{300}	S_{BET} (m^2/g)	D_{BJH} (nm)
	D_{002} (nm)	D_{300} (nm)			D_{002} (nm)	D_{300} (nm)			
N–HAp NPs	33	9.2	3.6	62	37	16	2.3	48	2.4
E–HAp NPs	35	16	2.2	69	34	18	1.9	42	2.4

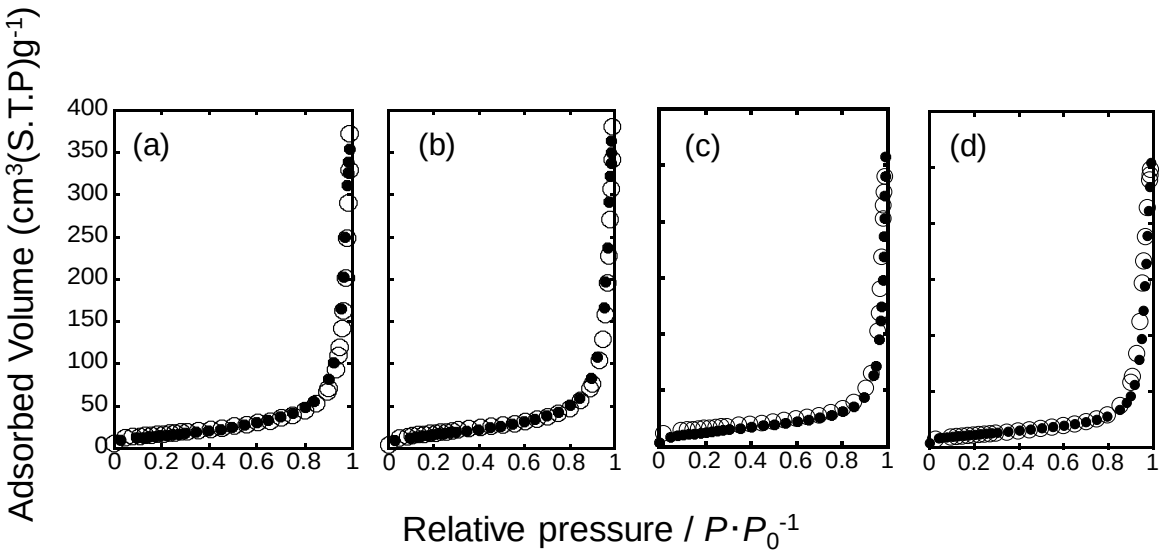

Figure 2.8. Nitrogen (●) adsorption and (○) desorption isotherms of (a, c) N–HAp and (b, d) E–HAp NPs before (a–b) and after (c–d) calcination respectively.

The **Figure 2.9** shows the particle size distribution and volume of the N–HAp and E–HAp NPs before and after calcination determined by nanoparticle qNano multianalyzer. The average particles sized were 111, 112, 114, and 130 nm, and the averages of volume were 0.00075, 0.00075, 0.001, and 0.0012 fL for N–HAp–bef, E–HAp–bef, N–HAp and E–HAp NPs respectively. The calculation was based the assumption of the cylindrical shapes and the average values of the short and long lengths for 100 particles. Before calcination the particle size distribution and volume are almost the same for both HAp NPs but after calcination of E–HAp NPs increase, that can be attributed to the aggregation of the HAp NPs during the measurement, suggesting that after calcination, the E–HAp NPs tend to form more aggregates than before calcination. The zeta potentials of the samples were calculated by qNano nanoparticle multianalyzer. The zeta potentials were –5 mV for N–HAp–bef NPs, –20.4 for E–HAp–bef NPs mV, –13.6 mV for N–HAp, and –23mV for E–HAp NPs. The zeta potentials in both HAp NPs increase after calcination which can facilitate the capacity of the HAp NPs of aggregation. The obtained particle sizes by qNano nanoparticle multianalyzer were larger than the obtained from XRD suggesting that the particle dispensability in PBS was not preserved during the measurement, indicating the aggregation of the particles.

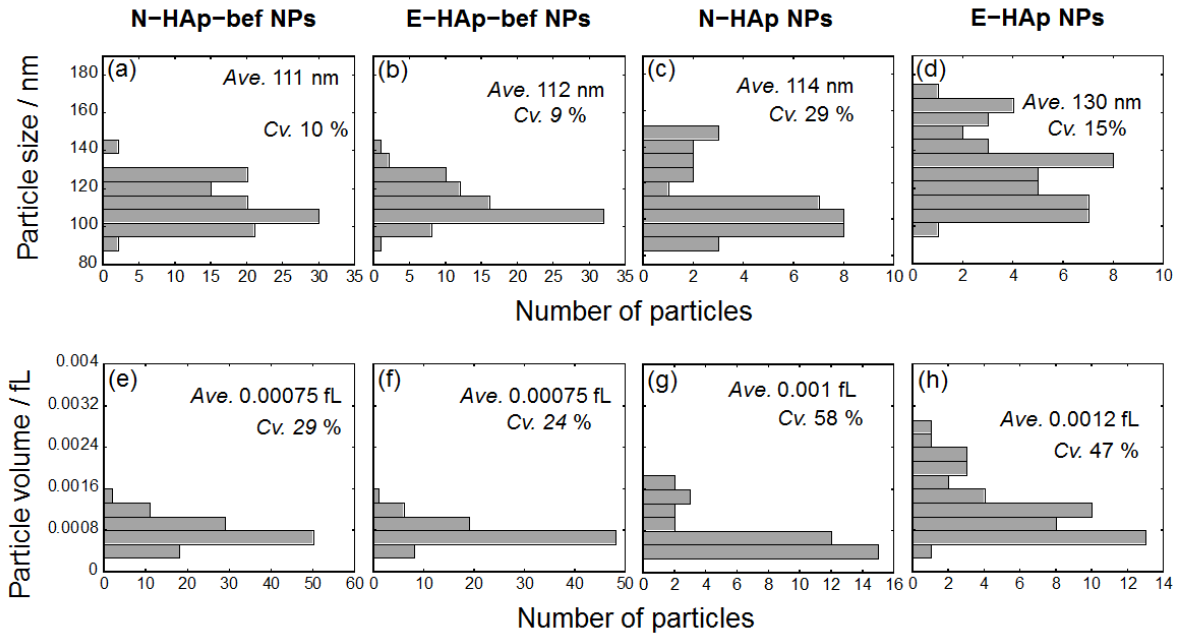

Figure 2.9. Particle size distribution (a–d), and particle size volume (e–h) of the N–HAp NPs (a, e) with a zeta potential of –5 mV, E–HAp–bef NPs (b, f) with a zeta potential of –20.4 mV, N–HAp–bef NPs (c, g) with a zeta potential of –13.6 mV, and E–HAp NPs (d, h) with a zeta potential of –23mV. Determined after calcination by qNano nanoparticle multianalyzer.

TEM images and particle size distributions of the E–HAp and N–HAp NPs were 23 and 1032 nm and 27 and 63 nm respectively (see **Figure 2.10)**. The average particle size of the *a*-axis and *c*-axis for All the HAp NPs exhibited the smaller crystalline sizes less than 100 nm. E–HAp NPs had elliptical shapes with the aspect ratio of 2.3. In contrast, the N–HAp NPs showed the needle–like shapes with the aspect ratio of 4.5 that correspond with the typical HAp NPs synthesized in aqueous suspension states.[83] These different morphologies would be attributed to the use of the other non-ionic surfactants. The crystalline sizes from the TEM images were longer as compared with the crystalline sizes from XRD patterns, indicating the polycrystalline states along with the *c*-axis. The elliptical morphology is the indication that the precipitation reactions between $CaCl_2 \cdot 2H_2O$ and K_2HPO_4 took continuously place only within the aqueous phase.[81]

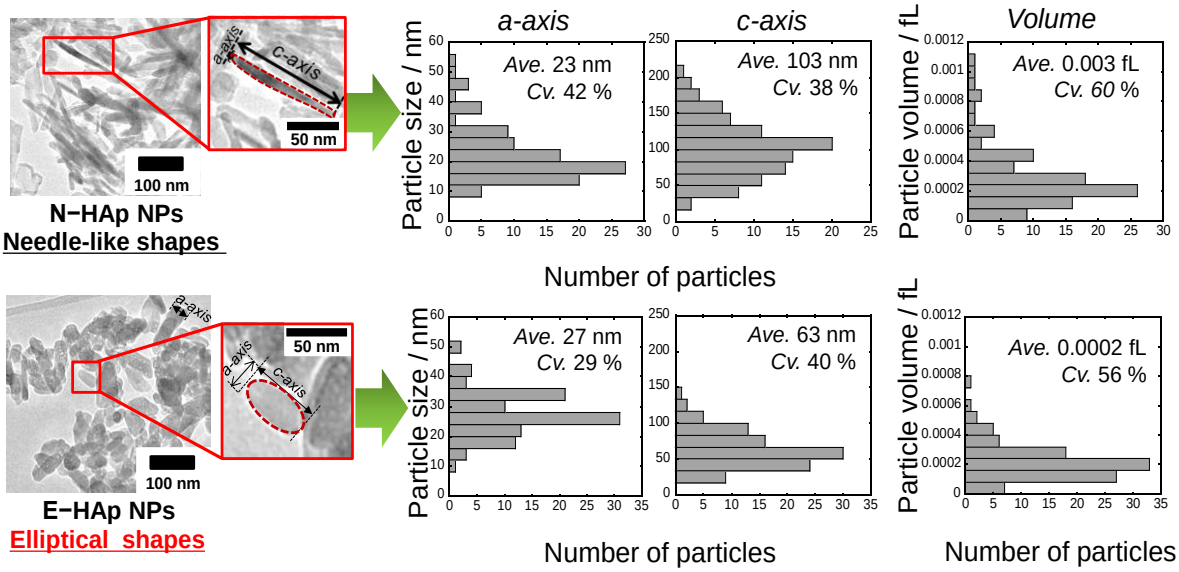

Figure 2.10. TEM images and their short and long axis size distributions and the particle volume distribution calculated from the TEM images of the N–HAp NPs with needle–like shape and average aspect ratio of 4.5 and E–HAp NPs with elliptical shape and an average aspect ratio of 2.3.

2.3.2. Corroboration of Wettability Change Mechanism of Au Substrate

For inducing the effective binding between the Au substrate and the HAp NPs, the wettability changes of the Au substrate were studied with the UV/O_3 treatment time. It have been reported that the Au surface generally exhibits a hydrophobic with the large contact angle for water at 50º.[89] In **Figure 2.11** the contact angle value before the UV/O_3 treatment was 83.7º and decreased with increasing treatment time to finally be 11º at 25 min, demonstrating the formation of hydrophilic surface. On the other hand, the UV/O_3 treatment promote the oxidation of the Au (i.e., the formation of a thin layer of Au O_x.[90,91] The oxidation layer immediately reacts with the environmental water molecules to form hydroxyl groups on the surfaces, which allows the hydrophilicity of the Au film.[92] The proposed mechanism is in accordance with the result of FT–IR spectral changes (**Figure 2.12 (a)**), where the centered absorption band at around 3400 cm^{-1} can be assigned to hydrogen-bonded hydroxyl groups,[93] indicating that the formation of Au–OH was observed as the stretching vibration of the O–H at the UV/O_3 treatment time of 15 min. In **Figure 2.12 (b)** for the component area ratio of bonding to free water molecules, the free water decreased and the bonding water increased with increasing the UV/O_3 treatment time,

demonstrating that the hydration structures on the substrate clearly altered by the treatment and the oxidation layer effectively interacted with the water molecules. Therefore, the water molecules strongly interacted with the oxidation layer of the Au substrate by the UV/O_3 treatment (**Figure 2.12 (c)**).

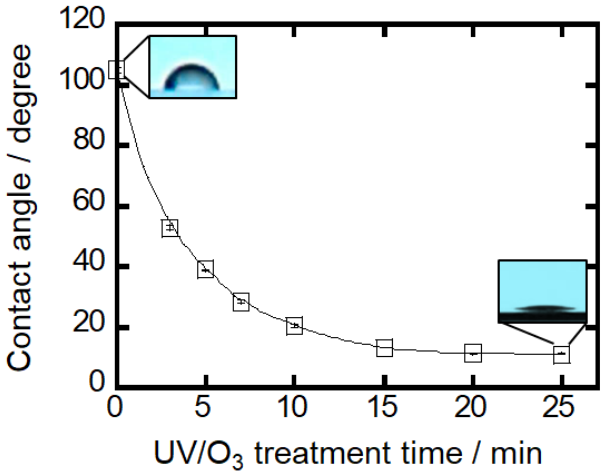

Figure 2.11. Contact angle of the Au substrate surface after different times of UV/O_3 treatment, corroborating the wettability of the Au surface after UV/O_3 treatment.

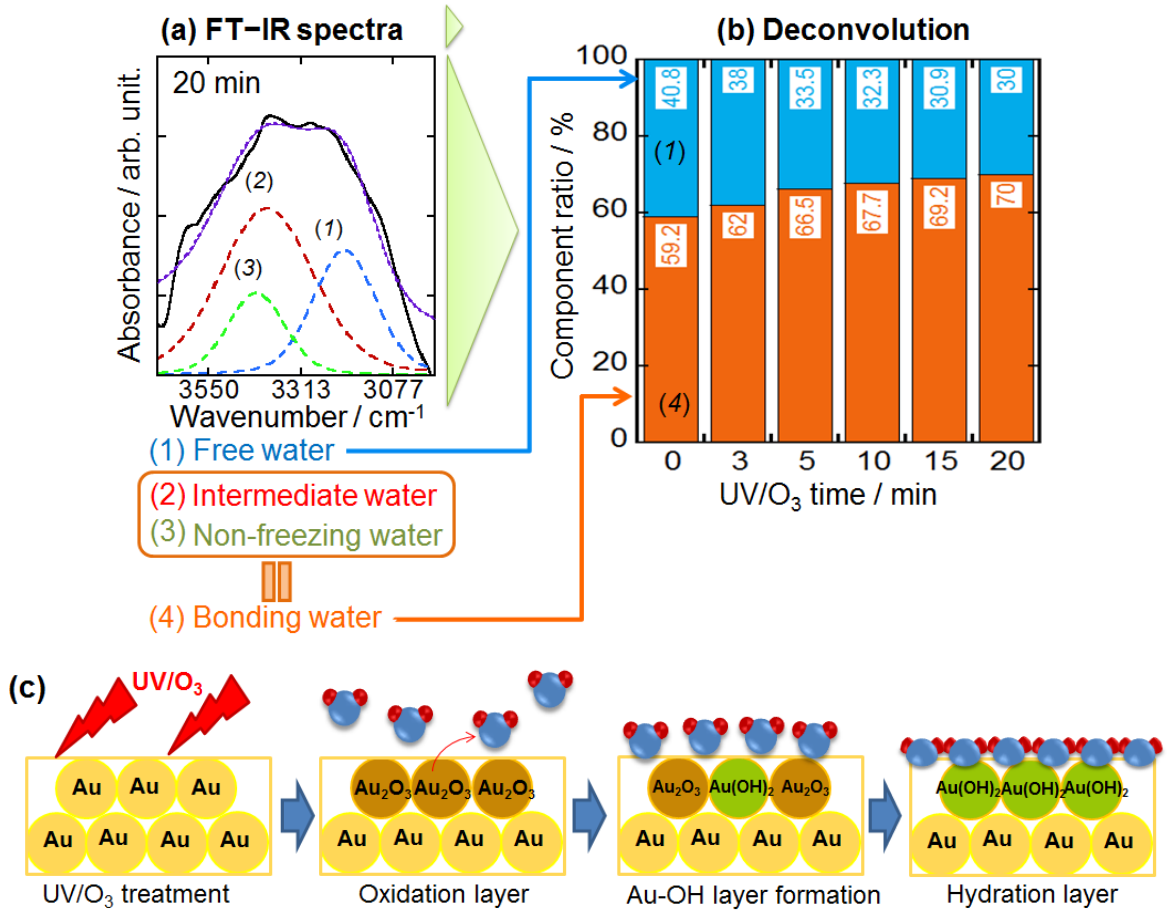

Figure 2.12. (a) Curve fitting and spectral separation results with the deconvolution of the hydrated Au surface at 20 minutes of UV/O_3. The three components are (1) free water @ 3200 ± 20 cm^{-1}, (2) intermediate water bending vibration @ 3400 ± 20 cm^{-1}, and (3) non-stretching vibration of non–freezing water @ 3600 ± 20 cm^{-1}. Here, the re-synthesized and raw spectra were represented by purple-colored dotted and black-colored solid lines, respectively. (b) component ratio of the two components of adsorbed water (1) free water (blue), and (2) bonding water (orange) on Au substrate surface after 0, 3, 5, 15, and 20 min of UV/O_3 treatment. (c) Scheme of the possible mechanism of the surface oxidation and hydration layer formation on Au substrate surface.

2.3.3. Characterization Results of E–HAp NP Film Surface Structures

The HAp NPs were used for the EPD on the Au substrate in the following experiment. At the deposition voltage of 100 V, the homogeneously HAp NPs-covered over Au was observed by the naked eye, indicating the dispersion of NPs in ethanol.[38,94,95] The high electric field can generate the greater mobility and pressure of the E–HAp NPs on Au with strong binding.[96]

Figure 2.13 shows the AFM topographic images (observation area: 2.0 × 2.0 μm^2) of the Au substrate, N–HAp and E–HAp NP films. The R_{RMS} values of the films were 0.4 nm for the Au substrate, 7.1 nm for N–HAp NP film and 7.9 nm for E–HAp NP film, and the value of the Au substrate was higher than that of the HAp NP films, indicating the successful deposition of the HAp NPs.[97] The response units (RU) monitored by SPR for the HAp NP and Au films are in **Table 2.3** The higher response value of the HAp NP film is due to the increase in the optical refractive index that is related with the formation of HAp NP monolayer. The refractive index is proportional to the mass covering over the Au, and the deposited E–HAp NP film weight was 4.9 ± 0.6 ng/cm^2.[98] Accordingly, the thickness of the E–HAp NP film was 15.6 ± 0.2 nm (HAp density: 3.14 g/cm^3).[99] Since the RU value is defined as 1000 RU is equal to 0.1 millidegree by the SPR detection, which corresponds to the layer of 0.1 ng/mm^2.[100] It was assumed that the HAp NP film was successfully formed as the NP monolayer state. The N–HAp and E–HAp NP films exhibit needle–like and elliptical particle shapes with the approximate sizes of 23 nm × 103 nm and 27 nm × 63 nm, respectively. The shape, size and roughness of the HAp NPs play an important role in the physicochemical properties,[101] and the HAp in the animal body has a spherical shape.[102] Thus, the E–HAp NP film can have a greater cytocompatibility due to the similarity of the shape and crystallinity with the human hard tissues. The specific surface area of N–HAp NP film was 49 m^2/g with a BJH pore size distribution of 3.0 nm, and the specific surface area of E–HAp NP film was 46 m^2/g with a pore size of 2.2 nm. As expected, N–HAp NP film that has a larger area because the NPs on this film are larger and therefore the pore size is also larger compared to E–HAp NP film, which have smaller pore size and surface area. The surface area of the film was very close with the surface area obtained for the powder state, suggesting that the EPD method do not affect the surface properties of the particles during the coating process.

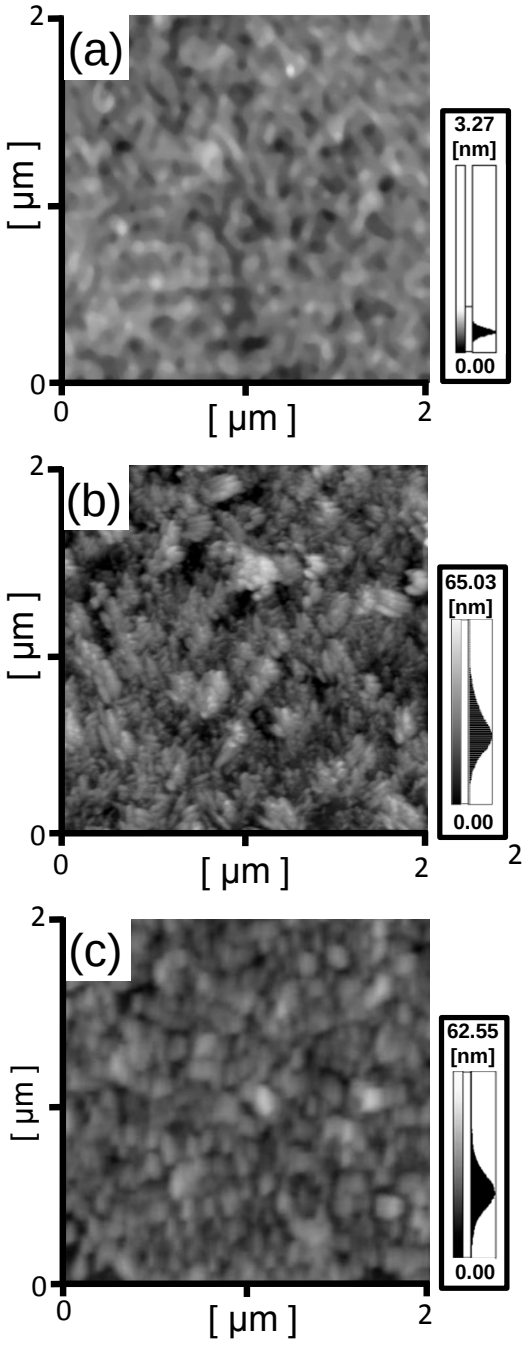

Figure 2.13. AFM topographic images of (a) Au substrate, (b) N–HAp and (c) E–HAp NP films after electrophoretic deposition and ultrasonification, (observation area: 2.0 μm^2) .

Table 2.3. AFM roughness, the concentration expressed in response units (RU), deposition weight, film thickness, pore size distribution, and surface area of the Au, N–HAp and E–HAp NP films.

Surface	R_{RMS} (nm)	Response (RU)	Deposition weight (ng/cm^2)	Film thickness (nm)	S_{BET} (m^2/g)	D_{BJH} (nm)
Au	0.4	13611 ± 106	----	----	----	----
N–HAp NP film	7.9	13957 ± 98	34.6 ± 0.5	11.0 ± 0.2	49.0	3.0
E–HAp NP film	7.1	14283 ± 96	49.0 ± 0.6	15.6 ± 0.2	46.0	2.2

2.3.4. FT–IR Spectra for Analyzing Hydration Layers on E–HAp NP Films

The FT–IR spectra of the stretching O–H absorption band were deconvoluted into the five principal components as the hydration layers[77] adsorbed on the Au substrate, N–HAp and E–HAp NP films in **Figure 2.14**. The FT–IR deconvolution spectrum of the hydration layers on N–HAp and E–HAp NP films was show in **Figure 2.14** at the temperature of 22ºC **(a–b)** and at 37ºC **(c–d)**. Only three of the five components assigned to the intermediate and non–freezing waters, which have been totally defined as a bonding water,[46] were thought to have spectra were in **Figure 2.14 (e)**. The component ratios of the free water for Au substrate, N–HAp and E–HAp NP films at 22ºC 4%, 51%, and 55%, for intermediate water 49%, 29% and 31%, and for non–freezing water 47%, 20% and 14%. In the other hand, the free water for Au substrate, N–HAp and E–HAp NP films at 37ºC were 3%, 53% and 60%, those of intermediate water were 0%, 27% and 30%, and those of the non–freezing water were 97%, 20% and 10%. The bonding water or HAp NP films decrease, while for the Au increased. It is known that the excess bonding water induces the protein denaturation.[103] In particular, the non–freezing water has a direct contact with the material surfaces,[47] and the content of can affect the protein adsorption. Here, the Au substrate has the highest amount of the non–freezing water, which enhances the direct contact with the proteins to cause the denaturation with strong interactions. The large increase in non–freezing water ratio on the surface of the Au can drastically affect the adsorption of proteins, so it is assumed that adsorption would be preferred at 22ºC rather than at 37ºC, in contrasts with the HAp NP films where it is assumed that the decrease in non–freezing water amount at 37ºC will enhance the protein adsorption. At 37ºC, although the intermediate water content on N–HAp NP film is almost same to that on E–HAp NP film, which of non–freezing water on N–HAp NP film is higher twice than that on E–HAp NP film. It was implied that the particle shape of the HAp NPs play an important role in the adsorption of non–freezing water, which is a physical and energetic impediment to the direct binding with proteins.[104] Therefore, the E–HAp NP film has the lowest amount of non–freezing water, which would allow a relationship with the subsequent adsorptive protein conformation.[105] The larger ratio of free water would be also preferable for the conformation.

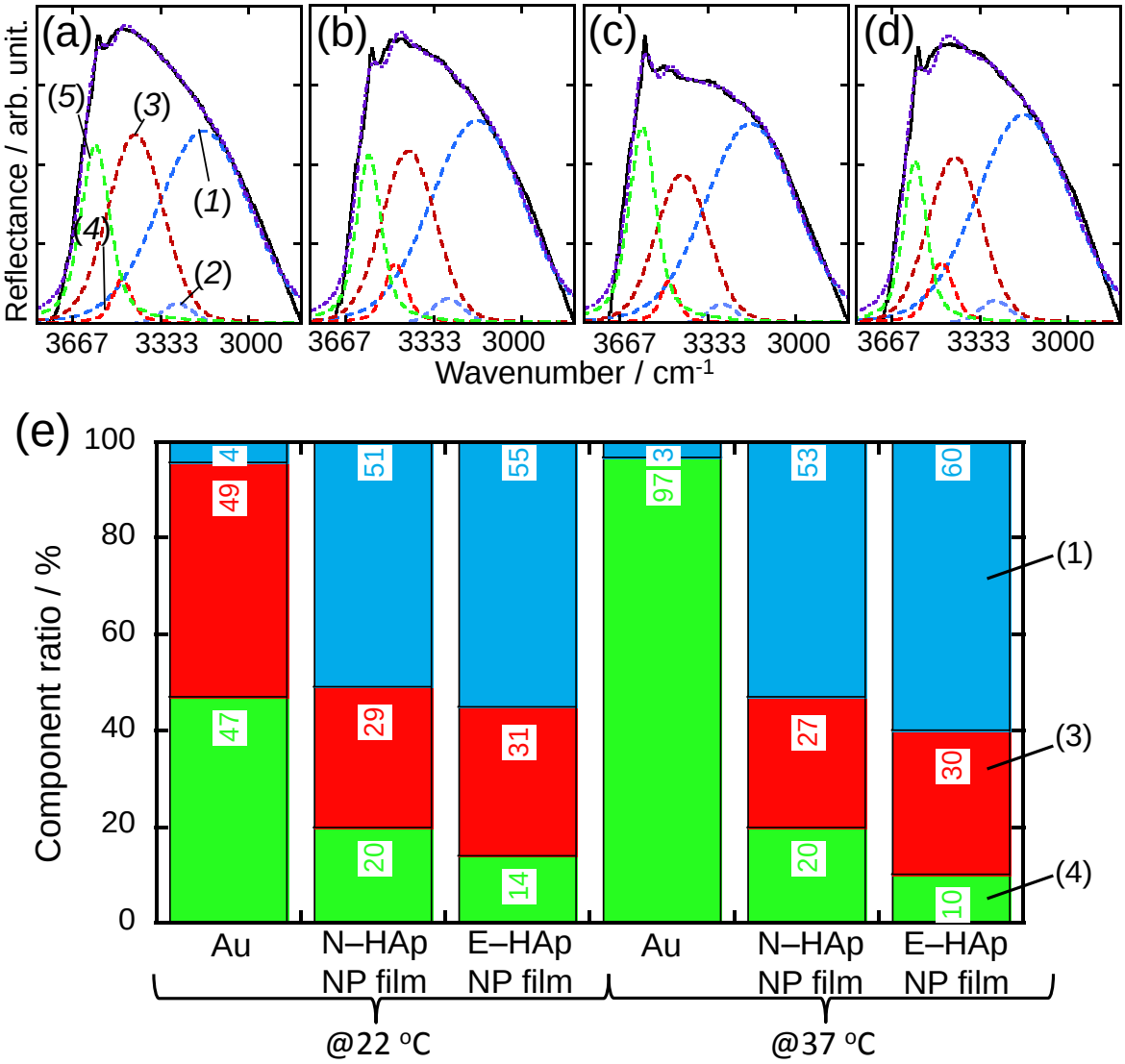

Figure 2.14. The detailed curve fitting and spectral separation results with the deconvolution of the hydrated (a, c) N–HAp and (b, d) E–HAp NP films at (a–b) 22°C, and (c–d) 37°C, were shown to exhibit five components of (1) asymmetric stretching vibration of the free water @ 3190 ± 20 cm^{-1}, (2) free water bending vibration @ 326 0± 20 cm^{-1}, (3) intermediate water bending vibration @ 3430 ± 20 cm^{-1}, (4) non-stretching vibration of intermediate water @ 3480 ± 20 cm^{-1}, (5) stretching vibration of non–freezing water @ 3610 ± 20 cm^{-1}. Here, the separated spectra of the non-stretching vibration of the hydroxyl group in the HAp structures at 3571 ± 1 cm^{-1} were non-displayed in (b, c), the re-synthesized and raw spectra were represented by purple-colored dotted and black-colored solid lines, respectively. Based on the FT–IR deconvolution results of the absorption band due to hydroxyl groups, three component area ratios of the hydration layers were represented in (d).

In order to corroborate if the cooling process during the freezing drying process affects the hydration layer structures, it was investigated the hydration layer structures without freeze-drying. The obtained hydration layer structures with and without freeze-drying were almost the same, suggesting that the drying process did not affected the hydration layer structures.

2. 3.5. Fgn Interfacial Interactions with E–HAp NPs

2.3.5.1. Investigation of Adsorption Behaviors by SPR

The Fgn adsorption kinetics was investigated by the SPR technique at the initial stage, and shows the kinetics of the Fgn adsorption processes on Au, N–HAp and E–HAp NP films at the dynamic states with the different concentrations were shown in **Figure 2.15 (a), (b),** and **(c)** respectively and their correlation plots between the C_f and k_{obs} were in **Figure 2.15 (d)**. When the protein contacts with the surfaces, the rapid adsorption causes an increase in the SPR angle. Intrinsic kinetics can be determined by the change in the adsorption rate. The rate of Fgn adsorption is essentially first-order in terms of the protein concentrations, which can be fitted with 1:1 Langmuir coupling model.[106,107] The intrinsic reaction rate is determined by the binding rate constant (k_a) of the ligate concentration in solution by the concentration of free ligand less the dissociation rate constant (k_d) of the concentration of ligate-ligand complex based on the **Eq. (8).**[108] The k_a and k_d for the Au, N–HAp and E–HAp NP films were summarized in **Table 2.4**. The k_d value for the N–HAp NP film (0.76×10^{-4} s^{-1}) was similar that the value obtained for E–HAp NP film (0.72×10^{-4} s^{-1}). The HAp NP films were much lower than that for the Au (17.3×10^{-4} s^{-1}). At the beginning of the kinetics, the desorption process can be limited by the hydration structures in Fgn as well as by the water adsorbed on the HAp NP films.[109,110]

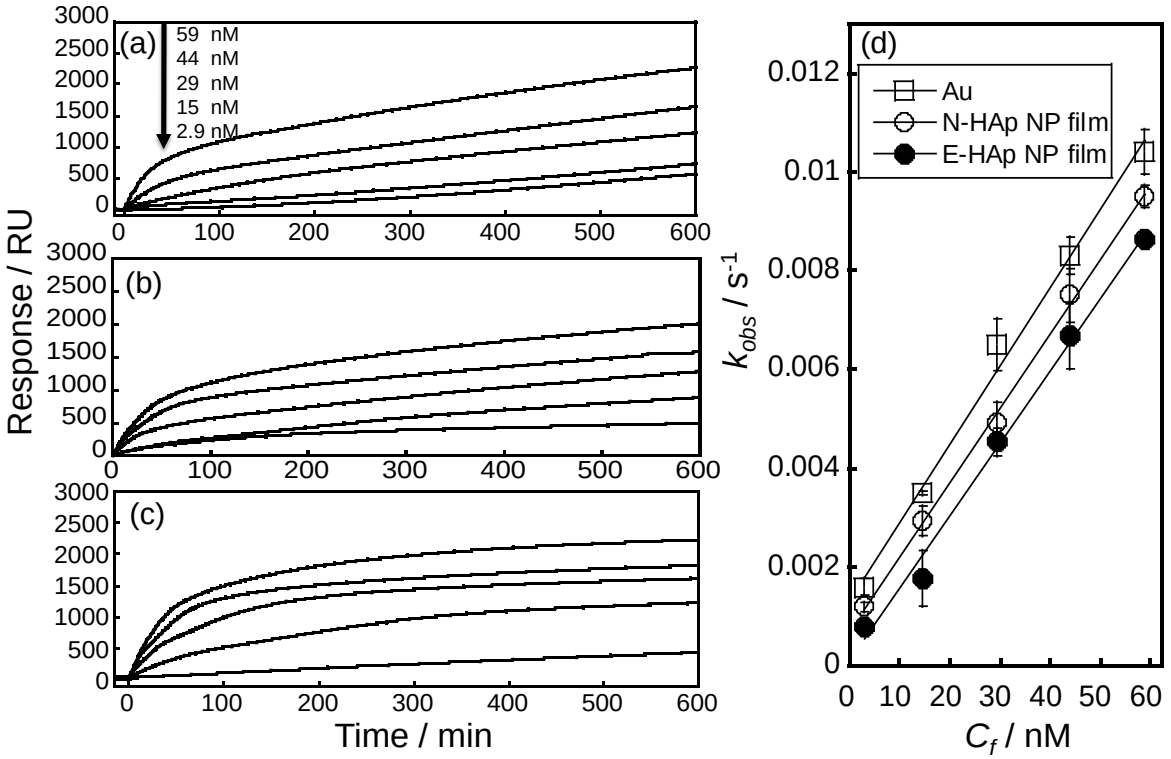

Figure 2.15. Initial Fgn adsorption processes on (a) Au, (b) N–HAp and (c) E–HAp NP films at the dynamic state and (d) Correlation plot between the C_f and k_{obs} at the initial Fgn adsorption stage under the dynamic state, which were fitted with 1:1 Langmuir coupling model.

The analysis of the equilibrium states for the Fgn adsorption on the Au, N–HAp and E–HAp NP films under static conditions was shown in **Figure 2.16**. The Fgn adsorption amount (W) was shown in **Figure 2.16 (a)** and the relationship between the C/W and C at the equilibrium states on the Au, N–HAp and E–HAp NP films in **Figure 2.16 (b)**. After the injection, the flow was immediately stopped, and the SPR adsorption profiles were collected for the plateau state with the Fgn adsorption, followed by rinsing with PBS. The adsorption isotherms were fitted with the first order Langmuir model. The W_{max} values of adsorbed Fgn on the Au, N–HAp, and E–HAp NP films were 1.51×10^{-3}, 1.17×10^{-3}, and 1.23×10^{-3} nmol·cm^{-2}, respectively (**Table 2.4**), indicating the abundant adsorption site on the Au surface.[106] The K_{eq} values on the N–HAp, and E–HAp NP films were 8.50×10^{-3}, 9.59×10^{-3}, and 9.73×10^{-3} nM^{-1}, indicating the preferential affinity, orientation and bond strength of Fgn with the E–HAp NP film. The Fgn molecule was adsorbed on a hydrophobic surface (e.g., Au) to be lengthened by the increase in the segments, which would induce the reversible binding (i.e., higher k_d value). On the charged surface (e.g., E–

HAp NP film), the reversibly adsorbed state occurred. Subsequently, the Fgn molecules could undergo the second adsorption state with the rearrangement, which is associated with the conformational change and considered irreversible, since the interfacial interactions are stronger and with the higher affinity.[111,112]

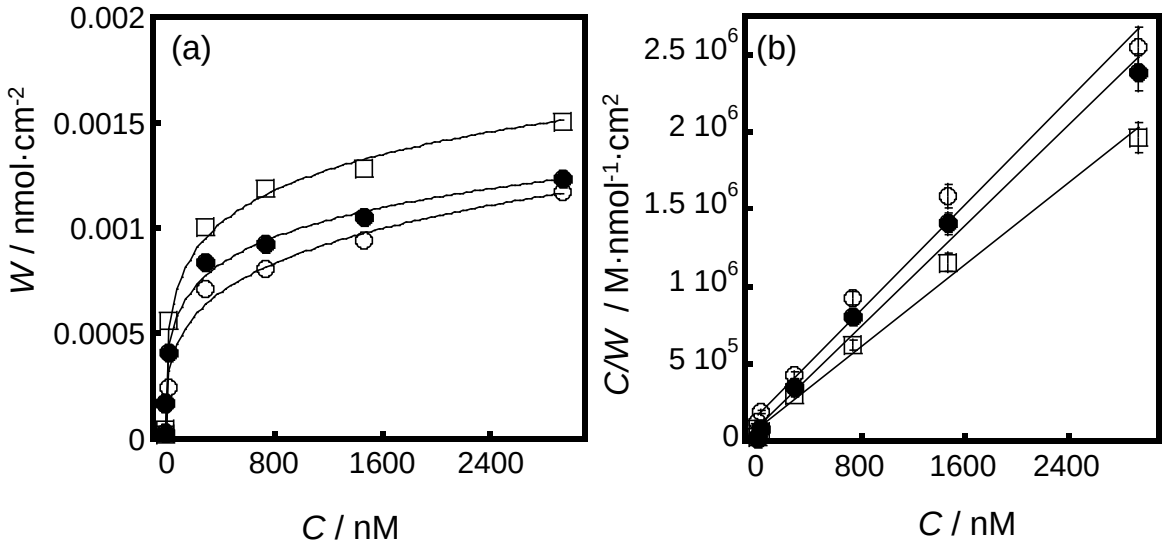

Figure 2.16. **(**a) Adsorption isotherms of Fgn under the static state, and (b) Relationship between the *C*/*W* and *C* at the equilibrium states on the Au (□), N–HAp (○), and E–HAp (●) NP films at different temperatures.

Table 2.4. Response value, binding constant (k_a) and dissociation constant (k_d), adsorption equilibrium constant (K_{eq}) and maximum adsorption amount (W_{max}) with the Fgn adsorption on the Au, N–HAp, E–HAp NP films.

Surface	k_a **(×10^{-4} nM^{-1} s^{-1})**	k_d **(×10^{-4} s^{-1})**	K_{eq} **(×10^{-3} nM^{-1})**	W_{max} **(×10^{-3} nmol cm^{-2})**
Au	1.49	17.3	8.50	1.51
N–HAp NP film	1.43	0.76	9.59	1.17
E–HAp NP film	1.45	0.72	9.73	1.23

The protein adsorption behaviors are influenced by the ionic strength in solution, which can modify the protein charge state. When the ionic strength in the physiological solution increase, the human plasma protein adsorption amount decrease. Thus, the change in the ionic strength allows the information on the interfacial interactions as well as the forces involved in the protein adsorption.[113] The dependence of the phosphate ion concentrations on the Fgn adsorption amount (*W*) was shown in **Figure 2.17**. The ionic strengths based on the Debye–Hückel theory were changed at the concentrations between 158–1580 mM. For the minimum value, it is known that 1 mM of the phosphate ions (e.g., HPO_4^{2-}, $H_2PO_4^-$) in the biological solution exhibited the ionic strength of 150 mM.[114] The maximum amount of the adsorbed Fgn on the surfaces was observed at the lower ionic strength regions, which is closest to the physiological ionic strength. In the case of the HAp NP films, the increase in the ionic strength didn't exhibit the remarkable impact on the adsorption amount. It has been reported that the primary Fgn adsorption stage was carried out by means of electrostatic interactions between the negatively-charged Fgn,[115] and the positively-charged calcium ions of HAp at the biological pH. The other forces such as van der Waals forces can contribute to stabilize the Fgn adsorption based on the binding between the Fgn and E–HAp NP film,[114,116,117] indicating the stable protection from the ions in the solutions.[118]

The N–HAp and E–HAp NP film had a similar behavior. In contrast, there was the pronounced decrease in the adsorption on the Au film with increasing the phosphate ion concentration, indicating that the higher phosphate ion amount on hydrophobic surface (e.g., Au) can interact with the terminal amino groups of Fgn and simultaneously increase the predominant intermolecular repulsions, resulting in the destabilizing effect on the solubility, which promotes the Fgn aggregation by the decrement in the solution of effective Fgn concentration (i.e., salting-out) to induce the low Fgn adsorption amount.[119,120] Therefore, the ionic strength clearly affected the Fgn adsorption behaviors, which is crucial for the investigation of the interactions between the Fgn and substrate surfaces.

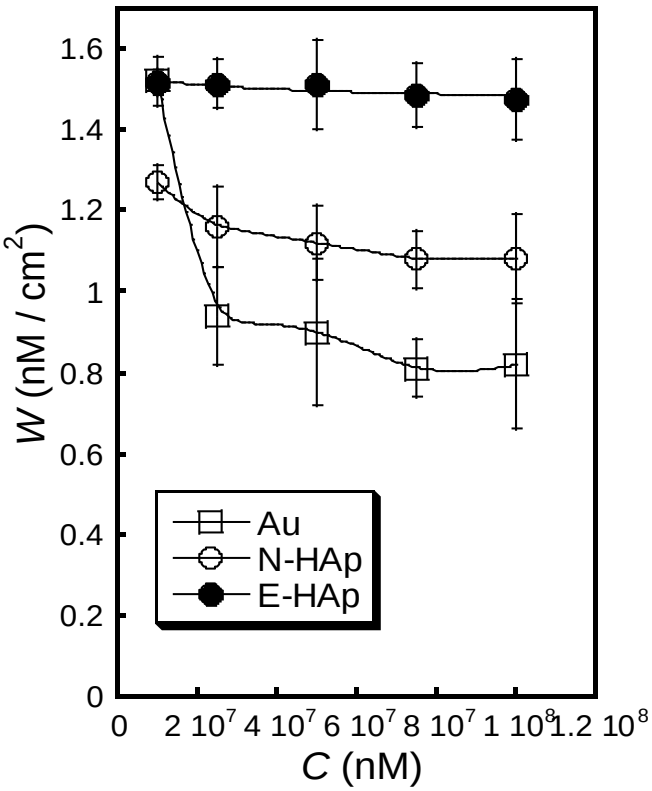

Figure 2.17. Fgn adsorption amount changes on the Au (□), N–HAp (○), and E–HAp (●) NP films at different phosphate ion concentrations.

Figure 2.18 shows the temperature dependence of Fgn adsorption amount on Au, N–HAp, and E–HAp NP films under the static conditions. As the temperature increased, the Fgn adsorption amount on the N–HAp and E–HAp NP film increased, whereas that on the Au film decreased. At the lower temperature (22°C), Fgn can bind to the HAp NP films with end–on orientation, the adsorption amount is small through the hydration layer.[121–123] With the increase in temperature, the water molecules start moving and leaving the HAp NP surfaces, suggesting the preferential mobility of the free water molecules as well as the peptide chains. Accordingly, the water molecules can interact and hydrophilize the Fgn structures; the hydrophobic *D* and *E* domains can go inside the structures through the electrostatic repulsions among leaving hydrophilic interactions at the outer layer.[124] The positively-charged αC domain can preferentially electrostatically interact with the phosphate ions of the HAp NP films to exchange with the free water molecules. Subsequently, the increase in the adsorbed Fgn amount causes the conformational changes to induce coiled-coil structure with almost perpendicular orientation (i.e., end–on orientation) due to the electrostatic Fgn-Fgn repulsions to minimize the water interactions.

In the concrete, the stacked Fgn proteins promote the separation of their backbones and subsequently the neighboring proteins would reduce water solvation around their hydrophobic domains to be interacted with each other.[125,126] In contrast, the hydrophobic interactions between the Au film and the hydrophilized Fgn are difficult, so that the Fgn amount of the Au film decreased. Thus, it was considered that hydrophobic interactions worked in addition to electrostatic interaction on the HAp NP films to increase the adsorption amount at the interface.[124,127,128] Although the N–HAp and E–HAp NP films had almost the same Fgn adsorption behavior and amount from 22 to 20ºC, and 37ºC, at 32ºC the adsorption of Fgn is higher in the N–HAp than in E–HAp NP film, this may be due to modifications in the hydration structures caused by the increase in temperature.

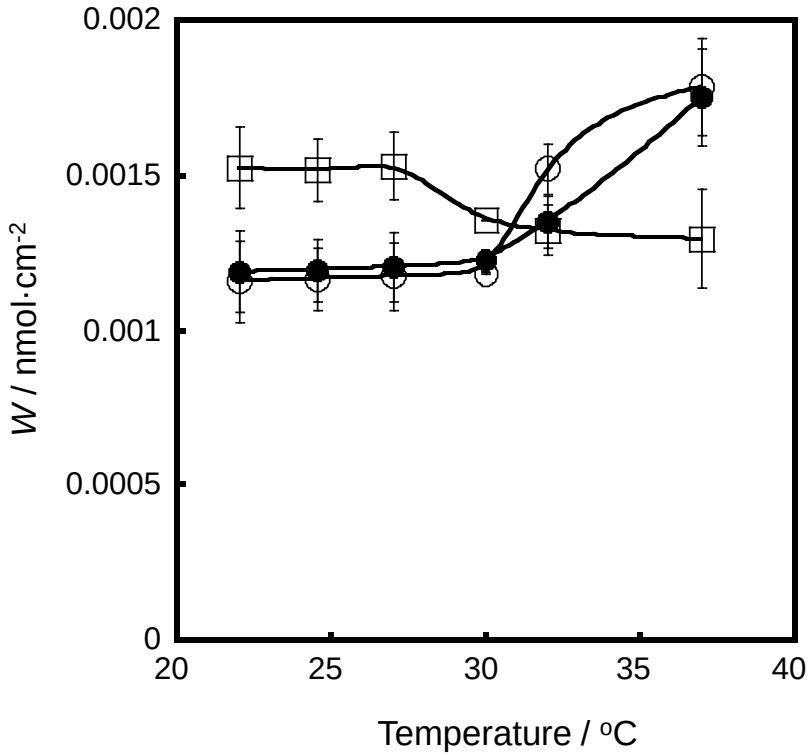

Figure 2.18. Fgn adsorption amount changes on the Au (□), N–HAp (○), and E–HAp (●) NP films at different temperatures.

2.3.5.2. Adsorption Process Measured by QCM-D

The **Figure 2.19** shows the Δ*f* and Δ*D* curves and the Δ*D*–Δ*f* plots of Fgn (1mg/mL) adsorbed on Au, N–HAp, and E–HAp NP films for 60 minutes at 37°C. The Δ*f* and Δ*D* curves indicates the adsorption equilibrium states at 60 min. However, the adsorption plateau was reached at 57 min on Au, 15 min on N–HAp NP film, and 32 min on E–HAp NP film. The Δ*f* and Δ*D* values at 60 min. were –61.2 Hz (3.9) on Au substrate, –94.2 Hz (4.6) on N–HAp NP film, and –90.5 Hz (5.9) on E–HAp NP film, and the saturated Δ*D*/Δ*f* values of the Fgn adlayer were 9.4 x 10^{-8} 1/Hz on Au substrate, 12.7 x 10^{-8} 1/Hz on N–HAp NP film, and 16.1 x 10^{-8} 1/Hz on N–HAp NP film. The Fgn adsorption amount on Au, N–HAp, and E–HAp NP films at 60 min. was 1.08, 1.68 and 1.63 μg/cm^2, respectively. The Higher adsorption amount of N–HAp NP film could be related to the increased area of the *a*-plane (calcium-rich plane) due to the increase of crystalline size. The adsorption amount and the saturated Δ*D*/Δ*f* values of the Fgn were larger for HAp NP films than Au substrate, indicating higher molecular weight and affinity of Fgn for HAp NP films, in particular for E–HAp NP film, which had the highest saturated Δ*D*/Δ*f* value. The Δ*D*–Δ*f* plots showed a linear change, suggesting a monomolecular adsorption on the HAp NP films.[129] It was observed two-step changes during the Fgn adsorption in all the films, indicating conformational changes during the adsorption.[130] The different adsorption behaviors of Fgn with almost similar pI value could be attributed to their secondary structure and different conformational orientations models ("Side–on", "end–on").[131] The behavior of the adsorbed Fgn on HAp NP films with dumbbell-like structure have been described.[132] The positively charged αC domain binds with the negatively charged phosphate or hydroxyl ions on the surface of the HAp NP films, which correspond with the "end–on" model. These results are in agreement with the results obtained in the curve fitting and spectral separation results of FT–IR deconvolution spectra of the amide I, corroborating the proposed hydrations layer–Fgn interfacial interactions on Au, N–HAp, and E–HAp NP films at 37°C. These differences in the viscoelastic properties of the adlayers could affect the cell behavior.

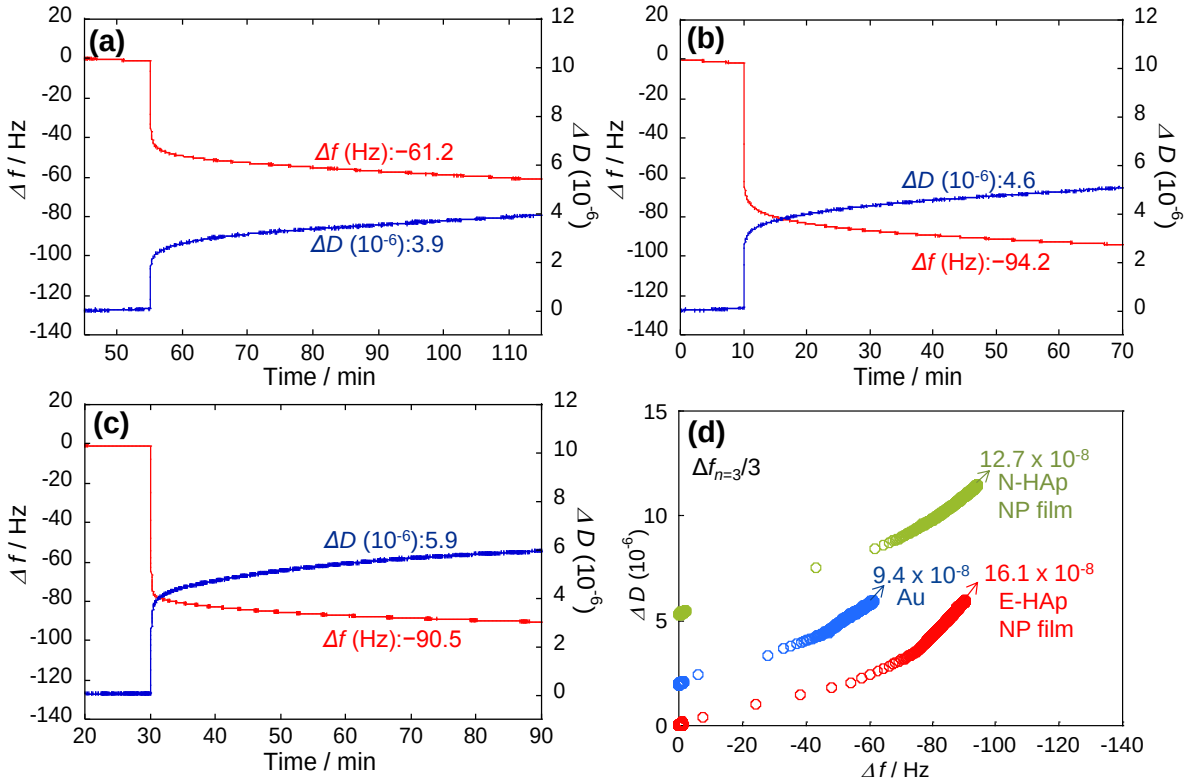

Figure 2.19. (a–c) Δf (fequency shift) and ΔD (dissipation shift) curves and the (d) ΔD–Δf plots of Fgn (1mg/mL) adsorbed on (a) Au, (b) N–HAp, and (c) E–HAp NP films for 60 minutes at 37°C. Δf was transformed into the value for the fundamental frequency of 15 MHz by dividing by 3, which is the harmonic overtone number.

2.3.5.3. Curve Fitting and Spectral Separation Results of FT–IR Deconvolution Spectra of Amide I in Adsorbed States

The secondary structures of the adsorbed Fgn on the HAp NP films at 22 and 37 °C were analyzed by the curve separation of the amide I band peak at around 1650 cm^{-1} through the Gaussian function fitting. Each secondary structure percentage was calculated from the separated band areas. The FT–IR deconvolution results of the adsorbed Fgn on the Au, N–HAp and E–HAp NP films at 22 and 37 °C were shown in **Figure 2.20**. The component ratios (%) at 22 and 37 °C on the Au, N–HAp and E–HAp NP films were shown in **Figure 2.21**. It has been known that the α–helix with helical shape is the most abundant and most stable ordered structure. The content of this structure has a strong effect on the three-dimensional conformation and subsequent biological activity.[133,134] The predominant secondary structural elements (α–helix and β–sheet) provide the information about the

protein conformational state.[135] In all the samples, the secondary structures of the adsorbed Fgn were more stereoscopic than the native Fgn, since the content of α–helix and β–sheet structures was higher than as compared with that of native Fgn. It is indicated that the E–HAp NP film quelled the adsorbed protein denaturation.[136] The α–helix and β–sheet contents of the adsorbed Fgn on the HAp NP films increased at the higher temperature. In concrete, the α–helix and β–sheet contents at 22°C for E–HAp NP film were 18.5±2.3 and 24.1±2.6 % and those at 37 ^{o}C were 19.2±2.5 and 25.3±0.8 %. In contrast, the contents of turn and β–turn decreased from 15.8 ± 4.2 to 14.8 ± 3.4 % and from 21.9 ± 4.3 to 11.2 ± 0.2 %, respectively. It is suggested that the adsorbed Fgn at 22^{o}C has three–dimensional conformation that is similar to the native Fgn.[137]

The results at 22^{o}C showed higher α–helix and β–sheet ratio than the ratios at 37^{o}C. In this case, the calculated surface coverage rate at the equilibrium state was 49 %, which indicates the adsorbed Fgn with both end–on and side-on orientations on the E–HAp NP film.[138] Thus, the water molecular behaviors affected the Fgn conformational states that correspond with the phenomena mentioned in the previous paragraph. It was suggested that the α–helix content of the adsorbed Fgn was mainly transformed to be the random structures of turn and β–turn.[139] It is indicated that the adsorption of Fgn on N–HAp NP film allows the secondary structure changes of the Fgn, which would promote the protein denaturation.[140,141] The α–helix and β–sheet are the components of the protein secondary structures, and the amount is related with the three-dimensional conformation, resulting in the bioactivity.[50,139]

The ratio of α–helix and β–sheet structures on the E–HAp NP film was significantly higher than those on the Au substrate and N–HAp NP film. In particular, the content of α–helix and β–sheet was 3.6 ± 2.6 % and 23.8 ± 4.3 % for Au substrate, 4.4 ± 2.4 % and 21.6 ± 4.3 %for N–HAp NP film, and 11.1 ± 2.3 % and 40.4 ± 3.4 % for E–HAp NP film. The lower contents of the α–helix and β–sheet structures for the Au substrate and N–HAp NP film would be attributed to the content of bonding waters, indicating that the planar protein structures would affect the lower bioactivity. On the other hand, the lower ratio of non–freezing water on the E–HAp NP film induced the stereoscopic and three-dimensional protein structures.

Therefore, it was found that the bonding waters play an important role in the Fgn conformational states. The results of the present paper also confirm the proposals suggested in our previous report, where the orientation of the Fgn adsorbed on the HAp NP films had both end–on and side–on orientations.[142] In this study, even if two orientations are present on the HAp NP films, the side–on (i.e., planar conformation)[143] and end–on orientation (i.e., stereoscopic, three-dimensional conformation)[144] was abundant on the N–HAp and E–HAp NP film, respectively. Thus, the rich in non–freezing water acts as a barrier which prevents from directly interacting with the ground material surfaces.

Accordingly, the positively-charged αC domains of the Fgn can electrostatically and strongly interact with the non–freezing water on the Au substrate and N–HAp NP film, and the hydrophobic character of D and E domains cause a slight conformational change in the angle coiled-coils,[38] which causes a decrease in the α–helix and β–sheet structures to be rich in the side–on states. [145] Since the amount of non–freezing water is lower on the E–HAp NP film, the αC domain could electrostatically interact with the bonding water as well as with the phosphate ions on the E–HAp NP film as the almost perpendicular end–on orientation at the initial stage.[146] Then, the decrease of the ratio of non–freezing water can allows the electrostatic interactions of the negatively charged D-domain with the calcium ions in the surface of the E–HAp NP film in and side–on orientation, but also the strong interactions between the positively charged αC domains with the phosphate ions and the repulsion between the Fgn molecules and the free water molecules on the E–HAp NP film promotes the perpendicular end–on orientation in the surface of E–HAp NP film, allowing the two orientations on E–HAp NP film, which avoids the loss of α–helix and β–sheet structures. Therefore, the conformational changes of the protein would depend on the bonding water states on the substrate surfaces. The secondary structures on E–HAp NP film at 37ºC were suitable for the active bio-functions.

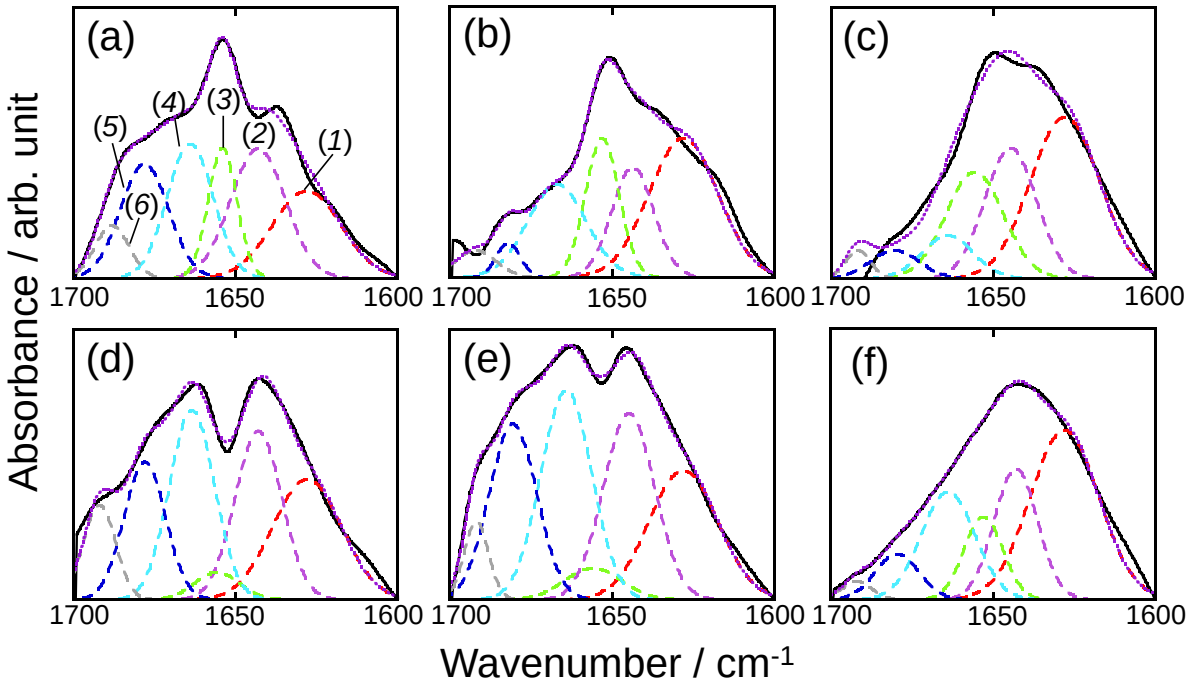

Figure 2.20. Curve fitting and spectral separation results of FT–IR deconvolution spectra of the amide I band of the adsorbed Fgn on (a, d) Au, (b, e) N–HAp and (c, f) E–HAp NP films at (a–c) 22, and (d–f) 37ºC. Their secondary structural component is (1) β–sheet, (2) random, (3) α–helix, (4) turn, (5) β–turn (1), and (6) β–turn (2).

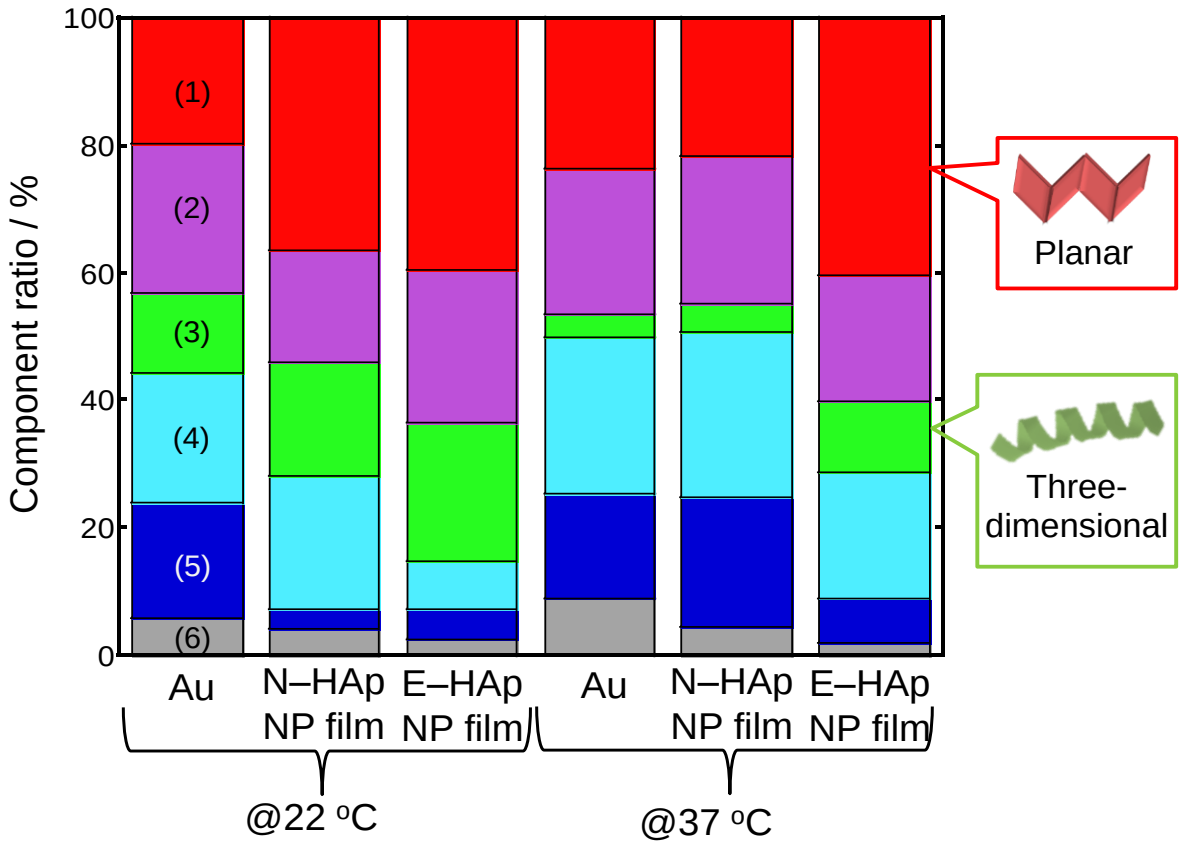

Figure 2.21. (a) The component ratios of the secondary structures calculated from the deconvolution spectral areas of the amide I band of the adsorbed Fgn on Au, N–HAp, and E–HAp NP films at 22, and 37 °C. Secondary structural component assignments of FT–IR deconvolution spectra are (1) β–sheet @ 1630 ± 2, (2) random @ 1645 ± 2, (3) α–helix @ 1655 ± 2, (4) turn @ 1665 ± 2, (5) β–turn @ 1680 ± 2, and (6) β–turn @ 1690 ± 2. (b) Outline of the possible conformational changes of the Fgn adsorbed on E–HAp NP film at different temperatures.

2.3.6. Localized FT– IR Spectra of the Fibroblasts

At two hours of culture, in all the films it is observed that the cells start spreading and there is the formation of pseudopods–like structures. The morphology of the cultivated cells is different in each film. The cells cultivated on the Au film (**Figure 2.22 (a)**) are smaller and rounder than the cells cultivated on HAp NP films. The morphology of the cells on the HAp NP films was also different. The cells on N–HAp NP film (**Figure 2.22 (b)**) had more elliptical shape. In contrast, the cells on E–HAp NP film (**Figure 2.22 (c)**) were more elongated cells and had more pseudopods than Au and N–HAp NP films. The FT–IR spectra of the top surfaces of the adhered cells measured with the aperture sizes of 50 × 50

mm^2 were shown in **Figure 2.22 (d)**. The components of the top surfaces would correspond to the cellular phospholipid membranes.[147,148]

The absorption band at around 3300 cm^{-1} was assigned to the N–H stretching of the amide A,[149] and the intensity for the Au substrate was higher than those for the HAp NP films. In the E–HAp NP film, the sharp spectral bands at around 3500 cm^{-1} due to the hydrogen-bonded N–H stretching were intensified. The bands at 2960, 2925 and 2853 cm^{-1}, which correspond to the C–H stretching bands of the alkyl chains, were observed in the cells on the HAp NP films.[150] The stretching vibrations of –COOH or H_2O at 1745 cm^{-1} was more pronounced in the cells on the HAp NP films. The band at 1658 cm^{-1} attributed to C=O stretching of the amide I and that at 1546 cm^{-1} attributed to N–H bending and C–N stretching of the amide II were clearly observed on all the cells.[136,151,152] The bands at 1460 and 1395 cm^{-1} corresponding to the scissoring of $C–H_2$ wag, and ν_s COO^- stretching were detected only on the HAp NP films.

The band intensity at 1262 cm^{-1} of the N–H deformation of the amide III for the E–HAp NP film was higher than that for the N–HAp NP film.[110] The presence of alcohol groups at around 1175 cm^{-1} was only found in the HAp NP films.[153] These results suggested that a rearrangement is occurring in the mosaic structures of the cell membranes, which would be caused by the underground substrate surface properties. With the changes of the lipid membranes, the cell realization occurred, and the morphologies and top surface structures of the cells were changed.

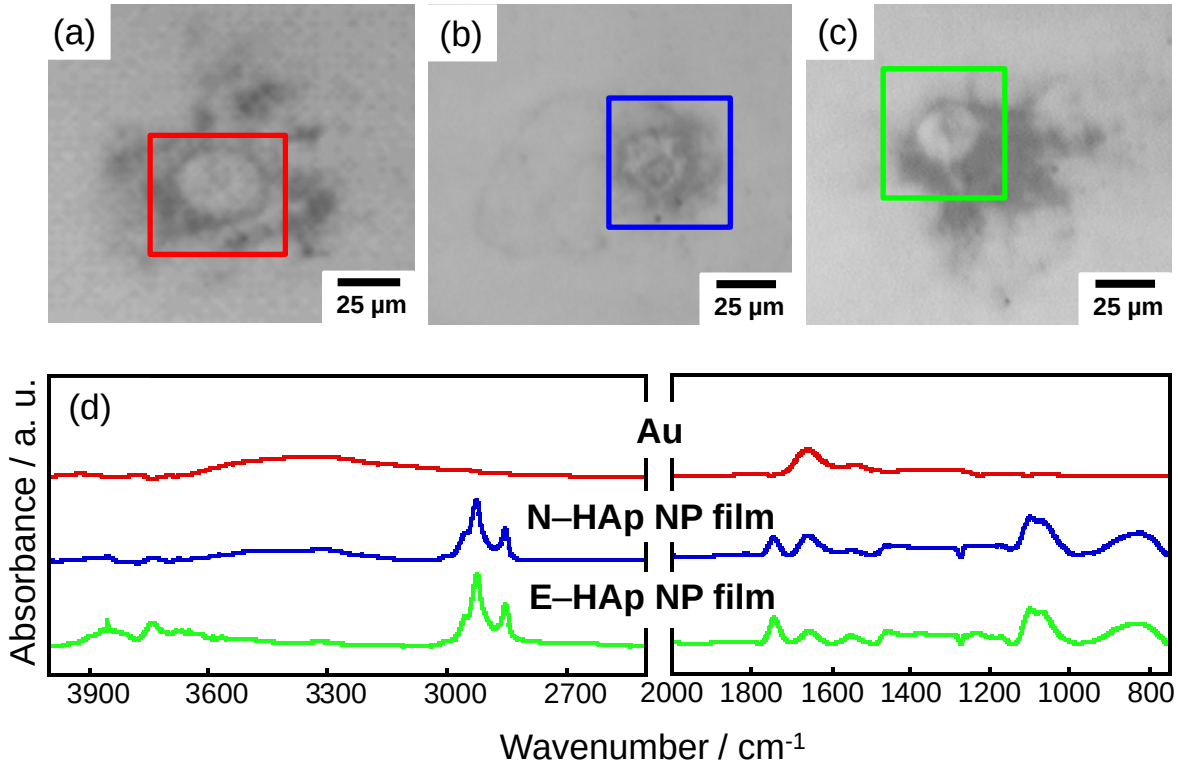

Figure 2.22. Microscope photographs of the inner surfaces of the cells adhered on (a) Au, (b) N–HAp and (c) E–HAp NP films , and the measured areas (aperture size: 50 × 50 mm^2, screen size: 359 × 476 mm^2) by a FT–IR microscopy were represented by the square marks and their spectra were shown in (d).

The FT–IR microscopy spectra of the measured areas (aperture size: 50 × 50 mm^2, screen size: 359 × 476 mm^2) of the outer surface of the cells adhered on Au, N–HAp and E–HAp NP films at two hours of culture are shown in **Figure 2.23**. The intensity of the bands at 3500 and 3300 cm^{-1} corresponding to N–H hydrogen bonded and N–H stretching of the amide A were higher for Au and E–HAp NP film and very low for N–HAp NP film. The corresponding bands assignment for the microscope FT–IR spectra of the cells on HAp NP films was shown in **Table 2.5**. The bands at 2960, 2925, 2873 cm^{-1}, assigned to C–H stretching band of the alkyl chain were more pronounced o0n N–HAp NP film, followed by E–HAp NP film, less pronounced in Au film. The intensity of the C=O stretching of the amide I at 1660 cm^{-1} and the intensity of the band of N–H bending and C–N stretching of the amide II at 1540 cm^{-1} showed higher intensity in E–HAp NP film, followed by Au film, and finally N–HAp NP film. The band at 1262 cm^{-1} that corresponds to the deformation of the N–H of the amide III showed higher intensity for N–HAp NP film, less intense for E–HAp NP film and the lowest intensity in Au film.

The presence of alcohol groups at 1170 cm^{-1} was only observed on the HAp NP films.[147,154,155] The outer surface of the cell is related to the extracellular matrix (ECM) proteins (such as collagen, fibrinogen, fibronectin, laminin, vitronectin).[148] These proteins play an important role in cell structure, and also favor the cell adhesion, spreading, and migration. In the interface of the cell and the ECM, the cytoskeleton of the cell, formed mainly of collagen, is formed, which is important contributes to adhesion and cell migration and to give the shape to the cell.[156]

The amide A, I, II and III showed different behavior in all the films which suggest that the cells in each film was binding with different adhesion protein of the ECM. It has been suggested that the cellular adhesion proteins of the ECM bind to proteins with the same conformation,[150] this is in agreement with our results because in each film, the amount of water adsorbed in the hydration layer modified the conformation of the Fgn adsorbed so that each conformation will bind to a different protein from the ECM.

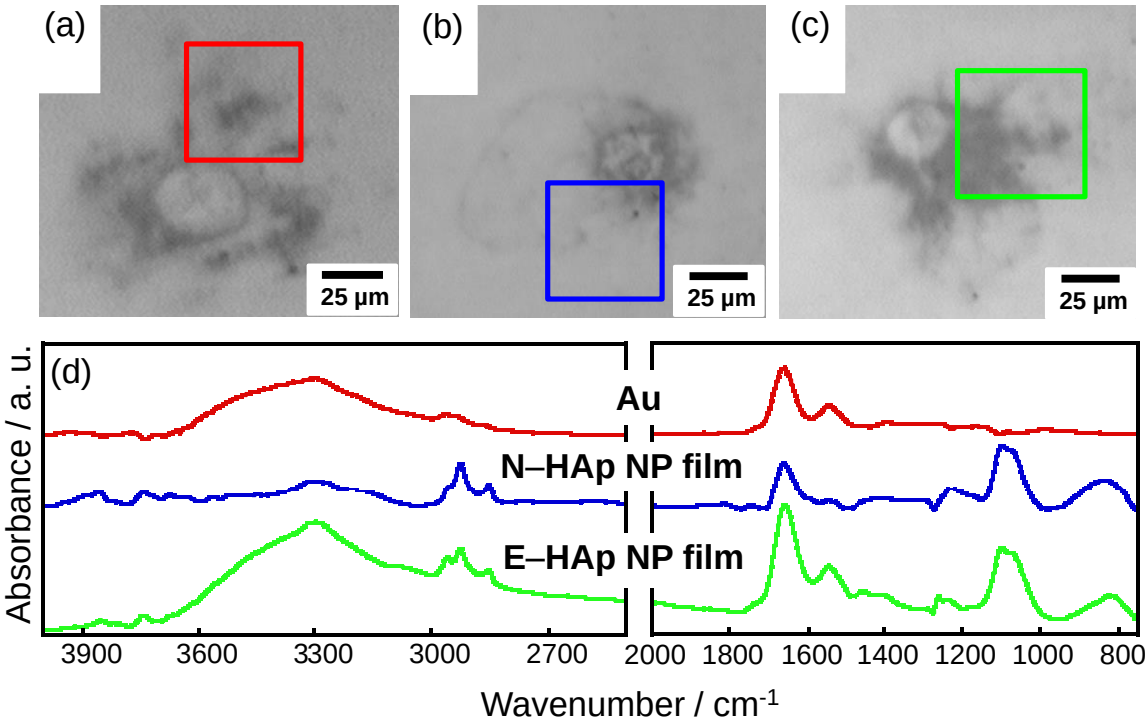

Figure 2.23. Microscope photographs of the outer area surfaces producing ECM at around the cells adhered on (a) Au, (b) N–HAp and (c) E–HAp NP films, and the measured areas (aperture size: 50 × 50 mm^2, screen size: 359 × 476 mm^2) by a FT–IR microscopy were represented by the square marks and their spectra were shown in (d).

Table 2.5. The corresponding bands assignment of microscope FT–IR spectrum of the cells on HAp NP films and Au film.

FT–IR peak (cm^{-1})	Bands assignment	Relations ship between inner and outer surface
3500	hydrogen bonded N–H	Inner < Outer
3300	N–H stretching of amide A	Inner < Outer
2960, 2925, 2873, 2853	(C–H stretching) Alkyl chain	Inner > Outer
1745	Stretching vibrations of –COOH or H_2O	Inner > Outer
1660	(Amide I (C=O stretching))	Inner < Outer
1540	(Amide II (N–H bending/C–N stretching))	Inner < Outer
1460, 1395	Scissoring of C–H_2 wag, v_s COO^- stretching	Inner > Outer
1262	(Amide III (N–H deformation))	Inner < Outer
1235	(P=O) Phospholipids in cell membrane	
1170	Presence of alcohol groups	Inner > Outer
1080	PSox	
840 or 828	Phosphate ions	Inner < Outer

2.3.7. Observation of Immunostaining State of Collagen Type I

The immunostaining results of the type I collagen in the fibroblasts cultured on Au, N–HAp and E–HAp NP films at 120 min conducted by fraction of continuously labeled mitoses (FCLSM) were shown in **Figure 2.25**. The immunostaining of the collagen type I in the fibroblasts at the culture time of 2 h was observed by a fluorescent confocal laser scanning microscopy (FCLSM). All the cells exhibited the fluorescence from the cells, indicating the cellular producing of the collagen type I.[157,158] The fluorescent intensity of the cell on the Au substrate was lower than those on the HAp NP films.

The result is in good agreement with those of the different band intensities of the alkyl chain and the amide II and III bands in the FT–IR spectra, suggesting the abundant collagen type I formation in the cells by the underground HAp NP films.[159] All the adhered cells exhibited the pseudopod formation, demonstrating the production of the ECM proteins with arranging the cytoskeleton.[160]

In particular, the cells adhered on the E–HAp NP film showed the highest number of pseudopod (6 pseudopodium), although those on the N–HAp NP film and Au substrate were shorter extension states with the lower florescence intensity. The results in the different number of pseudopod and fluorescent intensity of the cells are in concordance with those of the FT–IR spectra of the outer surface of the cells (i.e., the different intensities of the alkyl chains, the amide II and III bands). The pseudopodia on the E–HAp NP film were longer extension states, which would be affected by the producing activity of collagen type I. Therefore, the preferential affinity of the cells with the underground surface layers (i.e., the hydration and subsequent protein adsorption layer) on the E–HAp NP film is demonstrated to form the interfacial interactions based on the abundant connective proteins (e.g., collagen type I) and spread with the greater number of pseudopods.

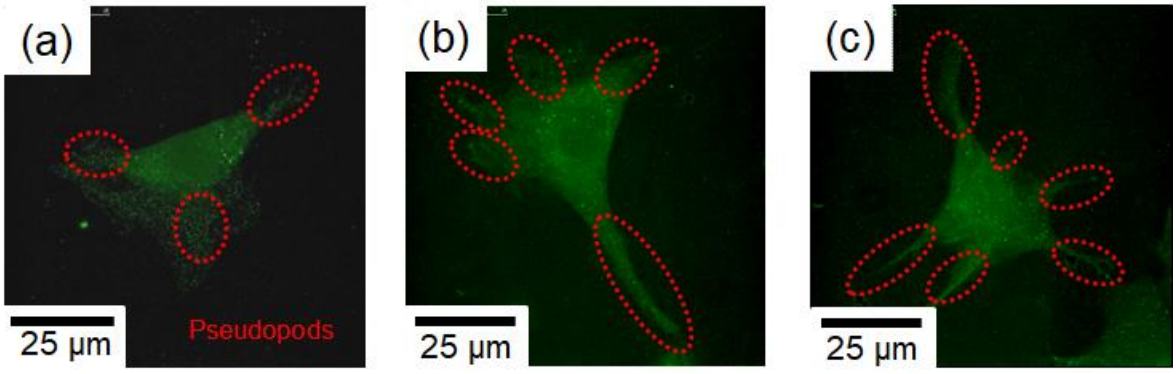

Figure 2.24. Fluorescent microscope images of the cells adhered on (a) Au, (b) N–HAp and (c) E–HAp NP films. The cells were stained with the polyclonal rabbit anti-mouse collagen type I α2 chain as a primary antibody and the FITC–labeled IgG as a secondary antibody. The pseudopods were circulated by a red-colored dot line, indicating the existence of the spread and sharpest pseudopods on the E–HAp NP film.

2.4. Conclusion

The chain length (*n*) of the poly(oxyethylene)cholesteryl ether (ChEO*n* (*n*= 15)) used in the HAp synthesis allows to control the formation of the HAp NPs based on the organic/inorganic hybrids, leading to be the elliptical E–HAp NPs. The added amount of ChEO*n* during the synthesis plays an important role in the shape, porosity and surface specific area of the E–HAp NPs, which had the direct impact on the Fgn−surface interactions and the conformation of the adsorbed Fgn. The SPR was used to study the Fgn−surface interactions in a comparative study between the Au, N–HAp and E– HAp NP film.

A comparative study of the hydration layer on E–HAp, N–HAp NP films and Au substrate was achieved in order to investigate the interfacial effect of the hydration layers on the conformation of the adsorbed Fgn and fibroblast adhesion properties. It was demonstrated that the wettability of the Au substrate after a UV/O_3 treatment was useful for the EPD deposition of the HAp NPs. The deposition of the HAp NPs on the Au substrate was corroborated by the AFM images, where was observed as the different morphologies of the E–HAp and N–HAp NPs. The ratios of three types of hydration layer states analyzed by a Fourier transform infrared (FT–IR) spectral deconvolution of the O–H stretching absorption band were 3 %, 53 % and 60 % as free water, 0 %, 27 % and 30 % as intermediate water, and 97 %, 20 % and 10 % as non–freezing water. Although the ratio of bonding water state (i.e., intermediate and non–freezing waters) is almost same between two HAp NP films, the E–HAp NP film with the elliptical shape and smaller particle size exhibited the smallest ratio of non–freezing water, which can suppress the denaturation of the adsorbed protein. Subsequently, the FTIIR spectral deconvolution results of the amide I band of the adsorbed Fgn on the E–HAp NP film indicated the higher content of α–helix and β–sheet secondary structures as compared with those on the N–HAp NP and Au films, suggesting that the smaller amount of non–freezing waters would play an important role in the stereoscopic Fgn conformation. Furthermore, the higher content of free water molecules on the E–HAp NP film would promote the perpendicular end–on orientation of the adsorbed Fgn. In contrast, the Au and N–HAp NP films with the lower content of non–freezing water would promote the loss of α–helix and β–sheet structures, due to the side–on orientation, which causes the denaturation based on the loss of stereoscopic conformation.

In the fibroblast culture on the films, the adhered cells started spreading with pseudopods formation in all the films. The cells had a more elongated appearance and had more pseudopod parts on E–HAp NP film than those on the N–HAp NP and Au films. The FT–IR spectra the adhered cells on the E–HAp NP, N–HAp NP and Au films exhibited the different absorbance intensities in the amide A, I, II, and III bands, suggesting the different amount of collagen producing states by the cells interacted with the underground films, which were also supported by an immunostaining results of the collagen type I. Therefore, the different hydration structures on the films clearly influenced the conformation of the adsorbed protein, and the preferential conformation was found at the interfaces between the fibroblasts and the underground E–HAp NP films by promoting the different ECM protein production and subsequent preferential binding.

References

(1) Okada, M.; Furuzono, T. Hydroxylapatite Nanoparticles: Fabrication Methods and Medical Applications. *Sci. Technol. Adv. Mater.* **2012**, *13* (6), 064103.

(2) Dorozhkin, S. Calcium Orthophosphates in Nature, Biology and Medicine. *Materials (Basel).* **2009**, *2* (2), 399–498.

(3) Komlev, V. S.; Barinov, S. M.; Girardin, E.; Oscarsson, S.; Rosengren, Å.; Rustichelli, F.; Orlovskii, V. P. Porous Spherical Hydroxyapatite and Fluorhydroxyapatite Granules: Processing and Characterization. *Sci. Technol. Adv. Mater.* **2003**, *4* (6), 503–508.

(4) Aoki; H. Science and Medical Applications of Hydroxyapatite. *JAA* **1991**, 123–134.

(5) Karageorgiou, V.; Kaplan, D. Porosity of 3D Biomaterial Scaffolds and Osteogenesis. *Biomaterials* **2005**, *26* (27), 5474–5491.

(6) Jarcho, M. Calcium Phosphate Ceramics as Hard Tissue Prosthetics. *Clin. Orthop. Relat. Res.* **1981**, No. 157, 259–278.

(7) Dorozhkin, S. V.; Epple, M. Biological and Medical Significance of Calcium Phosphates. *Angew. Chemie Int. Ed.* **2002**, *41* (17), 3130–3146.

(8) Gopi, D.; Indira, J.; Nithiya, S.; Kavitha, L.; Mudali, U. K.; Kanimozhi, K. Influence of Surfactant Concentration on Nanohydroxyapatite Growth. *Bull. Mater. Sci.* **2013**, *36* (5), 799–805.

(9) Sadat-Shojai, M.; Khorasani, M.-T.; Dinpanah-Khoshdargi, E.; Jamshidi, A. Synthesis Methods for Nanosized Hydroxyapatite with Diverse Structures. *Acta Biomater.* **2013**, *9* (8), 7591–7621.

(10) Yang, J. H.; Kim, K. H.; You, C. K.; Rautray, T. R.; Kwon, T. Y. Synthesis of Spherical Hydroxyapatite Granules with Interconnected Pore Channels Using Camphene Emulsion. *J. Biomed. Mater. Res. Part B Appl. Biomater.* **2011**, *99B* (1), 150–157.

(11) Bernhardt, A.; Dittrich, R.; Lode, A.; Despang, F.; Gelinsky, M. Nanocrystalline

Spherical Hydroxyapatite Granules for Bone Repair: In Vitro Evaluation with Osteoblast-like Cells and Osteoclasts. *J. Mater. Sci. Mater. Med.* **2013**, *24* (7), 1755–1766.

(12) Paul, W.; Sharma, C. P. Development of Porous Spherical Hydroxyapatite Granules: Application towards Protein Delivery. *J. Mater. Sci. Mater. Med.* **1999**, *10* (7), 383–388.

(13) Komlev, V. S.; Barinov, S. M.; Koplik, E. V. A Method to Fabricate Porous Spherical Hydroxyapatite Granules Intended for Time-Controlled Drug Release. *Biomaterials* **2002**, *23* (16), 3449–3454.

(14) Ribeiro, C. C.; Barrias, C. C.; Barbosa, M. A. Preparation and Characterisation of Calcium-Phosphate Porous Microspheres with a Uniform Size for Biomedical Applications. *J. Mater. Sci. Mater. Med.* **2006**, *17* (5), 455–463.

(15) Hong, M. H.; Son, J. S.; Kim, K. M.; Han, M.; Oh, D. S.; Lee, Y. K. Drug-Loaded Porous Spherical Hydroxyapatite Granules for Bone Regeneration. *J. Mater. Sci. Mater. Med.* **2011**, *22* (2), 349–355.

(16) Misiek, D. J.; Kent, J. N.; Carr, R. F. Soft Tissue Responses to Hydroxylapatite Particles of Different Shapes. *J. Oral Maxillofac. Surg.* **1984**, *42* (3), 150–160.

(17) Douglas, T.; Liu, Q.; Humpe, A.; Wiltfang, J.; Sivananthan, S.; Warnke, P. H. Novel Ceramic Bone Replacement Material CeraBall Seeded with Human Mesenchymal Stem Cells. *Clin. Oral Implants Res.* **2010**, *21* (3), 262–267.

(18) Bose, S.; Saha, S. K. Synthesis and Characterization of Hydroxyapatite Nanopowders by Emulsion Technique. *Chem. Mater.* **2003**, *15* (23), 4464–4469.

(19) Lim, G. K.; Wang, J.; Ng, S. C.; Gan, L. M. Nanosized Hydroxyapatite Powders from Microemulsions and Emulsions Stabilized by a Biodegradable Surfactant. *J. Mater. Chem.* **1999**, *9* (7), 1635–1639.

(20) Mohandes, F.; Salavati-Niasari, M. Simple Morphology-Controlled Fabrication of Hydroxyapatite Nanostructures with the Aid of New Organic Modifiers. *Chem. Eng. J.* **2014**, *252*, 173–184.

(21) Sato, T.; Hossain, M. K.; Acharya, D. P.; Glatter, O.; Chiba, A.; Kunieda, H. Phase Behavior and Self-Organized Structures in Water/Poly(Oxyethylene) Cholesteryl Ether Systems. *J. Phys. Chem. B* **2004**, *108* (34), 12927–12939.

(22) Takahashi, S.; Ikkai, Y.; Rodriguez-Abreu, C.; Aramaki, K.; Ohsuna, T.; Sakamoto, K. Application of a Water Soluble Alkoxysilane for the Formation of Mesoporous Silica from Nonionic Surfactant Micelles Bearing Cholesterol. *Chem. Lett.* **2007**, *36* (1), 182–183.

(23) Solans, C.; Solé, I. Nano-Emulsions: Formation by Low-Energy Methods. *Curr. Opin. Colloid Interface Sci.* **2012**, *17* (5), 246–254.

(24) Sagitani, H. Making Homogeneous and Fine Droplet O/W Emulsions Using Nonionic Surfactants. *J. Am. Oil Chem. Soc.* **1981**, *58* (6), 738–743.

(25) Tagaya, M.; Ikoma, T.; Hanagata, N.; Tanaka, J. Analytical Investigation of Protein Mediation Between Biomaterials and Cells. *Mater. Express* **2012**, *2* (1), 1–22.

(26) Tagaya, M. In Situ QCM-D Study of Nano-Bio Interfaces with Enhanced Biocompatibility. *Polym. J.* **2015**, *47* (9), 599–608.

(27) Roach, P.; Farrar, D.; Perry, C. C. Interpretation of Protein Adsorption: Surface-Induced Conformational Changes. *J. Am. Chem. Soc.* **2005**, *127* (22), 8168–8173.

(28) Tagaya, M.; Ikoma, T.; Takemura, T.; Hanagata, N.; Yoshioka, T.; Tanaka, J. Effect

of Interfacial Proteins on Osteoblast-like Cell Adhesion to Hydroxyapatite Nanocrystals. *Langmuir* **2011**, *27* (12), 7645–7653.

(29) Tagaya, M.; Ikoma, T.; Hanagata, N.; Yoshioka, T.; Tanaka, J. Competitive Adsorption of Fibronectin and Albumin on Hydroxyapatite Nanocrystals. *Sci. Technol. Adv. Mater.* **2011**, *12* (3), 034411.

(30) Gumbiner B. Cell Adhesion: The Molecular Basis of Tissue Architecture and Morphogenesis. *Cell* **1996**, *84*, 345–357.

(31) Ngandu Mpoyi, E.; Cantini, M.; Reynolds, P. M.; Gadegaard, N.; Dalby, M. J.; Salmerón-Sánchez, M. Protein Adsorption as a Key Mediator in the Nanotopographical Control of Cell Behavior. *ACS Nano* **2016**, *10* (7), 6638–6647.

(32) Alberts, B.; Johnson, A.; Lewis, J.; Raff, M.; Roberts, K.; Walter, P. *Molecular Biology of the Cell*; Garland Science, **2002**.

(33) Wang, X.; Chang, J.; Wu, C. Bioactive Inorganic/Organic Nanocomposites for Wound Healing. *Appl. Mater. Today* **2018**, *11*, 308–319.

(34) Rico, P.; Cantini, M.; Altankov, G.; Salmerón-Sánchez, M. Matrix Protein Interactions with Synthetic Surfaces. In *Polymers in Regenerative Medicine*; John Wiley & Sons, Inc: Hoboken, NJ, **2015**; pp 91–146.

(35) Cooke, M. J.; Phillips, S. R.; Shah, D. S. H.; Athey, D.; Lakey, J. H.; Przyborski, S. A. Enhanced Cell Attachment Using a Novel Cell Culture Surface Presenting Functional Domains from Extracellular Matrix Proteins. *Cytotechnology* **2008**, *56* (2), 71–79.

(36) Ikoma, T.; Tagaya, M.; Hanagata, N.; Yoshioka, T.; Chakarov, D.; Kasemo, B.; Tanaka, J. Protein Adsorption on Hydroxyapatite Nanosensors with Different Crystal Sizes Studied *In Situ* by a Quartz Crystal Microbalance with the Dissipation Method. *J. Am. Ceram. Soc.* **2009**, *92* (5), 1125–1128.

(37) Tagaya, M.; Ikoma, T.; Takemura, T.; Migita, S.; Okuda, M.; Yoshioka, T.; Hanagata, N.; Tanaka, J. Initial Adhesion Behavior of Fibroblasts onto Hydroxyapatite Nanocrystals. *Bioceram. Dev. Appl.* **2011**, *1*, 1–4.

(38) Monkawa, A.; Ikoma, T.; Yunoki, S.; Yoshioka, T.; Tanaka, J.; Chakarov, D.; Kasemo, B. Fabrication of Hydroxyapatite Ultra-Thin Layer on Gold Surface and Its Application for Quartz Crystal Microbalance Technique. *Biomaterials* **2006**, *27* (33), 5748–5754.

(39) Tunc, S.; Maitz, M. F.; Steiner, G.; Vázquez, L.; Pham, M. T.; Salzer, R. In Situ Conformational Analysis of Fibrinogen Adsorbed on Si Surfaces. *Colloids Surfaces B Biointerfaces* **2005**, *42* (3–4), 219–225.

(40) Roach, P.; Farrar, D.; Perry, C. C. Surface Tailoring for Controlled Protein Adsorption: Effect of Topography at the Nanometer Scale and Chemistry. *J. Am. Chem. Soc.* **2006**, *128* (12), 3939–3945.

(41) Tagaya, M.; Ikoma, T.; Hanagata, N.; Chakarov, D.; Kasemo, B.; Tanaka, J. Reusable Hydroxyapatite Nanocrystal Sensors for Protein Adsorption. *Sci. Technol. Adv. Mater.* **2010**, *11* (4), 045002.

(42) Green, R. J.; Frazier, R. A.; Shakesheff, K. M.; Davies, M. C.; Roberts, C. J.; Tendler, S. J. . Surface Plasmon Resonance Analysis of Dynamic Biological Interactions with Biomaterials. *Biomaterials* **2000**, *21* (18), 1823–1835.

(43) Chong, S. H.; Ham, S. Dynamics of Hydration Water Plays a Key Role in Determining the Binding Thermodynamics of Protein Complexes. *Sci. Rep.* **2017**, *7*

(1), 1–10.
(44) Papoian, G. A.; Ulander, J.; Wolynes, P. G. Role of Water Mediated Interactions in Protein-Protein Recognition Landscapes. *J. Am. Chem. Soc.* **2003**, *125* (30), 9170–9178.
(45) Huggins, D. J.; Marsh, M.; Payne, M. C. Thermodynamic Properties of Water Molecules at a Protein-Protein Interaction Surface. *J. Chem. Theory Comput.* **2011**, *7* (11), 3514–3522.
(46) Chen, S.; Li, L.; Zhao, C.; Zheng, J. Surface Hydration: Principles and Applications toward Low-Fouling/Nonfouling Biomaterials. *Polymer (Guildf).* **2010**, *51* (23), 5283–5293.
(47) Tanaka, M.; Mochizuki, A. Effect of Water Structure on Blood Compatibility - Thermal Analysis of Water in Poly(Meth)Acrylate. *J. Biomed. Mater. Res. - Part A* **2004**, *68* (4), 684–695.
(48) Tanaka, M.; Motomura, T.; Ishii, N.; Shimura, K.; Onishi, M.; Mochizuki, A.; Hatakeyama, T. Cold Crystallization of Water in Hydrated Poly(2-Methoxyethyl Acrylate) (PMEA). *Polym. Int.* **2000**, *49* (12), 1709–1713.
(49) Li, L.; Chen, S.; Zheng, J.; Ratner, B. D.; Jiang, S. Protein Adsorption on Oligo(Ethylene Glycol)-Terminated Alkanethiolate Self-Assembled Monolayers: The Molecular Basis for Nonfouling Behavior. *J. Phys. Chem. B* **2005**, *109* (7), 2934–2941.
(50) Yang, Q.; Zhang, Y.; Liu, M.; Ye, M.; Zhang, Y. Q.; Yao, S. Study of Fibrinogen Adsorption on Hydroxyapatite and TiO_2 Surfaces by Electrochemical Piezoelectric Quartz Crystal Impedance and FTIR-ATR Spectroscopy. *Anal. Chim. Acta* **2007**, *597* (1), 58–66.
(51) Peñaflor Galindo, T. G.; Kataoka, T.; Fujii, S.; Okuda, M.; Tagaya, M. Preparation of Nanocrystalline Zinc-Substituted Hydroxyapatite Films and Their Biological Properties. *Colloid Interface Sci. Commun.* **2016**, *10*, 15–19.
(52) Drits, V.; Środoń, J.; Eberl, D. D. XRD Measurement of Mean Crystallite Thickness of Illite and Illite/Smectite: Reappraisal of the Kubler Index and the Scherrer Equation. *Clays Clay Miner.* **1997**, *45* (3), 461–475.
(53) Brunauer, S.; Emmett, P. H.; Teller, E. *Adsorption of Gases in Multimolecular Layers*. *J. Am. Chem. Soc*. **1938**, *60* (2), 309–319.
(54) Barrett, E. P.; Joyner, L. G.; Halenda Vol, P. P.; -RnAtn Apj, R.; Vn-Rn Atn Ac, R. A. *Vp2 = R2AV2-R2AT2 ACi Generalizing Equation (4) and Substituting (6a) for Vm* Yields*.
(55) Willmott, G. R.; Vogel, R.; Yu, S. S. C.; Groenewegen, L. G.; Roberts, G. S.; Kozak, D.; Anderson, W.; Trau, M. Use of Tunable Nanopore Blockade Rates to Investigate Colloidal Dispersions. *J. Phys. Condens. Matter* **2010**, *22* (45), 454116.
(56) Kozak, D.; Anderson, W.; Vogel, R.; Chen, S.; Antaw, F.; Trau, M. Simultaneous Size and ζ-Potential Measurements of Individual Nanoparticles in Dispersion Using Size-Tunable Pore Sensors. *ACS Nano* **2012**, *6* (8), 6990–6997.
(57) De Aragão, B. J. G.; Messaddeq, Y. Peak Separation by Derivative Spectroscopy Applied to FTIR Analysis of Hydrolized Silica. *J. Braz. Chem. Soc.* **2008**, *19* (8), 1582–1594.
(58) Tanaka, M.; Hayashi, T.; Morita, S. The Roles of Water Molecules at the Biointerface of Medical Polymers. *Polym. J.* **2013**, *45* (7), 701–710.

(59) Westra, K. L.; Thomson, D. J. Effect of Tip Shape on Surface Roughness Measurements from Atomic Force Microscopy Images of Thin Films. *J. Vac. Sci. Technol. B Microelectron. Nanom. Struct.* **1995**, *13* (2), 344.

(60) Reimhult, E.; Larsson, C.; Kasemo, B.; Höök, F. Simultaneous Surface Plasmon Resonance and Quartz Crystal Microbalance with Dissipation Monitoring Measurements of Biomolecular Adsorption Events Involving Structural Transformations and Variations in Coupled Water. *Anal. Chem.* **2004**, *76* (24), 7211–7220.

(61) Hall, D. R.; Winzor, D. J. Use of a Resonant Mirror Biosensor to Characterize the Interaction of Carboxypeptidase A with an Elicited Monoclonal Antibody. *Anal. Biochem.* **1997**, *244* (1), 152–160.

(62) Morton, T. A.; Myszka, D. G.; Chaiken, I. M. Interpreting Complex Binding Kinetics from Optical Biosensors: A Comparison of Analysis by Linearization, the Integrated Rate Equation, and Numerical Integration. *Anal. Biochem.* **1995**, *227* (1), 176–185.

(63) Yamada, S.; Tagaya, M. Analytical Investigation of Hydration and Protein Adsorption Structures on Hydroxyapatite-Based Mesoporous Silica Particles. *Mater. Lett.* **2017**, *209*, 441–445.

(64) SAUERBREY; G. The Use of Quarts Oscillators for Weighing Thin Layers and for Microweighing. *Z. Phys.* **1959**, *155*, 206–222.

(65) Rodahl, M.; Kasemo, B. On the Measurement of Thin Liquid Overlayers with the Quartz-Crystal Microbalance. *Sensors Actuators A Phys.* **1996**, *54* (1–3), 448–456.

(66) Höök, F.; Kasemo, B.; Nylander, T.; Camilla Fant; Kristin Sott, and; Elwing, H. Variations in Coupled Water, Viscoelastic Properties, and Film Thickness of a Mefp-1 Protein Film during Adsorption and Cross-Linking: A Quartz Crystal Microbalance with Dissipation Monitoring, Ellipsometry, and Surface Plasmon Resonance Study. *Anal Chem.* **2001**, *73* (24), 5796–5804.

(67) Malmström, J., Agheli, H., Kingshott, P.; Sutherland, D. S. Viscoelastic Modeling of Highly Hydrated Laminin Layers at Homogeneous and Nanostructured Surfaces: Quantification of Protein Layer Properties Using QCM-D and SPR. *Langmuir* **2007**, *23* (19), 9760–9768.

(68) Tagaya, M.; Ikoma, T.; Takeguchi, M.; Hanagata, N.; Tanaka, J. Interfacial Serum Protein Effect on Biological Apatite Growth. *J. Phys. Chem. C* **2011**, *115* (45), 22523–22533.

(69) Tagaya, M.; Ikoma, T.; Takemura, T.; Hanagata, N.; Okuda, M.; Yoshioka, T.; Tanaka, J. Detection of Interfacial Phenomena with Osteoblast-like Cell Adhesion on Hydroxyapatite and Oxidized Polystyrene by the Quartz Crystal Microbalance with Dissipation. *Langmuir* **2011**, *27* (12), 7635–7644.

(70) Wang, X.; Zhang, L.; Liu, Z.; Zeng, Q.; Yang, M. Probing the Surface Structure of Hydroxyapatite through Its Interaction with Hydroxyl: A First-Principles Study . *RSC Adv.* **2018**, *8* (7), 3716–3722.

(71) Meejoo, S.; Maneeprakorn, W.; Winotai, P. Phase and thermal stability of nanocrystalline hydroxyapatite prepared via microwave heating. *Thermochim. Acta.* **2006**, *447* (1), 115–120.

(72) Ma, M. G. Hierarchically Nanostructured Hydroxyapatite: Hydrothermal Synthesis, Morphology Control, Growth Mechanism, and Biological Activity. *Int. J.*

Nanomedicine **2012**, *7*, 1781–1791.
(73) Gheisari, H.; Karamian, E.; Abdellahi, M. A Novel Hydroxyapatite -Hardystonite Nanocomposite Ceramic. *Ceram. Int.* **2015**, *41* (4), 5967–5975.
(74) Panda, R. N.; Hsieh, M. F.; Chung, R. J.; Chin, T. S. FTIR, XRD, SEM and Solid State NMR Investigations of Carbonate-Containing Hydroxyapatite Nano-Particles Synthesized by Hydroxide-Gel Technique. *J. Phys. Chem. Solids* **2003**, *64* (2), 193–199.
(75) Arsad, M. S. M.; Lee, P. M. Synthesis and Characterization of Hydroxyapatite Nanoparticles and β-TCP Particles. *2nd Int. Conf. Biotechnol. Food Sci.* **2011**, *7*, 184–188.
(76) Mondal, S.; Dey, A.; Pal, U. Low Temperature Wet-Chemical Synthesis of Spherical Hydroxyapatite Nanoparticles and Their in Situ Cytotoxicity Study. *Adv. nano Res.* **2016**, *4* (4), 295–307.
(77) Berzina-Cimdina, L.; Borodajenko, N. Research of Calcium Phosphates Using Fourier Transform Infrared Spectroscopy. *Infrared Spectrosc. - Mater. Sci. Eng. Technol.* **2012**, *12* (7), 251–263.
(78) Ślósarczyk, A.; Paszkiewicz, Z.; Paluszkiewicz, C. FTIR and XRD Evaluation of Carbonated Hydroxyapatite Powders Synthesized by Wet Methods. *J. Mol. Struct.* **2005**, *744–747*, 657–661.
(79) Wang, A.; Yin, H.; Liu, D.; Wu, H.; Wada, Y.; Ren, M.; Xu, Y.; Jiang, T.; Cheng, X. Effects of Organic Modifiers on the Size-Controlled Synthesis of Hydroxyapatite Nanorods. *Appl. Surf. Sci.* **2007**, *253* (6), 3311–3316.
(80) Sato, T.; Hossain, M. K.; Acharya, D. P.; Glatter, O.; Chiba, A.; Kunieda, H. Phase Behavior and Self-Organized Structures in Water/Poly(Oxyethylene) Cholesteryl Ether Systems. *J. Phys. Chem. B* **2004**, *108* (34), 12927–12939.
(81) Lim, G. K.; Wang, J.; Ng, S. C.; Gan, L. M. Formation of Nanocrystalline Hydroxyapatite in Nonionic Surfactant Emulsions. *Langmuir* **1999**, *15* (22), 7472–7477.
(82) Lim, G. K.; Wang, J.; Ng, S. C.; Chew, C. H.; Gan, L. M. Processing of Hydroxyapatite via Microemulsion and Emulsion Routes. *Biomaterials* **1997**, *18* (21), 1433–1439.
(83) Chen, C.-W.; Riman, R. E.; TenHuisen, K. S.; Brown, K. Mechanochemical–Hydrothermal Synthesis of Hydroxyapatite from Nonionic Surfactant Emulsion Precursors. *J. Cryst. Growth* **2004**, *270* (3–4), 615–623.
(84) Kataoka, T.; Shiba, K.; Tagaya, M. Preparation of Europium(III)-Doped Hydroxyapatite Nanocrystals in the Presence of Cationic Surfactant. *Colloid Interface Sci. Commun.* **2016**, *13*, 1–5.
(85) Zuo, G.; Wei, X.; Sun, H.; Liu, S.; Zong, P.; Zeng, X.; Shen, Y. Morphology Controlled Synthesis of Nano-Hydroxyapatite Using Polyethylene Glycol as a Template. *J. Alloys Compd.* **2017**, *692*, 693–697.
(86) Zhang, W.; Huang, Z.-L.; Liao, S.-S.; Cui, F.-Z. Nucleation Sites of Calcium Phosphate Crystals during Collagen Mineralization. *J. Am. Ceram. Soc.* **2003**, *86* (6), 1052–1054.
(87) Lim, G. K.; Wang, J.; Ng, S. C.; Gan, L. M. Nanosized Hydroxyapatite Powders from Microemulsions and Emulsions Stabilized by a Biodegradable Surfactant. *J. Mater. Chem.* **1999**, *9* (7), 1635–1639.

(88) Rouquerol, J.; Rouquerol, F.; Llewellyn, P.; Maurin, G.; Sing, K. S. W. *Adsorption by Powders and Porous Solids : Principles, Methodology, and Applications*; Academic Press, **1999**.

(89) Wang, X.; Andrews, L. Gold Is Noble but Gold Hydride Anions Are Stable. *Angew. Chemie - Int. Ed.* **2003**, *42* (42), 5201–5206.

(90) Stadlober, B.; Haas, U.; Gold, H.; Haase, A.; Jakopic, G.; Leising, G.; Koch, N.; Rentenberger, S.; Zojer, E. Orders-of-Magnitude Reduction of the Contact Resistance in Short-Channel Hot Embossed Organic Thin Film Transistors by Oxidative Treatment of Au-Electrodes. *Adv. Funct. Mater.* **2007**, *17* (15), 2687–2692.

(91) Klyushin, A. Y.; Rocha, T. C. R.; Hävecker, M.; Knop-Gericke, A.; Schlögl, R. A near Ambient Pressure XPS Study of Au Oxidation. *Phys. Chem. Chem. Phys.* **2014**, *16* (17), 7881–7886.

(92) Cherevko, S.; Topalov, A. A.; Zeradjanin, A. R.; Katsounaros, I.; Mayrhofer, K. J. J. Gold Dissolution: Towards Understanding of Noble Metal Corrosion. *RSC Adv.* **2013**, *3* (37), 16516–16527.

(93) Chen, J.; Pidko, E. A.; Ordomsky, V. V.; Verhoeven, T.; Hensen, E. J. M.; Schouten, J. C.; Nijhuis, T. A. How Metallic Is Gold in the Direct Epoxidation of Propene: An FTIR Study. *Catal. Sci. Technol.* **2013**, *3* (11), 3042–3055.

(94) Galindo, T. G. P.; Kataoka, T.; Tagaya, M. Morphosynthesis of Zn-Substituted Stoichiometric and Carbonate Hydroxyapatite Nanoparticles and Their Cytotoxicity in Fibroblasts. *J. Nanomater.* **2015**, *16* (1), *360*.

(95) Xiao, X. F.; Liu, R. F. Effect of Suspension Stability on Electrophoretic Deposition of Hydroxyapatite Coatings. *Mater. Lett.* **2006**, *60* (21–22), 2627–2632.

(96) Eliaz, N.; Sridhar, T. M.; Kamachi Mudali, U.; Raj, B. Electrochemical and Electrophoretic Deposition of Hydroxyapatite for Orthopaedic Applications. *Surf. Eng.* **2005**, *21* (3), 238–242.

(97) Farnoush, H.; Aghazadeh Mohandesi, J.; Haghshenas Fatmehsari, D.; Moztarzadeh, F. A Kinetic Study on the Electrophoretic Deposition of Hydroxyapatite–Titania Nanocomposite Based on a Statistical Approach. *Ceram. Int.* **2012**, *38* (8), 6753–6767.

(98) Drescher, D. G.; Selvakumar, D.; Drescher, M. J. Analysis of Protein Interactions by Surface Plasmon Resonance. *Adv. Protein Chem. Struct. Biol.* **2018**, *110*, 1–30.

(99) Zhang, Y.; Xu, H. H. K.; Takagi, S.; Chow, L. C. In-Situ Hardening Hydroxyapatite-Based Scaffold for Bone Repair. *J. Mater. Sci. Mater. Med.* **2006**, *17* (5), 437–445.

(100) Szunerits, S.; Boukherroub, R.; Boukherroub, R. *Introduction to Plasmonics*; Szunerits, S., Boukherroub, R., Eds.; Jenny Stanford Publishing, **2015**.

(101) Bystrov, V. S.; Paramonova, E.; Dekhtyar, Y.; Katashev, A.; Karlov, A.; Polyaka, N.; Bystrova, A. V.; Patmalnieks, A.; Kholkin, A. L. Computational and Experimental Studies of Size and Shape Related Physical Properties of Hydroxyapatite Nanoparticles. *J. Phys. Condens. Matter* **2011**, *23* (6) 065302.

(102) Wahl, D. A.; Czernuszka, J. T. Collagen-Hydroxyapatite Composites for Hard Tissue Repair. *Eur. Cells Mater.* **2006**, *11*, 43–56.

(103) Dolatshahi-Pirouz, A.; Skeldal, S.; Hovgaard, M. B.; Jensen, T.; Foss, M.; Chevallier, J.; Besenbacher, F. Influence of Nanoroughness and Detailed Surface Morphology on Structural Properties and Water-Coupling Capabilities of Surface-Bound Fibrinogen Films. *J. Phys. Chem. C* **2009**, *113* (11), 4406–4412.

(104) Chen, S.; Yu, F.; Yu, Q.; He, Y.; Jiang, S. Strong Resistance of a Thin Crystalline Layer of Balanced Charged Groups to Protein Adsorption. *Langmuir* **2006**, *22* (19), 8186–8191.
(105) Yamada, S.; Tagaya, M. Analytical Investigation of Hydration and Protein Adsorption Structures on Hydroxyapatite-Based Mesoporous Silica Particles. *Mater. Lett.* **2017**, *209*, 441–445.
(106) Wertz, C. F.; Santore, M. M. Fibrinogen Adsorption on Hydrophilic and Hydrophobic Surfaces: Geometrical and Energetic Aspects of Interfacial Relaxations. *Langmuir* **2002**, *18* (3), 706–715.
(107) Rabe, M.; Verdes, D.; Seeger, S. Understanding Protein Adsorption Phenomena at Solid Surfaces. *Adv. Colloid Interface Sci.* **2011**, *162* (1–2), 87–106.
(108) O'Shannessy, D. J.; Winzor, D. J. Interpretation of Deviations from Pseudo-First-Order Kinetic Behavior in the Characterization of Ligand Binding by Biosensor Technology. *Anal. Biochem.* **1996**, *236* (2), 275–283.
(109) Arima, Y.; Iwata, H. Effect of Wettability and Surface Functional Groups on Protein Adsorption and Cell Adhesion Using Well-Defined Mixed Self-Assembled Monolayers. *Biomaterials* **2007**, *28* (20), 3074–3082.
(110) Mallamace, F.; Corsaro, C.; Mallamace, D.; Vasi, S.; Vasi, C.; Dugo, G. The Role of Water in Protein's Behavior: The Two Dynamical Crossovers Studied by NMR and FTIR Techniques. *Comput. Struct. Biotechnol. J.* **2015**, *13*, 33–37.
(111) Wertz, C. F.; Santore, M. M. Fibrinogen Adsorption on Hydrophilic and Hydrophobic Surfaces: Geometrical and Energetic Aspects of Interfacial Relaxations. *Langmuir* **2002**, *18* (3), 706–715.
(112) Rabe, M.; Verdes, D.; Seeger, S. Understanding Protein Adsorption Phenomena at Solid Surfaces. *Adv. Colloid Interface Sci.* **2011**, *162* (1–2), 87–106.
(113) Sharpe, J. R.; Sammons, R. L.; Marquis, P. M. Effect of PH on Protein Adsorption to Hydroxyapatite and Tricalcium Phosphate Ceramics. *Biomaterials* **1997**, *18* (6), 471–476.
(114) Tsapikouni, T. S.; Missirlis, Y. F. PH and Ionic Strength Effect on Single Fibrinogen Molecule Adsorption on Mica Studied with AFM. *Colloids Surfaces B Biointerfaces* **2007**, *57* (1), 89–96.
(115) Zeliszewska, P.; Bratek-Skicki, A.; Adamczyk, Z.; Cieśla, M. Human Fibrinogen Adsorption on Positively Charged Latex Particles. *Langmuir* **2014**, *30* (37), 11165–11174.
(116) Samavedi, S.; Whittington, A. R.; Goldstein, A. S. Calcium Phosphate Ceramics in Bone Tissue Engineering: A Review of Properties and Their Influence on Cell Behavior. *Acta Biomater.* **2013**, *9* (9), 8037–8045.
(117) Mathes, J. Influence of PH and Ionic Strength on IgG Adsorption to Vials. *Eur. J. Pharm. Biopharm.* **2011**, *78* (2), 239–247.
(118) Anfinsen, C. B. (Christian B. *Advances in Protein Chemistry. Volume 47*; Academic Press, **1995**.
(119) Fedoseeva, M.; Fita, P.; Punzi, A.; Vauthey, E. Salt Effect on the Formation of Dye Aggregates at Liquid/Liquid Interfaces Studied by Time-Resolved Surface Second Harmonic Generation. *J. Phys. Chem. C* **2010**, *114* (32), 13774–13781.
(120) Dahal, Y. R.; Schmit, J. D. Ion Specificity and Nonmonotonic Protein Solubility from Salt Entropy. *Biophys. J.* **2018**, *114* (1), 76–87.

(121) Tanaka, M.; Mochizuki, A. Effect of Water Structure on Blood Compatibility? Thermal Analysis of Water in Poly(Meth)Acrylate. *J. Biomed. Mater. Res.* **2004**, *68A* (4), 684–695.
(122) Chang, Y.; Chu, W. L.; Chen, W. Y.; Zheng, J.; Liu, L.; Ruaan, R. C.; Higuchi, A. A Systematic SPR Study of Human Plasma Protein Adsorption Behavior on the Controlled Surface Packing of Self-Assembled Poly(Ethylene Oxide) Triblock Copolymer Surfaces. *J. Biomed. Mater. Res. Part A* **2010**, 93(1), 400–408.
(123) Jähnert, S.; Vaca Chávez, F.; Schaumann, G. E.; Schreiber, A.; Schönhoff, M.; Findenegg, G. H. Melting and Freezing of Water in Cylindrical Silica Nanopores. *Phys. Chem. Chem. Phys.* **2008**, *10* (39), 6039.
(124) Tsortos, A.; Ohki, S.; Zieba, A.; Baier, R. E.; Nancollas, G. H. The Dual Role of Fibrinogen as Inhibitor and Nucleator of Calcium Phosphate Phases: The Importance of Structure. *J. Colloid Interface Sci.* **1996**, *177* (1), 257–262.
(125) England, J. L.; Haran, G. Role of Solvation Effects in Protein Denaturation: From Thermodynamics to Single Molecules and Back. *Annu. Rev. Phys. Chem.* **2011**, *62*, 257–277.
(126) Prabhu, N.; Sharp, K. Protein-Solvent Interactions. *Chem. Rev.* **2006**, *106* (5), 1616–1623.
(127) Fuerstenau, D. W.; Pradip. Zeta Potentials in the Flotation of Oxide and Silicate Minerals. *Adv. Colloid Interface Sci.* **2005**, *114–115*, 9–26.
(128) Schmitt, A.; Varoqui, R.; Uniyal, S.; Brash, J. .; Pusineri, C. Interaction of Fibrinogen with Solid Surfaces of Varying Charge and Hydrophobic—Hydrophilic Balance: I. Adsorption Isotherms. *J. Colloid Interface Sci.* **1983**, *92* (1), 25–34.
(129) Yang, Q.; Zhang, Y.; Liu, M.; Ye, M.; Zhang, Y.; Yao, S. Study of Fibrinogen Adsorption on Hydroxyapatite and TiO_2 Surfaces by Electrochemical Piezoelectric Quartz Crystal Impedance and FTIR–ATR Spectroscopy. *Anal. Chim. Acta* **2007**, *597* (1), 58–66.
(130) Monkawa, A.; Ikoma, T.; Yunoki, S.; Yoshioka, T.; Tanaka, J.; Chakarov, D.; Kasemo, B. Fabrication of Hydroxyapatite Ultra-Thin Layer on Gold Surface and Its Application for Quartz Crystal Microbalance Technique. *Biomaterials* **2006**, *27* (33), 5748–5754.
(131) Lee, D. C.; Haris, P. I.; Chapman, D.; Mitchell, R. C. Determination of Protein Secondary Structure Using Factor Analysis of Infrared Spectra. *Biochemistry* **2005**, *29* (39), 9185–9193.
(132) Haris, P. I. Probing Protein-Protein Interaction in Biomembranes Using Fourier Transform Infrared Spectroscopy. *Biochim. Biophys. Acta - Biomembr.* **2013**, *1828* (10), 2265–2271.
(133) Sethuraman, A.; Vedantham, G.; Imoto, T.; Przybycien, T.; Belfort, G. Protein Unfolding at Interfaces: Slow Dynamics of α-Helix to β-Sheet Transition. *Proteins Struct. Funct. Bioinforma.* **2004**, *56* (4), 669–678.
(134) Steiner, G.; Tunc, S.; Maitz, M.; Salzer, R. Conformational Changes during Protein Adsorption. FT-IR Spectroscopic Imaging of Adsorbed Fibrinogen Layers. *Anal. Chem.* **2007**, *79* (4), 1311–1316.
(135) Snopok, B. A.; Kostyukevich, E. V. Kinetic Studies of Protein-Surface Interactions: A Two-Stage Model of Surface-Induced Protein Transitions in Adsorbed Biofilms. *Anal. Biochem.* **2006**, *348* (2), 222–231.

(136) Michel, R.; Castner, D. G. Advances in Time-of-Flight Secondary Ion Mass Spectrometry Analysis of Protein Films. *Surf. Interface Anal.* **2006**, *38* (11), 1386–1392.
(137) Young, B. .; Pitt, W. .; Cooper, S. . Protein Adsorption on Polymeric Biomaterials: II. Adsorption Kinetics. *J. Colloid Interface Sci.* **1988**, *125* (1), 246–260.
(138) Cieśla, M.; Adamczyk, Z.; Barbasz, J.; Wasilewska, M. Mechanisms of Fibrinogen Adsorption at Solid Substrates at Lower PH. *Langmuir* **2013**, *29* (23), 7005–7016.
(139) Czeslik, C.; Reichhart, C. Native-Like Structure of Proteins at a Planar PAA Brush. *Biophys. J.* **2009**, *96* (3), 585a.
(140) Soman, P.; Siedlecki, C. A. Effects of Protein Solution Composition on the Time-Dependent Functional Activity of Fibrinogen on Surfaces. *Langmuir* **2011**, *27* (17), 10814–10819.
(141) Evans-Nguyen, K. M.; Jorgenson, W. *Studies of The Influence of Charge and Wettability on Fibrinogen Adsorption and Fibrin Formation at Surfaces*, Chapel Hill; **2006**.
(142) Tagaya, M.; Ikoma, T.; Hanagata, N.; Tanaka, J. Analytical Investigation of Protein Mediation Between Biomaterials and Cells. *Mater. Express* **2012**, *2* (1), 1–22.
(143) Ikoma, T.; Tagaya, M.; Hanagata, N.; Yoshioka, T.; Chakarov, D.; Kasemo, B.; Tanaka, J. Protein Adsorption on Hydroxyapatite Nanosensors with Different Crystal Sizes Studied *In Situ* by a Quartz Crystal Microbalance with the Dissipation Method. *J. Am. Ceram. Soc.* **2009**, *92* (5), 1125–1128.
(144) Dolatshahi-Pirouz, A.; Jensen, T.; Foss, M.; Chevallier, J.; Besenbacher, F. Enhanced Surface Activation of Fibronectin upon Adsorption on Hydroxyapatite. *Langmuir* **2009**, *25* (5), 2971–2978.
(145) Tagaya, M.; Ikoma, T.; Hanagata, N.; Yoshioka, T.; Tanaka, J. Competitive Adsorption of Fibronectin and Albumin on Hydroxyapatite Nanocrystals. *Sci. Technol. Adv. Mater.* **2011**, *12* (3), 034411.
(146) Monkawa, A.; Ikoma, T.; Yunoki, S.; Yoshioka, T.; Tanaka, J.; Chakarov, D.; Kasemo, B. Fabrication of Hydroxyapatite Ultra-Thin Layer on Gold Surface and Its Application for Quartz Crystal Microbalance Technique. *Biomaterials* **2006**, *27* (33), 5748–5754.
(147) Reddy, A. S.; Warshaviak, D. T.; Chachisvilis, M. Effect of Membrane Tension on the Physical Properties of DOPC Lipid Bilayer Membrane. *Biochim. Biophys. Acta - Biomembr.* **2012**, *1818* (9), 2271–2281.
(148) Yu, J.; Hong, G.; Karttunen, M. Biochimica et Biophysica Acta Molecular Dynamics Simulations of Lipid Membranes with Lateral Force : Rupture and Dynamic Properties. *BBA - Biomembr.* **2014**, *1838* (3), 994–1002.
(149) Manley, G. Public Access NIH Public Access. **2013**, *71* (2), 233–236.
(150) Blume, A.; Kerth, A. Biochimica et Biophysica Acta Peptide and Protein Binding to Lipid Monolayers Studied by FT-IRRA Spectroscopy. *BBA - Biomembr.* **2013**, *1828*, 1–12.
(151) Eyler, J. R.; Helden, G. Von. Charge-State Resolved Mid-Infrared Spectroscopy of a Gas-Phase Protein. **2005**, 1345–1348.
(152) Glassford, S. E.; Byrne, B.; Kazarian, S. G. Recent Applications of ATR FTIR Spectroscopy and Imaging to Proteins. *Biochim. Biophys. Acta - Proteins Proteomics* **2013**, *1834* (12), 2849–2858.

(153) Dempsey, N. C.; Ireland, H. E.; Smith, C. M.; Hoyle, C. F.; Williams, J. H. H. Heat Shock Protein Translocation Induced by Membrane Fluidization Increases Tumor-Cell Sensitivity to Chemotherapeutic Drugs. *Cancer Lett.* **2010**, *296* (2), 257–267.
(154) Plant, A. L.; Bhadriraju, K.; Spurlin, T. A.; Elliott, J. T. Cell Response to Matrix Mechanics: Focus on Collagen. *Biochim. Biophys. Acta - Mol. Cell Res.* **2009**, *1793* (5), 893–902.
(155) Parsons, J. T.; Horwitz, A. R.; Schwartz, M. A. Cell Adhesion: Integrating Cytoskeletal Dynamics and Cellular Tension. *Nat. Rev. Mol. Cell Biol.* **2010**, *11* (9), 633–643.
(156) Manley, G. Public Access NIH Public Access. **2013**, *33* (5), 1201–1237.
(157) Friedman, S. L.; Roll, F. J.; Boylest, J.; Bissell, D. M. Hepatic Lipocytes: The Principal Collagen-Producing Cells of Normal Rat Liver (Hepatocytes/Sinusoidal Endothelium/Vitamin A/Liver Cell Culture). *Proc. Nati. Acad. Sci. USA* **1985**, *82* (December), 8681–8685.
(158) Gattazzo, F.; Urciuolo, A.; Bonaldo, P. Extracellular Matrix: A Dynamic Microenvironment for Stem Cell Niche. *Biochim. Biophys. Acta - Gen. Subj.* **2014**, *1840* (8), 2506–2519.
(159) Engler, A. J.; Sen, S.; Sweeney, H. L.; Discher, D. E. Matrix Elasticity Directs Stem Cell Lineage Specification. *Cell* **2006**, *126* (4), 677–689.
(160) Kumar, S.; Maxwell, I. Z.; Heisterkamp, A.; Polte, T. R.; Lele, T. P.; Salanga, M.; Mazur, E.; Ingber, D. E. Viscoelastic Retraction of Single Living Stress Fibers and Its Impact on Cell Shape, Cytoskeletal Organization, and Extracellular Matrix Mechanics. *Biophys. J.* **2006**, *90* (10), 3762–3773.

Chapter 3

“Preparation and Biological Evaluation of Nanoparticle Zinc-substituted Hydroxyapatite Films”

Chapter 3

Preparation and Biological Evaluation of Nanoparticle Zinc–substituted Hydroxyapatite Films

3.1. Introduction

A percutaneous device (PD) is a biomedical object that is implanted through the skin in order to establish an access to the internal organs, tissues, nervous, and cavities for transfer of mass, liquids, gases, drugs, energy or forces.[1–3] The applications of the PD include hemodialysis, neuroelectric stimulation of nerves and/or muscles, charging for cardiac pacemakers, artificial limbs, cancer therapy, peritoneal dialysis, among others.[4,5] One of the most used PD is the catheter, which is a connection between the inside of the body and the outside world for introducing or taking out liquids, gases, and drugs.[6] The catheter is primarily made by silicone rubber. The lack of bioactivity of this biomaterial impedes the binding with the surrounding tissues, creating a space between the catheter and the tissues, through which the bacteria can enter and leads to a bacterial infection.[6,7]

In order to prevent bacterial infection and enhance the cytocompatibility, the catheter have been coated with bioactive materials like hydroxyapatite (HAp; $Ca_{10}(PO_4)_6(OH)_2$).[8,9] The HAp is an extremely indispensable bioceramic due to the high cytocompatibility to be implementing the defective places and to improve the implant biointegration in animal bodies to encourage the healing process through the binding with living tissues.[10–12] For improving the cytocompatibility, it has been reported the chemical coating of catheters with HAp by a chemical synthetic process by corona-discharge treatment or using silane coupling agents.[13–15] The coating technique of catheters with HAp has been demonstrated to have more cytocompatibility. However, some problems have been found with these techniques among which are (a) the use of toxic agents stands out, which can generate cytoxicity for tissue cells, (b) the hydroxyapatite used is micrometric in size, so bacteria can permeate between the space of the microparticles and (c) the cytocompatibility obtained not only allows the attachment to the tissues, but also allows the adhesion of bacteria which form a biofilm on the surface, which promotes bacterial infection.[16–18] Thus, the surface modification of the silicone has been demanded to effectively bind with the human tissues

by improving the cytocompatibility in addition to the antibacterial property.

For improving the cytocompatibility by the heterogeneous ions, the substitution of carbonate ions into the HAp structure is very important. Generally, CO_2 can be dissolved into a synthetic solution as carbonate ions and eventually incorporated into the structure, replacing PO_4^{3-} or OH^- ions in the structure.[19,20] In the synthesis in the presence of sodium or potassium ions, these ions are partially substituted with the Ca^{2+} ions of the structure and are important for promoting new tissue (e.g., bone formation).[21]

For further catheter applications, the functionalization of antibacterial property is necessary to restrict the unexpected bacterial growth. Although a lot of antibacterial reagents have been researched (Ag^+, Zn^{2+}, Ti^{4+}, and Cu^{2+}).[22–24] In particular, Zn ion is present in the all biological hard tissues, and thought to stimulate bone mineralization and help in pathological calcification. Furthermore, the Zn ion also plays a vital role in the maintenance of membrane structure, function, protein synthesis, DNA synthesis, mitosis, and cell proliferation.[25–27] Zinc (Zn) ion is well-known as an effective chemical reagent to inhibit bacteria growth. Small amount of Zn ion in living hard tissues restricts the bacterial attachment. To achieve antibacterial property in a long time, it would be useful to stabilize the Zn ions in cytocompatible materials by the mineralization.[28] Therefore, we can suggest the Zn–substituted HAp nanoparticles (Zn:HAp NPs) as a cytocompatible and antibiotic material by dense coating on the Ti-PDMS.[29]

For the dense coating, an electrophoretic deposition (EPD) technique has been attracted. It is because the technique has strong merits, i.e., the deposition with preserving crystalline structure and purity, follow-up coatings on the complex shapes with uniform film thickness, and no requirement for binder chemical reagents such as silane coupling agents.[30] Therefore, the EPD technique would be useful for the coating of the functional materials on Ti-PDMS substrate. The EPD is a colloidal process and can shape directly on the substrates from the stable alcoholic suspension by a direct current (DC) electric field.[31,32] The EPD is a process due to the motion of charged particles in a suspension under the influence of an electric field.[33] Thus, we can propose the importance of the EPD coating of Zn:HAp NPs on the Ti-PDMS.

In this study, the films of Zn:HAp and carbonated HAp (Zn:CHAp) NPs, which were chemically synthesized at the initial (Ca+Zn/)P molar ratios of 1.67 and 2.00 with the

different initial Zn concentrations, respectively, were formed on titanium-coated polydimethylsiloxane (Ti−PDMS) by an EPD technique. Furthermore, the cytocompatible and antibacterial properties of the nanoparticle Zn:HAp and Zn:CHAp NP films were investigated using NHI3T3 fibroblasts and Escherichia coli (*E. coli* DH5α), respectively.

3.2. Experimental

3.2.1. Materials

Potassium phosphate dibasic trihydrate ($K_2HPO_4 \cdot 3H_2O$), zinc chloride ($ZnCl_2$), and sodium hydroxide (NaOH) as the special grade chemicals were purchased from Wako Chemical Co., Ltd. Calcium chloride ($CaCl_2$) as the special grade chemical was purchased from Nacalai Tesque, Inc. Phosphate Buffer Saline (PBS: DS Pharma Biomedical Co., Ltd) with the ions (K^+: 4.15 mM, Na^+: 153.09 mM, HPO_4^{2+}: 9.57 mM, Cl^-: 139.57 mM). Ethanol 99.5% (mass/mass) was purchased from Wako Co., Ltd. Inc. Silicon transparent conductive film (Kyohritsu Electronic Industry Co. Ltd). Fetal Bovine Serum (FBS: JRH biosciences Co. Ltd., model number: 12603C). For cell culture, phosphate buffered saline (PBS, Dullbecco Co., Ltd), 0.05 w/v% trypsin-0.053 M-ethylenediaminetetraacetate (trypsin-EDTA, Gibco), formaldehyde (37 vol %, Wako Co., Ltd.) Dulbecco´s modified eagle medium (DMEM without sodium pyruvate, Gibco) were used. NIH3T3 mouse embryonic fibroblast cells (RCB1862) purchased from BioResource Center of Japan. FBS was purchased from Bioscience Co., Ltd. (product number: 12603C, lot no. 6D0975: SAFC). For antibacterial test, 6-cm-petri dish (CELLSTAR dish, Greiner bio-one Co., Ltd. code No. 628160) and cover glass #1 (size: 18 mm×18 mm, Matsunami glass Co., Ltd., code No. : C218181) was used. All the reagents were used without further purification.

3.2.2. Synthesis of Zn–substituted HAp NPs

The $K_2HPO_4 \cdot 3H_2O$ (0.024 mol) was completely dissolved into 100 mL of deionized water at 40 ^oC and then stirring for 60 min to prepare phosphate solution. The aqueous solution containing 0.04 mol of both $CaCl_2$ and $ZnCl_2$ was added into the phosphate solution at the drop rate of 5 ml/min at 40 °C and then stirring for 60 min. The pH value of the mixture solution was adjusted up to 12 using 1N-NaOH aqueous solution. After the

aging period for 60 min, the precursor solution was then refluxed at 40 ^{o}C for 24 h. The solution was centrifuged (10000 *g*, 15 min, 4^{o}C) and the sediment solid was washed with ultrapure water 3 times. The washed product was dried at 100 ^{o}C for 24 h under air. Here, the Zn–substituted HAp NPs were synthesized from the initial molar ratio of (Ca+Zn)/P at 1.67 or 2.00 with the different initial Zn concentrations to the total (Ca+Zn) at 0.0, 2.5, 5.0 and 10 mol%, and these resultant sample form the ratio of (Ca+Zn)/P at 1.67 or 2.00 was abbreviated as *X*−Zn:HAp or *X*−Zn:CAp NPs (*X* = Zn/(Ca+Zn) = 0.0, 2.5, 5.0, 10), respectively.

3.2.3. Formation of Zn–substituted HAp NP Films

Before the EPD is carried out the preparation of the polymer, which consisted of covering the surface of the PDMS polymer with a very thin titanium layer. Using DC sputtering can deposit very thin layers of material from a "target" (titanium) that is a source onto a "substrate" such as a PDMS. DC diode sputtering system is constituted by a pair of flat electrodes. One of the electrodes is the cathode and the other anode. On the cathode side facing the plasma the target, that it is desired to evaporate, is located, and the other face is cooled with water. In the anode was placed the substrate (PDMS) on which is desired to evaporate. In a DC diode sputtering system, Argon is ionized by a strong potential difference, and these ions are accelerated to a target. After impact, target atoms are released and travel to the substrate where they form layers of atoms in the thin-film. The DC sputtering was carried with a voltage of 5 mA for 1 min in a vacuum.

Removal of the Cl^- ions and others impurities from the powders is very important because it can affect the suspension stability and deposition characteristics. The Zn–substituted HAp NPs was washed three times with ethanol (99.5 % (mass/mass), Wako Co., Ltd.) before EPD. The suspension was prepared by the dispersion of 1 wt% of the Zn–substituted HAp NPs in pure ethanol (99.5 % (mass/mass), Wako Co., Ltd.).

For the purpose of clean the materials; the electrode and the Ti-PDMS surfaces were undergoes to UV/O_3 treatment for 5 min. The coating was deposited onto Ti-PDMS substrates from suspensions containing 1 wt% of Zn–substituted HAp NPs (initial (Zn+Ca)/P = 1.67 and 2 with Zn/(Ca+Zn) = 0, 2.5, 5.0 and 10.0 mol%), dispersed in pure ethanol (99.5 % (mass/mass), Wako Co., Ltd.). The suspensions had been ultrasonically

agitated before EPD process for 3 minutes while deposition was carried out without stirring. The Zn–substituted HAp NPs were deposited onto the Ti-PDMS substrates (transparent silicon conductive film) and catheters surface through EPD method at deposition time of 1 min, and an electrode distance of 1 cm. In order to obtain the best coating, the different DC voltage were applied at 10, 50 and 100 V/cm, following by the ultrasonification in 20 mL in ethanol for 1 minute and the subsequent wash in 20 mL of ethanol¸ to remove excess of Zn–substituted HAp NPs. The coated samples were dried in air for 1h at room temperature.

3.2.4. Preparation of Fibroblast Suspension and Their Culture

Mouse embryonic fibroblast NIH3T3 cells (RCB1862), provided by Riken Bio Resource Center, were cultured in a plastic cell culture flask with an area of 75 cm^2 (BD Bioscience, USA) containing 15 mL of Dulbecco's modified Eagle's medium (DMEM: Invitrogen Co.,Ltd.) supplemented with 10 vol% fetal bovine serum (FBS: No. 12603C, SAFC Bioscience Co.,Ltd.) and 1vol% penicillin/streptomycin. The fibroblast cells were cultured at 37°C, in a humidified atmosphere of 5% CO_2 environment , and were subcultured after 7 days using 1 mL of 0.05 w/v% trypsin-0.053 M-ethylenediaminetetraacetic acid (trypsin-EDTA: No. 204-16935,Wako Co., Ltd.) for 10 min at 37 °C. After being washed with 15 mL of PBS, the cells were homogeneously dispersed in 15 mL of PBS, and were separated by centrifugation (2000 rpm, 2 min), and dispersed in 15 mL of 10 % FBS/DMEM. The centrifugation and dispersion were carried out twice. The number of cells in the suspension was counted and adjusted at the desired seeding density in subsequent procedures.

3.2.5. Characterization at Powder State

3.2.5.1. Characterization of Zn–substituted HAp NPs

The contents (mol %) of the atomic elements (Ca, Zn, P, and C) were determined using a wavelength dispersive X-ray fluorescence spectrometry (XRF) (ZSX Primus II, Rigaku Co., Ltd.).

The Thermogravimetric-Differential Thermal Analysis-Mass (TG-DTA-MS) experiments were performed using a TG-DTA/photoionization mass spectrometer (Thermo mass photo, Rigaku Co., Ltd.) The samples were dried for 3 h at 100ºC under vacuum to

remove the free water before experiments. Approximately 20 mg of each were dry from room temperature to 1000ºC in TG differential thermal analyzer at heating rate of 20ºC/min. The pyrolysis experiments were conducted in argon atmosphere and the purge gas flow rate of argon was 100 ml/min. The derived products were simultaneously measured with the photoionization mass spectrometer. The sample weight loss and the heat flow during the pyrolysis process were continuously recorded as a function of temperature and time through the TG analyzer. The types and traces of the product components for each of the experiments were targeted by Total Ion Current (TIC) measurement mode of MS.

Fourier Transform Infrared (FT–IR) spectra were recorded on a Jasco FT/IR-4100 spectrometer. The spectra were obtained at the wavenumbers between 400–4000 cm^{-1} with an accumulation of 128 times and resolution of 1.0 cm^{-1}. The methodology for carbonate ions quantification was calculated on based on the integrated intensities (or peak areas) of the vibrational domains of the $v_3(CO_3)$ of the carbonate ions and the $v_1v_3(PO_4)$ for phosphate ions. The totally contribution of $v_3(CO_3)$ the was integrated between 1570 and 1330 cm^{-1} and the $v_1v_3(PO_4)$ contribution was integrated between 1230 and 900 cm^{-1}. The calculation of the carbonate/phosphate ratio ($r_{c/p}$) between the integrated areas of the $v_3(CO_3)$ and $v_1v_3(PO_4)$.

$$r_{c/p} = \frac{[area\ v_3(CO_3)]}{[area\ v_1v_3(PO_4)]} \tag{3-1}$$

The carbonation amount (mass% CO_3) of the NPs was calculated by a validated FT–IR methodology using the **equation 3-2**:[34]

$$Mass\ \%CO_3 = 28.62 * r_{\frac{c}{p}} + 0.0843 \tag{3-2}$$

XRD patterns were recorded by a Smart Lab diffractometer (Rigaku Co., Ltd.) using monochromatized CuKa radiation. The crystalline phases were determined by comparing the X-ray patterns with HAp (JCPDS 9–432) standard, and the lattice parameters were determined by Rietveld refinement of the diffraction profiles with a PDXL2 program. For the hexagonal cell parameters *a* and *c* of the crystallographic system, the relationship

between the distance (*d*) of two adjacent net planes and the (*hkl*) Miller indices of the reflection planes, which is given by the **Eq. (3-3)**:[35,36]

$$d = \frac{1}{\sqrt{\frac{4h^2+hk+k^2}{3\ a^2}+\frac{l^2}{c^2}}} \tag{3-3}$$

The crystalline sizes of the nanoparticles were estimated using Scherrer equation **of Eq. (3-4)**:

$$D_{hkl} = \frac{K\lambda}{\beta cos\theta} \tag{3-4}$$

Where D_{hkl} indicates the crystalline size, λ is the X-ray wavelength (0.15418 nm), β is the full-width at half-maximum (in radians) of 002 and 300 diffraction, and θ is the diffraction angle, and *K* is 0.9.[37,38]

The morphology was observed by transmission electron microscopy (TEM) with a JEM-1400 (JEOL Co., Ltd.). The ethanoic suspension at the solid concentration of 0.01 wt% was dropped onto a carbon-coated copper (Cu) grid (Cu 200-A mesh, Okenshoji Co., Ltd.), and the grid was dried in desiccator under nitrogen atmosphere for 1 day. The nanoparticles were examined in bright mode at the magnifications typically up to ×1,000,000 under an accelerating voltage of 120 kV.

3.2.5.2. FT–IR Spectral Measurement for Analyzing Hydration Layers

The infrared spectra were obtained by a Fourier transform infrared spectrometer (FT−IR; JASCO Co., Ltd., FT/IR-4600ST) and were measured in the range between 400–4000 cm^{-1} with an accumulation of 128 times with a spectral resolution of 1 cm^{-1}. The Si(100) substrate pre-coated with a thin Au layer was used as the background.

For evaluating the hydration layers, the O–H stretching band was deconvoluted into the three components free water (3200 ± 20 cm^{-1}), intermediate water (3400 ± 20 cm^{-1}), and nonfreezing water molecules (3600 ± 20 cm^{-1}).[39] The components of the deconvoluted O–H stretching bands of the Au substrates were calculated as the integrated area ratio of the band

of bounding (i.e., intermediate and nonfreezing water molecules) to that of free water molecules.

3.2.5.3. Dissolution Behavior of Zn–substituted HAp NPs

The dissolved Ca^{2+} ratios from the total Ca^{2+} content in the Zn–substituted HAp NPs were investigated by the immersion in PBS for 48 h under static condition. The Ca^{2+} concentration was measured using a D73LAB equipped with an electrode (6583−10C, Horiba, Co., Ltd., Japan). The standard Ca^{2+} solution was prepared by mixing ultrapure water containing 1000 mg/L of $CaCl_2 \cdot 2H_2O$ and 0.1 M of KCl (support salt). 100, 10 and 1.0 mg/L of the Ca^{2+} solutions with KCl (0.1 M) were also used for drawing a calibration curve. The dissolved Ca^{2+} weight from the Zn–substituted HAp NPs was measured at the particle concentration of 100 μg/mL in PBS. The value obtained with PBS was subtracted from that obtained with PBS containing the Zn–substituted HAp NPs, and the dissolved Ca^{2+} weight was divided by the initial Ca^{2+} weight in the Zn–substituted HAp NPs determined by the XRF result.[40]

The dissolution model can be represented with the Korsmeyer-Peppas model that is expressed by the following **Eq. (3-5)**: [41]

$$ln(F) = \ln(M_t/M) \ = nln(K_m.t) \tag{3-5}$$

Where F is the fraction of the released Ca^{2+} at the time (t) and can be represented by M_t/M. The M is the total amount of Ca^{2+} in the particulate form, and Mt is the amount of the released Ca^{2+} at the time (t). K_m is the kinetic constant that indicates the release rate and n is the diffusional exponent that depends on the release mechanism as well as the geometry of the system. Here, the low K_m values are the index of slow dissolution behavior and n depends on the physicochemical properties of the materials irrespective of the dissolution behavior. As previously reported on the radial diffusion from the cylindrical geometry, the n value for pure Fickian diffusion is 0.45. It is known that the value for abnormal transport is more than 0.45, and that for Case II transport (e.g., polymer relaxation or swelling–controlled mechanism) is 0.89.[42]

3.2.6. Characterization of Surface Structures of Zn–substituted HAp NP Films

The surface structures of the Zn–substituted HAp NP Films and Ti-PDMS were analyzed by an atomic force microscope (AFM: Nanocute, SII Investments, Inc.). The surface roughness (R_{rms}) was calculated by the root mean squares in the height images, the parameters of mean mean square roughness (**equation (3-6)**), as follows:

$$R_{rms} = \sqrt{\frac{\sum_{n=1}^{N}(|z_n - \bar{z}|)^2}{N-1}} \tag{3-6}$$

Where z_n is a segment height, $\bar{z}$ is average height of all segments, and N is the number of segments. Roughness provides the information about area roughness trend across the swept area, whereas the roughness of the line yields the roughness value in a selected trajectory.[43]

HAp NP deposits obtained at the applied voltage below the critical saturated voltage showed preferable deposition of fine particles,[44] because smallest particles reached the highest electrophoretic velocity, and therefore these were the preferential deposited.[45] Both kind of Zn–substituted HAp NPs present good adherent and continuous coating after the deposition without cracks.

The deposit weight (W) in the EPD process could be described by the **equation (3-7)**:

$$W = \frac{C\mu U t}{d} \tag{3-7}$$

Where C and μ are the particle concentration and mobility, respectively; t is deposition time, and d is the distance between the electrodes. U is described as follows:

$$U = U_{ap} - U_{dep} \tag{3-8}$$

Where U_{ap} = applied voltage, U_{dep} = voltage drop in deposit. The electrophoretic mobility can be determined by the **equation (3-9)**:

$$\mu = \frac{\xi \varepsilon}{4\pi\eta} \tag{3-9}$$

where ξ = zeta potential, ε = dielectric constant, and η = viscosity of the medium.[46]

For the determination of the surface properties, the Zn-substituted HAp NP films were broken into small pieces and that small pieces of the films were used to fill the glass sample holder tubes (100 mg). Prior to the measurement, the films were dry and degassed under vacuum at 120ºC for 4 h using a pretreatment device (BELPREP-vacII, Microtrac/BEL Co., Ltd., Japan). For each film, the measurements were performed 3 times after conducting a 3-min leak check to ensure data reproducibility, sufficient sealing and complete drying of the specimens. The specific surface area (S_{BET}) and pore size distributions were determined through nitrogen (N_2) adsorption and desorption instrument (BELSORP-miniII, Microtrac/BEL Co., Ltd., Japan). The films was analyzed under N_2 conditions, 77 K, the adsorption relative pressure upper limit of 0.99, and desorption relative pressure lower limit of 0.05. The Brunauer-Emmett-Teller (BET) [47] surface areas and Barrett-Joyner-Halenda (BJH) [48] pore sizes distribution were applied to the analysis. These calculations were performed with the calculation software BELMASTER (TM) manufactured by Microtrac/Bel Co., Ltd.

The BET theory is for explain the multi-layer adsorption of gas molecules on a solid surface and is considered as an expansion of Langmuir equation, which is for the single layer gas adsorption. The BET equation can be described as:

$$\frac{P}{V(P_0 - P)} = \frac{1}{V_m C} + \frac{C-1}{V_m C} * \frac{P}{P_0} \tag{3-10}$$

By plotting the $P/v(P_0 - P)$ against the P/P_0, a straight line is obtained, where the slope is $(C-1)/V_m C$ and the intercept is$1/V_m C$. In the equation (3-10) P is the pressure of the gas, P_0 is the saturation pressure of the gas, V_m is the volume of the gas necessary to

form a unimolecular adsorbed layer, and $C = e^{(q_1 - q_2)/RT}$, where q_1 is the heat of the first adsorption layer, and q_2 is the heat of the liquefaction, R is the gas constant and T is the temperature. This graph is used to obtain the specific surface area, substituting V_m in **equation 3-11**:

$$S_{BET} = \frac{V_m}{22414} * K_A * s \tag{3-11}$$

Where K_A is the Avogadro´s number. Since the cross-sectional occupied area occupied by the adsorbed of nitrogen at the liquid nitrogen temperature is 0.162 m^2, s can be calculated as:

$$s = 4.35 * V_m \tag{3-12}$$

The BJH method was used for calculate the pore size distributions from experimental isotherms using the Kelvin model of pore filling (**eq. 3-13**).

$$r_k = r_p - t = \frac{-2\sigma V cos\theta}{RTln(P/P_0)} \tag{3-13}$$

Here, r_p is the pore diameter, r_k is the pore diameter where the capillary condensation occurs, t is the he thickness of the multilayer adsorption, σ is the surface tension of liquid nitrogen, and θ is the contact angle, V is the liquid molar volume of nitrogen. This technique was developed for porous adsorbents with a wide range of pore sizes. The theory can be summarized as (**eq. 3-14**):

$$V - V_x = \int_{rp_n}^{\infty} \pi (r - t)^2 L(r) dr \tag{3-14}$$

Where *V* is the total volume *Vx* is the volume of gas adsorbed at saturation pressure, *L(r)dr* is the total length of pores whose radii is between *r* and *r* + *dr*. rp_n is the radius of the largest pore still completely filled with liquid adsorbate at any pressure.

3.2.7. FT–IR Spectral Analysis for Fetal Bovine Serum (FBS) Adsorption Secondary Structures

For the FT–IR measurement, the adsorption of 10 vol% FBS in DMEM was used in the in situ adsorption experiments for 120 min was conducted at 37^{o}C, and was washed by ultrapure water and freeze-dried. Based on our previous report,[49,50] the adsorbed protein secondary structures on theZn–-substituted HAp NP films at the different temperature of 37^{o}C were measured by a Fourier transform infrared spectroscopy (FT–IR: JASCO Co., Ltd., FT/IR-4600ST) at the the cumulated number of 128 times and the spectral resolution of 1 cm^{-1}. The spectra were recorded after subtracting a background spectrum of pristine Si(100). The spectra of the freeze-dried films adsorbed Fgn at the equilibrium stage were measured and deconvoluted into six components at the wavenumber regions between 1600–1735 cm^{-1}. In the concrete, the C=O stretching band was deconvoluted into six components (1630±2, 1645 ± 2, 1655±2, 1665±2, 1680±2 and 1690±2 cm^{-1}) belonging to β–sheet, random, α–helix, turn, β–turn(1) and β–turn(2), respectively. All the deconvolutions were performed by fitting with the Gaussian functions using the SOLVER option in the software (Microsoft Co. Ltd., Excel 2013).[51] By the generalized reduced gradient method, the SOLVER calculation was done until the satisfied states of all the constraints and optimization conditions. The residual values decreased down to be less than 7.0 %. The ratio of the mono-component area was calculated from the separated spectrum. As the references, the spectra of Fgn alone without the further purifications were measured and deconvoluted as discribed above.

3.2.8. Antibacterial Test

The antibacterial text of the Zn:HAp and Zn:CHAp NP films at 0, 2.5, 5 and 10 mol%, and [reference: Ti-PDMS substrate], were conducted using *Escherichia coli* (*E. coli* DH5α) purchased from Takara Bio Co., Ltd.

LB medium and LB plate kit were purchased. LB culture medium solution was prepared by mixing Tryptone (Becton, Dickinson and Company (BD) Co., Ltd., code No. 211705), Yeast Extract (BD) Co., Ltd., code No. 211705), and NaCl (Wako Co., Ltd., code No. 191-01665). The LB medium was prepared by dissolving 10 g of tryptone, 5 g of yeast extract and 10 g of NaCl into 950 mL of deionized water and adjusting the pH of the medium to 7.0 using 1N-NaOH to bring volume up to 1 L. The medium was treated by an autoclave before the culture. On the other hand, LB plate culture medium for preparing colony plate was prepared by adding Agar (Wako Co., Ltd., code No. 010-15815) into LB culture medium solution, and the resulting solution was casted on sterile 10-cm- petri dish (AS ONE Co., Ltd., code No. 3-1491-01). LB plate was prepared by adding 15 g/L agar before the autoclaving in the same preparation procedure to LB medium as above. After the autoclaving, the liquid at the temperature of 55°C was poured into petri dishes (diameter: 10 cm). After harden, the plate was inverted and stored at +4°C in the dark.

For coating of the cultured colony solution on the LB plate in the dish, T-shape spreading pole (product name: bacteria spreader, AS ONE Co., Ltd., code No. : 2-6424-04) was used. The *E. coli* DH5α bacteria were cultured in a plastic cell culture dish (diameter: 10 cm) with LB medium plate containing 10 mL of LB medium at 37°C in a humidified air atmosphere, and then sub-cultured every 2 days to finally keep the cultured *E. coli* DH5α bacteria at 4^{o}C. After being washed with 15 mL of LB medium, the bacteria were dispersed in 15 mL of PBS, separated by centrifugation (2000 rpm, 2 min). The centrifugation and dispersion were carried out twice.

Based on a McFarland turbidimetric method, the bacteria liquid was adjusted by McFarland standard solution. The McFarland No. 3 solution was prepared in the admixture solution of 1 wt%-$BaCl_2$/water (0.3 mL) and 1 wt%- H_2SO_4/water (9.7 mL). As a result, the turbidity by a turbidimetric measurement (CO7500 Colorimeter UK, Biochrom Ltd.) was 26 % of transmittance at 590 nm (0.4 of absorbance at 590 nm) and 1.0×10^9 CFU (Colony Forming Unit)/mL of number of bacteria, indicating that the prepared bacteria liquid of *E. coli* DH5α was McFarland standard turbidity No. 3. Then, the diluted dispersion solution of *E. coli* DH5α was prepared at the concentration of 1.0×10^8 CFU/mL (900 μL), 1.0×10^7 CFU/mL (900 μL) and 1.0×10^6 CFU/mL (900 μL).

The sample films were which were pre-sterilize by 70 vol%-ethanol/water solution and then dried inside clean bench. 50 μL of the *E. coli* DH5α bacterial liquid at the concentration of 1.0×10^6 CFU/mL (i.e., 5.0×10^4 CFU) was seeded on the sample film surface in 60-mm-cell-culture-dish. The seeded surface layer was immediately put over and homogeneously coated by a speeding stick. The surfaces were softly capped by a cover glass (area: 18 mm × 18 mm), and the culture dishes were put on a closed container with the 100 % of humidity and contiguously pre-cultured for 17 h under room temperature.

After the pre-culture, the cover glass/*E. coli* DH5α fungi/sample film substrate was moved into 10 mL of LB medium in 50-mL-tube-container and oscillated in order to extract all the *E. coli* DH5α fungi (ca. 5.0×10^4 CFU) and prepare the dispersion medium solution (i.e., secondary fungus liquid). Then, 200 μL of the secondary fungus liquid (ca. 1000 CFU/200 μL), 200 μL of the 10-fold-dilution liquid (ca. 100 CFU/200 μL), 200 μL of 100-fold-dilution liquid (ca. 10 CFU/200 μL) were adjusted by LB medium and the liquid (200 μL) was seeded on the solid and dry state agar gel medium, which is a commercially-available LB agar plate, at three different concentrations. The seeded surface layer was immediately put over and homogeneously coated by a speeding stick. The culture of viable fungi was conducted at 37°C under air with 100 %-humidity for 24 h, and then the number of the viable fungi was counted. As the characterization method of the antibacterial properties, the viability rate after the viable fungi growth of second culture was investigated by measuring the number of viable *E. coli*, which is famous evaluation method. The number was averaged between three same sample films (n=3).

3.2.9. Evaluation of Cytocompatibility

Before the seeding procedure, the samples were kept in phosphate buffered saline (PBS) for three hours and then sterilized with ethanol 50 and 70 vol% of concentration for 12 h each of them, then rinsed twice with PBS 30 min, and finally swelled in Dulbecco's modified Eagle's medium (DMEM) for 30 minutes two times, in order to clean the samples. NIH3T3 mouse embryonic fibroblast cells were cultured at 37°C, 95% relative humidity and 5% CO_2 environment. The culture medium was 90 % Dulbecco's modified Eagle's medium (DMEM) supplemented with 10 % fetal bovine serum (FBS) and 1%

penicillin/streptomycin. The cells were cultured in a cell culture flask containing 15 mL of the FBS dispersed into DMEM at 10 vol% (10 % FBS/DMEM). The cells were incubated at 37 °C in a humidified atmosphere of 5 % CO_2, and subcultured every 7 days with 1 mL of the trypsin-EDTA. After being washed with 15 mL of PBS and treated with 1 mL of the trypsin-EDTA for 10 min at 37 °C, the cells were dispersed in 15 mL of PBS, separated by centrifugation (2000 rpm, 2 min), and dispersed in 15 mL of 10 % FBS/DMEM. The centrifugation and dispersion were carried out twice. The number of cells in the suspension was counted and adjusted at the seeding density of 8000 cells·mL^{-1}. The suspension was seeded on Zn:HAp and Zn:CHAp NPs at 0, 2.5, 5 and 10 mol% in petri tissue culture dish 35 × 10 mm, at a density of 800 cells/cm^2. Polystyrene tissue culture (PS) dish was used as a control and PDMS as a polymer reference. The cells were used for imaging and characterization purposes after 72 h of culture. The washed surfaces (e.g., adhered cells) were immediately fixed with formaldehyde and then were observed by an optical microscopy (Olympus Co., Ltd., CKX41) to obtain the adhered cell density and aspect ratio. To determine the cell area, approximately 50 cells were per image were analyzed using Cellsens software. For each sample six images were analyzed to obtain an unbiased estimate of the cell density and morphology. The results were based on three independent experiments were performed (n=3). The aspect ratio was calculated by dividing the long length and the short length of the cells using the Cellsens software, similarly 50 cells were per image were analyzed. For each sample six images were used and simultaneously three independent experiments were performed (n=3). The measurements were assessed statistically using a one-way analysis of variance (ANOVA) test followed by the Student's t Test with a significance criterion of $p < 0.05$.

3.3. Results and Discussion

3.3.1. Characterization of Zn–substituted HAp NPs

Figure 3.1 shows the (a) resultant concentrations of Zn, and (b) resultant (Ca+Zn)/P ratio a of the Zn:HAp and Zn:CHAp NPs at Zn substituted concentrations of 0.0, 2.5, 5.0, and 10.0 mol% of each element found in the synthesized nanoparticles by the XRF analysis. The Ca content decreased with increasing the Zn ion amount and the maximum

substituted Zn content is ca. 5 mol% from the initial concentration of 10 mol%, indicating the successful Zn ion incorporation into the HAp NPs structures. Furthermore, the C content increased with increasing the Zn ion amount, and that in the Zn:CHAp NPs was higher than that in the Zn:HAp NPs , indicating the carbonate ion (e.g., CO_3^{2-}, HCO_3^-) inclusion in the crystal formation. The existence of carbonate ions in the initial Ca-rich aqueous solution for the Zn:CHAp NPs effectively leads the carbonate HAp NPs formation. Accordingly, the Zn:CHAp NPs have the lower content of phosphorous as compared with the typical HAp NPs, assuming that the carbonate ions are replacing with the phosphate ions in the structures. Thus, the Zn:CHAp NPs are thought to be B-type carbonate apatite,[52] which is important for mimicking human bone mineral. The resultant (Zn+Ca)/P molar ratios for 0.0−Zn:HAp and 0.0−Zn:CHAp NPs were 1.64 and 1.94 and the molar ratio decreased with increasing the Zn ion amount. It was suggested that the carbonate ion inclusion with the Zn ion substitution induced the negative charge decrease caused by replacing phosphate ions to resultantly lost the positive charge (i.e., generate the Ca defects) for compensating. Therefore, the Zn−substitution in the NP was successfully achieved, and the weight percentage of Zn ions in the 10−Zn:HAp and 10−Zn:CHAp NPs contains 0.76 and 0.68 wt%, which are safety for cells in the animal body because of the toxic threshold at 1.5−2 wt%.[53]

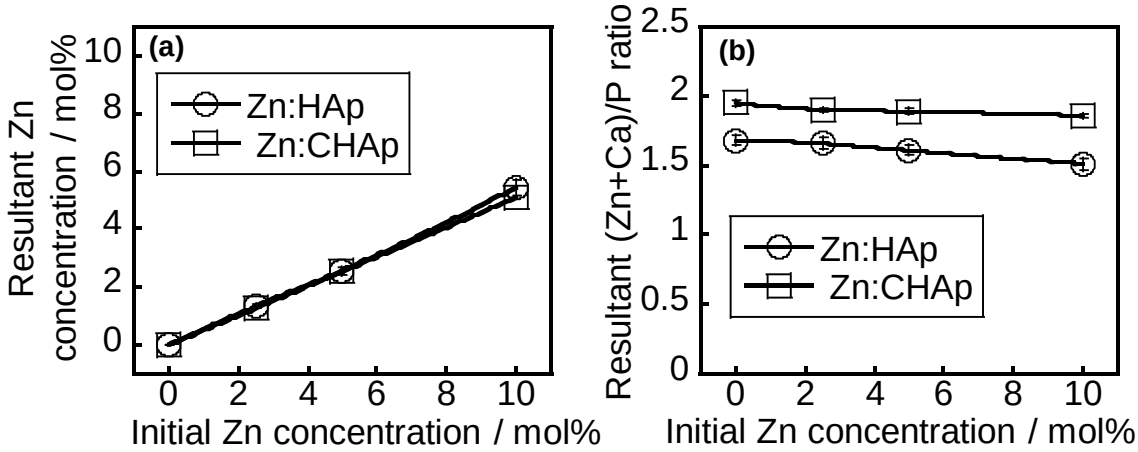

Figure 3.1. (a) Resultant concentrations of Zinc (Zn), and (b) resultant (Ca+Zn)/P ratio a Zn:HAp and Zn:CHAp NPs at Zn substituted concentration of 0.0, 2.5, 5.0, and 10.0 mol%.

DTA−MS curve of (a) 5.0−Zn: HAp and (b) 5.0−Zn:CHAp NPs are shown in **Figure 3.2**. It was confirmed the occurrence of m/z:18 that corresponded to the water (H_2O), and m/z: 44 that corresponded to the carbon dioxide (CO_2). Below 200 ºC corresponded to the dehydration of the adsorbed H_2O at the surface. The weight loss of 580 ° C is thought to be due to the carbon dioxide (CO_2). The CO_2 is observed in a wide temperature range. In the measurement results, CO_2 is output at x10. Although a higher amount of CO_2 was observed in Zn:CHAp NPs, it was not possible to determine the quantity of CO_2 by DTA−MS due to exact content of the CO_2 because it is generated at the same time as H_2O.[54] However, it is very small compared to H_2O, and the decrease in TG is considered to reflect H_2O dominantly.

In **Figure 3.2,** TG−DTA curves of (c) Zn:HAp and (d) Zn:CHAp NPs substituted at different Zn ion concentrations. The correlation with the H_2O and CO_2 loss in mass percent was inserted graphic in the TG−DTA curves. In all the TG curves, the weight that was loss below 300 ºC was caused by the desorption of adsorbed H_2O and CO_2 on the surface of Zn:HAp and Zn:CHAp NPs. The weight loss above 600 ºC was attributed to is the liberation of CO_2 existing as carbonate ions in the NPs. This weight loss was higher in Zn:CHAp NPs than for Zn:HAp NPs, demonstrating the higher content of carbonate ions in Zn:CHAp NPs .[55]

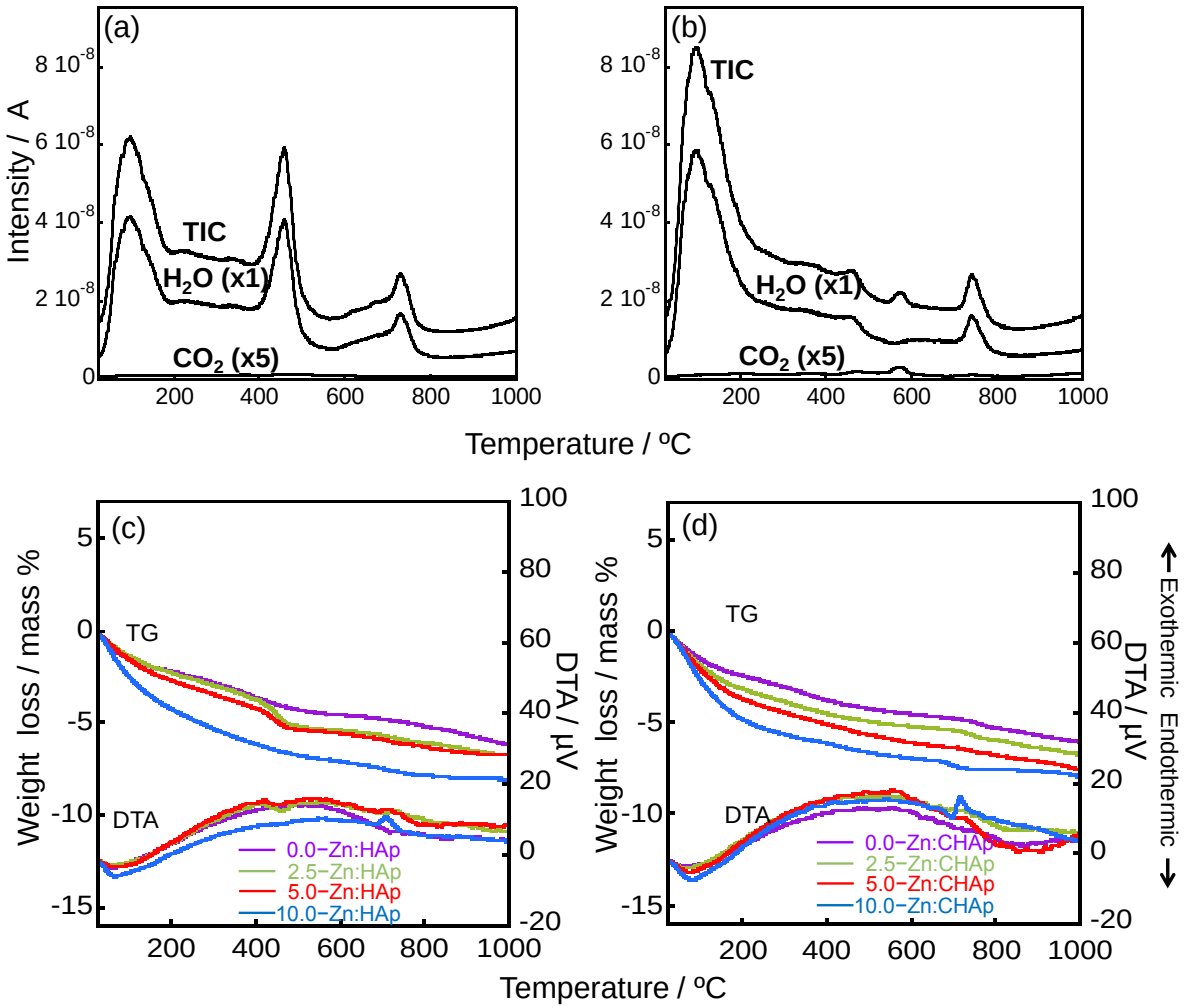

Figure 3.2. (a−b) DTA−MS curve of (a) 5.0−Zn: HAp and (b) 5.0−Zn:CHAp NPs. In the curve, the total combined intensity and the two detached gases (H_2O and CO_2) were observed. (c−d) TG−DTA curves of (a) Zn:HAp and (b) Zn:CHAp NPs substituted at different Zn ion concentrations. The correlation with the H_2O and CO_2 loss in mass percent is inserted graphic in the TG−DTA curves.

Figure 3.3 shows the FT–IR spectra of the Zn:HAp and Zn:CHAp NPs with the different Zn concentrations. The peak observed at around 3530 cm^{-1} is due to the presence of structural hydroxyl group in the HAp NPs structure. The broad band at around 3400 cm^{-1} attributed to the surface OH groups on the nanoparticles as well as the adsorbed water molecules was observed, which was enhanced with increasing the Zn substitution. The bands at 1076 cm^{-1}, 1030 cm^{-1}, 957 cm^{-1}, 601 cm^{-1}, 572 cm^{-1} and 460 cm^{-1} can be assigned to the P−O vibrations of the phosphate ions.[56–59] Although the phosphate bands of the Zn:CHAp NPs are almost same to the Zn:HAp NPs, the double bands at around 1440 and

1420 cm^{-1}, are attributed to the carbonate ions (e.g, HCO_3^-, CO_3^{2-}) in the structures,[60,61] strongly appeared in the Zn:CHAp NPs. The carbonate ions were derived from atmospheric carbon dioxide and dissolved into the solution.

The bands at around 1440 and 1420 cm^{-1} are attributed to the symmetric mode with its transition moment parallel to the C–O bond (n_s) and the asymmetric mode with its transition moment perpendicular to the same C–O bond (n_{as}). The variation in the relative band intensity ratio (n_s/n_{as}) with increasing the initial Zn ion substitution is attributed to changes in the inclusion state of the carbonate ions in the HAp NPs structure. The band at 957 cm^{-1} is assigned to a no degenerated symmetric stretching mode of the P−O bond of the phosphate group, which was clearly observed in the Zn:CHAp NPs. The double bands at 601 cm^{-1} and 572 cm^{-1} are assigned to a triply degenerated bending mode of the O−P−O. The weak band at around 460 cm^{-1} is assigned to the components of the doubly degenerated bending mode in the phosphate ion.[62]

Because the large water content present in the nanoparticles prevented determining the amount of carbonate ions contained in the nanoparticles with the TGA-DTA-MS, whereby the FT−IR spectrum was determined (see **Figure 3.4**).[63] The results coincide with the results obtained in XRF. Increasing the concentration of zinc increases the concentration of carbonates, suggesting that zinc allows the introduction of carbonate ions into the structure of the nanoparticles. The carbonate ion content is much higher in Zn:CHAp NPs than for Zn:HAp NPs. The content of carbonate ions for 10−Zn:HAp NPs was 0.1 mass% and for 10−Zn:CHAp NPs was 0.18 mass %.

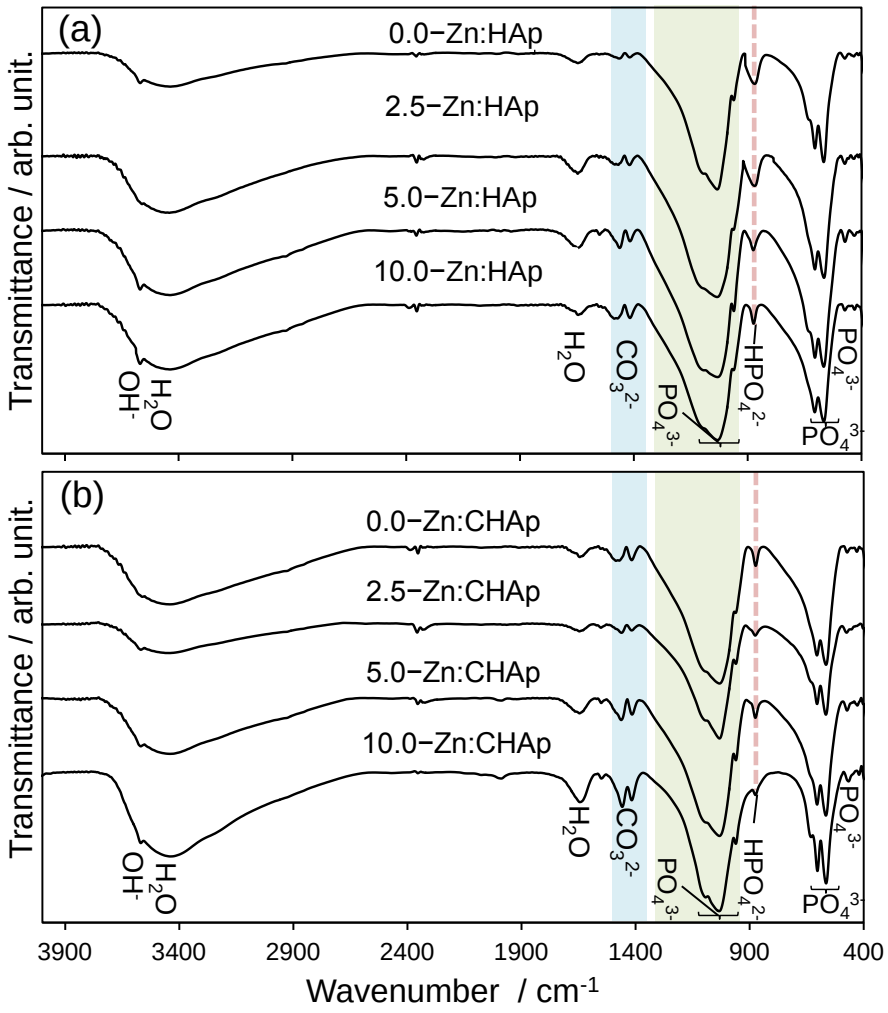

Figure 3.3. FT−IR spectra of the (a) Zn:HAp and (b) Zn:CHAp NPs with the different Zn concentrations.

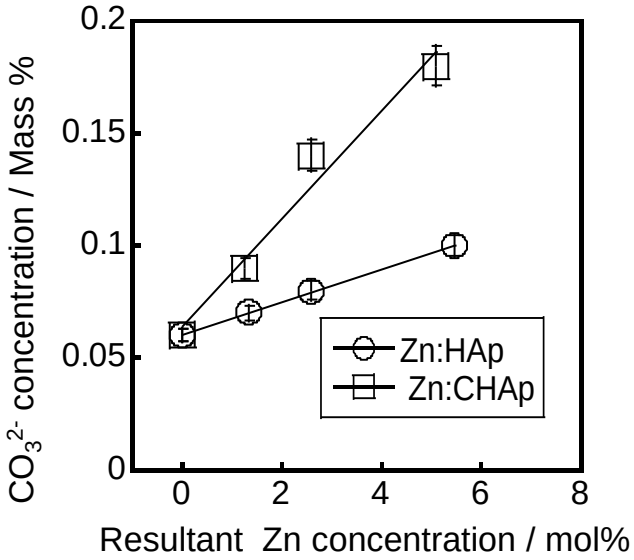

Figure 3.4. Carbonate ion content in weight percent in the (a) Zn:HAp and (b) Zn:CHAp NPs substituted at Zn ion at the concentration of 0.0, 2.5 , 5.0 and 10.0 mol %. The carbonate ion content was calculated from the FT−IR spectra.

Figure 3.5 shows the XRD patterns of the Zn:HAp and Zn:CHAp NPs with the different Zn concentrations. All the peaks were assigned to a HAp single phase (JCPDS No. 09−0432). With the increase in the Zn ion substitution, the peaks are slightly broadening, which would be attributed to the decreased crystallinity by the Zn ion (radius: ca. 0.6 nm) substitution with calcium ion (radius: ca. 0.1 nm) in the HAp NPs structure.[64,65]

The calculated hexagonal unit cell (*a* and *c*) and crystalline sizes (d_{002} and d_{300}) are shown in **Table 3.1**. The 0.0−Zn:HAp and 0.0−Zn:CHAp NPs are a = 9.40 Å and c = 6.88 Å and a = 9.43 Å and c = 6.91 Å, respectively, which are almost similar to the literature of HAp (a = 9.42 Å, c = 6.88 Å).[66]

The decrease in the *a* lattice parameter with increasing the Zn ion substation suggested that the replacement of calcium ions with Zn ion causes the defects as well as suppress the crystal growth along with the *a*-plane.[67] In the case of Zn:CHAp NPs, the decreasing in the *c* lattice parameter with increasing the Zn ion substitution was more pronounced than in Zn: HAp NPs (see **Table 3.1**), suggesting that the phosphate ions were replaced with carbonate ions in the *c*-plane surfaces to suppress the crystal growth along with the plane. Thus, the synthesis in the Zn:CHAp NPs can induce the higher replacement of the phosphate ions

with carbonate ions to totally suppress both the *a*- and *c*-plane crystal growing, and the phenomena would make the crystalline size smaller in the Zn:CHAp NPs. The crystalline sizes (d_{300} and d_{002}) decreased with increasing the Zn ion substitution amount, indicating that the Zn ion addition suppresses the HAp NP growth to form smaller NPs.[64,65,68] Thus, the Zn ion substitution suppressed the NP growth by the exchange of the native calcium and phosphate ions at the near-surfaces.

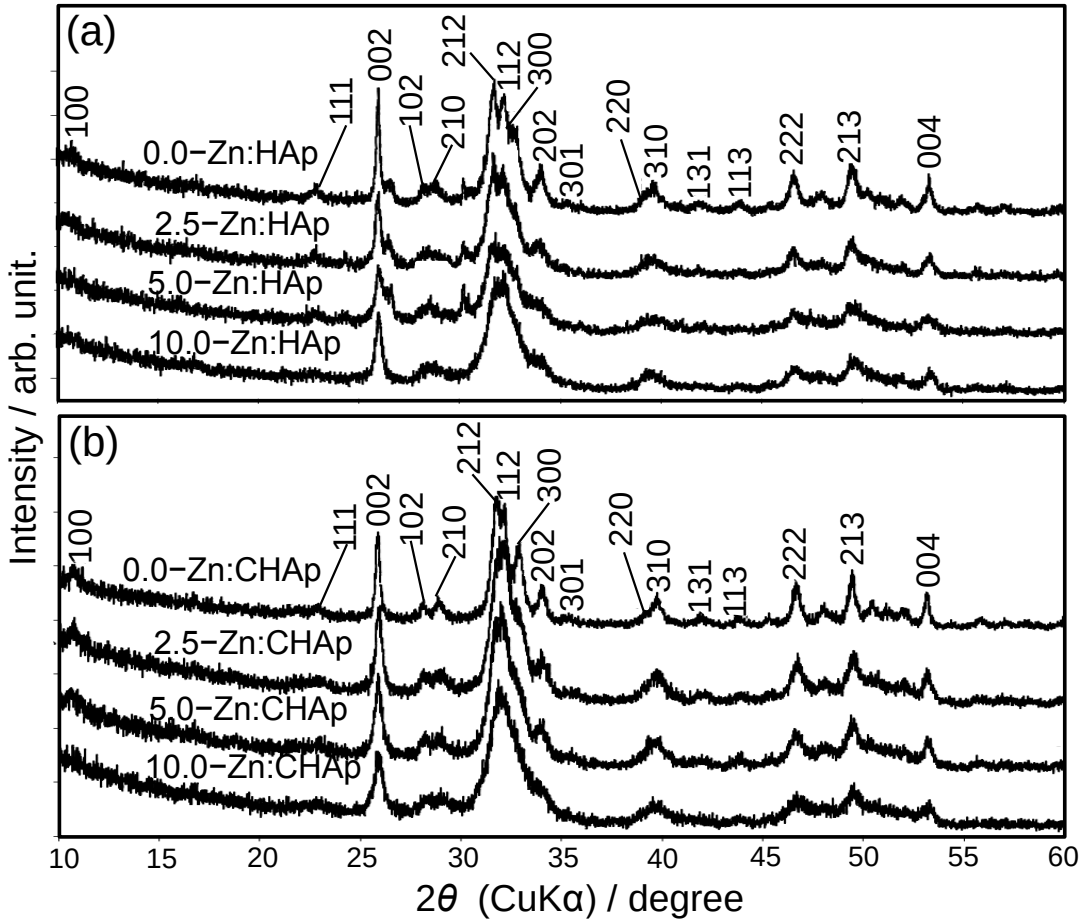

Figure 3.5. XRD patterns of the (a) Zn:HAp and (b) Zn:CHAp NPs with the different Zn concentrations.

Table 3.1. Lattice parameters, crystalline sizes, S_{BET} and zeta potential of the Zn:HAp and Zn:CHAp NPs with the different Zn concentrations.

Sample	Lattice Parameters		Crystalline Sizes		Zeta potential (mV)
	a (Å)	*c* (Å)	d_{002} (nm)	d_{300} (nm)	
0.0−Zn:HAp	9.40	6.88	40	20	−22.2 ± 25.0
2.5−Zn:HAp	9.42	6.88	24	5.7	−17.4 ± 11.5
5.0−Zn:HAp	9.33	6.84	14	5.4	−19.9 ± 15.7
10−Zn:HAp	9.28	6.83	13	5.0	−20.4 ± 5.5
0.0−Zn:CHAp	9.43	6.91	34	15	−16.9 ± 17.4
2.5−Zn:CHAp	9.29	6.91	21	6.0	−20.2 ± 7.7
5.0−Zn:CHAp	9.27	6.84	20	5.6	−20.6 ± 12.4
10−Zn:CHAp	9.24	6.70	18	4.6	−20.0 ± 4.9

The particle size and aspect ratio calculated by TEM images are shown in **Figure 3.6** where the *a*-axis is decreasing due to the increasing the Zn amount which promoted the incorporations of carbonate ion.[69–71] The increase in carbonate ions prevents growth along the *c*-axis, generating a decrease in the *c*-axis but also in the *a*-axis.[72] In both particles the aspect ratio decreased however the decrease in the aspect ratio is higher in Zn:HAp NPs than in Zn:CHAp NPs. The mechanism of decrease in the crystalline size is shown in **Figure 3.7.** The *a*-axis is decreasing due to the increasing the Zn amount[73] which promoted the incorporations of carbonate ion. The increase in carbonate ions prevents growth along the *c*-axis, generating a decrease in the *c*-axis**.** Defects caused by the replacement of phosphate ions with carbonate ions could allow a better interaction between carbonate ions and atmospheric water. These interactions between carbonate ions and atmospheric water could generate more defects, which could favor the dissolution behavior of NPs.

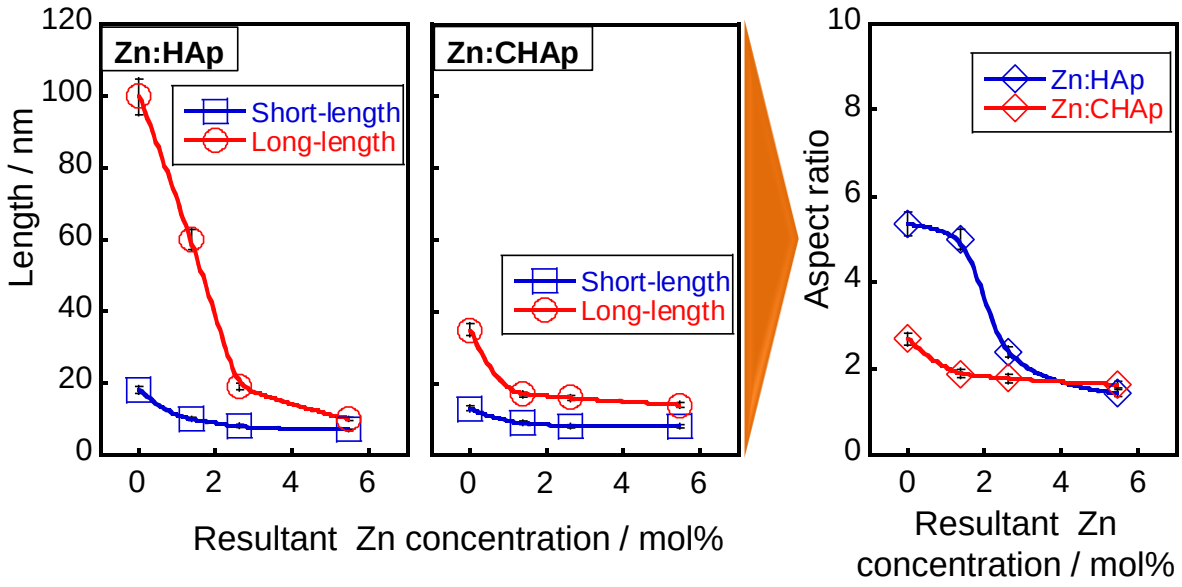

Figure 3.6. Particle size and aspect ratio of the Zn:HAp and Zn:CHAp NPs calculated from TEM images distribution.

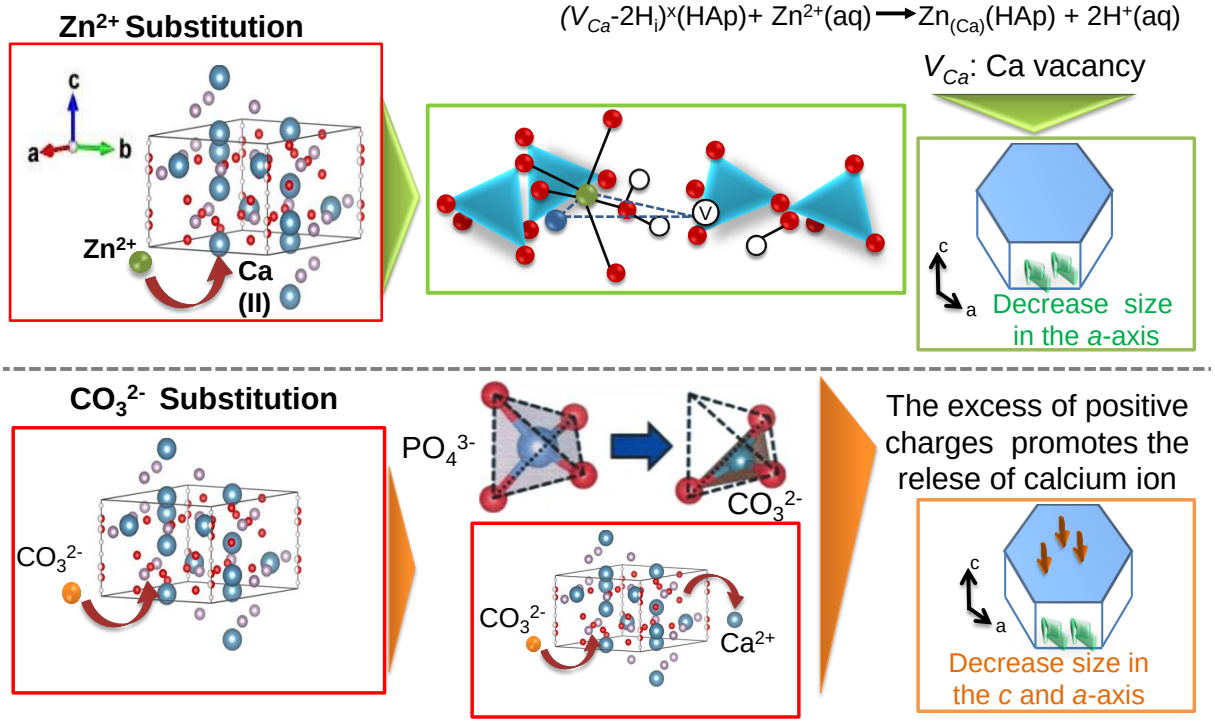

Figure 3.7. Proposed mechanism of the Zn and carbonate ion substitution on the HAp NPs, which explain the decrease in the particle size generated by the defects.

The TEM images and the calculated particle size of the Zn:HAp and Zn:CHAp NPs with the different Zn ion concentrations are shown in **Figure 3.8** and **Figure 3.9**, respectively. All the nanoparticles exhibit the smaller crystalline sizes less than 100 nm. The crystal sizes observed in the TEM correspond to those calculated by the Scherrer equation, indicating the single crystal of one nanoparticle. In the 0.0 and 2.5−Zn:HAp NPs significantly exhibits the typical HAp prism needle–like shape morphologies, and the needle–like shapes were changed to particulate shapes and aggregation states with increasing the Zn ion substitution. On the other hand, the Zn:CHAp NPs exhibit the particulate shapes at the lower Zn ion concentrations, and the higher concentration of Zn also induce the spherical shapes and aggregation states.

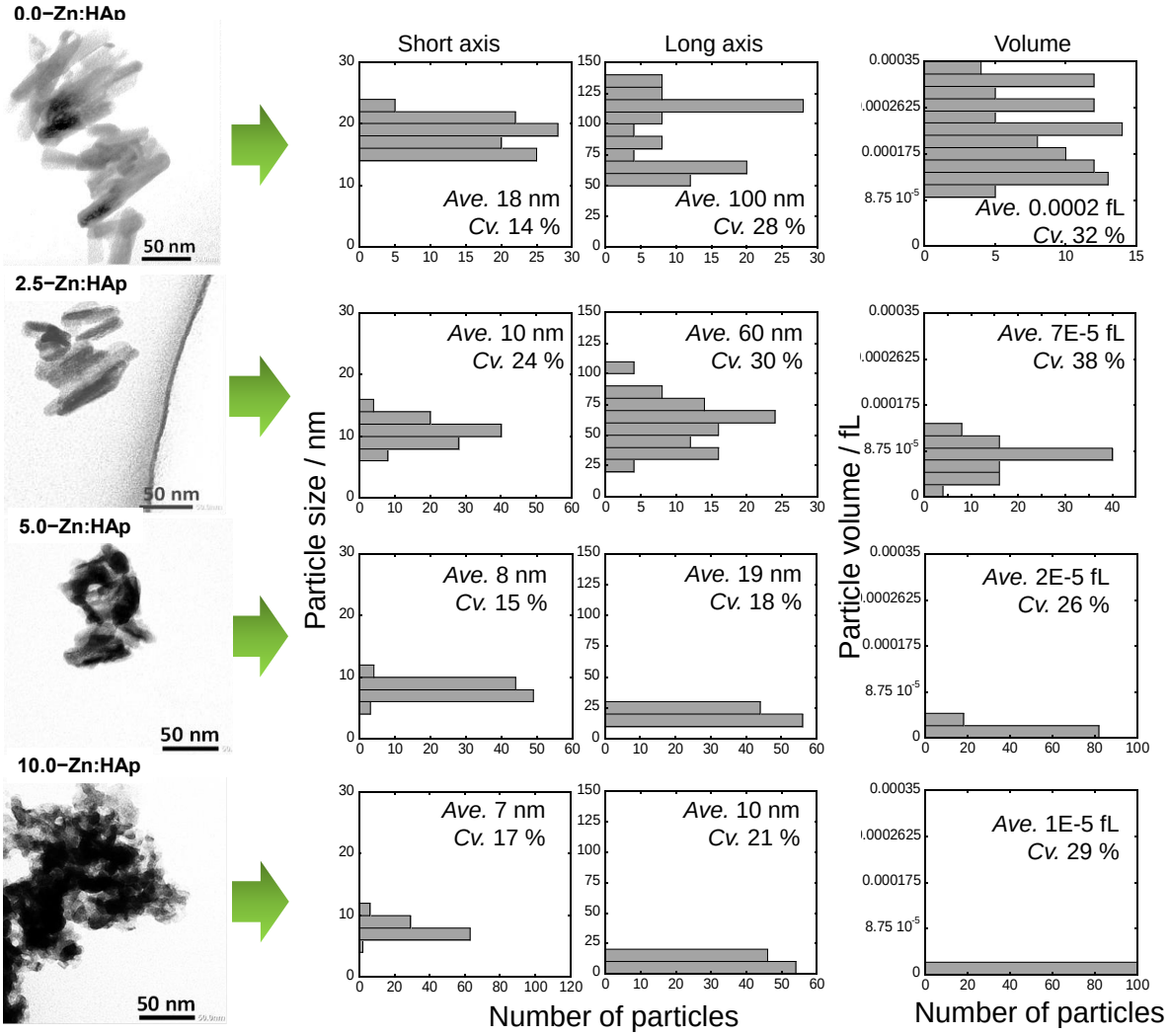

Figure 3.8. TEM images with their short and long axis size distributions and the particle volume distribution calculated from the TEM images of the Zn:HAp NPs at different Zn concentrations.

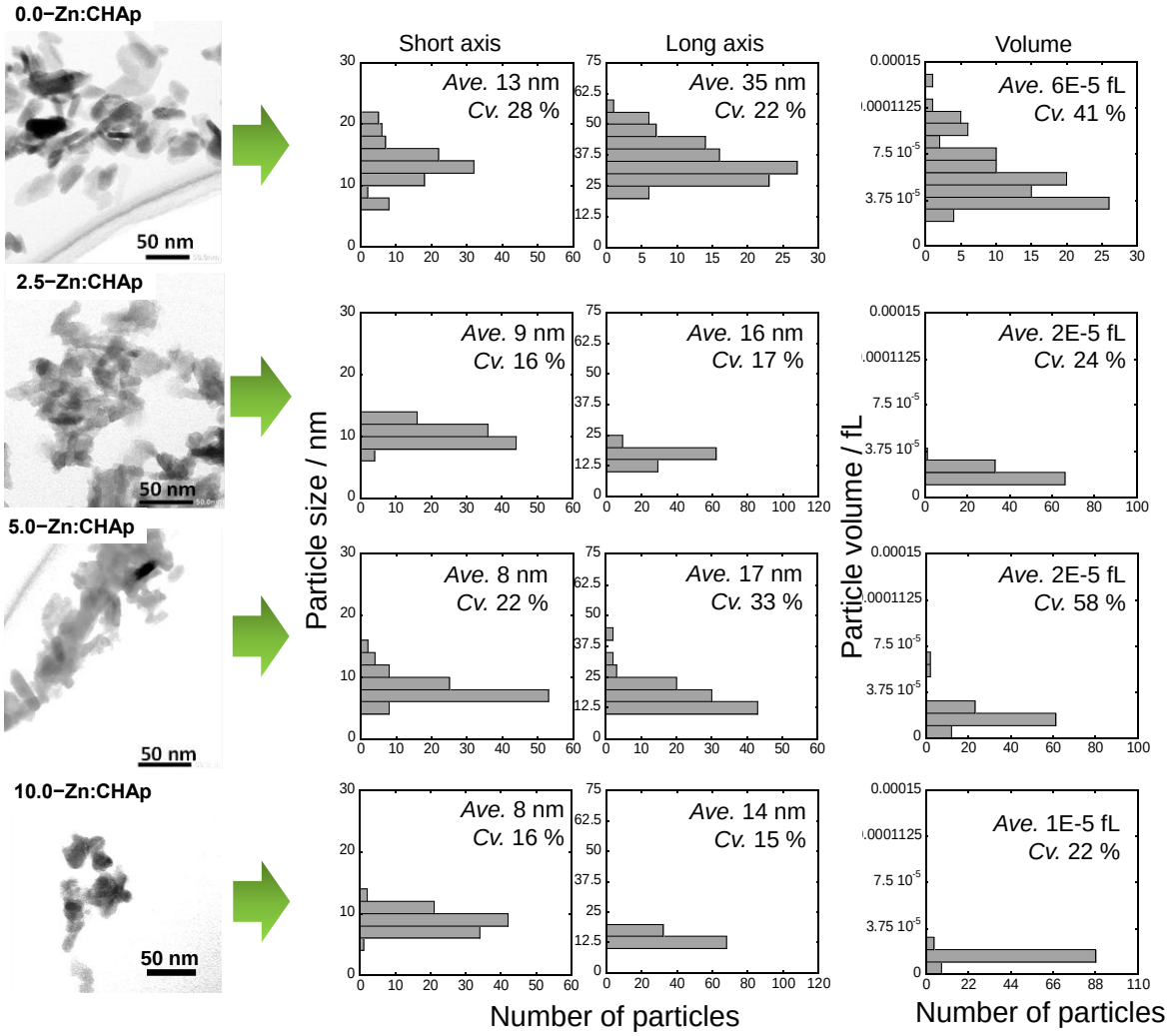

Figure 3.9. TEM images with their short and long axis size distributions and the particle volume distribution calculated from the TEM images of the Zn:CHAp NPs at different Zn concentrations.

The **Figure 3.10** and **3.11** shows the particle size distribution and volume of the Zn:HAp and Zn:CHAp NPs with the different Zn ion, respectively, determined by the qNano particle analyzer. The particle size calculated from TEM and the particle obtained by the qNano particle multianalyzer different for both, Zn:HAp and Zn:CHAp NPs. The particle size was bigger in the qNano analyzer, suggesting that nanoparticles tend to form more aggregates in the PBS solution. The 10.0−Zn:HAp and 10.0−Zn:CHAp NPs showed bigger particle size, which suggest that the increase of the zinc ion content promote the aggregation capacity of the nanoparticles.

The zeta potentials of the samples were calculated from qNano particle multianalyzer of the Zn:HAp and Zn:CHAp NPs are in **Table 3.1**.measurements. The zeta potentials in both HAp NPs increase after calcination which can facilitate the capacity of the HAp NPs of aggregation.

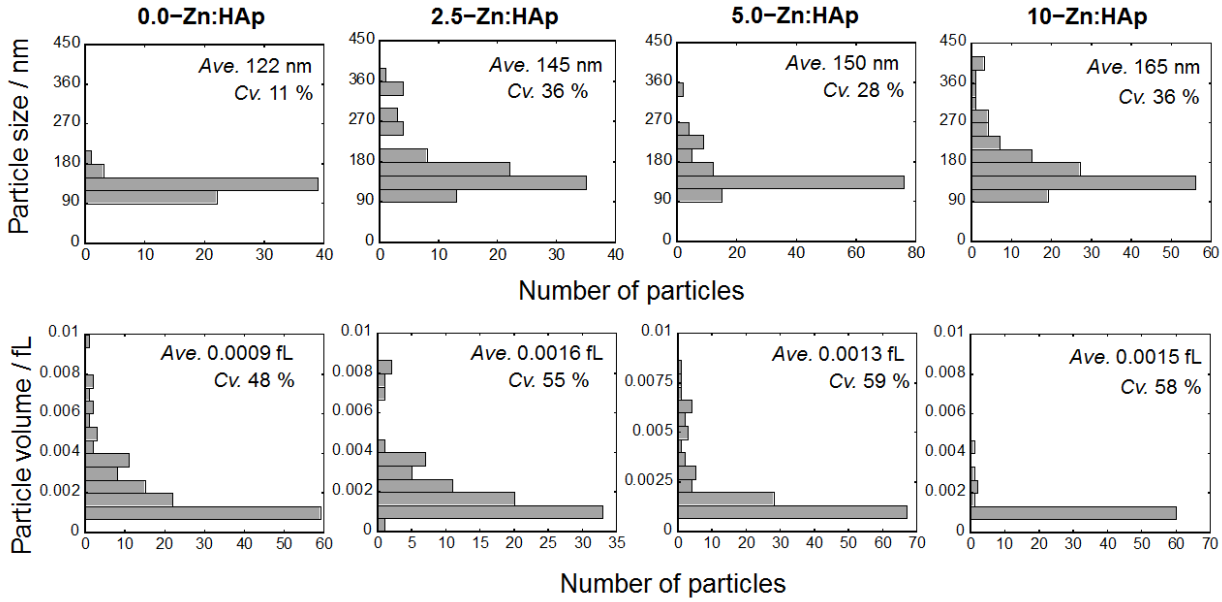

Figure 3.10. Particle size and volume distribution of Zn:HAp NPs doped with the Zn ion concentration of 0.0, 2.5 , 5.0 and 10.0 wt %. Determined after dispersion in PBS by qNano particle multianalyzer.

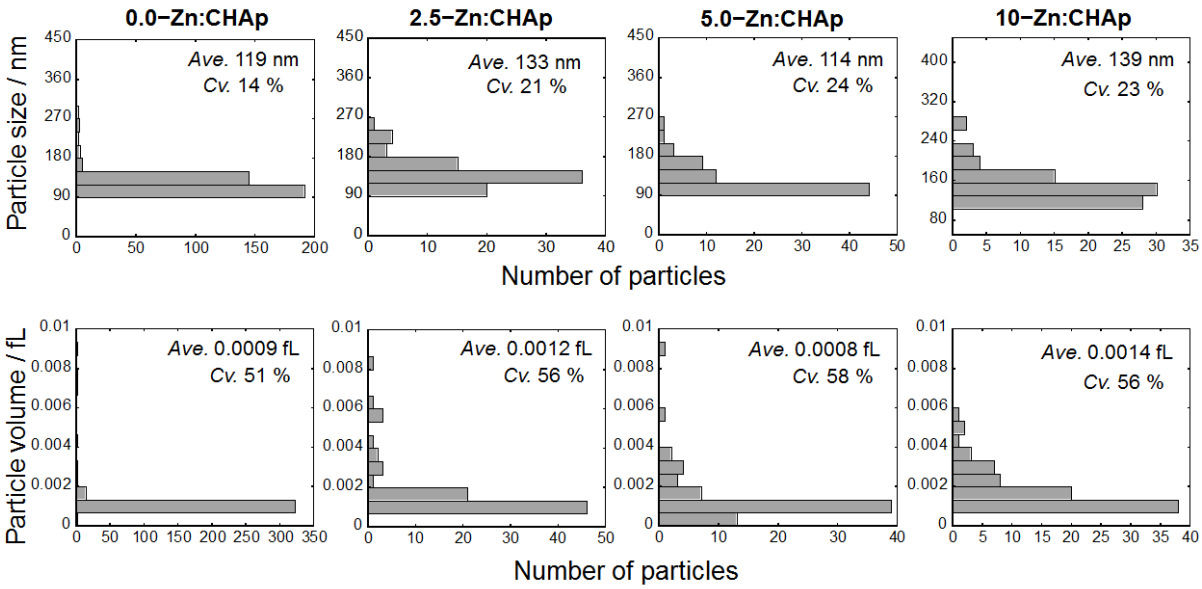

Figure 3.11. Particle size and volume distribution of Zn:CHAp NPs doped with the Zn ion concentration of 0.0, 2.5 , 5.0 and 10.0 wt %. Determined after dispersion in PBS by qNano particle multianalyzer.

Figure 3.12 shows the FT–IR spectra of the stretching O–H absorption band were deconvoluted into the three principal components as the hydration layers[74] adsorbed on the Zn:HAp NPs (**Figure 3.12 (a–d)**) and Zn:CHAp NPs (**Figure 3.12 (e–h)**) with the different Zn ion concentrations. The three components ratios that was assigned to the intermediate and non–freezing waters, which have been totally defined as a bonding water,[75] were thought to have spectra were in **Figure 3.12 (i)**. The component ratios of the free water for Zn:HAp NPs at 0.0, 2.5, 5.0 and 10.0 mol% were 52 %, 53.2 %, 55.9 %, and 48.7 %, for intermediate water 33.8 %, 32.6 % 32.6 %, and 34.8 %, and for non–freezing water 14.2 %, 14.2 %, 14.5 % and 16.5 %, respectively. In the other hand, the free water Zn:CHAp NPs at 0.0, 2.5, 5.0 and 10.0 mol% were 48.6 %, 51.4 % 50.1 %, and 45.8 %, for intermediate water 36.4 %, 31.6 %, 27.7 %, and 23.1 %, and those of the non–freezing water were 15 %, 17 %, 22.2 % and 31.1 %, respectively.

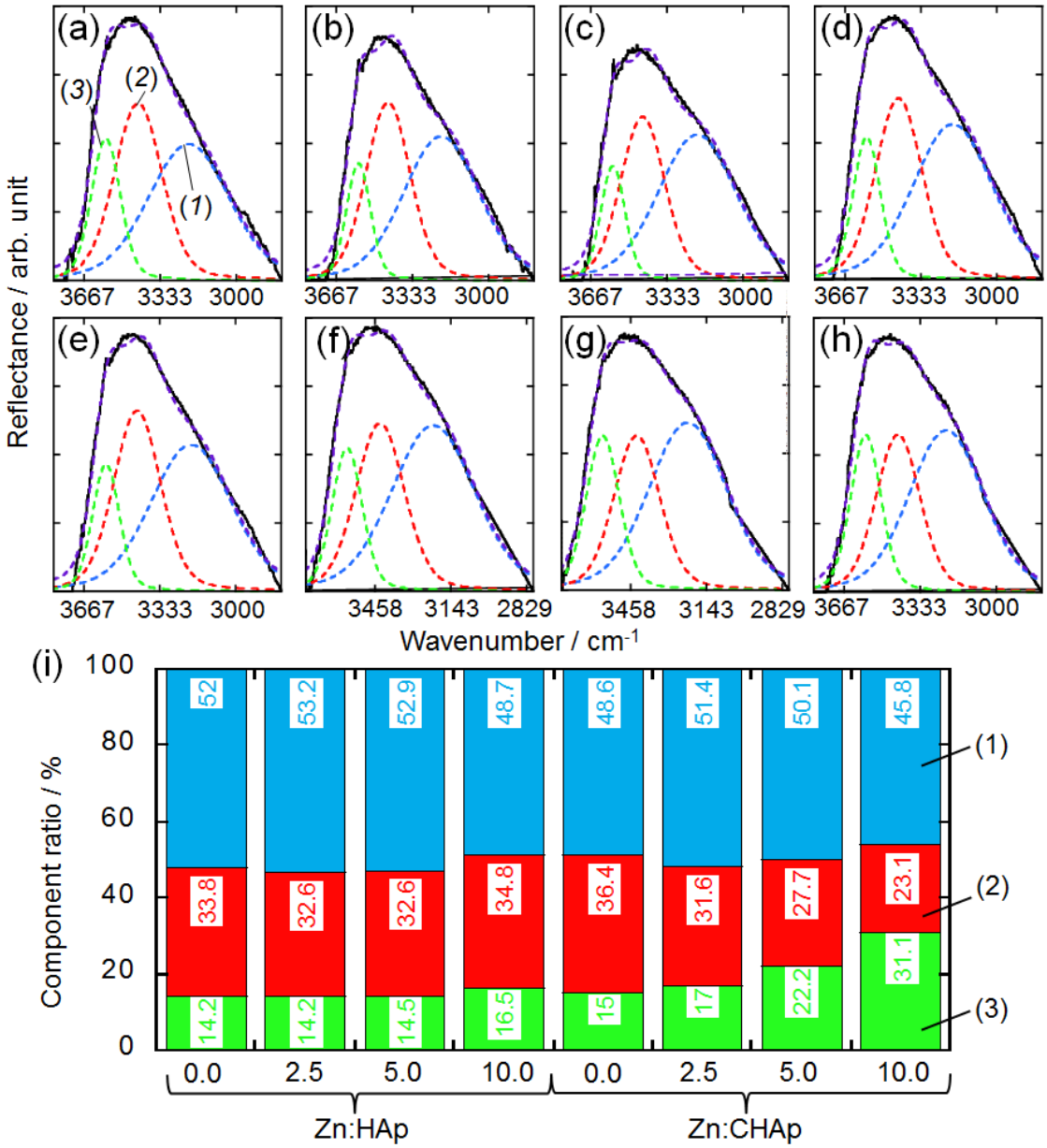

Figure 3.12. Curve fitting and spectral separation results of FT–IR deconvolution spectra of the hydroxyl groups of the hydration layer at 2 hours on (a−d) Zn:HAp NPs with the Zn ion concentration of 0.0, 2.5 , 5.0 and 10.0 wt %, respectively and (e−h) Zn:CHAp NPs with the Zn ion concentration of 0.0, 2.5 , 5.0 and 10.0 wt %, respectively. The separation in 3 of the components are based of the Gaussian-Voigt function and correspond to (1) asymmetric stretching vibration of the (1) free water @ 3200±20 cm^{-1}, (2) intermediate water bending vibration @ 3400±20 cm^{-1}, (3) stretching vibration of non–freezing water @ 3600±20 cm^{-1}, and non-stretching vibration of the hydroxyl group in the HAp structure @ 3571± 1 cm^{-1}. From the deconvolution spectral areas, the component ratios of the secondary structures were represented in (i).

In all the Zn:HAp and Zn:CHAp NPs with the different Zn ion concentrations the non–freezing water ratio increase with the increase of the Zn amount, indicating that the incorporation of Zn allows the formation of hydration structures in the surface of the nanoparticles. The ratio of the bonding water was higher for the Zn:CHAp NPs than for Zn:HAp NPs, in particular, for Zn:CHAp NPs , the non–freezing ratio increase dramatically in the with the increase of Zn amount. The non–freezing water has a direct contact with the material surfaces,[76] thus the obtaining results suggesting a strong interaction between the carbonate ion in the surface of Zn:CHAp NPs at different concentrations and the hydration layer which can generate disorder in the structure and can promote the dissolution of the nanoparticles. In order to corroborate if the cooling process during the freezing drying process affects the hydration layer structures, it was investigated the hydration layer structures without freeze-drying. The obtained hydration layer structures with and without freeze-drying were almost the same, suggesting that the drying process did not affected the hydration layer structures.

The **Figure 3.13 (a–b)** shows the dissolved Ca^{2+} ratios from the total Ca^{2+} content in the Zn–substituted HAp NPs as a function of immersion time in PBS. The dissolution rate of Ca^{2+} from the total Ca^{2+} content in the Zn:HAp NPs at different Zn concentrations were less than 3 wt% and for Zn:CHAp NPs at different Zn concentrations were less than 6 wt% the dissolution amount increase as the Zn concentration increased. The dissolution behavior agreed well with Korsmeyer-Peppas model (**Figure 3.13 (c–d)**).[41] Here, the low *Km* values are the index of low dissolution behavior and depends on the physicochemical properties of the materials irrespective of the dissolution behavior. A previously reported on the radial diffusion from the cylindrical geometry, the value for pure Fickian diffusion is 0.45.[77] It is known that the value for abnormal transport is more than 0.45, and that for Case II transport (e.g., polymer relaxation or swelling–controlled mechanism) is 0.89.[78]

The Zn–substituted nanoparticles were proved to show a very higher dissolution behavior, suggesting that the Zn ion incorporation promotes the Ca^{2+} dissolution. In particular, 5.0–Zn:CHAp and 10.0–Zn:CHAp NPs showed the highest dissolution behavior, these results are in agreement with the hydration layer results, were 5.0–Zn:CHAp NPs and 10.0–Zn:CHAp NPs has higher bonding water ratio, corroborating that the incorporation of

carbonate ions enhanced the adsorption of hydration layer and promote the dissolution. It was observed that the structural changes of the NPs have a direct impact on the solubility of the NPs. The incorporation of Zn and carbonate ions will promote the formations of vacancies and will generate defects in the structure, which can allow having better diffusion of the water from the atmosphere and also stronger interactions with the water, promoting the formation of hydration layer structures and subsequently favoring the dissolution of the Zn:CHAp NPs.

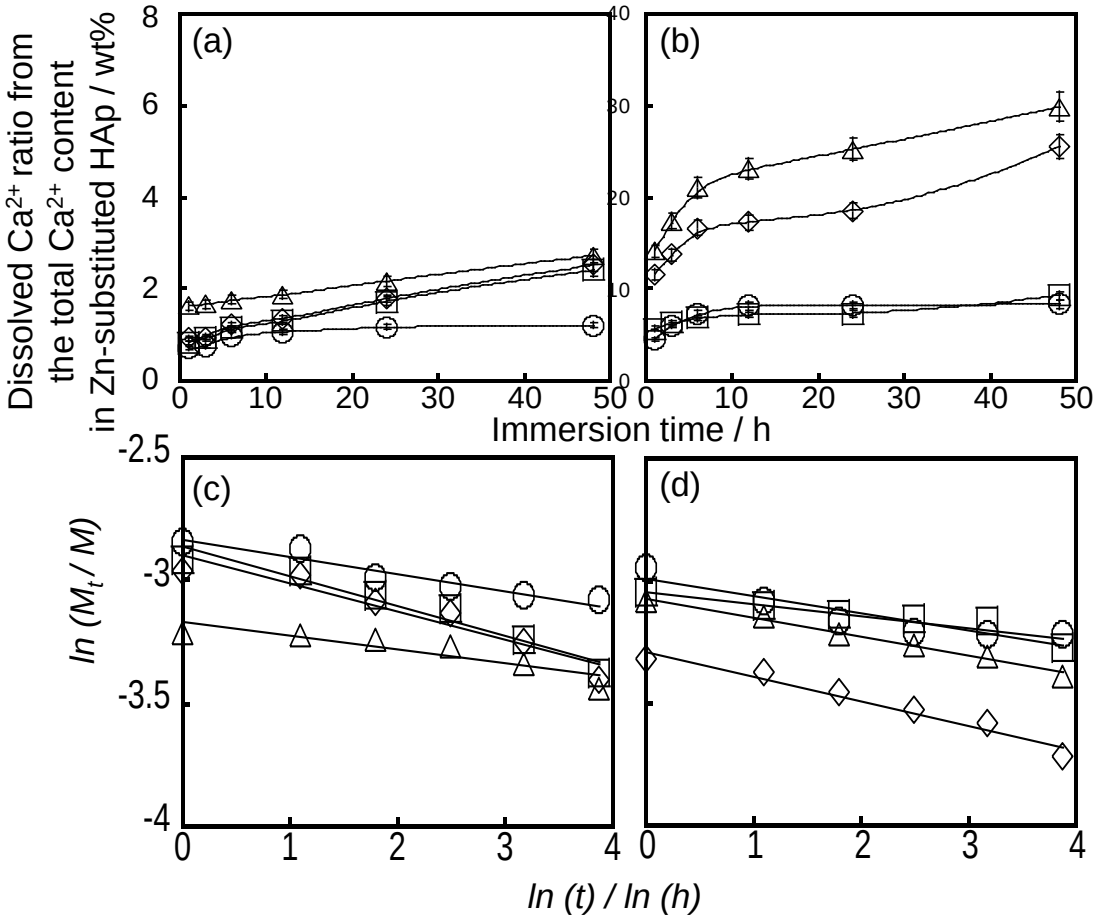

Figure 3.13. (a–b) Dissolved Ca^{2+} and Zn^{2+} ions ratios from the total Ca^{2+} content in the Zn:HAp (a, c) and Zn:CHAp NPs (b, d) with the Zn ion concentration of (○) 0.0, (□) 2.5, (◇) 5.0, and (△)10.0 as a function of immersion time in PBS. The Korsmeyer-Peppas function (c–d) calculated from the dissolved Ca^{2+} and Zn^{2+} ions ratios from the total Ca^{2+} content in the Zn:HAp and Zn:CHAp NPs with different Zn ion concentration is inserted on the graphs.

3.3.2. Characterization of Surface Structures of Zn–substituted HAp NP Films

By the EPD, the Ti-PDMS substrate was successfully covered with the nanoparticles in **Fig. 3.14 (b).** The surplus the nanoparticles were removed to obtain the highly-transparent nanoparticle film on the Ti-PDMS in **Fig. 3.14 (c)** and preserve their substrate flexibility. The nanoparticles would be stabilized at the monolayer states on the Ti surface.[79] The R_{rms} values of the PDMS and Ti-coated PDMS substrates were 0.5 ± 0.1 nm and 0.7 ± 0.2 nm, respectively, as shown in **Fig. 3.14 (f, g**). In the EPD process, the Ti−PDMS surface at 10 V was almost bare and the nanoparticles only remain sporadically, and the surface coverage rates were 50−70 %. In the 50 V, the Ti-PDMS was almost covered with the nanoparticles, and the coverage rates were 80−90 %. In the 100 V, the Ti-PDMS was completely covered with the nanoparticles in the thickness 20−50 nm.

Thus, with increasing the applied voltage, the surface coverage rates of the nanoparticles increased, and those at the 100 V were ca. 100 % in **Table 3.2**, indicating the dense and flat surface coatings on the Ti-PDMS of Zn:HAp and Zn:CAp NPs. These results well correspond to the previous reports on the nanoparticles deposited on metal substrates.[80–83] The representative AFM topographic images of the NP 5.0−Zn:HAp and 5.0−Zn:CHAp NP films on the Ti-PDMS were shown in **Fig. 3.14 (f, g).** The NP 5.0−Zn:HAp and 5.0−Zn:CHAp NP films clearly exhibited the needle-like and particulate shape morphologies, respectively. The R_{rms} values of the NP films were 2−6 nm in **Table 3.2**, indicating the successful preparation of homogeneous NP film formation.

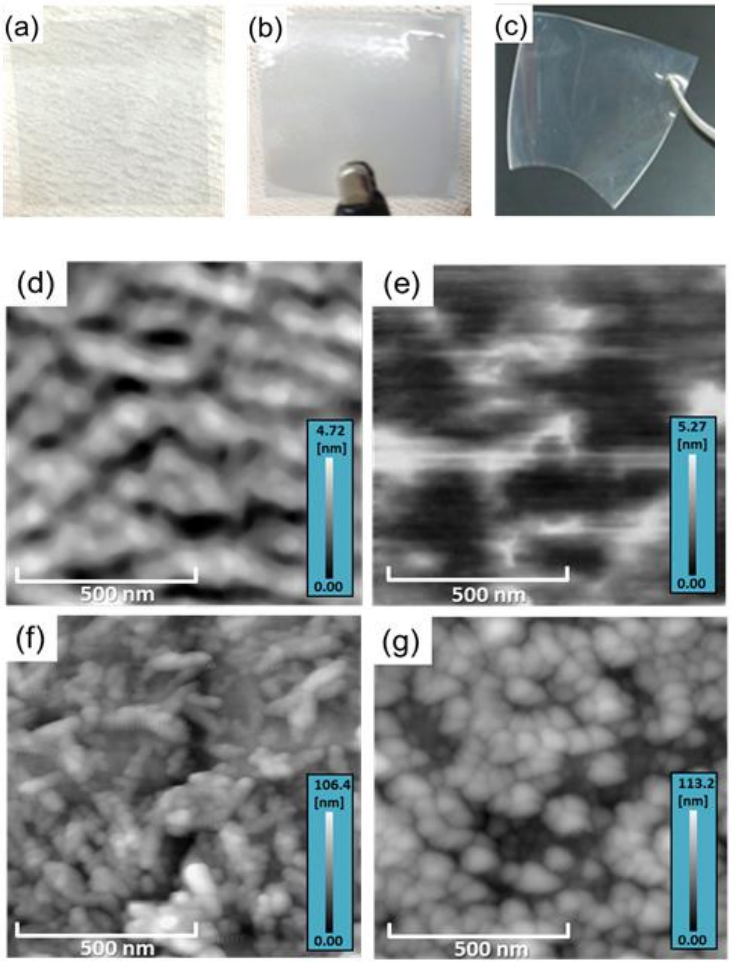

Figure 3.14. Digital images of PDMS substrate (a) before, (b) after electrophoretic deposition of Zn:HAp NPs, (c) after ultrasonification, and AFM topographic images (area: 1.0 × 1.0 μm^2) of the PDMS substrates (d) before, and (e) after Ti-deposition and the surfaces subsequently-deposited with (f) 5.0−Zn:HAp and (g) 5.0−Zn:CHAp NPs. The surface roughnesses were (d) 0.6 nm, (e) 1.2 nm, (f) 6.3 nm and (g) 6.5 nm.

The N_2 adsorption/desorption isotherms of the Zn:HAp and Zn:CHAp NP films are shown in **Figure 3.15**, and the S_{BET} and zeta potential values with the different Zn ion concentrations are summarized in **Table 3.2**. The S_{BET} value significantly increased with increasing the Zn ion substitution, which would be attributed to the smaller nanoparticle formation through the nucleation and NP growth process accompanied with high surface concentration steps, kinks and vacancies. All the samples give typical type IV adsorption isotherms with a slight H3 hysteresis loop as defined by IUPAC,[84] indicating the mesopores and aggregation form by the nanoparticles based on the adsorption on adsorbents with strong interactions as the unrestricted monolayer-multilayer adsorption state.[50,85] This result

suggests the change in the nanoparticle sizes as well as the aggregation states among the smaller-sized spherical nanoparticles.[86] The hysteresis loop is gradually opening a little more with increasing the Zn ion substitution, indicating the aggregation states to form the mesoscale pores,[85] suggesting the nanospaces confined by the nanoparticle aggregation form. The average pore sizes determined by D_{BJH} were in the range between 9−10 nm. All the samples were in the same range with almost no change with increasing the Zn ion amount substitution.

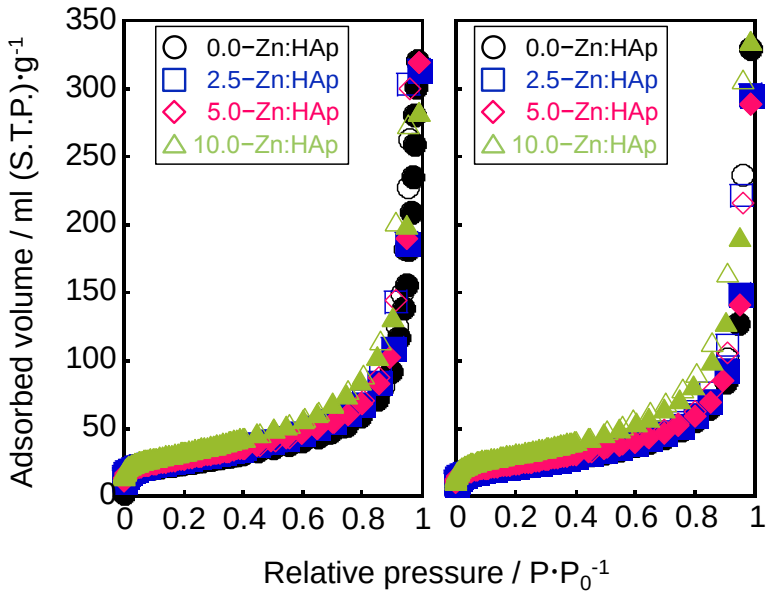

Figure 3.15. Nitrogen adsorption (close figures) and desorption (open figures) isotherms of the (a) Zn:HAp and (b) Zn:CHAp NP films with the different Zn concentrations of 0.0, 2.5, 5.0 and 10.0 mol%.

Table 3.2. Summarized results of surface coverage rates, roughness changes from the AFM topographic images (area: 2.5 × 2.5 μm^2), and the S_{BET} and D_{BJH} of the Zn−substituted NP films.

Sample	Surface Coverage (%)	Surface Roughness, R_{rms} (nm)	S_{BET} (m^2/g)	D_{BJH} (nm)
0.0−Zn:HAp	95.2	2.6 ± 1.2	78	3.4
2.5−Zn:HAp	95.6	6.1 ± 0.7	82	3.3
5.0−Zn:HAp	98.8	6.3 ±1 .5	85	3.1
10.0−Zn:HAp	94.8	5.6 ± 1.2	112	3.0
0.0−Zn:CHAp	96.9	4.3 ± 0.6	87	3.3
2.5−Zn:CHAp	94.4	6.3 ± 0.9	99	3.2
5.0−Zn:CHAp	97.6	6.5 ± 2.1	100	3.1
10.0−Zn:CHAp	94.8	5.8 ± 1.3	118	3.1
Ti-PDMS	----	0.7 ± 0.2	----	----

3.3.3. FT–IR Spectral Analysis for FBS Adsorption Secondary Structures

The adsorption of multiple proteins derived from fetal bovine serum (FBS) in minimum essential medium (DMEM) was shown in **Figure 3.16**. The adsorption behavior depends on the sensor surface. The adsorptive ions in the solvents and the Zn ion content on Zn:HAp and Zn:CHAp NP films and components of the surfaces induce different adsorption behaviors. FBS contains many proteins such as fibronectin, fibrinogen, BSA, and laminin as acidic proteins, IgG, etc. Acidic proteins with a negative charge at neutral pH of the buffers would preferentially adsorb onto the HAp NP surface.[50,87–89] The adsorption would be attributed to the carbonate ions. The carbonate ions adsorb strongly on the hydroxyl group through hydrogen bonds as well as on the Ca site through electrostatic interaction on the HAp NP surface. The bands at around 1500 and 1420 cm^{-1} are attributed to the symmetric mode with its transition moment parallel to the C–O bond (v_s) and the asymmetric mode with its transition moment perpendicular to the same C–O bond (v_{as}).

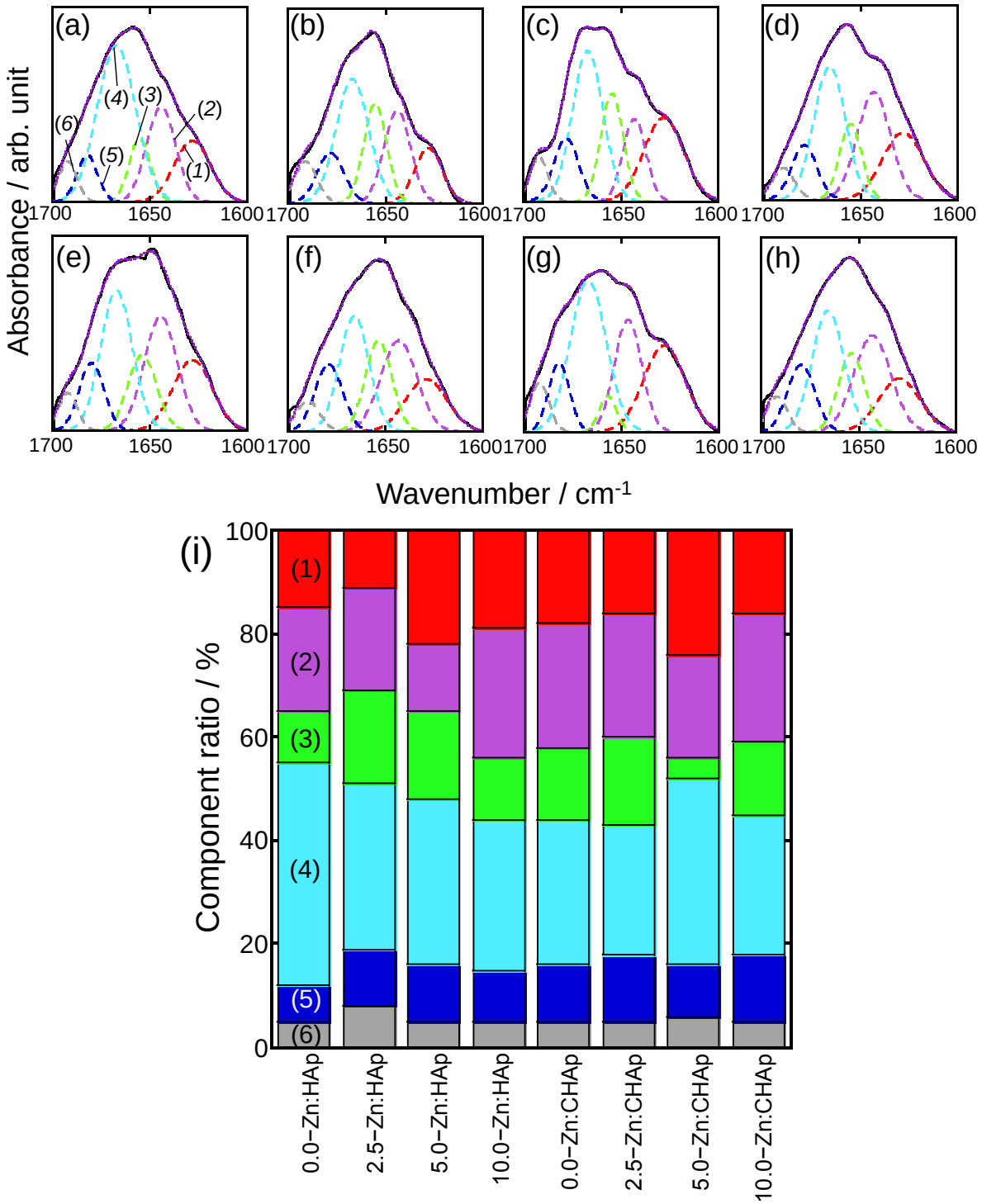

Figure 3.16. Curve fitting and spectral separation results of FT-IR deconvolution spectra of the amide I band of the adsorbed FBS on (a−d) Zn:HAp and (e−h) Zn:CHAp NP film doped with the Zn ion concentration of 0.0, 2.5, 5.0 and 10.0 wt %. Their secondary structural components are (1) β−sheet, (2) random, (3) α−helix, (4) turn, (5) β−turn, and (6) β−turn. The component ratios of the secondary structures calculated from the deconvolution spectral areas of the amide I band were shown in (i).

The variation in the relative band ratio (νs/νas) with increasing concentration can be attributed to changes in the bonding state of the adsorbed carbonate ions on the HAp NP surface.[50] In the component ratios of the adsorbed FBS (**Fig. 3.16 (i)**) was observed that the α–helix ratio was higher in the Zn–substituted HAp NP films, indicating that the Zn ion prevents the denaturalization of the adsorbed proteins. The 5.0–Zn:CHAp NP film and 5–Zn:HAp NP film had the higher β–sheet ratio in comparison with the others NP films, suggesting that the substitution of 5.0 mol% of zinc is appropriate for the promoting the β–sheet conformation. The secondary structural arrangements of the proteins will depend on the interactions with the NPs, and in this case with the Zn. It has been noticed that the Zn ion is more thermodynamically prone to join and promote beta-sheet conformation, promoting the fouling of the protein.[90] In the case of 5.0–Zn:CHAp NP film, it was observed the highest beta-sheet ratio, which could be attributed to the interactions between the proteins and the Zn ions; which can be interpreted as that 5.0–Zn:CHAp NP film promotes adsorption of the proteins in the β–sheet conformation.

3.3.4. Antibacterial Properties

Table 3.3 shows the results of viable number of *E. coli* DH5α. All the Zn–substituted NP films decreased the number of viable *E. coli* DH5α colonies with the increase in the Zn substitution amount. The antibacterial activity of the Zn:CHAp NP films were better than that of the Zn:HAp NP films, which would be attributed to the near-surface dissolving activity of Zn ion by the existence of rich carbonate ions, even though the Ti-PDMS suppressed the *E. coli* DH5α binding, which would be attributed to the hydrophobic surface properties.

The substituted Zn ion amount in the nanoparticles was 0.76 and 0.68 wt% by the XRF analysis for the 10.0−Zn:HAp and 10.0−Zn:CHAp NPs. These contents are non-cytotoxic concentrations for the cells based on the threshold at 1.5 wt%,[91,92] which were clarified by in vitro experiments for mouse osteoblastic MC3T3-E1 growth. The eluted Zn ions in the culture medium would affect the cell activity and these mechanisms were not investigated. It is suggested the successful preparation of the 5.0 and 10−Zn:CHAp NP films with the cytocompatibility as well as antibacterial activity. It is thought that the antibacterial activity

would be derived from the dissolved Zn ion and reactive oxygen atoms at the near-surfaces of the NPs. Indeed, the other studies showed that the membranes of *E. coli* DH5α can be damaged after the contact with dissolved Zn ions,[93,94] causing nutrients, proteins and other essential components of the cytoplasm within the bacteria to 'leak out', resulting in the death.[95,96] In this study, there is a slight elution of Zn ions at the near-surfaces of the nanoparticles, and the eluted ions are the significant concentration to affect the attached antibacterial activity.

The Zn ion would interact with the cytoplasm to form the bonding with the membrane proteins of *E. coli* DH5α, leading to the death. When the activated oxygen is assumed, the oxygen radical species by the Zn ions substituted in the nanoparticles would be rapidly deactivated.

Table 3.3. Summarized results of the viable number of *E. coli* DH5α after the second culture at the lower seeding concentration (first culture: 1×10^3 CFU/μL and second culture: 5 CFU/200 μL) and at the higher seeding concentration (first culture: 1×10^6 CFU/mL and second culture: 1×10 CFU/200 μL).

Sample	Viable Number of *E. coli* DH5α at the Lower Seeding Concentration	Viable Number of *E. coli* DH5α at the Higher Seeding Concentration
0.0−Zn:HAp	80	800
2.5−Zn:HAp	70	700
5.0−Zn:HAp	60	638
10.0−Zn:HAp	48	575
0.0−Zn:CHAp	102	1038
2.5−Zn:CHAp	83	790
5.0−Zn:CHAp	81	775
10.0−Zn:CHAp	50	463
Reference	38	375

3.3.5. Cytocompatible Properties

Figure 3.17 shows the density and aspect ratio of the cells adhered on the Zn:HAp and Zn:CHAp NP films and the reference Ti-PDMS. In all the Zn−substituted HAp NP films, the density increased with increasing the culture time, whereas the Ti-PDMS inhibited the cellular growth. In particular, the densities on the 5.0 and 10.0−Zn:CHAp NP films were higher than those on the other surfaces, suggesting the CHAp NP films promotes the fibroblast adhesion. As shown in **Figure 3.18**, the optical microscope images of the adhered cells at the culture time of 24 h revealed the cellular growth patterns on the Zn−substituted HAp NP films. The Zn:CHAp NP films exhibited good adhesion/spreading behaviors, indicating that the carbonate ions play an important role in the cytocompatibility. The larger aspect ratios of the cells adhered on the Zn:CHAp NP films (0.0 and 5.0−Zn:CHAp NP films) is indicative of the uniaxial spreading due to the strongly binding to the surfaces. It was observed that the fibroblast at 24 h of culture on Zn:CHAp NP films had pseudopods formation, unlike the other Zn:HAp NP films, where cells had more round shapes. Especially 5.0−Zn:CHAp NP films had a formation of larger pseudopods and good spreading, indicating a preferential affinity for this film. Since the cell survival is significantly affected by the adherent cellular shape,[97] the Zn:CHAp NP films would provide long cell survival.[98,99] Based on the multiple viewpoints on the anchorage-dependent cell adhesion/spreading and proliferation,[61,100,101] it is suggested that the 5.0−Zn:CHAp NP film is the best for fibroblast adhesion/spreading and could provide a suitable environment for binding with fibroblasts.

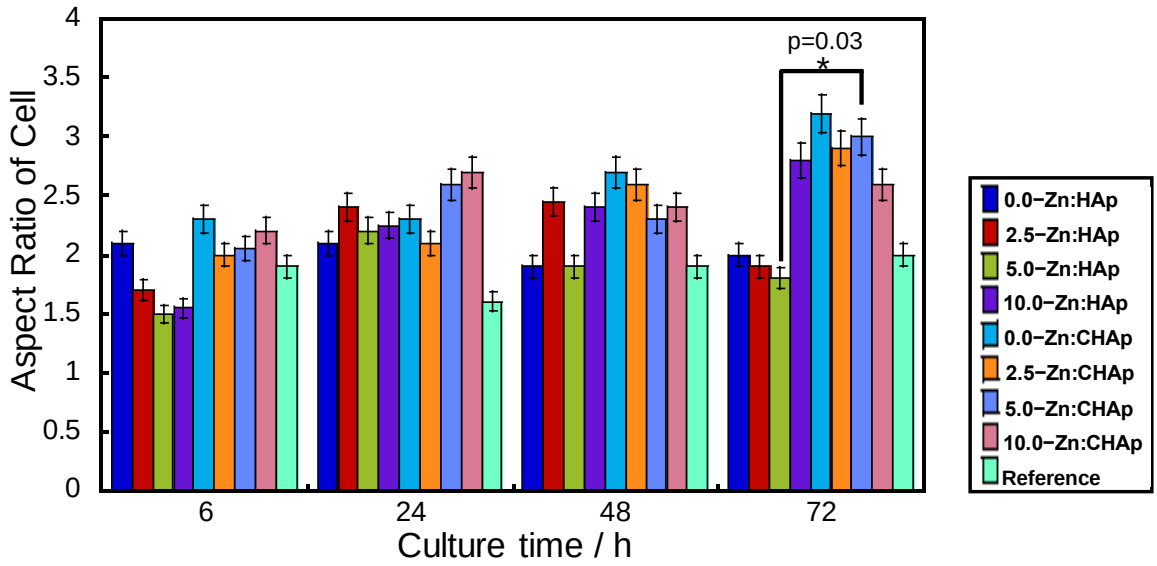

Figure 3.17. Aspect ratio of the fibroblasts adhered on the Zn:HAp and Zn:CHAp NP films with the different Zn concentrations of Zn concentrations at 0.0, 2.5, 5.0 and 10.0 mol% and the reference Ti-PDMS film at different culture time.

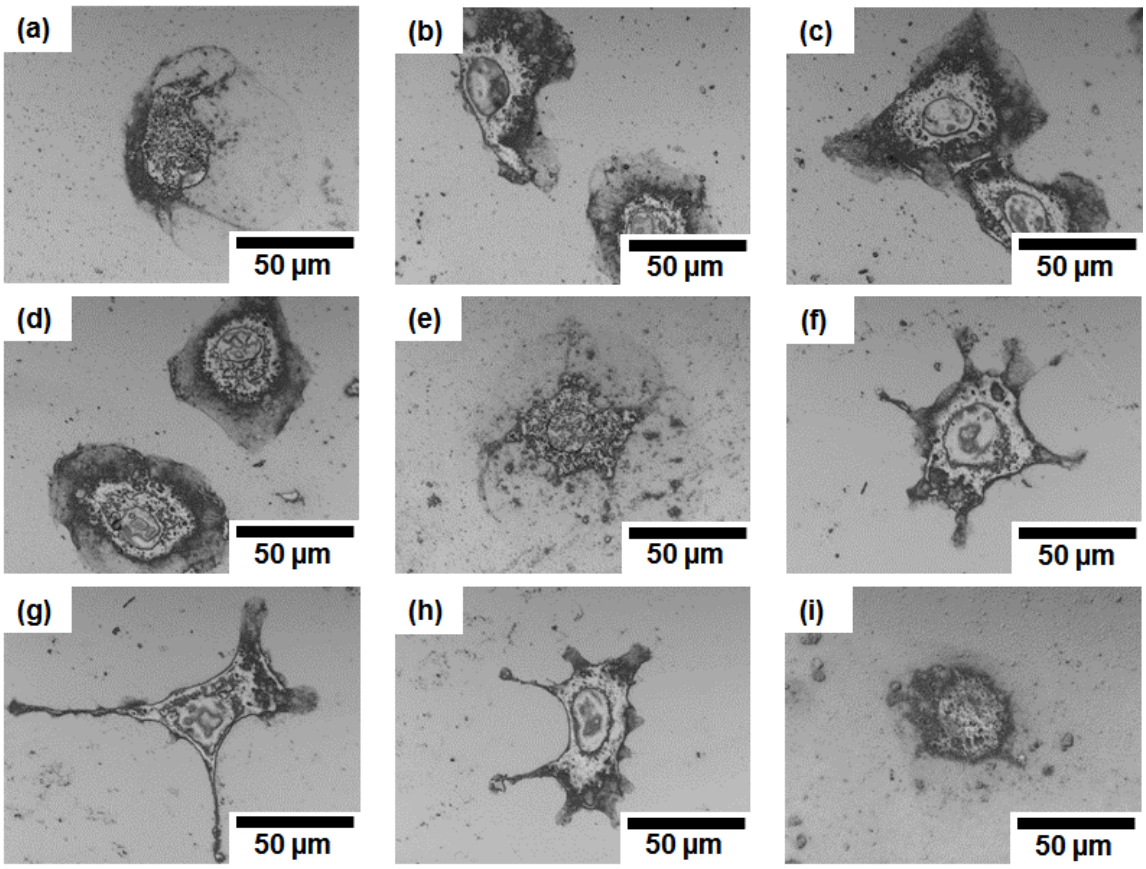

Figure 3.18. Micrographs of the fibroblast adhered at the culture time of 24 hours on the (a−d) Zn:HAp and (e−h) Zn:CHAp NP films with the different Zn concentrations at (a, e) 0.0, (b, f) 2.5, (c, g) 5.0 and (d, h) 10.0 mol% and (i) the Ti-PDMS film as the reference.

Figure 3.19 shows the densities of the fibroblast on Zn−substituted HAp NP films. The lowest cell density was observed on Ti-PDMS due to the bioinert property of the reference. Zn:CHAp NP films higher densities than Zn:HAp NP films. In particular, 5.0 and 10.0−Zn:CHAp NP films, exhibited the preferential adhesion due to the interactions of the cells and ECM proteins with the carbonate and Zn ions, suggesting that Zn:CHAp NP films promotes the fibroblast adhesion. The optical microscope images of the adhered fibroblasts on Zn−substituted HAp NP films at 72 hours are shown in **Figure 3.20.** The cells on Zn: HAp NP films **(Fig. 3.20 (a−d))** had almost the same cellular shapes that the cells on the reference Ti-PDMS **(Fig. 3.20 (i))**. In contrast, the cells on the 2.5, 5.0 and 10.0−Zn:CHAp NP films showed good adhesion and fibrous spreading shapes. The cell survival known to be affected by the adherent cell shapes and areas,[102–104] indicating that the Zn:CHAp NP film would provide long cell survival without cytotoxicity. Therefore, the Zn:CHAp NP film could provide a suitable surface properties for fibroblast interactions, suggesting both the carbonated and Zn−substituted HAp NP films promotes the fibroblast adhesion.[105] Therefore, the optimized cytocompatible properties of the nanoparticles were successfully suggested, which can be useful as the implant surface modification.

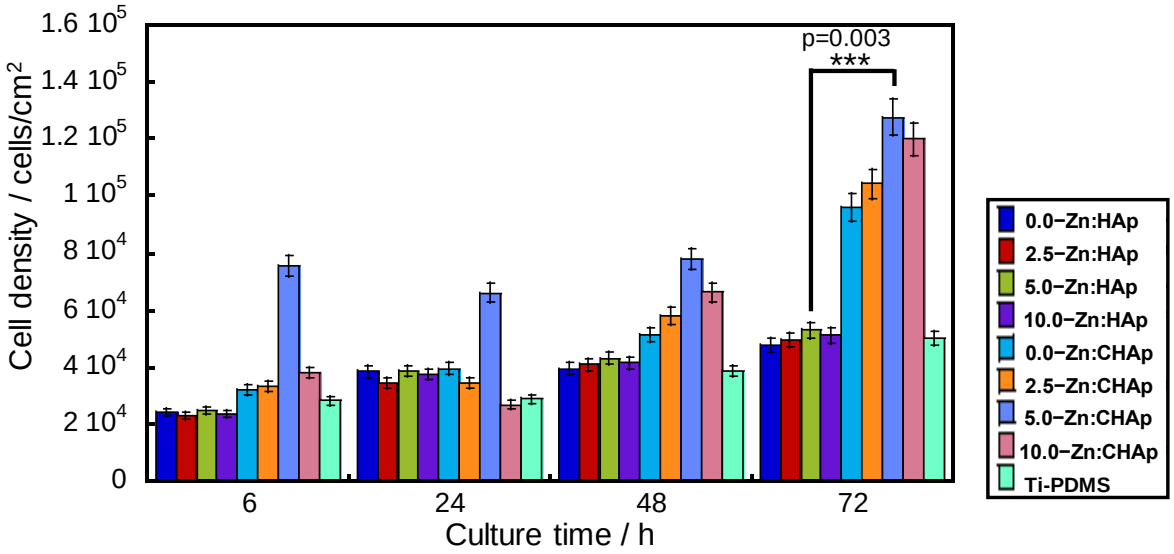

Figure 3.19. Densities of the fibroblasts adhered on the Zn:HAp and Zn:CHAp NP films with the different Zn concentrations of Zn concentrations at 0.0, 2.5, 5.0 and 10.0 mol% and the reference Ti- PDMS film at different culture time.

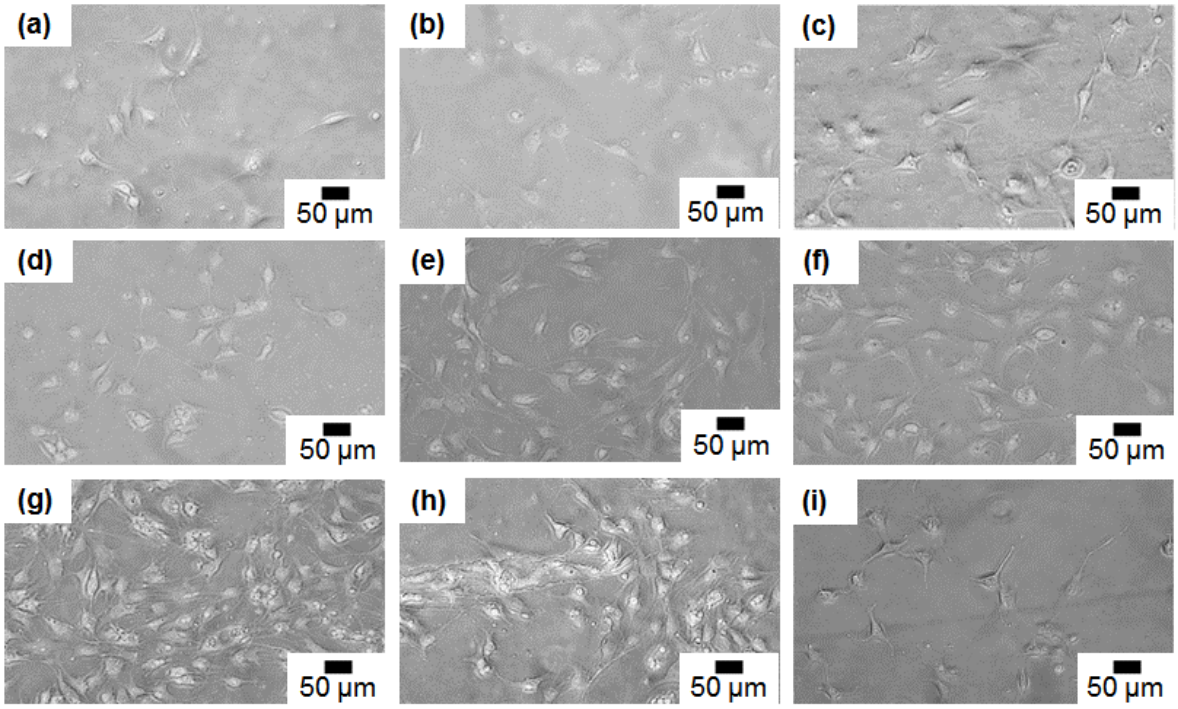

Figure 3.20. Micrographs of the fibroblasts adhered on the (a−d) Zn:HAp and (e−h) Zn:CHAp NP films with the different Zn concentrations at (a, e) 0.0, (b, f) 2.5, (c, g) 5.0 and (d, h) 10.0 mol% and (i) the Ti-PDMS film as the reference at the culture time of 72 h.

Based on the anchored-dependent cell adhesion/spreading and proliferation, it was proposed that the 5.0−Zn:CHAp NP film is the best for fibroblast adhesion /spreading because it provides a suitable environment for binding with fibroblast but also have antibacterial activity. The proposed mechanism for cytocompatibility as well as antibacterial activity of 5.0−Zn:CHAp NP film is illustrated in **Figure 3.21**. The proposed mechanism of the cytocompatibility and antibacterial activity can be explained due to the incorporation of both Zn and carbonate ions in the HAp. The incorporation of carbonate ions favors the formation of defects, which could promote the diffusion of water and therefore the interactions between carbonate ions and water, thus promoting the adsorption of hydration layers, especially non-freezing water , this promotes the dissolution of the NP from the film. As the ions are in solution, it is easier for them to interact with the cells. In the case of cytocompatibility, Zn ions can bind with the proteins of the culture medium, promoting their absorption in beta-sheet conformation, which promotes cell adhesion. Zn ions can also bind to ECM proteins of the cells, which helping to anchor cells on the NP film. Zinc ions can enter cells using zinc channels and inside the cells can help cells to form

new proteins necessary for cell growth. Carbonate ions and calcium ions also help cell anchoring, favoring their adhesion. Instead, for antibacterial activity, the zinc ions can bind to the membrane of the bacteria because the cell membrane of the bacteria is different from that of the cells, this union can cause disruption of the membrane. If the Zn ions permeate in the bacteria, the Zn ions can interact with the proteins which cause their denaturation, also can cause DNA and mitochondrial damage. It can also cause oxidative stress and lysis of the bacteria, generating the death of the bacteria.

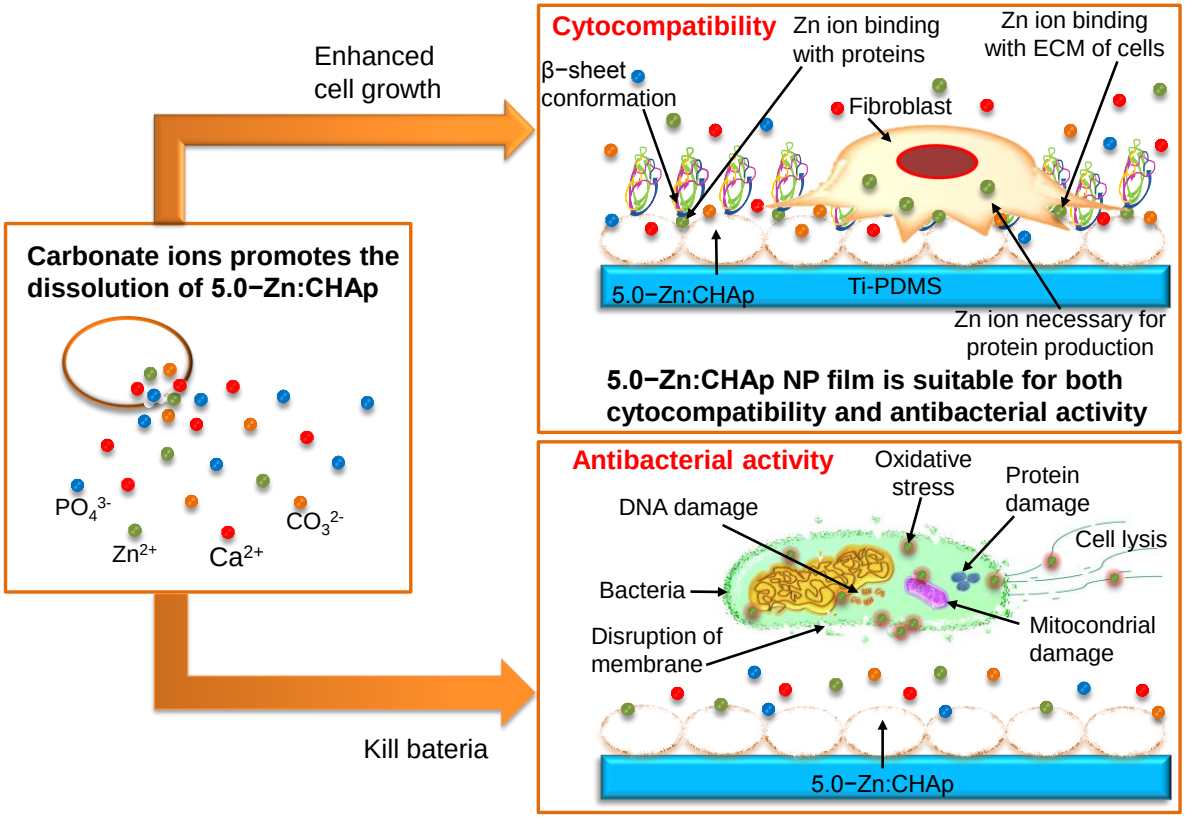

Figure 3.21. Proposed Zn and carbonate ion mechanism of the cytocompatible and antibacterial activity properties of 5.0−Zn:CHAp NP film.

3.4. Conclusion

The Zn−substituted HAp NPs were successfully synthesized at the initial molar ratios of (Ca+Zn)/P at 1.67 and 2.00, providing the stoichiometric Zn:HAp and carbonate Zn:CHAp NPs and the maximum Zn ion substitution in the structure is ca. 5 mol% by the XRF analysis. The 10.0−Zn:HAp and 10.0−Zn:CHAp NPs contain 0.76 and 0.68 wt% of Zn at the maxima, respectively, which is safety for cells in the animal body. The increase in the Zn ion concentration significantly induced the carbonate ion including. The crystalline size decreased with the increasing Zn ion substitution, indicating the suppression of the crystal growth by the Zn ion addition to resultantly increase the specific surface area. TEM observation clearly indicated that the needle–like shape nanoparticles were changed to the particulate shapes with increasing the Zn ion substitution to form aggregation form with the mesostructures. Thus, the morphological control by the Zn−substitution in stoichiometric and carbonate HAp NPs was successfully achieved. The Zn:HAp and Zn:CHAp NPs were deposited on the Ti-PDMS by an EPD technique obtaining an uniform and transparent Zn:HAp and Zn:CHAp NPs.

The fibroblasts on the Zn−substituted HAp NP films exhibited good adhesion/spreading. In particular, the Zn:CHAp NP films are very cytocompatible. By the antibacterial test, the viable *E. coli* DH5α reduction was significantly observed in the films with the higher Zn amounts. Resultantly, the 5.0 and 10−Zn:CHAp NP films. Furthermore, all the nanoparticle films electrically plated on a Ti-PDMS substrate give no cytotoxicity, and the Zn:CHAp NP films significantly provided the bioactive properties for fibroblast ingrowth, suggesting the effect of Zn and carbonate ions on the cytocompatibility. Summarizing, The Zn:HAp and Zn:CHAp NP films with the optimized cytocompatible and antibacterial properties were successfully prepared as the Ti-PDMS surface modification technique.

References

(1) Affeld, K.; Grosshauser, J.; Goubergrits, L.; Kertzscher, U. Percutaneous Devices: A Review of Applications, Problems and Possible Solutions. *Expert Rev. Med. Devices* **2012**, *9* (4), 389–399.

(2) Von-Recum, A. F. Applications and Failure Modes of Percutaneous Devices: A Review. *J. Biomed. Mater. Res.* **1984**, *18* (4), 323–336.

(3) von Recum, A. F.; Park, J. B. Permanent Percutaneous Devices. *Crit. Rev. Bioeng.* **1981**, *5* (1), 37–77.

(4) Mooney, V.; Schwartz, S. A.; Roth, A. M.; Gorniowsky, M. J. Percutaneous Implant Devices. *Ann. Biomed. Eng.* **1977**, *5* (1), 34–46.

(5) Gerritsen, M.; Lutterman, J. A.; Jansen, J. A. Wound Healing around Bone-Anchored Percutaneous Devices in Experimental Diabetes Mellitus. *J. Biomed. Mater. Res.* **2000**, *53* (6), 702–709.

(6) Affeld, K.; Grosshauser, J.; Goubergrits, L.; Kertzscher, U. Percutaneous Devices: A Review of Applications, Problems and Possible Solutions. *Expert Rev. Med. Devices* **2012**, *9* (4), 389–399.

(7) Okada, T.; Ikada, Y. Surface Modification of Silicone for Percutaneous Implantation. *J. Biomater. Sci. Polym. Ed.* **1995**, *7* (2), 171–180.

(8) Furuzono, T.; Wang, P. L.; Korematsu, A.; Miyazaki, K.; Oido-Mori, M.; Kowashi, Y.; Ohura, K.; Tanaka, J.; Kishida, A. Physical and Biological Evaluations of Sintered Hydroxyapatite/Silicone Composite with Covalent Bonding for a Percutaneous Implant Material. *J. Biomed. Mater. Res.* **2003**, *65B* (2), 217–226.

(9) Wen, J.; Li, Y.; Zuo, Y.; Zhou, G.; Li, J.; Jiang, L.; Xu, W. Preparation and Characterization of Nano-Hydroxyapatite/Silicone Rubber Composite. *Mater. Lett.* **2008**, *62* (19), 3307–3309.

(10) Szcześ, A.; Hołysz, L.; Chibowski, E. Synthesis of Hydroxyapatite for Biomedical Applications. *Adv. Colloid Interface Sci.* **2017**, *249*, 321–330.

(11) Jao, D.; Mou, X.; Hu, X. Tissue Regeneration: A Silk Road. *J. Funct. Biomater.* **2016**, *7* (3), 22.

(12) Yeo, I. S. Reality of Dental Implant Surface Modification: A Short Literature Review. *Open Biomed. Eng. J.* **2014**, *8*, 114–119.

(13) Furuzono, T.; Sonoda, K.; Tanaka, J. A Hydroxyapatite Coating Covalently Linked onto a Silicone Implant Material. *J. Biomed. Mater. Res.* **2001**, *56* (1), 9–16.

(14) Oyane, A.; Kawashita, M.; Nakanishi, K.; Kokubo, T.; Minoda, M.; Miyamoto, T.; Nakamura, T. Bonelike Apatite Formation on Ethylene-Vinyl Alcohol Copolymer Modified with Silane Coupling Agent and Calcium Silicate Solutions. *Biomaterials* **2003**, *24* (10), 1729–1735.

(15) Cisneros-Pineda, O. G.; Herrera Kao, W.; Loría-Bastarrachea, M. I.; Veranes-Pantoja, Y.; Cauich-Rodríguez, J. V.; Cervantes-Uc, J. M. Towards Optimization of the Silanization Process of Hydroxyapatite for Its Use in Bone Cement Formulations. *Mater. Sci. Eng. C* **2014**, *40*, 157–163.

(16) Katsikogianni, M.; Missirlis, Y. F.; Harris, L.; Douglas, J. Concise Review of Mechanisms of Bacterial Adhesion to Biomaterials and of Techniques Used in Estimating Bacteria-Material Interactions. *European Cells and Materials*. AO Research Institute Davos 2004, pp 37–57.

(17) Khatoon, Z.; McTiernan, C. D.; Suuronen, E. J.; Mah, T.-F.; Alarcon, E. I. Bacterial Biofilm Formation on Implantable Devices and Approaches to Its Treatment and Prevention. *Heliyon* **2018**, *4* (12), e01067.
(18) Dunne, W. M.; Jr. Bacterial Adhesion: Seen Any Good Biofilms Lately? *Clin. Microbiol. Rev.* **2002**, *15* (2), 155–166.
(19) Chen, C. S.; Mrksich, M.; Huang, S.; Whitesides, G. M.; Ingber, D. E. Geometric Control of Cell Life and Death. *Science* **1997**, *276* (5317), 1425–1428.
(20) Russo, L.; Taraballi, F.; Lupo, C.; Poveda, A.; Jiménez-Barbero, J.; Sandri, M.; Tampieri, A.; Nicotra, F.; Cipolla, L. Carbonate Hydroxyapatite Functionalization: A Comparative Study towards (Bio)Molecules Fixation. *Interface Focus* **2014**, *4* (1), 20130040.
(21) Vallet-Regí, M.; González-Calbet, J. M. Calcium Phosphates as Substitution of Bone Tissues. *Prog. Solid State Chem.* **2004**, *32* (1–2), 1–31.
(22) Boanini, E.; Gazzano, M.; Bigi, A. Ionic Substitutions in Calcium Phosphates Synthesized at Low Temperature. *Acta Biomater.* **2010**, *6* (6), 1882–1894.
(23) Bir, F.; Khireddine, H.; Touati, A.; Sidane, D.; Yala, S.; Oudadesse, H. Electrochemical Depositions of Fluorohydroxyapatite Doped by Cu2+, Zn2+, Ag+ on Stainless Steel Substrates. *Appl. Surf. Sci.* **2012**, *258* (18), 7021–7030.
(24) Mocanu, A.; Furtos, G.; Rapuntean, S.; Horovitz, O.; Flore, C.; Garbo, C.; Danisteanu, A.; Rapuntean, G.; Prejmerean, C.; Tomoaia-Cotisel, M. Synthesis; Characterization and Antimicrobial Effects of Composites Based on Multi-Substituted Hydroxyapatite and Silver Nanoparticles. *Appl. Surf. Sci.* **2014**, *298*,
(25) Bettger, W. J.; O'Dell, B. L. A Critical Physiological Role of Zinc in the Structure and Function of Biomembranes. *Life Sci.* **1981**, *28* (13), 1425–1438.
(26) Thian, E. S.; Konishi, T.; Kawanobe, Y.; Lim, P. N.; Choong, C.; Ho, B.; Aizawa, M. Zinc-Substituted Hydroxyapatite: A Biomaterial with Enhanced Bioactivity and Antibacterial Properties. *J. Mater. Sci. Mater. Med.* **2013**, *24* (2), 437–445.
(27) Girija, E. K.; Kumar, G. S.; Thamizhavel, A.; Yokogawa, Y.; Kalkura, S. N. Role of Material Processing on the Thermal Stability and Sinterability of Nanocrystalline Hydroxyapatite. *Powder Technol.* **2012**, *225*, 190–195.
(28) Salih, V.; Patel, A.; Knowles, J. C. Zinc-Containing Phosphate-Based Glasses for Tissue Engineering. *Biomed. Mater.* **2007**, *2* (1), 11–20.
(29) Stanić, V.; Dimitrijević, S.; Antić-Stanković, J.; Mitrić, M.; Jokić, B.; Plećaš, I. B.; Raičević, S. Synthesis, Characterization and Antimicrobial Activity of Copper and Zinc-Doped Hydroxyapatite Nanopowders. *Appl. Surf. Sci.* **2010**, *256* (20), 6083–6089.
(30) Suchanek, W.; Yoshimura, M. Processing and Properties of Hydroxyapatite-Based Biomaterials for Use as Hard Tissue Replacement Implants. *J. Mater. Res.* **1998**, *13* (1), 94–117.
(31) Besra, L.; Liu, M. A Review on Fundamentals and Applications of Electrophoretic Deposition (EPD). *Prog. Mater. Sci.* **2007**, *52* (1), 1–61.
(32) Sarkar, P.; Nicholson, P. S. Electrophoretic Deposition (EPD): Mechanisms, Kinetics, and Application to Ceramics. *J. Am. Ceram. Soc.* **1996**, *79* (8), 1987–2002.
(33) Dong, G.; He, L.; Pang, D.; Wei, L.; Deng, C. An in Situ Study of the Deposition of a Calcium Phosphate Mineralized Layer on a Silicon-Substituted Hydroxyapatite Sensor Modulated by Bovine Serum Albumin Using QCM-D Technology. *Ceram.*

Int. **2016**, *42* (16), 18648–18656.
(34) Grunenwald, A.; Keyser, C.; Sautereau, A. M.; Crubézy, E.; Ludes, B.; Drouet, C. Revisiting Carbonate Quantification in Apatite (Bio)Minerals: A Validated FTIR Methodology. *J. Archaeol. Sci.* **2014**, *49*, 134–141.
(35) Monshi, A.; Foroughi, M. R.; Monshi, M. R. Modified Scherrer Equation to Estimate More Accurately Nano-Crystallite Size Using XRD. *Artic. World J. Nano Sci. Eng.* **2012**, *2*, 154–160.
(36) Muniz, F. T. L.; Miranda, M. A. R.; Morilla dos Santos, C.; Sasaki, J. M.; IUCr. The Scherrer Equation and the Dynamical Theory of X-Ray Diffraction. *Acta Crystallogr. Sect. A Found. Adv.* **2016**, *72* (3), 385–390.
(37) Puvvada, N.; Panigrahi, P. K.; Pathak, A. Room Temperature Synthesis of Highly Hemocompatible Hydroxyapatite, Study of Their Physical Properties and Spectroscopic Correlation of Particle Size. *Nanoscale* **2010**, *2* (12), 2631.
(38) Huang, Y. T.; Imura, M.; Nemoto, Y.; Cheng, C.-H.; Yamauchi, Y. Block-Copolymer-Assisted Synthesis of Hydroxyapatite Nanoparticles with High Surface Area and Uniform Size. *Sci. Technol. Adv. Mater.* **2011**, *12* (4), 045005.
(39) Tanaka, M.; Hayashi, T.; Morita, S. The Roles of Water Molecules at the Biointerface of Medical Polymers. *Polym. J.* **2013**, *45* (7), 701–710.
(40) Kataoka, T.; Shiba, K.; Tagaya, M. An Investigation into Nanohybrid States of Europium (III) Complex with Hydroxyapatite Nanocrystals. *Opt. Mater. (Amst).* **2018**, *84*, 252–258.
(41) Korsmeyer, R. W.; Von Meerwall, E.; Peppas, N. A. Solute and Penetrant Diffusion in Swellable Polymers. II. Verification of Theoretical Models. *J. Polym. Sci. Part B Polym. Phys.* **1986**, *24* (2), 409–434.
(42) Machín, R.; Isasi, J. R.; Vélaz, I. Hydrogel Matrices Containing Single and Mixed Natural Cyclodextrins. Mechanisms of Drug Release. *Eur. Polym. J.* **2013**, *49* (12), 3912–3920.
(43) Evans-Nguyen, K. M.; Jorgenson, W. *Studies Of The Influence Of Charge And Wettability On Fibrinogen Adsorption And Fibrin Formation At Surfaces Chapel Hill*; **2006**.
(44) Reza Gardeshzadeh, A.; Gardeshzadeh, A. R.; Raissi, B. *Thick Film Deposition of Carbon Nanotubes by Alternating Electrophoresis*; 2010.
(45) Beatrice Plešingerová, Gabriel Súèik, Martin Maryška*, D. H. Hydroxyapatite Coatings Deposited From Alcohol Suspensions By Electrophoretic Deposition On Titanium Substrate. *Ceramics* **2007**, *1*, 15–23.
(46) Zhitomirsky, I.; Gal-Or, L. Electrophoretic Deposition of Hydroxyapatite. *J. Mater. Sci. Mater. Med.* **1997**, *8* (4), 213–219.
(47) Brunauer, S.; Emmett, P. H.; Teller, E. *Adsorption of Gases in Multimolecular Layers*; **1938**.
(48) Barrett, E. P.; Joyner, L. G.; Halenda, P. P. The determination of pore volume and area distributions in porous substances. I. Computations from nitrogen isotherms. *J. Am. Chem. Soc.* **1951** *73* (1), 373–380.
(49) Tagaya, M.; Ikoma, T.; Takemura, T.; Okuda, M.; Hanagata, N.; Yoshioka, T.; Chakarov, D.; Kasemo, B.; Tanaka, M. Adsorption of Proteins Derived from Fetal Bovine Serum onto Hydroxyapatite Nanocrystals with Quartz Crystal Microbalance Technique. *Key Eng. Mater.* **2008**, *396–398*, 47–50.

(50) Tagaya, M.; Ikoma, T.; Migita, S.; Okuda, M.; Takemura, T.; Hanagata, N.; Yoshioka, T.; Tanaka, J. Fetal Bovine Serum Adsorption onto Hydroxyapatite Sensor Monitoring by Quartz Crystal Microbalance with Dissipation Technique. *Mater. Sci. Eng. B* **2010**, *173* (1–3), 176–181.

(51) Yamada, S.; Tagaya, M. Analytical Investigation of Hydration and Protein Adsorption Structures on Hydroxyapatite-Based Mesoporous Silica Particles. *Mater. Lett.* **2017**, *209*, 441–445. https://doi.org/10.1016/J.MATLET.2017.08.072.

(52) Barralet, J.; Best, S.; Bonfield, W. Carbonate Substitution in Precipitated Hydroxyapatite: An Investigation into the Effects of Reaction Temperature and Bicarbonate Ion Concentration. *J. Biomed. Mater. Res.* **1998**, *41* (1), 79–86.

(53) Bozym, R. A.; Chimienti, F.; Giblin, L. J.; Gross, G. W.; Korichneva, I.; Li, Y.; Libert, S.; Maret, W.; Parviz, M.; Frederickson, C. J.; et al. Free Zinc Ions Outside a Narrow Concentration Range Are Toxic to a Variety of Cells *in Vitro*. *Exp. Biol. Med.* **2010**, *235* (6), 741–750.

(54) Yasukawa, A.; Kandori, K.; Ishikawa, T. TPD-TG-MS Study of Carbonate Calcium Hydroxyapatite Particles. *Calcif. Tissue Int.* **2003**, *72* (3), 243–250.

(55) Kaflak, A.; Kolodziejski, W. Complementary Information on Water and Hydroxyl Groups in Nanocrystalline Carbonated Hydroxyapatites from TGA, NMR and IR Measurements. *J. Mol. Struct.* **2011**, *990* (1–3), 263–270.

(56) Tagaya, M.; Ikoma, T.; Takeguchi, M.; Hanagata, N.; Tanaka, J. Interfacial Serum Protein Effect on Biological Apatite Growth. *J. Phys. Chem. C* **2011**, *115* (45), 22523–22533.

(57) Brundavanam, R. K.; Poinern, G. E. J.; Fawcett, D. Modelling the Crystal Structure of a 30 Nm Sized Particle Based Hydroxyapatite Powder Synthesised under the Influence of Ultrasound Irradiation from X-Ray Powder Diffraction Data. *Am. J. M aterials Sci.* **2013**, *2013* (4), 84–90.

(58) Popa, C. L.; Deniaud, A.; Michaud-Soret, I.; Guégan, R.; Motelica-Heino, M.; Predoi, D. Structural and Biological Assessment of Zinc Doped Hydroxyapatite Nanoparticles. *J. Nanomater.* **2016**, *2016*, 1–10.

(59) Koutsopoulos, S. Synthesis and Characterization of Hydroxyapatite Crystals: A Review Study on the Analytical Methods. *J. Biomed. Mater. Res.* **2002**, *62* (4), 600–612.

(60) Tank, K. P.; Sharma, P.; Kanchan, D. K.; Joshi, M. J. FTIR, Powder XRD, TEM and Dielectric Studies of Pure and Zinc Doped Nano-Hydroxyapatite. *Cryst. Res. Technol.* **2011**, *46* (12), 1309–1316.

(61) Predoi, D.; Iconaru, S. L.; Deniaud, A.; Chevallet, M.; Michaud-Soret, I.; Buton, N.; Prodan, A. M. Textural, Structural and Biological Evaluation of Hydroxyapatite Doped with Zinc at Low Concentrations. *Materials (Basel).* **2017**, *10* (3).

(62) Costa, A. M.; de Almeida Soares, G. D.; Calixto, R.; Rossi, A. M. Preparation and Properties of Zinc Containing Biphasic Calcium Phosphate Bioceramics. *Key Eng. Mater.* **2003**, *254–256*, 119–122.

(63) Grunenwald, A.; Keyser, C.; Sautereau, A. M.; Crubézy, E.; Ludes, B.; Drouet, C. Revisiting Carbonate Quantification in Apatite (Bio)Minerals: A Validated FTIR Methodology. *J. Archaeol. Sci.* **2014**, *49*, 134–141.

(64) Lee, Y. J.; Elzinga, E. J.; Reeder, R. J. Sorption Mechanisms of Zinc on Hydroxyapatite: Systematic Uptake Studies and EXAFS Spectroscopy Analysis.

Environ. Sci. Technol. **2005**, *39* (11), 4042–4048.

(65) Feng, Y.; Gong, J.-L.; Zeng, G.-M.; Niu, Q.-Y.; Zhang, H.-Y.; Niu, C.-G.; Deng, J.-H.; Yan, M. Adsorption of Cd (II) and Zn (II) from Aqueous Solutions Using Magnetic Hydroxyapatite Nanoparticles as Adsorbents. *Chem. Eng. J.* **2010**, *162* (2), 487–494.

(66) Kay, M.I.; Young, R.A.; Posner, A.S. Crystal Structure of Hydroxyapatite. *Nature* **1964**, *204* (4963), 1050–1052.

(67) Astala, R.; Stott, M. J. First Principles Investigation of Mineral Component of Bone: CO3 Substitutions in Hydroxyapatite. *Chem. Mater.* **2005**, *17* (16), 4125–4133.

(68) Furuzono, T.; Wang, P.-L.; Korematsu, A.; Miyazaki, K.; Oido-Mori, M.; Kowashi, Y.; Ohura, K.; Tanaka, J.; Kishida, A. Physical and Biological Evaluations of Sintered Hydroxyapatite/Silicone Composite with Covalent Bonding for a Percutaneous Implant Material. *J. Biomed. Mater. Res.* **2003**, *65B* (2), 217–226.

(69) Siddiqui, H. A.; Pickering, K. L.; Mucalo, M. R. A Review on the Use of Hydroxyapatite-Carbonaceous Structure Composites in Bone Replacement Materials for Strengthening Purposes. *Materials* **2018**, *11* (10) 1813.

(70) Shih, W. J.; Chen, Y. F.; Wang, M. C.; Hon, M. H. Crystal Growth and Morphology of the Nano-Sized Hydroxyapatite Powders Synthesized from $CaHPO_4 \cdot 2H_2O$ and $CaCO_3$ by Hydrolysis Method. *J. Cryst. Growth* **2004**, *270* (1–2), 211–218.

(71) Wei, X.; Fu, C.; Savino, K.; Yates, M. Z. Carbonated Hydroxyapatite Coatings with Aligned Crystal Domains. *Cryst. Growth Des.* **2012**, *12* (7), 3474–3480.

(72) Chickerur, N. S.; Tung, M. S.; Brown, W. E. A Mechanism for Incorporation of Carbonate into Apatite. *Calcif. Tissue Int.* **1980**, *32* (1), 55–62.

(73) Matsunaga, K.; Murata, H.; Mizoguchi, T.; Nakahira, A. Mechanism of Incorporation of Zinc into Hydroxyapatite. *Acta Biomater.* **2010**, *6* (6), 2289–2293.

(74) Berzina-Cimdina, L.; Borodajenko, N. Research of Calcium Phosphates Using Fourier Transform Infrared Spectroscopy. *Infrared Spectrosc. - Mater. Sci. Eng. Technol.* **2012**, *12* (7), 251–263.

(75) Chen, S.; Li, L.; Zhao, C.; Zheng, J. Surface Hydration: Principles and Applications toward Low-Fouling/Nonfouling Biomaterials. *Polymer* **2010**, *51* (23), 5283–5293.

(76) Tanaka, M.; Mochizuki, A. Effect of Water Structure on Blood Compatibility - Thermal Analysis of Water in Poly(Meth)Acrylate. *J. Biomed. Mater. Res. - Part A* **2004**, *68* (4), 684–695.

(77) Peppas, N. A.; Sahlin, J. J. A Simple Equation for the Description of Solute Release. III. Coupling of Diffusion and Relaxation. *Int. J. Pharm.* **1989**, *57* (2), 169–172.

(78) Machín, R.; Isasi, J. R.; Vélaz, I. Hydrogel Matrices Containing Single and Mixed Natural Cyclodextrins. Mechanisms of Drug Release. *Eur. Polym. J.* **2013**, *49* (12), 3912–3920.

(79) Tagaya, M.; Scott, C.; Ikoma, T.; Tanaka, J. Handbook of Advanced Ceramics: Chapter 7.2. Application of a Quartz Crystal Microbalance with Dissipation for In Situ Monitoring of Interfacial Phenomena. **2013**.

(80) Plesingerova, B.; Sucik, G.; Maryska, M.; Horkavcova, D. Hydroxyapatite Coatings Deposited from Alcohol Suspensions by Electrophoretic Deposition on Titanium Substrate. *ceramics silikaty,* **2007**,*51*(1), 15.

(81) Monkawa, A.; Ikoma, T.; Yunoki, S.; Yoshioka, T.; Tanaka, J.; Chakarov, D.; Kasemo, B. Fabrication of Hydroxyapatite Ultra-Thin Layer on Gold Surface and Its

Application for Quartz Crystal Microbalance Technique. *Biomaterials* **2006**, *27* (33), 5748–5754.

(82) Zhitomirsky, D.; Roether, J. A.; Boccaccini, A. R.; Zhitomirsky, I. Electrophoretic Deposition of Bioactive Glass/Polymer Composite Coatings with and without HA Nanoparticle Inclusions for Biomedical Applications. *J. Mater. Process. Technol.* **2009**, *209* (4), 1853–1860.

(83) Hlaváč, J. Ceramic Coatings on Titanium for Bone Implants. *ceramics-silikaty.* **1999**, *43* (3), 133–139.

(84) Leofanti, G.; Padovan, M.; Tozzola, G.; Venturelli, B. Surface Area and Pore Texture of Catalysts. *Catal. Today* **1998**, *41* (1–3), 207–219.

(85) Sing, K. S. W.; Williams, R. T. Physisorption Hysteresis Loops and the Characterization of Nanoporous Materials. *Adsorpt. Sci. Technol.* **2004**, *22* (10), 773–782.

(86) Burda, C.; Chen, X.; Narayanan, R.; El-Sayed, M. A. Chemistry and Properties of Nanocrystals of Different Shapes. *Chem. Rev.* **2005**, *105* (4), 1025–1102.

(87) Ikoma, T.; Tagaya, M.; Hanagata, N.; Yoshioka, T.; Chakarov, D.; Kasemo, B.; Tanaka, J. Protein Adsorption on Hydroxyapatite Nanosensors with Different Crystal Sizes Studied *In Situ* by a Quartz Crystal Microbalance with the Dissipation Method. *J. Am. Ceram. Soc.* **2009**, *92* (5), 1125–1128.

(88) Tagaya, M.; Ikoma, T.; Hanagata, N.; Tanaka, J. Analytical Investigation of Protein Mediation Between Biomaterials and Cells. *Mater. Express* **2012**, *2* (1), 1–22.

(89) Tagaya, M.; Ikoma, T.; Takemura, T.; Hanagata, N.; Yoshioka, T.; Tanaka, J. Effect of Interfacial Proteins on Osteoblast-like Cell Adhesion to Hydroxyapatite Nanocrystals. *Langmuir* **2011**, *27* (12), 7645–7653.

(90) Kim, C.A.; Berg, J.M. Thermodynamic β -Sheet Propensities Measured Using a Zinc-Finger Host Peptide. *Nature* **1993**, *362* (6417), 267–270.

(91) Puvvada, N.; Panigrahi, P.; Pathak, A. Room Temperature Synthesis of Highly Hemocompatible Hydroxyapatite, Study of Their Physical Properties and Spectroscopic Correlation of Particle Size. *Nanoscale,* **2010**, *2* (12), 2631–2638.

(92) Ito, A.; Ojima, K.; Naito, H.; Ichinose, N.; Tateishi, T. Preparation, Solubility, and Cytocompatibility of Zinc-Releasing Calcium Phosphate Ceramics. *J. Biomed. Mater. Res.* **2000**, *50* (2), 178–183.

(93) Kaweeteerawat, C.; Ivask, A.; Liu, R.; Zhang, H.; Chang, C. H.; Low-Kam, C.; Fischer, H.; Ji, Z.; Pokhrel, S.; Cohen, Y.; et al. Toxicity of Metal Oxide Nanoparticles in *Escherichia Coli* Correlates with Conduction Band and Hydration Energies. *Environ. Sci. Technol.* **2015**, *49* (2), 1105–1112.

(94) Stanić, V.; Dimitrijević, S.; Antić-Stanković, J.; Mitrić, M.; Jokić, B.; Plećaš, I. B.; Raičević, S. Synthesis, Characterization and Antimicrobial Activity of Copper and Zinc-Doped Hydroxyapatite Nanopowders. *Appl. Surf. Sci.* **2010**, *256* (20), 6083–6089.

(95) Li, J.; Tan, L.; Liu, X.; Cui, Z.; Yang, X.; Yeung, K. W. K.; Chu, P. K.; Wu, S. Balancing Bacteria–Osteoblast Competition through Selective Physical Puncture and Biofunctionalization of ZnO/Polydopamine/Arginine-Glycine-Aspartic Acid-Cysteine Nanorods. *ACS Nano* **2017**, *11* (11), 11250–11263.

(96) Kim, T. N.; Feng, Q. L.; Kim, J. O.; Wu, J.; Wang, H.; Chen, G. C.; Cui, F. Z. Antimicrobial Effects of Metal Ions (Ag+, Cu2+, Zn2+) in Hydroxyapatite. *J. Mater.*

Sci. Mater. Med. **1998**, *9* (3), 129–134.

(97) Chen, C.; Mrksich, M.; Huang, S.; Whitesides, G. M.; Ingber, D. E. Geometric Control of Cell Life and Death. *Science*. **199**7, *276* (5317), 1425–1428

(98) Tang, Y.; Chappell, H. F.; Dove, M. T.; Reeder, R. J.; Lee, Y. J. Zinc Incorporation into Hydroxylapatite. *Biomaterials* **2009**, *30* (15), 2864–2872.

(99) Fujii, E.; Ohkubo, M.; Tsuru, K.; Hayakawa, S.; Osaka, A.; Kawabata, K.; Bonhomme, C.; Babonneau, F. Selective Protein Adsorption Property and Characterization of Nano-Crystalline Zinc-Containing Hydroxyapatite. *Acta Biomater.* **2006**, *2* (1), 69–74.

(100) Mavropoulos, E.; Hausen, M.; Costa, A. M.; Albuquerque, S. R.; Alves, G.; Granjeiro, J. M.; Rossi, A. M. Biocompatibility of Carbonated Hydroxyapatite Nanoparticles with Different Crystallinities. *Key Eng. Mater.* **2011**, *493–494*, 331–336..

(101) Uysal, I.; Severcan, F.; Tezcaner, A.; Evis, Z. Co-Doping of Hydroxyapatite with Zinc and Fluoride Improves Mechanical and Biological Properties of Hydroxyapatite. *Prog. Nat. Sci. Mater. Int.* **2014**, *24* (4), 340–349.

(102) Huang, X.; Teng, X.; Chen, D.; Tang, F.; He, J. The Effect of the Shape of Mesoporous Silica Nanoparticles on Cellular Uptake and Cell Function. *Biomaterials* **2010**, *31* (3), 438–448.

(103) Galindo, T. G. P.; Chai, Y.; Tagaya, M. Hydroxyapatite Nanoparticle Coating on Polymer for Constructing Effective Biointeractive Interfaces. **2019**, *2019.*

(104) Migita, S.; Tagaya, M.; Ikoma, T.; Takemura, T.; Okuda, M.; Yoshioka, T.; Hanagata, N.; Tanaka, J. Initial Adhesion Behavior of Fibroblasts onto Hydroxyapatite Nanocrystals. *Bioceram. Dev. Appl.* **2011**, *1*, D110165.

(105) Thian, E. S.; Konishi, T.; Kawanobe, Y.; Lim, P. N.; Choong, C.; Ho, B.; Aizawa, M. Zinc-Substituted Hydroxyapatite: A Biomaterial with Enhanced Bioactivity and Antibacterial Properties. *J. Mater. Sci. Mater. Med.* **2013**, *24* (2), 437–445.

Chapter 4

“Summary”

Chapter 4

Summary

In the area of biomedicine, a wide variety of medical devices had developed with the help of diagnosis and recovery of the patient's health. The most commonly used materials for the manufacture of these medical devices are biometals such as gold (Au), and titanium (Ti) and polymers such as polydimethylsiloxane (PDMS). Au has been used in creams and masks in the consumables, has also been used as an implant, as a drug delivery system (DDS), as a bactericide, and more recently cardiac patches have been designed to repair the myocardium of the infarcted heart. Ti has been used in many implants. However, it has been reported that these biometals can cause contact dermatitis and inflammation of the surrounding soft tissues, and long-term chronic cytotoxicity has reported. In the case of PDMS, its uses include blood containers, breast prostheses, contact lenses, DDS, cardiac pacemaker, facial prosthetics, artificial skin, finger joins, and percutaneous devices as catheters. However, the lack of binding to surrounding soft tissues can lead to inflammation, fibrous encapsulation, and tunnel infection. So that these materials, known as bio-inert, increase their cytocompatibility, it is necessary to develop a coating technique with a bioactive material such as hydroxyapatite.

Hydroxyapatite nanoparticles ($Ca_{10}(PO_4)_3(OH)_2$, HAp NPs) due to their similarity with the inorganic component of the hard tissues, have the ability to effectively bind with the cells, for that reason, the HAp NPs have been widely used in several biomedical applications, however, the interactive mechanism is not precise. Therefore, this study not only seeks to develop a composite material (bioinert-bioactive) with improved cytocompatibility but also to understand the interfacial phenomenon that occurs when this material is implanted.

In **Chapter 1**: "*General Introduction*," several studies have been tried to develop a material capable of regenerate bone. HAp NPs have been extensively researched in bone tissue engineering due to its compositional similarity to the mineral bone and their excellent cytocompatibility. However, HAp NPs has low mechanical strength, which limits its applications. Therefore, HAp NPs has been deposited on cytocompatible polymer matrix, obtaining a composite with enhanced mechanical, thermal and rheological properties and

also with and higher cytocompatibility and bioactivity. This chapter reviews some of the most common coating techniques for obtaining HAp NPs/polymer fusion interfaces as well as the in vitro studies of the interfacial interactions between the HAp NPs/polymer fusion interfaces and the cells, demonstrating better cytocompatibility. Studies above the interfacial interactions between the hydration layers, proteins, cells, and HAp NPs and how these interactions can be affected by the specific protein pre-adsorption are also mentioned.

In **Chapter 2**: "*Study on Preparation of Elliptical Hydroxyapatite Nanoparticle Films and Their Protein Mediation Ability for Cell Adhesion*", elliptical HAp NPs were synthesized by a wet chemical method using a Poly(oxyethylene) cholesteryl ether [ChEOn (n=15)] as a template, obtaining the elliptical hydroxyapatite (E–HAp) NPs, without ChEOn was received the needle-like HAp (N–HAp) NPs, E–HAp and N–HAp NPs were electrophoretically deposited on gold (Au) substrate. A comparative study of the hydration layer on Au, N–HAp, E–HAp NP films was achieved to investigate the interfacial effect of the hydration layers on the conformation of the adsorbed fibrinogen (Fgn) and fibroblast adhesion properties. As a result, the ratios of three types of hydration layer states analyzed by a Fourier transform infrared (FTIR) spectral deconvolution of the O–H stretching absorption band were 3%, 53% and 60% as free water, 0%, 27% and 30% as intermediate water, and 97%, 20% and 10% as non–freezing water. The ratio of bonding water state (i.e., intermediate and non-freezing waters) is almost same between two HAp NP films, the E–HAp NP film with the elliptical shape and smaller particle size exhibited the lowest ratio of non–freezing water, which can suppress the denaturation of the adsorbed protein. The Fibrinogen (Fgn) adsorption mechanism, interfacial interactions and conformational information on the E-HAp NP film surfaces were investigated using surface plasmon resonance (SPR) and Fourier transform infrared spectroscopy (FTIR). The FT-IR and SPR results demonstrated the higher affinity of Fgn for the HAp NP film. The physicochemical properties of the E-HAp NP film affected the protein conformation and orientation upon the adsorption through the surface-protein interactions, leading to the sufficient bioactivity for the cell binding. Subsequently, the FTIR spectral deconvolution results of the amide I band of the adsorbed Fgn on the E–HAp NP film indicated the higher content of α–helix and β–sheet structures as compared with those on the Au and N–HAp NP films, suggesting that the smaller amount of non–freezing waters would play an essential role in the stereoscopic

Fgn conformation. In the fibroblast culture in the films, the adhered cells started spreading with pseudopods formation in all the films. The cells had a more elongated appearance and had more pseudopod parts on E–HAp NP film than those on the Au and N–HAp NP films. The FT-IR spectra the adhered cells on the E–HAp NP, N–HAp NP and Au films exhibited the different absorbance intensities in the amide A, I, II, and III bands, suggesting the unusual amount of collagen-producing states by the cells interacted with the underground films, which were also supported by an immunostaining results of the collagen type I. Therefore, the different hydration structures on the films clearly influenced the conformation of the adsorbed protein, and the preferential formation was found at the interfaces between the fibroblasts and the underground E–HAp NP films.

The chain length (n) of the ChEOn with n= 15 used in the HAp NPs synthesis allows controlling the formation of the HAp NPs based on the organic/inorganic hybrids, leading to being the elliptical E–HAp NPs. The added amount of $ChEO_{15}$ during the synthesis plays a vital role in the shape, porosity, and surface specific area of the E–HAp NPs, which had a direct impact on the Fgn−surface interactions and the conformation of the adsorbed Fgn. The SPR was used to study the Fgn−surface interactions in a comparative study between the Au, N–HAp and E– HAp NP films. A comparative study of the hydration layer on Au, N–HAp and E–HAp NP films was achieved to investigate the interfacial effect of the hydration layers on the conformation of the adsorbed Fgn and fibroblast adhesion properties. It was demonstrated that the wettability of the Au substrate after a UV-ozone treatment was useful for the EPD deposition of the HAp NPs. The Fibrinogen (Fgn) adsorption mechanism, interfacial interactions and conformational information on the Au, N-HAp and E-HAp NP film surfaces were investigated using surface plasmon resonance (SPR) and Fourier transform infrared spectroscopy (FTIR). The FT-IR and SPR results demonstrated the higher affinity of Fgn for the HAp NP film. The physicochemical properties of the E-HAp NP film affected the protein conformation and orientation upon the adsorption through the surface-protein interactions, leading to the sufficient bioactivity for the cell binding. The deposition of the HAp NPs on the Au substrate was corroborated by the AFM images, where was observed as the different morphologies of the E–HAp and N–HAp NPs. The ratios of three types of hydration layer states analyzed by a Fourier transform infrared (FTIR) spectral deconvolution of the O–H stretching absorption band

were 3%, 53% and 60% as free water, 0%, 27% and 30% as intermediate water, and 97%, 20% and 10% as non–freezing water. Although the ratio of bonding water state (i.e., intermediate and non-freezing waters) is almost same between two HAp NP films, the E–HAp NP film with the elliptical shape and smaller particle size exhibited the lowest ratio of non–freezing water, which can suppress the denaturation of the adsorbed protein. Subsequently, the FTIR spectral deconvolution results of the amide I band of the adsorbed Fgn on the E–HAp NP film indicated the higher content of α–helix and β–secondary sheet structures as compared with those on the Au and N–HAp NP films, suggesting that the smaller amount of non–freezing waters would play an essential role in the stereoscopic Fgn conformation.

Furthermore, the higher content of free water molecules on the E–HAp NP film would promote the perpendicular end-on orientation of the adsorbed Fgn. In contrast, the Au and N–HAp NP films with the lower content of non–freezing water would promote the loss of α–helix and β–sheet structures, due to the side-on orientation, which causes the denaturation based on the loss of stereoscopic conformation. In the fibroblast culture in the films, the adhered cells started spreading with pseudopods formation in all the films. The cells had a more elongated appearance and had more pseudopod parts on E–HAp NP film than those on the Au and N–HAp NP films. The FT-IR spectra the adhered cells on the Au, N–HAp, and E–HAp NP films exhibited the different absorbance intensities in the amide A, I, II, and III bands, suggesting the unusual amount of collagen-producing states by the cells interacted with the underground films, which were also supported by an immunostaining results of the collagen type I. Therefore, the different hydration structures on the films clearly influenced the conformation of the adsorbed protein, and the preferential conformation was found at the interfaces between the fibroblasts and the underground E–HAp NP films by promoting the different ECM protein production and subsequent preferential binding.

In **Chapter 3**: "*Preparation and Biological Evaluation of Nanoparticle Zinc-substituted Hydroxyapatite Films*," Zn:HAp NPs were synthesized by a wet chemical method with a dopant concentration of Zn/(Ca+Zn) = 0.0, 2.5, 5.0 and 10 mol%. An electrophoretic deposition at the optimized voltage of 100 V was used for the surface modification of biomedical polymers. As a result, the nanocrystalline Zn:HAp NP films on the surfaces was

successfully achieved. The nanocrystalline Zn-substituted HAp NP films were characterized using thin-film-XRD and FTIR. The XRD and FTIR spectra are similar between both nanocrystals. The nanocrystalline Zn-substituted HAp NP films with the initial HAp (Ca+Zn)/P ratio of 2.00 corresponding to the peak carbonate ions is more pronounced than for the nanocrystalline Zn-substituted HAp NP films with the initial HAp (Ca+Zn)/P ratio of 1.67. Also, the deposited Zn:HAp NPs on three different catheters were successfully achieved. Due to the medical catheters is a complex component, the surface of the catheter is conductive for preventing static electricity, and occur the EPD of the Zn:HAp NPs on the surfaces of the catheters. Because it is desired to use this material as a covering material for biomedical applications, the dissolution test is essential. 5.0–Zn:CHAp and 10.0–Zn:CHAp NPs showed the highest dissolution behavior, these results are in agreement with the hydration layer results, were 5.0–Zn:CHAp NPs and 10.0–Zn:CHAp NPs has higher bonding water ratio, corroborating that the incorporation of carbonate ions enhanced the adsorption of hydration layer and promote the dissolution. Nanocrystalline Zn-substituted HAp NP films were evaluated by *in vitro* assays with NIH3T3 fibroblast cells. In the fibroblast compatibility test, all the nanocrystalline Zn-substituted HAp NP films presented higher bio- and cytocompatibility as compared with only the polymer substrate using the reference PDMS, nevertheless the nanocrystalline Zn-substituted HAp NP films with the initial HAp (Zn+Ca)/P ratio=2.00 showed better possibility of usage for tissue engineering scaffold because the nanocrystalline Zn-substituted HAp NP films with the initial HAp (Zn+Ca)/P ratio=2.00 presented the higher bio- and cytocompatibility, more cell density and aspect ratio than the nanocrystalline Zn-substituted HAp NP films with the initial HAp (Zn+Ca)/P ratio=1.67. The nanocrystalline Zn-substituted HAp NP film with the initial HAp (Zn+Ca)/P ratio=2.00 and, in particular, Zn concentration of 5.0 mol% was the more cytocompatible sample with the highest cell density amount. These results indicated that the properties of the Zn:HAp NPs deposited in the conductive polymer films affected the adhesion and spreading of the fibroblast cells, and the best conditions were Zn:HAp NPs with the initial HAp Ca/P =2.00 and Zn/(Ca+Zn)=5 mol%. For the antibacterial activity, *E. coli* DH5α was used in the experimental procedure of the exposure and culture (fist culture) on the sample films, and the cultured bacteria were extracted from the sample films after 17 hours and the

subsequent viable bacterial growth culture (second culture) and finally counting the viable *E. coli* DH5α colonies after 24 h were conducted. In general, viable *E. coli* DH5α colonies could still observed for all the nanocrystalline Zn-substituted HAp NP films. In the nanocrystalline Zn-substituted HAp NP films with the initial (Zn+Ca)/P of 1.67 and 2.00 with increasing concentration of Zn, the number of viable bacteria decreased. The lowest amount of viable bacteria was at the concentration of 10 mol%, indicating the anti-bacterial properties. However, the nanocrystalline Zn-substituted HAp NP films with the initial HAp NPs (Zn+Ca)/P ratio of 2.00 exhibits less number of viable *E. coli* DH5α colonies at the concentration of 10 mol% than the nanocrystalline Zn-substituted HAp NP films with the initial (Zn+Ca)/P ratio of 1,67 at the same concentration. The lowest amount of viable *E. coli* DH5α colonies was with the nanocrystalline Zn-substituted HAp NP films with initial (Zn+Ca)/P ratio of 2.00 containing 10.0 mol% of Zn ion. It was successfully demonstrated the antibacterial properties.

The chemically precipitated Zn-substituted HAp NPs (initial (Zn+Ca)/P ratio of 1.67 and initial (Zn+Ca)/ratio of 2.0 and containing 0, 2.5, 5.0 and 10.0 mol%) were electrophoretically deposited on a conductive polymer substrate as a continuous coating without cracks. The Zn:HAp NPs coatings provide a bioactive surface as compared with only the medical polymer substrate for fibroblast growth. The Zn-substituted HAp NP films showed viable cell reduction of *E. coli* DH5α colonies. The reduction assay suggested that the n Zn-substituted HAp NP films were capable of inhibiting bacteria growth; nevertheless, for ultimately prevent bacterial infections it is necessary to provide more amount of Zn in practical applications. Therefore, the Zn-substituted HAp NP films on biomedical polymer surfaces were summarized to provide excellent cytocompatibility as well as antibacterial properties, suggesting useful catheter surface modification techniques of these materials.

Understanding the interfacial interactions between the HAp NPs-hydration layer-protein adsorption for cells adhesion, allows designing and developing more cytocompatible biomedical devices using a mild coating technique to minimize the patient's immune reactions.

Achievement List

Publication Papers

1. Tania Guadalupe Peñaflor Galindo, Iori Yamada, Shota Yamada, Motohiro Tagaya, "Studies on Preparation of Surfactant-assisted Elliptical Hydroxyapatite Nanoparticles and Their Protein-Interactive Ability.", ***Materials Chemistry and Physics***, 221, 367–376 (2019).
2. Tania Guadalupe Peñaflor Galindo, Takuya Kataoka, Shuji Fujii, Mitushiro Okuda, Motohiro Tagaya, "Preparation of Nanocrystalline Zinc-substituted Hydroxyapatite Films and Their Biological Properties", ***Colloids and Interface Science Communications,*** 10-11, 15–18 (2016).
3. Tania Guadalupe Peñaflor Galindo, Takuya Kataoka, Motohiro Tagaya, "Morphosynthesis of Zn-substituted Stoichiometric and Carbonate Hydroxyapatite Nanoparticles and Their Cytotoxicity in Fibroblasts", ***Journal of Nanomaterials***, Volume 2015, Article ID: 376045, 8 pages (2015).

Other Related Publication Papers

1. Tania Guadalupe Peñaflor Galindo, Yadong Chai, Motohiro Tagaya, "Hydroxyapatite Nanoparticle Coating on Polymer for Constructing Effective Biointeractive Interfaces.", ***Journal of Nanomaterials***, Volume 2019, Article ID 6495239, 23 pages (2019).
2. Tania Guadalupe Peñaflor Galindo, Kota Shiba, Motohiro Tagaya, "Particulate Titania Coating on Poly(dimethylsiloxane) Films for Improving Osteoconductive Ability.", ***Key Engineering Materials***, 782, 151–157 (2018).

Presentation in International Conference and Symposium

1. Shota Yamada, Tania Guadalupe Peñaflor Galindo; Motohiro Tagaya, "Preparation of Nanoporous Silica/Hydroxyapatite Hybrid Particles for Effectively Controlling Protein-interactions.", ***The 11th International Conference on the Science and Technology for Advanced Ceramics***, 2019 年 7 月 (Tsukuba, Japan).
2. Peñaflor Galindo Tania Guadalupe, Kota Shiba, Motohiro Tagaya, "Particulate Titania Coating on Poly(dimethylsiloxane) Films for Improving Osteoconductive Ability", ***30th Symposium and Annual Meeting of the International Society for Ceramics in Medicine – Bioceramics 30***, 2018 年 10 月 (Higashiyama Campus, Nagoya University, Japan).
3. Tania Guadalupe Peñaflor Galindo, Iori Yamada, Motohiro Tagaya, "Effect of Non-ionic Surfactant Organization on Hydroxyapatite Nanocrystal Formation", ***The 8th International Symposium on Surface Science (ISSS-8)***, 2017 年 10 月 (Tsukuba, Japan).

4. Tania Guadalupe Peñaflor Galindo; Tadashi Yamaguchi; Motohiro Tagaya, “Synthesis of Zinc-Containing Hydroxyapatite Nanocrystals towards Catheter Surface Modification”, ***MANA International Symposium 2015***, 2015 年 10 月 (Tsukuba, Japan).

Presentation in Domestic Conference and Symposium.

1. Tania Guadalupe Peñaflor Galindo, Motohiro Tagaya, “Biological Evaluation of Synthesized Zn-substituted Stoichiometric and Carbonate Apatite Nanocrystals”, ***The 1st Nanobioceramic-based Cell Function Control Technology Workshop***, 2015 年 8 月 (Nagaoka, Japan).